Investigating the role of nuclear packing in neuroepithelial development

Lucrezia Camilla Ferme

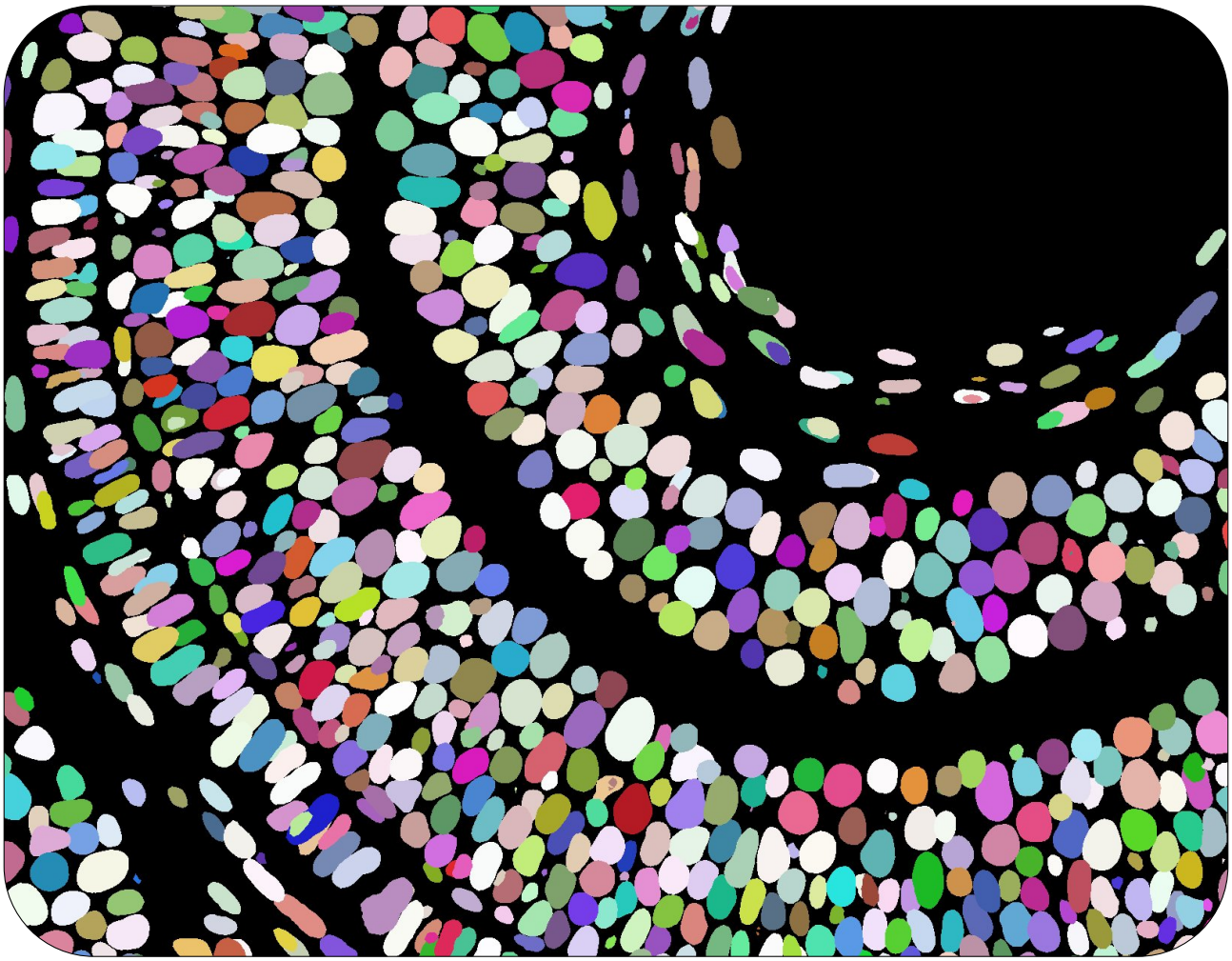

Dissertation presented to obtain the **Ph.D degree in**

Integrative Biology and Biomedicine

Oeiras, August, 2024

INSTITUTO DE TECNOLOGIA QUÍMICA E BIOLÓGICA ANTÓNIO XAVIER | UNIVERSIDADE NOVA DE LISBOA

Investigating the role of nuclear packing in neuroepithelial development

This document was created with the (pdf/Xe/Lua)LaTeX processor and the NOVAthesis template (v7.1.27) [121].

The work described in this PhD thesis received financial support from **Fundação Calouste Gulbenkian, Fundação para a Ciência e a Tecnologia**, and the **European Research Council** through the grants: FCT PhD studentship 2020.06407.BD, awarded to Lucrezia C. Ferme; ERC Consolidator Grant ERC-2018-COG-819046 - makingtheretina, awarded to Dr. Caren Norden.
This work was conducted at Instituto Gulbenkian de Ciência (IGC), Oeiras, Portugal, under the supervision of Dr. Caren Norden.

Acknowledgements

First and foremost, I would like to express my deepest gratitude to my scientific mentor, Caren Norden, for always supporting me over the past few years. It was important to know that I could count on her guidance, even when I was disheartened and wanted to quit. I am thankful for the trust she gave me, as she let me take in a project that was completely different from every other ones in the lab. Even though we both embarked on a journey that was quite challenging (I had to find my own way to lead this project and she had to lead a whole research institute as the new scientific director), I knew I could always count on her prompt and honest feedback, both for scientific and personal matters, and this was extremely helpful and valuable to me. I am also grateful for all the amazing opportunities I was given to educate myself, extend my network and be exposed to diverse stimulating environments, for instance during my frequent visits to the MPI-CBG and my participation to the Embriology course at Woods Hole. I was looking for a good mentor and I found a great one. Thank you for all the fish!

I would like to thank our main collaborator, Carl Modes, for his extremely valuable insights and his contribution to the development of this project. I am so grateful for the warm welcome I received when visiting his group and for his constant commitment to the project. I am extremely thankful to Robert Haase, another outstanding collaborator, for his joy and his generosity in sharing with me his expertise in image analysis. Working with Robert was for sure one of the highlights of my PhD. Moreover, I would like to express all my gratitude to Elias Barriga and Moises Mallo for their feedback and guidance during my TAC meetings.

A special thanks to my colleagues in the Norden lab and in the Modes group, current and past members, for always sharing insightful comments on my project and for all the good moments we spent inside and outside of IGC in Lisbon and MPI-CBG/CSBD in Dresden. In particular, I want to thank Diana Garcia Morales for all the good chats about science and life in general. They really helped me to keep positive. I thank Elisa Nerli for always being a curious and stimulating person to talk to, besides being a great partner for

our occasional fun bike rides around Sintra. I also want to thank Mauricio Rocha-Martins, Patricia Ramos and Jaakko Lethimaki for the extremely valuable inputs and scientific discussions, in addition to the fun chatting during lunch about whatever, but especially climbing. I also want to thank the Modes group, in particular Allyson, for their help and friendship.

All this work would have not been possible without the IGC facilities: I would like to thank the Zebrafish facility, the Advanced imaging Unit, the Hystopathology Unit and the Microfabrication service and the Education and Training Unit at IGC, with a special mention to Ana Aranda. In addition, I would like to thank Riccardo Maraspini from the Imaging facility at MPI-CBG for his help during my visit.

To all the people who shared meaningful moments with me outside the lab and who made the completion of this journey possible.: thank you. I am so thankful for having moved to Lisbon with Rocco, one of my best friends, and to have found there my dear friend Chloé. Both of them made living in Lisbon before, during and after the pandemic a bearable experience at first and an exciting adventure later on. I thank Christian for being at times the best friend I needed and for sharing doubts and laughs over the course of our PhD journey. I would like to thank my portuguese family, the cooperative Rizoma, since it enabled me to actually feel part of this city, to integrate for real and to meet outstanding people from all paths of life, like my surf partners Iona and Vattani.

Last but not least, I would like to express my biggest gratitude to my family and my friends back in Italy. Doing a PhD can be quite challenging on someone's mental health, but you all helped me out immensely. To Sofia, Charlotte, Sara for being my best friends and lifeline since forever. To all the rest of the crew, i.e. Tea, Chiara, Francesca, Rocco, Ale (Uzzo), Ascanio, Pietro, Daniele, thank you for making me feel at home whenever and wherever, you represent the most genuine form of friendship I know. To my parents, Silvia and Cristiano, for always supporting me and lending me a listening ear whenever I needed. Everything I accomplished so far was possible because of your love, thus the least I can do is to dedicate this dissertation to you.

Thank you all.

”

“O caos é uma ordem por decifrar.”

— José Saramago, O homem duplicado
(Writer and journalist)

Abstract

Pseudostratified epithelia (PSE) are critical for organogenesis across various species due to their unique structure, where elongated cells with nuclei positioned at different levels create dense nuclear stratification. This configuration is hypothesized to enhance cell packing within a monolayered tissue, potentially aiding in precise organ development. The current study aimed to investigate this hypothesis by employing advanced deep learning techniques to achieve accurate 3D segmentation of nuclei in the zebrafish retina during its development.

To accomplish this, we imaged the zebrafish retina at multiple developmental stages and trained a StarDist model to segment nuclei within this densely packed tissue. The resulting segmentation enabled the development of an image analysis pipeline that extracted single-nuclear features, allowing for the quantification of key tissue-wide parameters, such as local nuclear alignment and neighborhood statistics. This capability allowed us to monitor changes in nuclear orientation and provided insights into the physical properties of the developing retina, which are challenging to measure directly. Through this approach, we observed that retinal PSE approach theoretical maximum packing densities just before neuronal lamination, with distinct packing states corresponding to different nuclear layers within the laminated retina. Comparing these findings to nuclear packing in the developing hindbrain PSE revealed that nuclear density in this tissue increases only upon neuronal lamination. Nevertheless, both neuroepithelia exhibited a nematic-like order, characterized by orientationally ordered yet positionally disordered nuclei, indicating that this structure is a hallmark of pseudostratification. regardless of packing densities. As the laminated retina matured, this nematic-like order transitioned toward a more crystalline-like structure, although nuclei retained long-range orientation along the radial axis of the tissue.

Our study also demonstrated that mechanical properties of the retinal PSE were sensitive to perturbations in cell number and nuclear packing density, with disruptions leading to tissue buckling. Direct perturbation of the architecture of the retinal PSE also led to shape deformations of the neural retina, even though neuronal precursors managed to navigate to their final position and form all the three layers of a mature retina.

Additionally, neurogenesis played a pivotal role in remodeling nuclear shape over time, significantly influencing the growth and morphology of the developing retina.

These findings were made possible through comprehensive 3D nuclear segmentation during the proliferative and neurogenic phases of retinal development. Coupled with genetic and mechanical perturbations and the use of transgenic reporter lines, this research illuminated the emergent physical architecture of the developing zebrafish retina. The insights gained from this study provide a quantitative framework for understanding nuclear packing in proliferative PSE, with potential applications in guiding future experimental designs and establishing similar frameworks for studying epithelial structures in other developmental contexts.

Keywords: pseudostratified epithelia, nuclear packing, 3D segmentation, neurogenesis, retina

Resumo

Os epitélios pseudoestratificados (PSE) são fundamentais para a organogénese em várias espécies devido à sua estrutura única, em que células alongadas com núcleos posicionados a diferentes níveis criam uma estratificação nuclear densa. Esta configuração é hipotetizada para melhorar o empacotamento celular dentro de um tecido monocamada, potencialmente ajudando no desenvolvimento preciso de órgãos. O presente estudo teve como objetivo investigar essa hipótese empregando técnicas avançadas de aprendizado profundo para obter uma segmentação 3D precisa de núcleos na retina do peixe-zebra durante seu desenvolvimento.

Para conseguir isso, nós capturamos imagens da retina do peixe-zebra em vários estágios de desenvolvimento e treinamos um modelo StarDist para segmentar núcleos dentro desse tecido densamente compactado. A segmentação resultante permitiu o desenvolvimento de um pipeline de análise de imagem que extraiu caraterísticas de um único núcleo, permitindo a quantificação de parâmetros-chave em todo o tecido, como o alinhamento nuclear local e as estatísticas de vizinhança. Esta capacidade permitiu-nos monitorizar alterações na orientação nuclear e forneceu informações sobre as propriedades físicas da retina em desenvolvimento, que são difíceis de medir diretamente. Através desta abordagem, observámos que o PSE da retina se aproxima de densidades de empacotamento máximas teóricas imediatamente antes da laminação neuronal, com estados de empacotamento distintos correspondentes a diferentes camadas nucleares dentro da retina laminada. A comparação destes resultados com o empacotamento nuclear no PSE do rombencéfalo em desenvolvimento revelou que a densidade nuclear neste tecido aumenta apenas após a laminação neuronal. No entanto, ambos os neuroepitélios exibiram uma ordem do tipo nemático, caracterizada por núcleos ordenados orientacionalmente, mas desordenados posicionalmente, indicando que essa estrutura é uma marca registrada da pseudoestratificação, independentemente das densidades de empacotamento. À medida que a retina laminada amadurecia, esta ordem do tipo nemático transitou para uma estrutura mais cristalina, embora os núcleos mantivessem uma orientação de longo alcance ao longo do eixo radial do tecido.

O nosso estudo também demonstrou que as propriedades mecânicas do PSE da retina

eram sensíveis a perturbações no número de células e na densidade de empacotamento nuclear, com rupturas que levavam à deformação do tecido. A perturbação direta da arquitetura da PSE da retina também conduziu a deformações da forma da retina neural, embora os precursores neuronais tenham conseguido navegar até à sua posição final e formar as três camadas de uma retina madura. Adicionalmente, a neurogénese desempenhou um papel fundamental na remodelação da forma nuclear ao longo do tempo, influenciando significativamente o crescimento e a morfologia da retina em desenvolvimento.

Estas descobertas foram possíveis através da segmentação nuclear 3D abrangente durante as fases proliferativa e neurogénica do desenvolvimento da retina. Juntamente com perturbações genéticas e mecânicas e com a utilização de linhas de repórteres transgénicos, esta investigação iluminou a arquitetura física emergente da retina do peixe-zebra em desenvolvimento. Os conhecimentos adquiridos com este estudo fornecem um quadro quantitativo para a compreensão do empacotamento nuclear na PSE proliferativa, com potenciais aplicações na orientação de futuras concepções experimentais e no estabelecimento de quadros semelhantes para o estudo de estruturas epiteliais noutros contextos de desenvolvimento.

Palavras-chave: epitélios pseudoestratificados, empacotamento nuclear, segmentação 3D,, neurogénese, retina

Contents

List of Figures

List of Tables

Acronyms

ACs Amacrine Cells
AEL after egg laying
AFM Atomic Force Microscopy
AiP Apoptosis-inducing pathway
aPKC atypical Protein Kinase C
ASPP1 Apoptosis Stimulating Protein of p53
Atoh7 Atonal bHLH transcription factor 7

BCs Bipolar Cells
BMP Bone Morphogenetic Protein

CMZ Ciliary Marginal Zone
CNS Central Nervous System

Dkk-1 Dickkopf 1
Dpp Decapentaplegic

ECM Extracellular Matrix

FCC Face-Centered Cubic
FGF Fibroblast Growth Factor
FGFR FGF receptor

GFP Green Fluorescent Protein

HCP Hexagonal-Close Packing
HCs Horizontal Cells
Hdac-1 Histone deacetylase 1
hpf hours post fertilization

IKNM Interkinetic Nuclear Migration
INL Inner Nuclear Layer
IPL Inner Plexiform Layer

KD Knock Down
KO Knock Out

LSCM Laser Scanning Confocal Microscopy
LSFM Light-sheet Fluorescence Microscopy

MBT Midblastula transition
MDCK Madin-Darby Canine Kidney cells
MG Müller Glia

ONL Outer Nuclear Layer
OPL Outer Plexiform Layer

PCP Planar Cell Polarity
PRs Photoreceptors
PSE Pseudostratified Epithelia
PSNE Pseudostratified Neuroepithelia
PTEN Phosphatase and TENsin homolog
Ptf1a Pancreas-associated transcription factor 1a

RCP Random Close Packing
RDF Radial Distribution Function
RFP Red Fluorescent Protein
RGCs Retinal Ganglion Cells
RGL Retinal Ganglion cell Layer
RLP Random Loose Packing
RNAi RNA interference
RNE Retinal Neuroepithelium
ROI Region of interest
RPE Retinal Pigmented Epithelium
Rx Retinal homeobox

SHH Sonic Hedgehog

TGF-β Transforming Growth Factor β

Vsx1 Visual system homeobox gene 1,

Wnt Wingless/Int-1

ZO Zonula Occludens

1 Introduction

1.1 Form follows function

Organogenesis is a multistep process that encompasses the coordination of several cellular events, including proliferation, differentiation and cell migration. Organogenesis ultimately results in the formation of functional organs, each with a specific structure and tasks necessary for the organism's survival or reproduction. This process relies on the complex interplay of genetic, biochemical, and physical factors that guide the formation of well-defined tissue architecture and ensure proportional and reproducible tissue patterning. However, it is still not fully understood how the interplay of these factors is coordinated in space and time to ensure tissue growth and the formation of ordered tissue arrangements during organogenesis. One outstanding example of the orchestration between proliferation and differentiation programmes during development is the formation of the central nervous system (CNS), where progenitor cells proliferate to promote growth while generating postmitotic neurons that relocate within the tissue to the positions at which they later function. The formation of neuronal layers, where different neuronal types are separated and packed in an ordered fashion, ensure that a functional nervous system is formed [7]. Thus, when the positioning of progenitor stem cells and neuronal precursors is impaired, mature tissues are pathological or dysfunctional [33]. While many studies have shed a light on how proliferation and neurogenesis are genetically encoded and regulated, little is known about the physical principles that govern morphogenesis in the CNS and how ordered structures arise during development of densely packed neural tissues.

Neurons canonically originate from pseudostratified epithelia (PSE), which are prominent tissue arrangements serving as organ precursors in diverse developmental contexts [135]. Most areas of the CNS including the neocortex, neural tube and retina derive from PSE as do brain and retinal organoids [53, 146, 113]. Thus, PSE appear to be highly conserved as organ precursor not only across evolution, but also in in vitro neural tissues. The broad occurrence of PSE in development suggests an advantage of this tissue arrangement for organogenesis, especially in the CNS. However, it is still poorly understood what

characteristics make pseudostratification a functionally relevant tissue arrangement for neuroepithelial development.

While many hypotheses have been made regarding the advantages of pseudostratification for organogenesis, none of them has been formally proven by a conclusive study. However, three main characteristics of PSE seem to be conserved: elongated epithelial cell shape, cell-cycle-dependent nuclear translocations and tissue packing. Several studies have focused on characterizing the molecular machineries involved in cell shape changes and nuclear movements in PSE, whilst little is known regarding the effects that increasing tissue packing can have on the morphogenesis of proliferating neuroepithelia. Recent studies have proposed that nuclear positioning and packing could drive mechanical changes in developing neuroepithelia [42, 100]. Though, these findings have been limited to two-dimensional (2D) analysis and do not capture the complexity of the three-dimensional (3D) nature of the tissue. A 3D characterization of densely packed PSE can have the potential to guide further investigations of morphogenesis in pseudostratified neuroepithelia to better understand how ordered cell arrangements emerge during the formation of the CNS.

In the next sections, I will introduce the key features that characterize pseudostratification and describe the heterogeneity of PSE in several developmental contexts, with a special focus on the vertebrate CNS. Then, I will discuss recent studies that delve into the role of tissue packing in the regulation of cellular events and tissue fluidity in biological systems. Lastly, I will introduce the model system used in this study, i.e. zebrafish retinal neuroepithelium, and argue why the vertebrate retina is an optimal system to study the emergence of ordered tissue patterning during organogenesis.

1.2 Pseudostratified epithelia

Epithelia are composed of confluent layers of epithelial cells that are generally found at the interface between the external environment and internal organs to form a protective barrier against pathogens and various toxic agents. Besides protecting the body, epithelia can filter molecules to promote selective absorption of nutrients and excretion of waste products or to regulate osmosis. To achieve all this, epithelial cells are tightly connected to one another via adherent and tight junctions and form a quasi-impenetrable tissue sheet. Epithelia are generally classified based on the number of cell layers that form them, i.e. simple or monolayered versus stratified or multi-layered, and based on the shape of their cells, i.e. squamous, cuboidal or columnar (Fig. 1.1) [134]. A particular type of simple epithelia are the so-called Pseudostratified Epithelia, where nuclei are arranged at different positions along the apicobasal axis, therefore giving the impression of stratification, but cells are elongated and basally attached to the basement membrane. Unlike other epithelia, PSE serve as barriers only in few instances within the adult organism, where their cilia play a crucial role in physiology of the organ. For example, in humans, they can be typically found in the respiratory tract, including the nasal cavity, trachea, and bronchi, as well as in parts of the male reproductive system, such as the epididymis and vas deferens [134].

More widely, PSE are often found as organ precursors in many developmental contexts across evolution. For example, PSE are found building the Drosophila imaginal discs and optic lobe and the embryonic ectoderm of Nematostella [135, 174].In vertebrates, they are involved in organogenesis of liver, lungs, pancreas, nasal placode epithelia, otic and optic vesicles and most parts of the CNS [29, 152]. Additionally, several organoids, including retinal and cerebral organoids, derive from PSE [53, 146, 113].

Overall, the broad occurrence of PSE as basic tissues for emerging organs suggests an advantage of this tissue arrangement for successful organogenesis. However, how exactly pseudostratification could positively influence organ development is not yet clear.

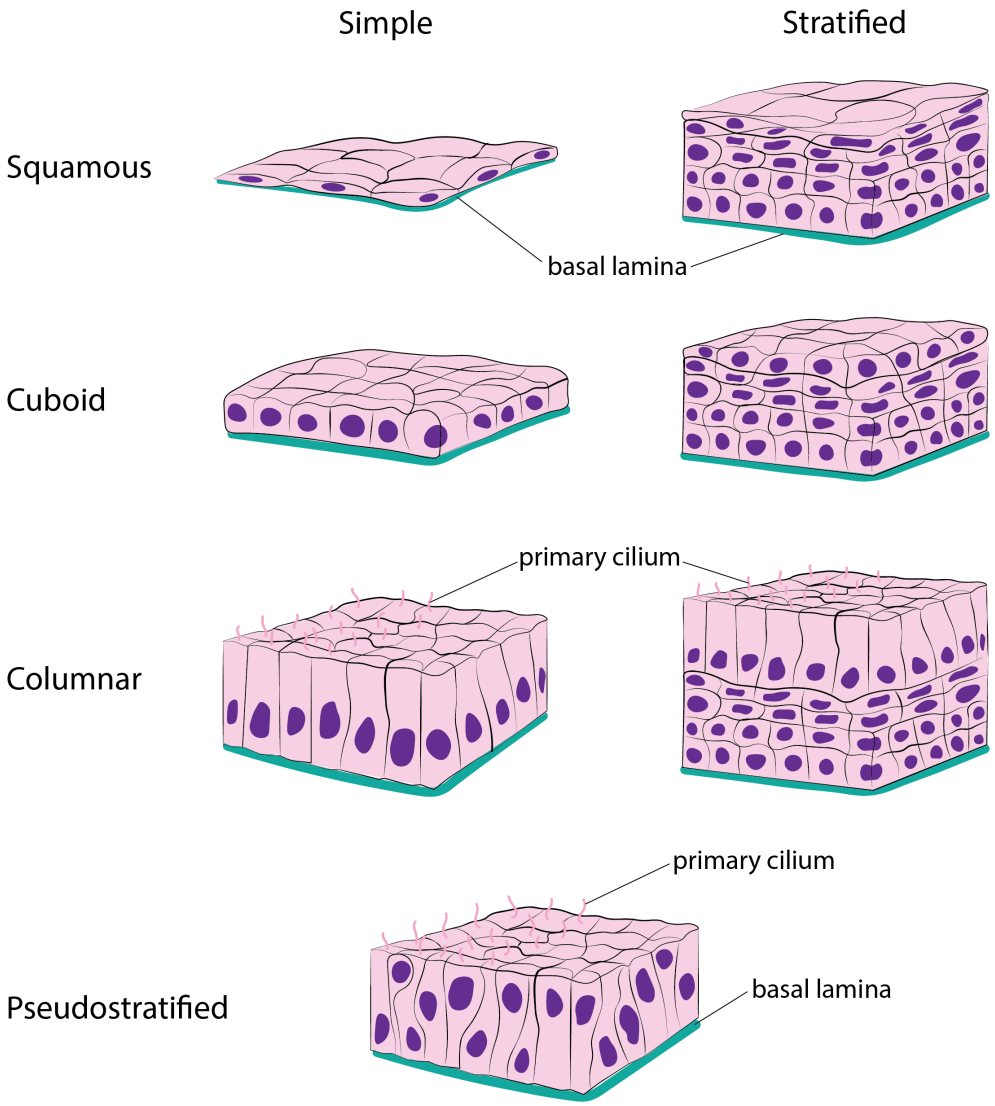

Figure 1.1: **Classification of epithelial tissues.** Simple epithelia are composed of one cell layer, while stratified epithelia features several layers. Depending on their cell shape, epithelia are generally classified into squamous, cuboid or columnar. Pseudostratified epithelia are a type of simple columnar epithelium showing an apparent multilayered arrangement.

1.2.1 Cell biology of PSE

Pseudostratification defines a particular arrangement observed in epithelial tissues, called pseudostratified epithelia (PSE), where cells feature elongated shapes and their nuclei position at different depths along the apicobasal axis(Fig. 1.2). This nuclear arrangement gives the impression of stratification, when in reality all cells within the tissue touch both the apical and basal surfaces and the epithelium is organized in a single layer [176, 189]. Epithelial cells within PSE share many features with other epithelia: they are characterized by clear apicobasal polarity, feature apical adherens and tight junctions and attach to the extracellular matrix via specialized basal processes. The identity of the apical polarity domain is of fundamental importance for pseudostratification and is determined by a set of conserved polarity factors, like the Par and Crumbs complexes and the scaffolding protein PALS1/Stardust [10, 34]. One of the main effectors of apical identity is the atypical Protein Kinase C (aPKC), which is part of the Par complex [10]. Localization of aPKC is restricted to the apical side, where this kinase phosphorylates other junctional and lateral polarity factors, such as Par-3, to exclude them from the apical domain [141]. In addition to this, aPKC has been shown to regulate actomyosin distribution in several epithelial contexts [171, 56]. In the zebrafish retinal PSE, alteration of aPKC localization interferes with the structure of the actin cytoskeleton and impairs apical mitosis [199]. As a result, neuroepithelial cells divide subapically and daughter cells fail to reintegrate correctly into the tissue, leading to perturbation of the overall tissue architecture [86, 199]. Therefore, preserving apical polarity and apical mitosis is crucial to ensure correct development of those organs that originate from PSE. Besides these polarity factors, the apical domain is characterized by the presence of the centrosome, which is found at apical positions throughout the cell cycle.

The centrosome contains a pair of centrioles, an evolutionary conserved microtubule-based structure, and a matrix of pericentriolar material and it acts as the main microtubule-organizing factor in most animal cells (the structure and functions of the centrosome are extensively reviewed in Conduit et al, 2015 [44]). The positioning of the centrosome is generally associated with the location of the primary cilium at the apical end-foot (Fog. 1.2), since it serves as a basal body for the emergence of cilia (biogenesis of the primary cilium is reviewed in Breslow and Holland, 2019[31]). The centrosome moves away from the apical side only upon entry into mitosis, when it moves basically to meet the nucleus. While centrosomes contribute to the efficiency of the mitotic spindle assembly, they are not essential for mitosis and, in some PSE, they are not a prerequisite for apical nuclear translocation [199]. While the centrosome is always found at the apical side, the Golgi apparatus is located apically to the nucleus, more specifically in the apical process of epithelial cells, but it is not pericentrosomal [203]. Interestingly, the Golgi relocate to the basal process upon delamination of neuronal progenitors, in line with the general notion that this organelle is involved in regulating directional cell migration [203, 168, 137]. Besides the Golgi apparatus, no other organelle localizes specifically at the apical

side [152].

Just as in other simple epithelia, cells in PSE are tightly connected to one another to form a confluent monolayer. This attachment is mediated by several junctions, i.e. tight and adherens junctions at the apical-lateral domains. The most apical junction, which is the tight junction in vertebrates and the adherens junction in invertebrates, define the boundary between the apical and lateral domains and it represents a hub for signalling complexes and proteins involved in mechanical interactions. The Zonula Occludens proteins ZO-1 and ZO-2 have been shown to localize at the apical-lateral domains together with Par-3 and create phase-separated condensates where tight junction proteins are recruited, both in in vitro and in vivo epithelia[24, 184]. Tight junctions appear to be involved in sensing and responding to mechanical forces also in proliferating PSE. For instance, it has been described that the depletion of the ASPP1 protein, a Par-3 interactor and component of apical junctions, results in structural defects of the mouse epiblast due to loss of epithelial integrity under increasing mechanical tension [172].

While many studies have dissected the polarity factors involved in establishing and maintaining the apical and lateral domains in epithelial cells, much less is known regarding what characterizes the basal domain. The basal end-foot of epithelial cells connects to the basement membrane, a dense mesh of extracellular matrix (ECM) that lies at the basal side of epithelial and endothelial tissues. Most basement membranes are formed by an evolutionarily conserved group of secreted glycoproteins, proteoglycans and glycosaminoglycans [144]. Among them, laminin and type IV collagen proteins are able to self-assemble and form intricate polymeric networks. The overlay and cross-linking of these networks serve as a scaffold for the formation of the basement membrane itself, together with other factors such as the glycoprotein nidogen and the heparan sulfate proteoglycan perlecan. [144]. Epithelial cells connect to the basement membrane via cell surface receptors, called integrins, that bind to ECM glycoproteins. The intracellular domain of integrins connects to multi-protein complexes called focal adhesion complexes that anchor the basal plasma membrane to the rest of the cytoskeleton. As a result, the cytoskeleton directly connects to the basement membrane through focal adhesion. Specifically to PSE, it has been shown that growth of the basal process is more directed and faster than growth of the apical process after cell division [86]. However, it is not clear why this is the case and whether it is related to some dependency of the cell on contacting the ECM to maintain tissue integrity.

In fact, basement membranes have been shown to actively shape epithelial tissue architectures and influence cell behaviour both in in vitro and in vivo contexts. One such example is given by the impact of collagen deposition and concentration within the basement membrane, where it can act as an external constraint to epithelial tissues and directly affects cell shape. For instance, inhibition of post-embryonic collagen expression in the *Drosophila* larva revealed that collagen deposition is crucial for establishing and maintaining correct organ shape: cells in the wing imaginal disc, which normally consists of ordered columnar epithelial cells arranged in a PSE, were laterally expanded and

flattened upon treatment with RNAi against collagen IV [162]. Correct incorporation of collagen is necessary to enable cell shape changes and does so by producing a basally constricting force that shapes the tissue and by recruiting perlecan [162]. Therefore, changes in the composition and topology of ECM proteins in the basement membrane can directly influence cellular shape and polarity and, ultimately, tissue shape of PSE [144, 190].

Overall, epithelial cells in PSE closely resemble cells that populate other simple epithelia in the composition of their apical, lateral and basal domains. In addition to these similarities, PSE present several features that are more unique to this tissue arrangement, such as dense nuclear stratification along their apicobasal axis. Nuclear positioning is however dynamic, since nuclear location within each single epithelial cell is not fixed, but fluctuates depending on the cell cycle stage (Fig. 1.2). This is a key feature of PSE that was first described in 1930's and is often referred to as "interkinetic nuclear migration" (IKNM) [176]. IKNM is considered a hallmark of pseudostratification, even though its exclusivity to PSE has been debated: for example, apical nuclear migration has also been reported in columnar cells in murine intestinal organoids [37]. Over the years, several studies have dissected the kinetics and mechanisms underlying nuclear movements during IKNM. Directed nuclear translocations occur during the G2 phase of the cell cycle and ensure that cell divisions always take place at the apical side of the tissue (1.2). This apical migration is highly conserved in PSE across evolution and represent a key feature of pseudostratification [135, 147]. The translocation of the nucleus to the apical side is an active process dependent on cell intrinsic forces generated by the actomyosin cytoskeleton [153] or microtubules in the very elongated PSE of the neocortex [152]. The fact that cell divisions always take place at the apical surface effectively creates a spatially restricted "proliferative zone" within the tissue. This spatial organization of the tissue seem to be a key element during organogenesis. When this process is perturbed, daughter cells fail to integrate in the tissue and epithelial integrity and maturation is impaired [199, 172]. After cell division is successfully completed at the apical surface, newly formed daughter cells move basally their nuclei, and thereby their soma, probably to make space for other epithelial nuclei to reach the apical side and divide. Depending on tissue context, this basal nuclear movement can be an active or passive process. Currently it is unclear whether cells can respond to local nuclear crowding or to other signalling cues to move their nucleus in a specific direction.

1.2.2 PSE are heterogeneous tissue types

While all PSE share this same general tissue architecture, where elongated epithelial cells allow for the dense packing of nuclei along the apicobasal axis, they differ in their tissue thickness, shape and nuclear packing. PSE are generally classified according to their height into three categories: short, intermediate and extended. Short PSE (below 30 μm) are found in both invertebrates, such as in the optic lobe in *Drosophila* [174], and

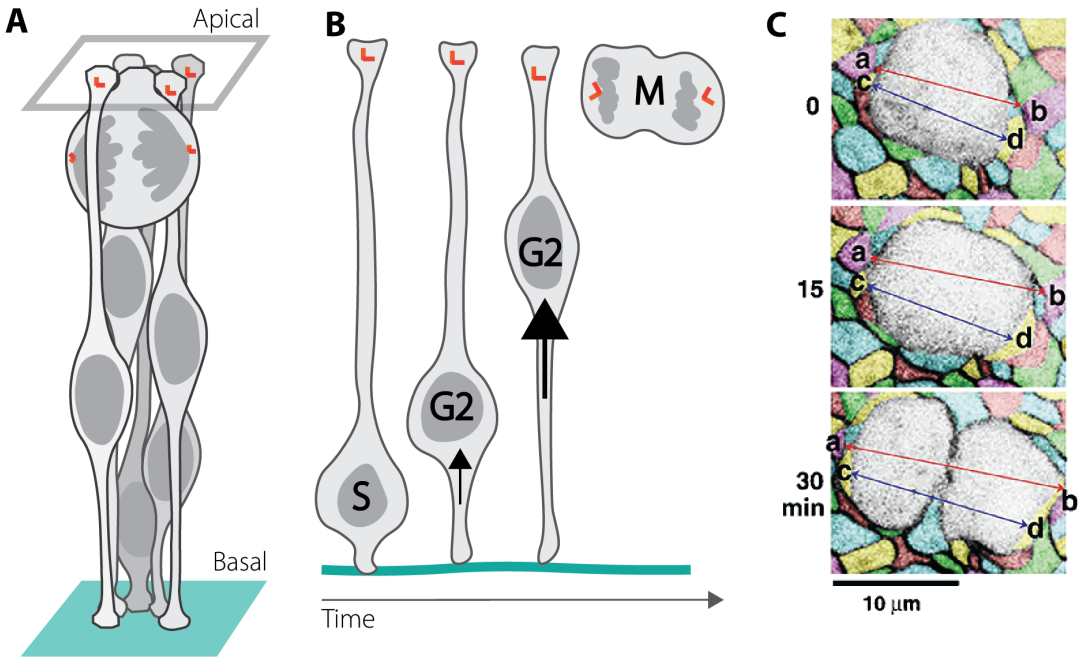

Figure 1.2: **Cellular arrangements in PSE.** A) Three-dimensional diagram of elongated epithelial cells in an intermediate PSE. Cells present a polygonal shape at the apical surface and centrosomes (in orange) in the apical processes. One cell is in mitosis (anaphase) and its volume has increased. Adapted from [189]. B) Two-dimensional diagram of apical IKNM: after DNA duplication (S), the nucleus is actively moved to the apical side during the G2 phase and undergoes mitosis (M) at the apical surface. Centrosomes in orange. Basal lamina in green. C) Time-lapse confocal microscopy showing the apical surface of the ventricular zone (VZ) in the developing CNS. A cell undergoing mitosis increases its volume and compresses the apical processes of the surrounding neighbors. Apical process of each cell are color coded to follow their cell shape changes and rearrangements over time. Images from [139]

vertebrates, such as in the endodermal buds in mouse embryos [29]. In all these cases, epithelial cells show columnar shapes and nuclei are ordered in a maximum of two layers. Intermediate PSE range between 30 μm and 60 μm and nuclei can be stacked in multiple layers depending on their size. Epithelial cells are elongated and extend thin cellular processes spanning the whole apicobasal axis. For example, intermediate PSE are found in the fly imaginal discs and the Nematostella ectoderm [135], the zebrafish retinal and hindbrain neuroepithelium [153] and in the mouse intestine [69]. Extended PSE can reach around 100 μm height and are found in the CNS of vertebrates, like the developing neural tube and retinal neuroepithelia of mammals [89]. An extreme case scenario is the neocortex, where extended PSE of 100 μm and up to 1 mm were found in rodents and primates, respectively [139, 167]. Neuroepithelial cells populating these tissues are composed of thin protrusions and the main volumetric region is the one occupied by the nucleus, therefore giving the impression of a 'bead on a string'.

Overall, these observations demonstrate the huge variety in sizes of PSE in various developmental contexts. Not only can different PSE present different sizes, but they can

vary their height over time. Tissue growth mediated by TGF-β and Wnt signaling leads to increase of the apicobasal height of the PSE via sustained proliferation and remodeling of actomyosin polymerization, localization and activity [223]. For instance, this is the case of the wing pouch in *Drosophila* larvae, where Dpp controls the transition from a short to an intermediate PSE by regulating RhoA activity and phosphorylation of the myosin light chain [223]. In the developing vertebrate retina, disrupting the canonical Wnt signaling pathway has been shown to reduce proliferation and impair the potential of neuronal progenitors in *Xenopus* embryos, leading to reduced tissue growth and shorter neuroepithelium [211]. As a matter of fact, epithelial cells have a columnar shape and low nuclear-to-cytoplasmic ratio at lower packing densities. As proliferation continues and tissue packing increases, cells progressively transform into more elongated cells, characterized by thin protrusions and a bulky cell body where the nucleus is positioned. One example of this dynamic growth is represented by the development of the spinal cord in amniotes. The neural plate is initially composed of a short pseudostratified neuroepithelium (PSNE). Over the first hours of development, this PSNE undergoes intense proliferation, leading to a two-to-three-fold increase of the tissue thickness and dense packing of nuclei within the tissue [98, 58, 182]. Also in this context, paracrine signaling molecules, like Wnts and BMPs from the dorsal side and SHH from the ventral side, pattern the neural tube into different domains across the dorso-ventral axis and this impacts the rate of differentiation of progenitor cells [98]. Consequently, the length of the apicobasal tissue axis changes along the dorsoventral axis of the neural tube, both in mouse and chick embryos [98]. This means that overall, PSE can vary their size and packing state depending on the balance between proliferation and differentiation and on the regulation of cell fate specification, which directly regulates their cell cycle progression and thereby tissue growth.

In addition to differences in tissue height, PSE can vary in their shape. They can occur as tubular or straight and curved epithelia. Curved PSE can bend basally to extend their apical surface, as in the retinal neuroepithelium, or apically, as in the liver buds in vertebrates [152, 29]. Depending on the shape of the tissue, epithelial cells will vary their own shape accordingly. For instance, in curved or folded PSE, epithelial cells are either apically or basally constricted. This constriction is reflected by differential distribution of the cytoskeleton during development, as shown in the case of the retinal neuroepithelium, where a nuclear exclusion zone is observed in retinal progenitor cells due to accumulation of actin at the basal side [130, 225]. Similarly, different apicobasal distributions of nuclei are observed in distinct folds with opposing curvatures in the Drosophila wing discs at later developmental stages, i.e. 120 h after egg laying (AEL)[104]. These differences have been shown to result in greater nuclear density in apically expanded folds compared to apically constricted ones and this observation seems to inversely correlate with velocity of apical nuclear migration[104]. Differences in tissue shape were also shown to influence how nuclei move through the apicobasal axis of differently-shaped zebrafish PSE by using two different molecular machineries, both dependent on actomyosin contractility[225].

Overall, these findings suggest that tissue architecture can influence not only cell shape but also the molecular mechanisms underlying specific cell behaviors, such as nuclear positioning in proliferating PSE.

In conclusion, PSE are a heterogeneous group of epithelial tissues displaying various tissue sizes, packing states and shapes. These parameters directly impact the morphology of epithelial cells and the positioning of nuclei throughout the apicobasal tissue axis. How nuclear packing within proliferating PSE changes over time and can influence other processes of organogenesis, such as differentiation and cellular migration, is not fully understood yet.

1.2.3 Nuclear movements and positioning in PSE

Independently of their final tissue sizes, packing states and shapes, all PSE share the same tissue arrangement, where nuclei are dynamically positioned at different depths along the apicobasal axis. This process is a key feature of pseudostratification and it is tightly connected to the cell cycle. While nuclei occupy different apicobasal positions in interphase and in these phases their movements appear to be the result of stochastic motions [106, 117, 14], apical IKNM is always the result of a fast, directed and active process [153]. This apical movement is driven by the cytoskeleton and requires different molecular machineries depending on the height and shape of the PSE. For instance, it had been shown that IKNM is dependent on actomyosin contractility in short and intermediate PSE. Though, for short PSE cell rounding seems to be sufficient to locate the mitotic nucleus at the apical side[135, 174], while apical movements are decoupled from cell rounding in intermediate PSE [199]. In the case of extended PSE, like the rodent neocortex, microtubules appear to be the main driver of apical IKNM [23]. These differences in cytoskeletal machineries could be due to the necessity to generate a big enough force to cover longer distances and to move the nucleus through a densely crowded environment. Besides tissue height, the specific cytoskeletal mechanisms that move the nucleus apically can differ depending on cell and tissues shapes. For example, in *Danio rerio* epithelial cells within the retinal and hindbrain neuroepithelia showcase two different actomyosin-dependent mechanisms to translocate nuclei to the apical side: in the retina, which is characterized by an hemispheric shape and cells show a basally-constricted morphology, nuclei are pushed to the apical side by a formin nucleated expanding network; while, nuclei in the tubular hindbrain neuroepithelium are translocated via an actomyosin contractility-dependent mechanism[225].

Regardless of the way nuclei are moved to the apical side, mitosis is always performed apically and, following cell division, daughter cells are displaced from the apical side and localize to more basal positions[117, 186, 14]. Immediately after mitosis and cell division this basal motion, each nucleus' trajectory resembles a random walk [153]. It is not clear whether interphase nuclei are passively displaced or they are still moved by the cytoskeleton, even without any apparent unidirectionality. It had been proposed that this

stochastic motion could be the result of direct transfer of kinetic energy from neighboring nuclei undergoing apical IKNM[153]. Though, more recent studies found no evidence of this random motion of nuclei in G1 and S phases being a direct effect of the directed motion of nearby nuclei in G2[186, 14]. Another hypothesis to explain the basal motion of nuclei after cell division points to the formation of a nuclear concentration gradient in the PSE due to apical mitosis[106]. According to this hypothesis, the concentration of nuclei would be higher closer to the apical surface due to IKNM, therefore establishing a gradient of nuclear density across the tissue. This in turn would drive the net movement of nuclei towards lower concentration areas, i.e. the basal side[14]. Experimental work and theoretical modelling indicate that this could be the case for the zebrafish retinal neuroepithelium: a passive diffusive process that takes into consideration the steric hindrance of nuclear volume, cytoplasmic friction and nuclear packing in the tissue, could reproduce the changes of experimental distribution of nuclei within the retinal tissue over few hours of development[14]. This nonlinear model provides an intriguing framework to question how nuclei are positioned in relation to IKNM and differential nuclear crowding within the tissue[14]. Interestingly, it was shown that basal-ward somal translocation becomes a directed and active movement upon neuronal differentiation in the zebrafish retina that is driven via microtubule polymerization [148, 93, 170]. In this case, the basal translocation of photoreceptor progenitors' nuclei prevents apical congestion and ensure that proliferating multipotent progenitors can still divide apically while photoreceptors are generated [170]. In this way, the emergence of mechanical stress in the densely crowded retinal neuroepithelium can be avoided [170]. Overall, these experimental evidences demonstrate that nuclear positioning within proliferating PSE can vary over time an in differently shaped and sized epithelia. In addition, nuclear movements can be directly influenced and regulated by cell fate specification, like during differentiation of multipotent progenitors in neuroepithelia. Whether epithelial cells can sense and respond to local packing densities to position their nuclei within the tissue is still not clear, even though more recent studies have shown that the nucleus can sense spatial constraints *in vitro* [213, 120].

Depending on the developmental stage and the shape and crowding of the tissue, nuclei do not occupy the whole apicobasal axis. The vertebrate retinal neuroepithelium exhibits a basal exclusion zone, where nuclei cannot position due to accumulated basal actin, during the first stages of organogenesis [130]. When the retinal PSNE proliferate and cells elongate, more nuclei can occupy the basal exclusion zone, which is freed from actin accumulation at the basal side. This is not just a passive effect of increasing tissue packing. When actin is not actively redistributed at the later cell side, epithelial cells cannot elongate, the basal exclusion zone does not disappear and, as a result, the retinal neuroepithelium cannot scale its size [130]. At the same time, proliferation is necessary for cellular elongation, as retinas treated with hydroxyurea and aphidicolin do not increase their tissue height [130]. Last but not least, an intact ECM represents an important requirement for isotropic tissue growth and maintenance of tissue shape in

the zebrafish retina, as discussed above in the case of the *Drosophila* wing disc [130, 162]. Therefore, it appears that the concerted processes of actin redistribution, cell proliferation and ECM deposition ensure correct growth of developing PSE and therefore influences nuclear positioning.

1.2.4 Pseudostratification and its biological relevance for organogenesis

In the previous chapters, we have defined pseudostratified epithelia as follows: confluent monolayered tissues of elongated epithelial cells whose nuclei are positioned along the apicobasal axis and whose movements occur radially in a directed or stochastic manner. We have also seen that, while PSE are relatively sparse in adult organisms, they are often found as organ precursors in many developmental contexts. However, the evolutionary forces that shaped PSE and made this tissue arrangement so widespread in development are not fully understood.

Several ideas have been formulated to explain the biological significance of pseudostratification, based on three main characteristics: the elongated shape of their epithelial cells, the stereotypical movements of their nuclei to reach the apical surface, i.e. IKNM, and their capacity to reach high packing densities. While each one of these features has been linked to different hypotheses, all of them appear to be tightly connected and dependent on each other. Therefore, it is possible that not one, but multiple of the following theses held true to explain the evolutionary relevance of PSE.

1.2.4.1 Interkinetic nuclear migration

Since the first description of IKNM [176], several hypotheses have been put forward to explain why progenitor cells need to divide at the apical surface. One of them states that apical cell division is crucial to promote the inheritance of apical factors and for integration of both daughter cells in the tissue. In this case, apical cell division might allow for symmetric inheritance of apically localized factors, therefore facilitating the re-integration of both daughter cells in the tissue. Indeed, when IKNM is impaired and cells divide at more basal positions, at least one of the daughter cells fails to re-integrate in the tissue and continues dividing ectopically, therefore interfering with the integrity of the tissue architecture [199]. As a consequence, we would expect that the plane of cell division plays a role as well. Indeed, perturbation of the cleavage plane orientation leads to extrusion of one daughter cell in several PSE, like the *Drosophila* wing disc, the mouse epiblast and the chick neural tube [143, 145, 172].

In the context of intermediate and extended PSE, like vertebrate neuroepithelia in general, the sustained proliferation of progenitor cells leads to high nuclear packing densities. Despite traveling through a crowded tissue, nuclei are still actively moved over increasing distances to reach apical positions before mitosis. A thesis formulated in the 1970s states that, since rounded mitotic cells occupy more space, cell division at the apical surface avoids cell congestion, given that the surface area correspondingly increases

[189]. If this was the case, high nuclear densities were expected to hinder rounding of cells at non-apical positions. However, subapical mitosis has been shown to occur in the densely populated zebrafish retinal neuroepithelium when apical IKNM is impaired or when the apical surface is occupied by photoreceptor precursors [221, 199, 170]. In all cases, no tissue jamming was observed and cells keep dividing at basal positions despite high nuclear density. So, it does not seem that mitosis is constrained at the apical surface because of confinement at more basal positions due to tissue packing. Though, more recent findings do suggest that tissue mechanics can impact nuclear movements and viceversa. For instance, an inverse correlation between apical IKNM velocity and nuclear density has been reported in the Drosophila wing disc. In this PSE, more cells divide at subapical positions when nuclear density is increased, for instance upon compression of the tissue or disruption of the basement membrane [104]. Under these conditions, higher forces might be required to move the nucleus towards the apical side and ensure cell rounding, making this process more susceptible to increasing nuclear density. Whether apical IKNM might be influenced by the packing state of nuclei in different developmental contexts remains elusive. Alternatively, it has been proposed that IKNM itself ensures tissue fluidization by driving cell rearrangements in the proliferating PSE. This has shown to be the case during gastrulation in chick embryos, where cell divisions promote extensive cellular rearrangements and potentially fluidize the epiblast, which is composed of a short columnar pseudostratified epithelium [59]. In thicker PSE, not only the directed apical nuclear translocation, but also the basal movements of nuclei allow to keep the apical surface unjammed [139, 170]. In the mouse neural tube, cell rearrangements decline as a function of proliferation and the fluidity of the PSE is maintained by the active stresses generated by apical cell divisions [28]. Altogether, these findings indicate that restricting the proliferative zone of PSE to the apical side promote cellular rearrangements and drive cell shape changes that have the potential to directly affect tissue fluidity. This could act as a positive feedback loop that enables the accumulation of more cells within proliferative PSE during early stages of morphogenesis.

1.2.4.2 Cell shape

One hypothesis that has been recently formulated is that smaller average cell diameters at the apical surface could enhance the precision of morphogen-based patterning and that pseudostratification itself could be advantageous because it promotes the reduction of cellular cross-sectional areas (Fig. 1.3 A) [85]. According to this thesis, pseudostratification ensures that the apical end foot of epithelial cells reduces its diameter over time in concert with cell elongation and proliferation [2, 66]. This in turn could improve the precision of morphogen gradients (Fig. 1.3 B, C, D).

How sharp boundaries are formed during gradient-based patterning is a long-standing question, especially considering the effect of noise of the morphogen gradient at longer

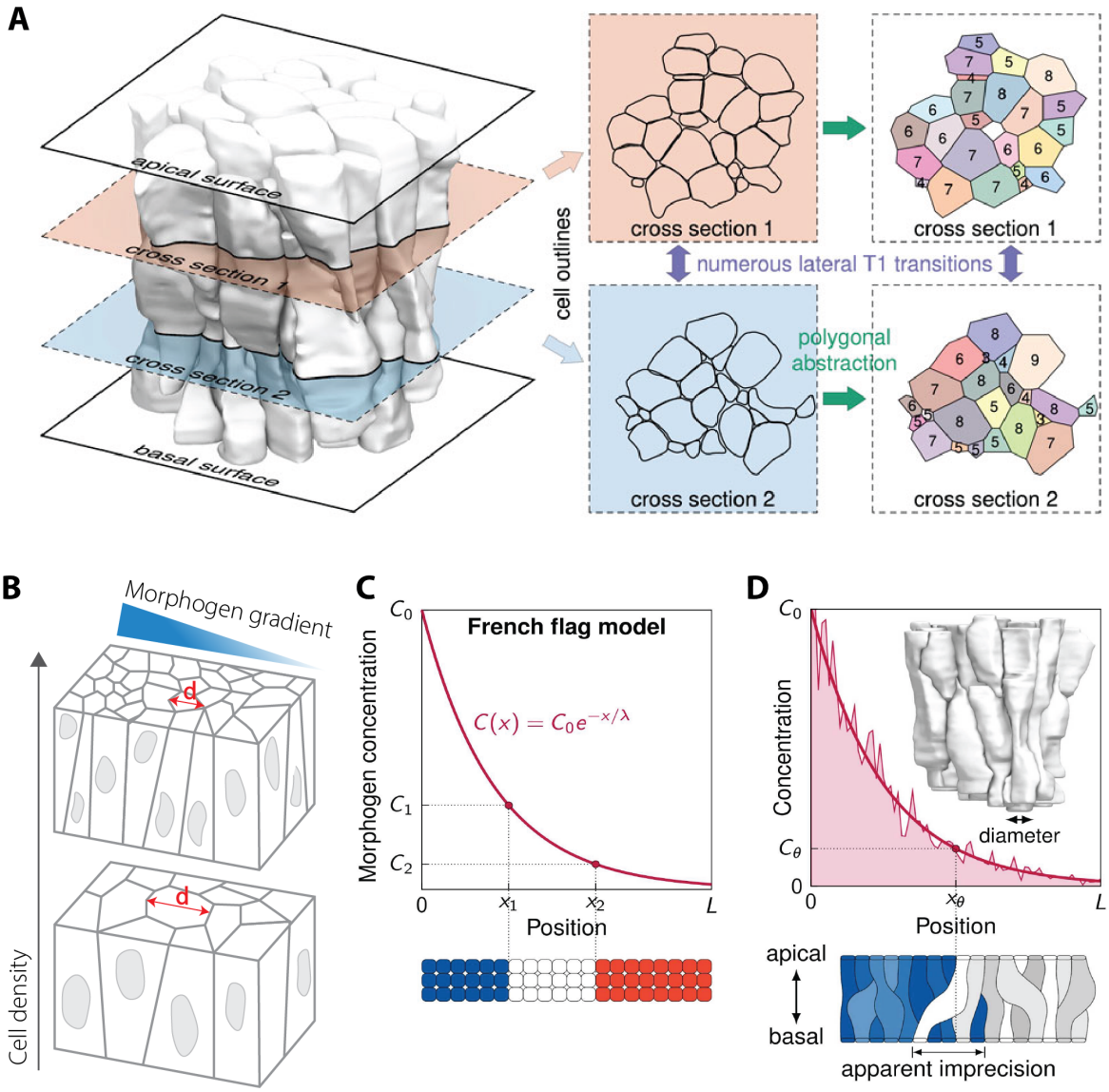

Figure 1.3: **3D organisation of cells in a PSE and its relation to morphogen gradients.A)** Slicing through segmented epithelial cells in the mouse embryonic lung along the apicobasal axis reveals the true complex shape and 3D neighbor relationships. of PSE. Colours in the last column indicate cell identity, values are cross-sectional neighbour numbers. Adapted from [84]. **B)** Schematics showing a proliferating PSE in the presence of a morphogen gradient. As more cells are accumulated over time, the diameter of the apical cell surfaces decrease. **C)** Schematics of the French-flag patterning model: spatial decoding of the concentration of a given morphogen result in tissue patterning and formation of tissue boundaries. Adapted from [85]. **D)** Example of morphogen-gradient patterning in PSE. The complex noncolumnar shape of cells in PSE may give rise to an apparent imprecision of domain boundaries (blue/white).A cell undergoing mitosis increases its volume and compresses the apical processes of the surrounding neighbors. Adapted from [85].

distances from the source and the natural variation in the read-out process in the receiving cell. For instance, during the development of the mammalian and avian neural tube, distinct domains of neuronal progenitors are specified early on along the dorsoventral axis to organize the intricate spatial distribution of sensory and motor neurons that will be produced later in development. To achieve this, opposing gradients of multiple morphogens, eg. SHH, BMP-4 and Wnts, pattern the neural tube so that multipotent progenitors in the pseudostratified neuroepithelium respond differently at different concentration thresholds, therefore forming separate tissue domains and precise boundaries [227, 214]. It has been proposed that high precision of tissue patterning in the vertebrate neural tube is obtained through decoding of the noisy antiparallel morphogen gradients [227] Alternatively, it has been shown that single gradients can be precise enough to pattern the neural tube [214]. In both cases, morphogen gradient variability theoretically decreases with increasing cross-sectional areas and viceversa, according to recently published numerical simulations [2]. Indeed, analysis of literature data hints to a correlation between small average apical cell areas and morphogen-gradient-mediated patterning, where the smaller areas were found in pseudostratified epithelia like the chick and mouse neural tube or the fly wing disc [70, 105, 28, 2]. Further experimental work needs to be done to address whether changes in shape of epithelial cells directly affect the precision of morphogen-gradient-based patterning.

While smaller apical cell area might affect the precision of gradient patterning, morphogens have been shown to drive the remodeling of tissue shapes. This is the case of TGF/Dpp signaling, which controls the transition from a cuboidal to a columnar cell shape of epithelial cells in the wing imaginal disc of Drosophila [223]. In this tissue, overactivation of Dpp signaling results in increased apico-basal cell length and small apical areas in the center of the wing pouch [223, 51]. Smaller average apical area is achieved thanks to the progressive elongation of epithelial cells, which is mediated by redistribution of actin cytoskeleton and proliferation in many PSE [130]. Since morphogens are known regulators of proliferation and cell specification, they consequently have the potential to impact cell shape changes in PSE and this could improve other morphogen-mediated patterning.

In addition to smaller cross-sectional diameters, the elongated morphology of epithelial cells results in higher numbers of contacts between neighbors (Fig. 1.3 A) [66]. Indeed, the number of contacts is mainly dictated by the cellular cross-sectional area, which varies along the apicobasal axis and is mainly influenced by the location of the nucleus [66]. Because of IKNM, the nucleus is the main determinant for the dynamics of neighbor changes and it influences the cellular rearrangements of nearby cells [66]. Therefore, the complex noncolumnar and elongated shape of epithelial cells in PSE directly affect their neighbor exchanges, together with IKNM. This has potential implications not only on cell-to-cell signaling pathways, such as Notch-Delta, but also on the physical state of the PSE. The extent to which neighbor contacts are exchanged over time has been shown to be indicative of the fluidity of the tissue and to directly affect its mechanical properties.

Ultimately, progenitor cells in PSE undergo differentiation and change their position and morphology within the tissue over development. As a result, cellular rearrangement events decrease over time and the tissue show features of a progressive transition from a fluid-like to a solid-like behavior [70, 28]. Taken together, these findings suggest that both complex elongated cell shape and IKNM are two key feature of pseudostratification that could make this tissue arrangement beneficial due to its fluid-like properties.

1.2.4.3 Nuclear packing

The stratification of nuclei within the monolayered epithelium increases over time as proliferation progresses [130, 98, 97]. High nuclear packing densities can be reached in developing PSE thanks to the capacity of epithelial cells to elongate and to position their nuclei along the whole apicobasal axis. One long-standing hypothesis is that PSE allows to pack high numbers of progenitor cells within a monolayered epithelium and that this could help correct organogenesis. However, formal proof of this idea does not yet exist.

This thesis was first formulated upon observation of proliferation and cell specification dynamics of ependymal cells forming the pseudostratified neuroepithelium (PSNE) in the mouse neural tube [189]. Based on this observation, it was speculated that the proliferative capacity of progenitor cells in the developing neural tube is temporally restricted and, because of this, differentiation must be delayed in order to produce the maximum number of neurons [189]. Indeed, many developing organs go through distinct developmental phases to establish correct tissue patterning, produce the right amount of differentiated cells and reach the correct size [97]. Besides the aforementioned example of the neural tube, distinct phases set the pace of development in other developing neuroepithelia, i.e. in the retina and in the brain. As a matter of fact, most tissues of the CNS originate from PSNE, where progenitor cells progressively differentiate into neuronal precursors and undergo a finite number of cell divisions before committing to one cell fate and becoming terminally differentiated postmitotic neurons. Correct development of neural tissues relies on tight spatiotemporal regulation of proliferation and differentiation - and, later on, apoptosis - to produce all the necessary neuronal types at the right time, in the right place and in the right proportions and generate a functional tissue architecture. These developmental phases of proliferation and cell specification tend to extensively overlap, perhaps to regulate the variability in cell numbers or patterning errors. In this context, the particular arrangement of cells within PSNE could be beneficial to enable the accumulation of high numbers of progenitor cells before neurogenesis.

Dense stratification of nuclei in PSNE can have other implications, besides enabling the packing of more cells within the tissue. Especially in the context of proliferating PSNE, nuclei end up occupy most of the volume of the monolayered epithelium. Since the nucleus is the bulkiest and stiffest organelle in the cell [71], the reduction in the cytoplasm-to-nuclear ratio and the increasing packing of nuclei within the tissue is expected to drive significant changes in the mechanical properties of the tissue according to numerical

simulations [93, 100]. This can be achieved also via differential proliferation within the PSE and spatial variations in nuclear positioning. For instance, it has been proposed that stalling of nuclei at the luminal side in the developing mouse cochlea can cause local tissue extension and can theoretically account for the bending of the epithelium [88]. Therefore, these findings suggest that increasing nuclear densities and spatial differences in nuclear packing within the tissue could affect the mechanical properties of the PSE and its overall shape. Besides this effect at the tissue level, increasing nuclear packing densities have the potential to impact cell behavior as well. In fact, the nucleus itself can act as a mechanical ruler and instruct specific cellular responses. Nuclear deformations due to spatial confinement in vitro translate into differences in the mechanical state of the nuclear envelope, which subsequently trigger a signaling cascade that leads to an active contractile response [213, 120]. Whether nuclei in proliferating PSE act as passive organelles or whether they can sense the increasing nuclear packing and trigger different cell responses in *in vivo* tissues is still not fully clear, but represents an exciting avenue for future studies.

Overall, these findings suggest that nuclear packing could affect organogenesis both at the cell- and tissue-level. While several studies have focused on dissecting the mechanisms and effects of IKNM and cell shape in proliferating PSE, less is known regarding the influence that tissue packing, and especially nuclear packing, might have on tissue morphogenesis. However, more evidence needs to be collected to support the aforementioned thesis and to illustrate how pseudostratification affects the ultimate organization of densely packed epithelia, such as neural tissues in the developing CNS.

1.3 Cell packing in biological systems

Over the course of animal development, complex structures emerge as a result of proliferation, cell fate specification and spatial organization of cells. While the biochemical and genetic mechanisms underlying morphogenesis have been and still are extensively investigated, we know less regarding the physical mechanisms that help sculpt specific tissue structures. Recent experimental and theoretical studies have shown that biological tissues can undergo changes in tissue material properties resembling phase transitions. Examples include the fluidization of the blastoderm during zebrafish gastrulation due to changes in cell-to-cell connectivity [164] and the elongation of the germband in Drosophila as a consequence of cellular rearrangements and actomyosin contractility [21, 27, 204]. New technologies have enabled the direct measurement of tissue material properties, such as viscosity and Young's modulus, that help understanding the contribution of these material properties to tissue morphogenesis [18, 140, 205, 163]. This, together with theoretical modelling of active matter, has allowed to uncover conserved physical mechanisms that shape embryos across different species[30]. Therefore, the study of the physical and mechanical properties of multicellular tissues, together with molecular biology approaches, has the

potential to shine a light on the emergence of self-organization in embryonic tissues [11, 116, 75].

Several theoretical models have been proposed for characterizing possible phase transitions in biological tissues. The geometrical and material properties of epithelial confluent monolayers have often been described using vertex models [5]. In these mathematical formulations, rigidity transitions are the result of forces generated by cell-to-cell contact and cortical tension, using cell shape as the main control parameter to describe the state of the system [57, 125, 25, 26, 219, 101]. These vertex models have allowed the understanding of how subcellular changes in actomyosin distribution or in cell adhesion can impact tissue mechanics and therefore have an effect on complex morphogenetic processes, independently of cell density. Alternatively, active particle models have been used to describe the dynamics of collective cell migration and predict density-dependent rigidity transitions [9, 183, 19, 64]. Together with the predictions generated by these models, recent experiments have shown that cells in densely populated tissues exhibit changes in their mechanical properties that have been commonly described in colloidal systems, such as caging effect, dynamical heterogeneities and viscoelastic behavior [11]. As a result, cell movements in confluent epithelial monolayers can feature glass-like dynamics, as also observed in colloidal systems, that can impact on physiological processes of the epithelium [161].

So far, most of these formulations have described biological tissues as two-dimensional (2D) systems and therefore fail to capture the complexity of three-dimensional (3D) shape changes. Consequently, more and more efforts are made nowadays towards 3D models of multicellular tissues [133, 109, 175, 115]. The applications of these theoretical models, together with experimental work and improved imaging techniques, has the potential to improve our understanding of the processes that govern tissue arrangements in confluent and non-confluent tissues in 3D. This is particularly relevant if we consider that tissue structure and form often directly define organ functions.

1.3.1 Liquid, solid and liquid crystal states in biology

The way molecules are arranged in a medium directly affects their physical state and changes in their arrangement result in phase transitions from a liquid, solid or gaseous state to another. Phase transitions occur when a key parameter of the system changes, like density, applied stress and temperature (Fig. 1.5) [158]. For instance, most liquids undergo a simple phase transition to a crystalline solid when they are cooled down below a freezing set temperature. Many other substances are known to undergo other intermediate phase transitions between a liquid state, where molecules show no orientational and positional ordering, and a solid state, where molecules are locked into a rigidly ordered arrangement, thereby showing high degree of orientational and positional ordering.

One such thermodynamical stable phase is seen in liquid crystals, which feature rod-like molecules aligning along a main direction and lacking a 3D lattice arrangement [195]. Different types of liquid crystal phases exist, depending on the degree of organization

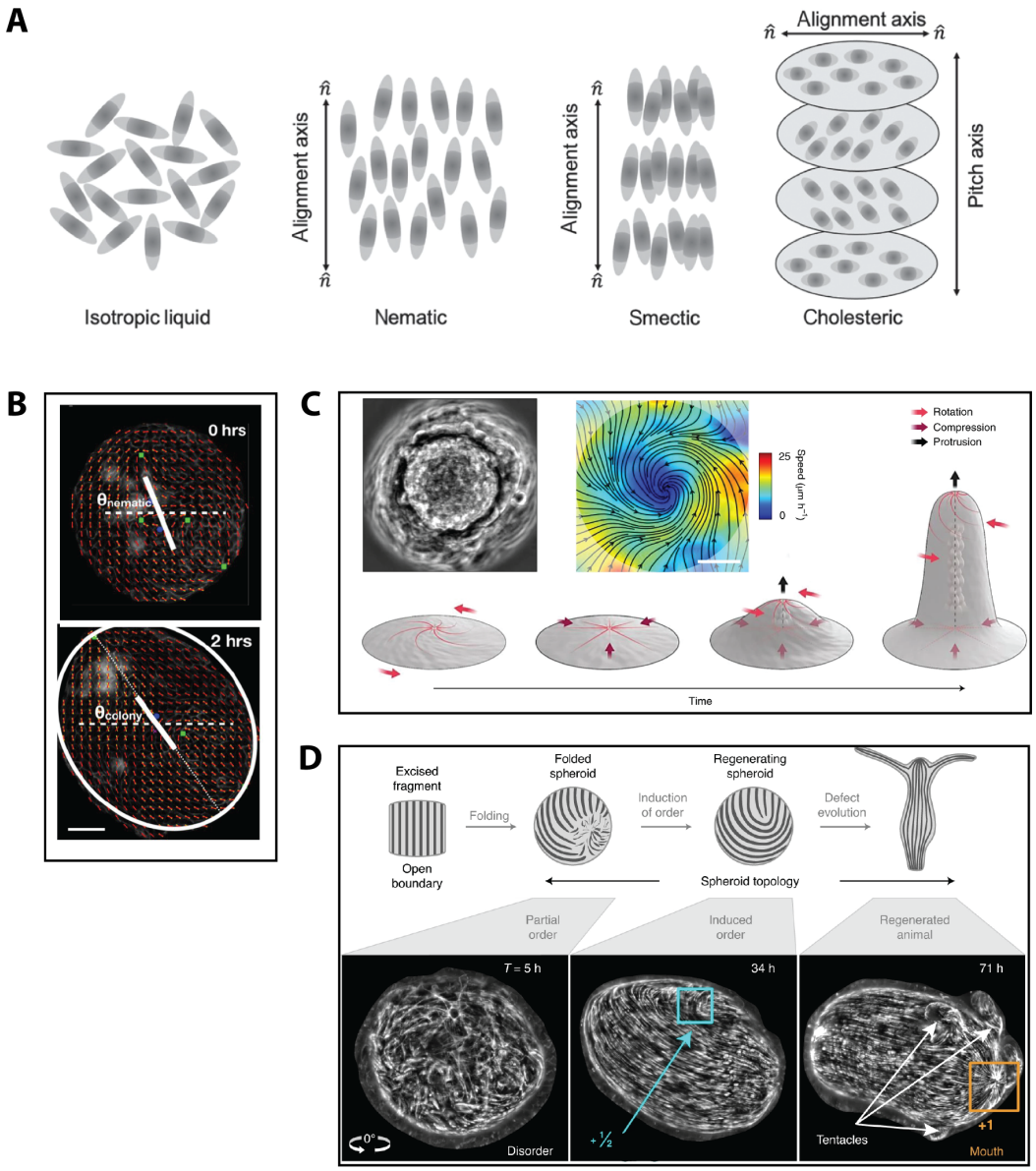

Figure 1.4: **Different liquid crystalline phases and the role of nematic ordering and topological defects in biology.A)** Schematics of the different subclasses of the liquid crystal phases. The simplest liquid crystal is the nematic one, where the molecules tend to align along a common axis, but are free to move around. In a smectic liquid crystal, an additional degree of order emerges: the molecules organise into layers, while keeping overall orientational order. A chiral (nematic or smectic) liquid crystal is formed when molecules posses helicity and periodically rotate along the alignment axis. Image from [48]. **B)** A colony of MDCK cells shows long-range alignement after removal of a stencil that was confining it. Cell shape is quantified using a nematic field (red segments) and .the mean orientation θ nematic for the entire colony is obtained. Images from [43]. **C)** Integer topological defects in confined cell cultures organize stresses in 3D nematic tissues. Phase contrast image of a protruding myoblast culture (first left top) and corresponding average velocity field (second left top). Schematics showing the generation of a 3D protrusion from a 2D culture of myoblasts organized in a nematic order. Adapted from [72]. **D)** Actin fibers organize into a nematic order during regeneration of tissue fragments in *Hydra*. Topological defects drive the emergence of mouth and anus structures. Adapted from [127].

of the anisotropic molecules: nematic, smectic and cholesteric or chiral (Fig. 1.4 A). The nematic order is the simplest liquid crystal phase and defines the arrangement of anisotropic molecules aligned along a common axis, but still lacking positional order. In a smectic order, molecules are orientationally ordered and organize into layers so that they behave like a liquid within each layer. In a cholesteric liquid crystal, molecules are chiral and periodically rotate along the axis of alignment. Depending on the intermediate order, molecules can flow to various extents as seen in a more liquid-like state, while the material can resist deformations like in a solid-like state.

Several analogies have been drawn between liquid crystals and the emerging physical properties of biological systems. Cholesteric liquid crystal ordering has been found in the arrangement of nucleic acids, chromatin, polysaccharides and proteins and smectic order has often been shown to occur in the packing and structure of lipids [138, 90]. Moreover, an isotropic-to-nematic transition has been observed in the reorganization and alignment of actin networks in fibroblasts cultured on stiffer substrates *in vitro* [49]. Therefore, several biopolymers seem to behave like liquid crystals.

Nematic ordering was identified not only in subcellular structures, but also in multicellular systems [48]. Liquid crystalline features have been described in tissues where cells present anisotropic shapes, either due to cellular elongation or to external stresses, and in this case their organization resembles a nematic phase (Fig. 1.4 B, C) [72]. In this active nematic system, the long-range orientational ordering can be locally lost and therefore result in topological defects that lead to self-organizing structures in tissues. These topological defects can produce local stresses that correlate with cell extrusions or changes in cell density [178, 94]. While most of these studies have been performed in *in vitro* monolayers, topological defects have been recently described also during *Hydra* morphogenesis, where nematic actin fibers alignement is established early on during regeneration of tissue fragments and where topological defects act as organizing centers for head and foot regeneration (Fig. 1.4 D)[127].

Overall, these findings support the idea that long-range orientational ordering of intracellular structures, such as actin fibers, or of cellular collectives can organize stresses within tissues and drive morphogenetic processes. Hence, studying how cells are packed and arranged within a biological system provides additional insights into the physical state of the tissue. This, in turn, can help us to better understand how organs are shaped and structured during development, regeneration and homeostasis.

1.3.2 Biological implications of disordered tissue packing

During the early phases of embryogenesis, cell populations are often found in disordered arrangements as they undergo cellular mixing and unmixing to perform complex biological events, like gastrulation [163, 164]. To do this, cells in a tissue need to locally move while the tissue is still mechanically stable. Because of this behavior, multicellular collectives have been shown to undergo fluid-to-solid jamming transitions and glass transitions,

similarly to amorphous and inert particulate materials like foams, colloidal suspensions, and granular media (Fig. 1.5) [9, 160, 12]. In these particulate systems, matter can exhibit a transition from a liquid-like phase, where particles are free to flow, to a glass-like phase, where particles are locked in a disordered and rigid arrangement (Fig. 1.5) [22]. For instance, colloidal suspensions can jam into colloidal glasses when density is progressively increased [22, 11]. In this scenario, particle-particle interactions grow continuously until each particle is constrained by its neighbors in a density-dependent way and cannot move freely anymore. Eventually, the number of constraints in the system increases to the point that all particles are jammed in a disordered collective. Behaviors like this have been described across different scales in various collective systems, whether inert or active: grains in a silo, sand in a pile, coffee beans in a grinder, people in a concert and cells in a confluent multicellular tissue.

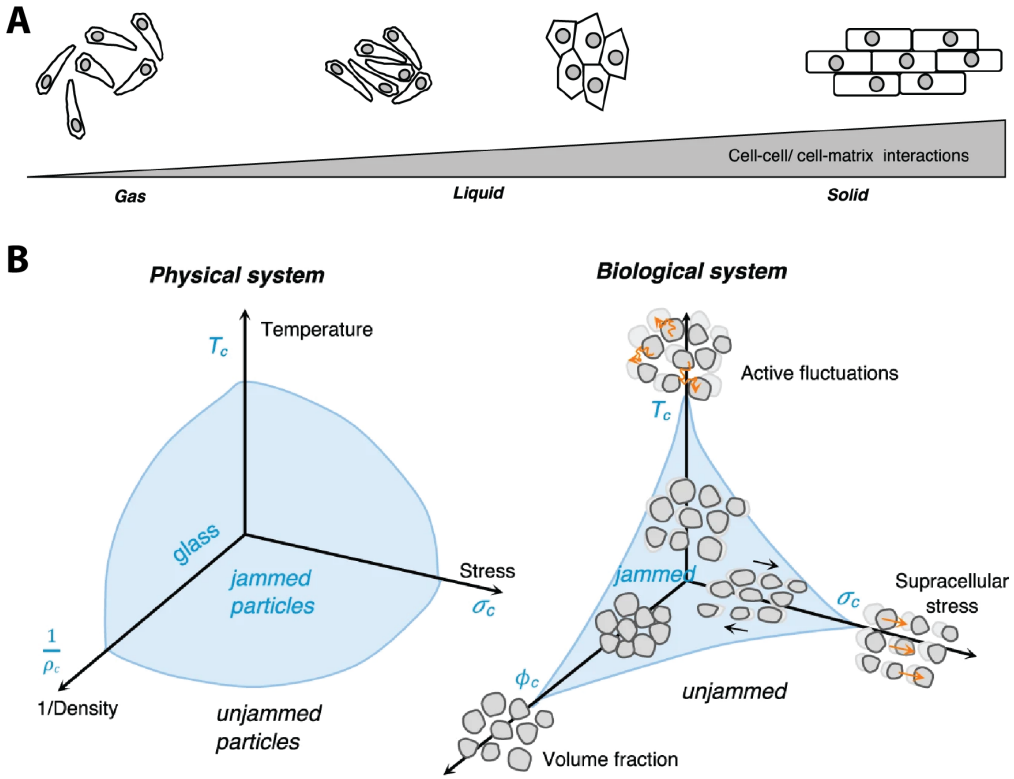

Figure 1.5: **Phase and jamming transitions in biological tissues. A)** Biological systems can display fluid-like and solid-like properties at the population level, depending on their interactions with other cells and with the extracellular matrix . **B)** Particulate materials can change their physical state by undergoing jamming and glass transitions. This occurs when external parameters, such as temperature, density or pressure, rapidly change. Similarly, changes in cell motility, cell density and applied stresses can cause a multicellular tissue to transition to a different order and acquire different material properties. Adapted from [116].

Indications that jamming and glass transitions can occur in biological tissues were found in confluent cultures of Madin-Darby canine kidney (MDCK) epithelial cells, where

direct measurement of traction forces proved the existence of long-range force transmissions within the advancing epithelial sheet [207]. This, together with the close packing and structural disorder of migrating MDCK cells, suggested that collective migration in confluent epithelial monolayers can share common mechanisms with glass transitions of granular materials [207]. Since then, the relevance of biological jamming and glassy dynamics has been further investigated in other *in vitro* cultures systems recapitulating the pathophysiology of the asthmatic airway epithelium and breast cancer invasion, among others [157, 160, 12, 87]. Many features typical of jamming and glassy dynamics have been identified in various developmental contexts as well, like in body axis elongation of the chick and zebrafish embryos [20, 140]. These findings suggest that phase transitions might play a role in embryonic morphogenesis and raise the question of how the material properties of multicellular tissues can be actively regulated to sculpt organs.

Increasing particle density often drives rigidity transitions in foams and colloidal suspensions, so that particle-particle contacts between neighbors result in a caging effect [22]. Analogously, proliferation of cells in a confined environment can lead to density-dependent rigidity transitions in *in vitro* epithelial systems [9, 183, 19]. Alternatively, glassy dynamics can be uncoupled from cell density variations in non-confluent tissues: jamming transitions can be driven by increasing volume fraction occupied by cells. This can occur as a consequence of changes in cell adhesion, as shown during gastrulation and body axis elongation of zebrafish embryos [163, 140]. Random cell divisions were shown to reduce cell cohesion and connectivity, leading to fluidization of the zebrafish blastoderm center around 4 hours post fertilization [164]. Meanwhile, cells at the margin of the blastoderm do not undergo fluidization due to noncanonical Wnt signalling that re-establishes and strengthens cell-to-cell contacts after cell division [163]. Later on during zebrafish development, an anterior-posterior N-cadherin-dependent gradient of yield stress is established in the pre-somitic mesoderm, leading to a fluid-to-solid jamming transition that facilitate tail bud elongation [140]. In both instances, jamming and fluidization of the tissues seem to be instrumental for completing blastoderm spreading and unidirectional axis elongation in *Danio rerio*, respectively.

In contrast to other non-confluent tissues, no space is found between cells in epithelia, meaning that the volume fraction occupied by cells is at its maximum and does not change. In these systems, single cell properties like cell adhesion and cortical tension can drive density-independent rigidity transitions in multicellular tissues at constant cell packing density [25]. Vertex models of confluent epithelia provide geometrical descriptions of these tissues where jammed and unjammed states are defined by cell shape [125, 101, 133]. For example, cells in the *Drosophila* germband epithelium are tightly packed and changes in their mechanical behavior are not correlated to changes in cellular volume fractions [219]. Therefore, variations in cell shape, cell contractility, cell alignment and disordered packing correlate with cell rearrangements and predict the fluidity of the tissue [12].

Altogether, the aforementioned examples indicate that phase transitions are common physical processes in confluent and non-confluent embryonic tissues. Many embryonic

tissues appear to exist in proximity of phase transition boundaries, so that mechanical changes are made with little variation in few parameters [13, 116]. In these scenarios, glassy dynamics appear to be a favorable low-energy mechanism to control the physical state of the tissue and produce collective cell behaviors [11]. A key feature of these jamming and glass transitions is that the tissue will eventually reach a mechanically stable configuration that is rigid and disordered, which means that single cells are caged by their neighbors and cell rearrangements requires energy expenditure. Because many biological functions require specialized cell populations to be arranged into ordered cellular arrangements, it is fundamental to understand how regular structures arise from disordered collective of cells during development to understand the physical parameters of organogenesis.

1.3.3 Establishing ordered packing in epithelia

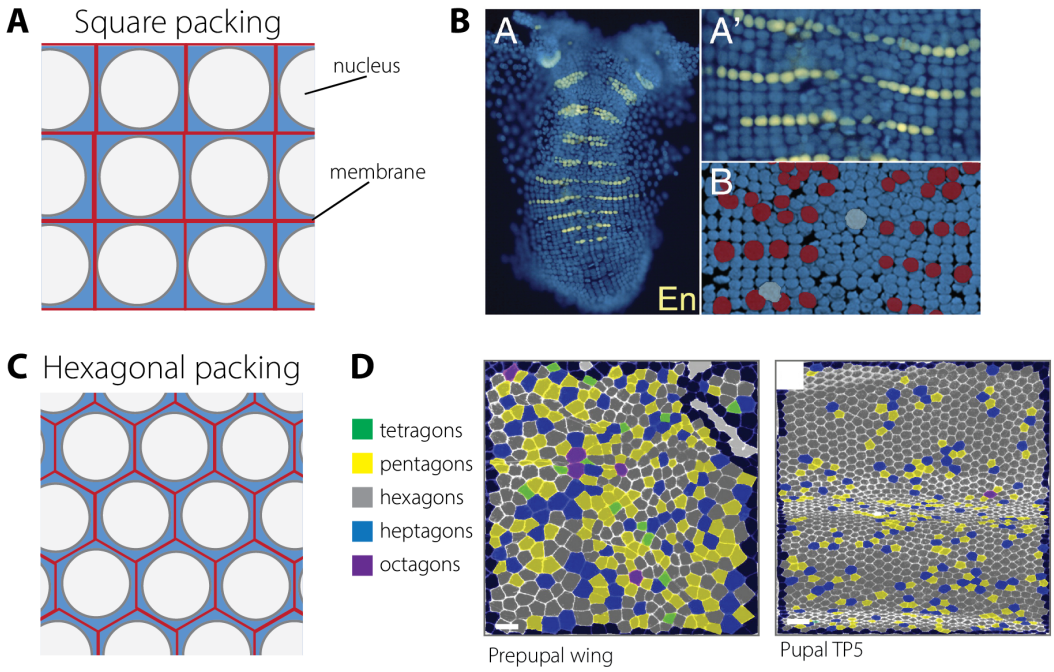

Figure 1.6: **Ordered packing of epithelial cells. A)** Example of 2D lattices of square-packed epithelia. Gray spheres represent nuclei, red squares the cell membranes and the cytoplasm is marked in blue. **B)** Panel images showing the ectoderm of *Paryhale hawaiensis*: (A–B) Stage 15 (80 hpf) embryos, anterior to the top. (A, *A*′) Ventral view. (*A*′) Thoracic segments of embryo(A). Nuclear DAPI staining in blue; engrailed (En) protein staining in yellow. (B) Dorsal view; showing mesoderm (false colored red cells) and vitellophages (false colored light blue cells) under the segmental ectoderm. Images from [77]. **C)** Example of 2D hexagonal packing, same color code as in panel (A). **D)** Epithelia become hexagonally packed during pupal wing development in *Drosophila melanogaster*.Processed images of Cadherin-stained wings where the number of neighbors per cell is color coded as shown in the legend. Scale bars = 10 μm. Adapted from [41]

Disordered arrangements of cells can undergo phase transitions as a result of changes

in cell density or in single-cell mechanical properties, like cell adhesion, cortical tension and contractility. In this way, embryonic tissues become mechanically stable over development, which ensures the formation of correct 3D body shape. However, the aforementioned rigidity transitions, i.e. jamming and glass transitions, occur in a regime of structural cellular disorder, which is not the final state of many adult tissues. How densely packed tissues manage to transition from a disordered to an ordered arrangement during morphogenesis is still an open question.

Epithelia are confluent and highly polarized tissues, where cells are often packed in ordered cellular arrangements (Fig. 1.6 A, C). Indeed, the function of many epithelial tissues depends on the formation of precise geometrical arrays of the constituent cells. For example, hair cells in the mammalian inner ear need to arrange in regular patterns to sense sound waves [132, 42]; ommatidia are organized into a hexagonally packed grid to minimize light scattering and ensure a most efficient vision in the compound invertebrate eye [102], while different photoreceptors are regularly spaced throughout the outermost layer of the vertebrate retina to improve vision acuity [3]. Since rearrangements of neighboring cells are typically disordered, active energy expenditure is required to establish ordered tissue structures, both at short and long range. A remarkable example is the regular grid of ectodermal cells in the *Payhale hawaiensis* embryo (Fig. 1.6 B). In this crustacean, ordered cellular geometries delineate the body plan at early stages of development, which is then implemented via extensive proliferation [32]. Before this outgrowth, the monolayered ectoderm is organized in a grid of orientationally ordered cells, where each row corresponds to segments of the adult body [32]. The four-fold ordering of cells is established by cell divisions, whose axis of orientation is actively aligned along the anterior-posterior axis [40]. Timed regulation of oriented cell divisions establishes a long-range orientational order of the ectodermal grid, while avoiding fluid-like rearrangements that could mix cells and alter ordered packing [40]. Interestingly, the square cell packing that characterizes the presumptive pharynx of *Drosophila* is also formed as a consequence of regulated cell alignment and oriented cell division, together with concerted apicobasal elongation of epithelial cells [202]. The timely regulation of cell rearrangements that produces ordered packing of epithelia indicates that cell packing is coordinated with other developmental processes, like proliferation and cell fate commitment. However, the mechanisms that drive this coordination are still elusive.

Until recently, most studies have focused on quantifications of the apical cell surface of epithelia to study their cell organization and changes thereof over development. In the *Drosophila* wing epithelium, which originates from a PSE, apical cell shapes and sizes vary across intervein regions, showing a disordered arrangement of various polygonal shapes [41]. The same epithelial cells are repacked into a hexagonal array shortly after pupal molt and before hair formation and organize themselves into strikingly regular honeycomb patterns that are found across many biological tissues at later stages of organ development (Fig. 1.6 B, D) [41]. It has been proposed that quasi-hexagonal packing and, in general, regular polygonal arrangements, follow physical and geometrical laws that help minimize

the cell-to-cell lateral contact surface energy, namely Euler's polyhedron formula, Lewis's law and Aboav-Wearie's law [119, 1, 41, 105]. Interestingly, these geometrical relationships hold true even when considering the complex 3D cell shapes of epithelial cell in PSE [67, 66]. This suggests that remodeling of cell shapes is actively regulated over development to reach an energetically favorable state.

So far, most studies have dissected the role of a noncanonical Wnt singaling pathway, i.e. the planar cell polarity (PCP) pathway, in the formation of ordered cell arrangements in developing epithelia. Hexagonal cell shape and packing is actively established by proteins of the PCP pathway that localize at adherens and tight junctions and contribute to regulate the extent of epithelial cell rearrangements, both in invertebrates and vertebrates [220]. Planar cell rearrangements directly affect cell shape and allow for the remodeling of tissues while maintaining their cohesivity [96]. Activity of other proteins involved in apical cell polarity have been shown to regulate the formation and the stability of cell junctions, thereby establishing ordered honeycomb-like patters. For instance, loss of function of the lipid phosphatase PTEN disrupts epithelium cell packing and leads to the formation of cobblestone patterns in the *Drosophila* wing pouch [17]. This is due to altered cortical distribution of myosin II upon loss of PTEN activity, leading to instable cell junctions during cell rearrangements. Interestingly, this cobblestone pattern generated by PTEN KO cells in the fly wing is reminiscent of the ectodermal grid found in *Paryhale*. This suggests that similar cellular patterns can be generated in different ways and similar cellular mechanisms that have been shown to impact density-independent phase transitions can regulate the formation of hexagonal patterns at later stages. This is possible thanks to the activity of factors of the PCP pathway, that regulate cell rearrangements to establish ordered packing.

Most of what we know regarding ordered cell arrangements comes from studies in invertebrate animals, as outlined in the previous paragraphs. New insights into the mechanisms that regulate ordered epithelial packing might come from studies in vertebrate tissues. One striking example of ordered complexity is the neural retina, which exhibits a multi-layered structure that is highly organized both along the radial axis and within each neuronal layer [82]. In particular, the zebrafish retina holds great potential for investigating epithelial cell arrangements during development *in vivo* due to its accessibility, tissue transparency and fast embryogenesis.

1.4 The zebrafish retina as a key tissue to investigate pseudostratification and packing dynamics

Ordered cellular packings play a functional role in many sensory organs, such as the inner ear and the eye [132, 82]. In the eye, the the physics of light dictates the structure of the tissue [114]. Visual systems have evolved multiple times to different sizes, shapes and designs to being able to focus and bend light rays and absorb photons [150]. As a result,

the structures evolved for photoreception show a vast degree of complexity that ranges from simple pigmented eye spots found, for example, in ascidians and cnidarians [55, 165], to the compound eye found in arthropods and the camera-type eye found in some mollusks and vertebrates [150, 15, 193]. In particular, the compound and camera-type eyes allow for high-resolution vision that can be adapted even for nocturnal and deep-sea use, thanks to the introduction of the lens to focus light beams on the photoreceptive tissue [150]. In vertebrates, the retina is the neural tissues that is responsible for functional vision and its structure and cellular composition is highly conserved [82, 73]. This has raised the possibility to compare conserved features in retinal design across different species and to translate findings from one species to another.

Because of the stereotypicality of the final tissue architecture, our knowledge regarding retinal morphogenesis comes from findings in a plethora of different bilaterian vertebrate species. The developing retina of the teleost *Danio rerio* is a particularly convenient tissue for investigating retinal morphogenesis: even though it is part of the CNS, it is more accessible than the rest of the brain because of its position within the eye bulb at the left and right sides of the head (Fig. 1.7 A). This, together with its tissue transparency, makes the zebrafish retina particularly amenable for fixed and live imaging. In addition, the zebrafish embryo is characterized by a small size and fast, *ex utero* development. The generation of transgenic zebrafish lines that enable the labelling of specific cell types or cellular structures allows to visualize the spatiotemporal dynamics of proliferation, differentiation and neuronal lamination in retinal tissues over development. This, together with genetic and chemical and mechanical perturbations, has generated a detailed understanding of morphogenesis of the vertebrate retina.

1.4.1 Structure and composition of the retina

In vertebrates, the retina is located at the back of the eyeball and opposite to the lens. In this way, light enters through the pupil and is focused by the lens on the retina, where light-sensitive cells capture the light and convert it into electrical signals in a process called phototransduction. These signals are then sent to the optic tectum (in non-mammalian vertebrates) or the superior colliculus (in mammalian vertebrates) via the optic nerve. In the occipital lobe of the neocortex that further processes the signals and decodes them to create an image. To achieve this, the retina shows a hemispheric shape and feature a laminated structure with distinct layers of neurons interconnected by synapses (Fig. 1.7).

The mature vertebrate retina is composed of six major neuronal types and one glial cell type, arranged in three nuclear layers, where the neuronal cell bodies are segregated, and two plexiform layers, where axonal and dendritic processes of retinal neurons form connections (Fig. 1.7 D, E). The specialized neuroepithelial cells that ensure visions are called photoreceptor cells (PRs) and lie at the outermost layer of the retina, adjacent to the Retinal Pigmented Epithelium (RPE), a tissue that is essential for photoreceptors' survival. Two main types of PRs exist: rods, which are sensitive to light intensity and

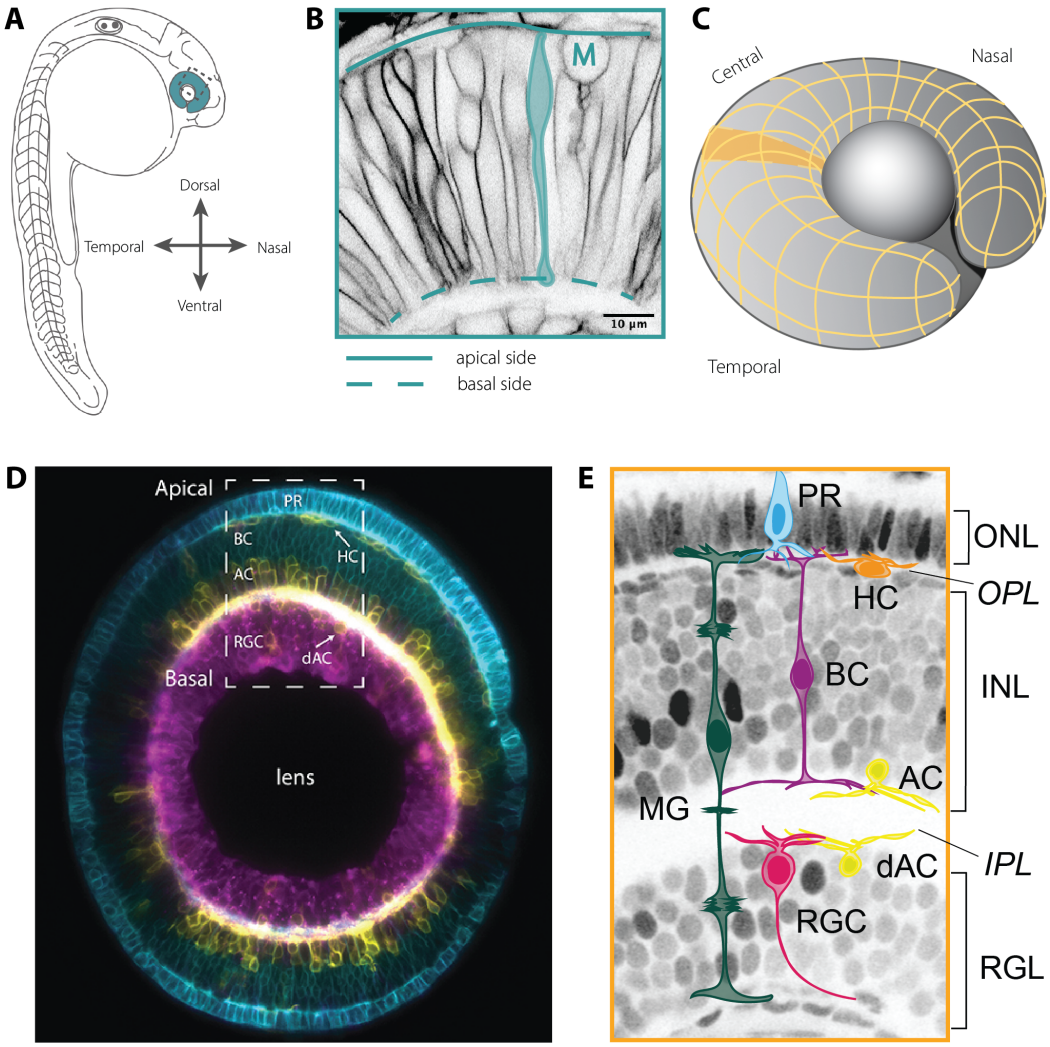

Figure 1.7: **Anatomy, composition and structure of the zebrafish vertebrate retina. A)** Schematics of a zebrafish embryo at 24 hpf. The retinal neuroepithelium is colored in blue. **B)** Optical slice of the Retinal Neuroepithelium at 24 hpf. Cell membranes are labeled by Tg(actb1::HRAS-EGFP).The profile of one individual cells is drawn in light blue. Solid line: apical side. Fragmented line: basal side. M: mitosis. **C)** 3D rendering of the optic cup. The orange shaded area is the part of the retina shown in panel (E). **D)** Optical slice of the retina of a zebrafish embryo at 80 hpf. The retinal cells are labeled with a combination of membrane-tagged fluorescent proteins that allows the identification of all the major neuronal types. In Cyan, the photoreceptors and bipolar cells under Crx promoter (Crx:gapCFP). In yellow, the horizontal cells, amacrine cells, and displaced amacrine cells under Ptf1a promoter (Ptf1a:Gal4/UAS:gapYFP). In magenta, the retinal ganglion cells under Ath5 promoter (Atoh7:gapRFP). Arrows indicate horizontal cells and displaced-amacrine cells. Image from [7]. **E)** Different neuronal types arrange their nuclei along the radial axis of the laminated vertebrate retina. Abbreviations: AC, amacrine cell; BC, bipolar cell; dAC, displaced amacrine cell; GCL, ganglion cell layer; HC, horizontal cell; INL, inner nuclear layer; IPL, inner plexiform layer; LGN, lateral geniculate nucleus; MG, Müller glia cell; ONL, outer nuclear layer; OPL, outer plexiform layer; PR, photoreceptor; RGC, retinal ganglion cell. Adapted from [151]

are involved in crepuscular and night vision, and cones, which are responsible for color perception. The cell bodies of PRs form the outer nuclear layer (ONL). Both rods and cones establish synapses in the first Outer Plexiform Layer (OPL) with Bipolar Cells (BCs), which are long-projecting neurons that receive visual inputs from PRs and send their axonal projections to Retinal Ganglion Cells (RGCs), thereby connecting the outer and inner layers of the retina. The information transfer between PRs and BCs is modulated by horizontal cells (HCs), named after their wide and diffuse horizontal projections. HCs are GABAergic interneurons that provide inhibitory inputs to both BCs and rods and cones. HCs are not the only interneurons found in the retina: Amacrine Cells (ACs) form connections with both BCs and RGCs at the innermost plexiform layer (IPL) and filters the information between these two neuronal cell types. To do this, ACs release the inhibitory neurotransmitters GABA or glycine, but can induce both inhibitory and excitatory responses. The cell somas of horizontal, bipolar and amacrine cells form the so-called Inner Nuclear Layer (INL). RGCs reside in the innermost layer, called RGC layer (RGL), and receive both excitatory and inhibitory inputs from ACs and BCs. Their axons form the optic nerve, which transmit the visual information to the brain. Finally, Müller Glia cells (MGs) are the only type of radial glia found in the retina. Their cell bodies are positioned in the INL, but their processes span the whole height of the retinal tissue. As other glial cells in the brain, MGs' function is to maintain tissue organization and structure, secrete neurotrophins and promote synaptic turnover [122, 210]. Only a distinct region of the mature retina is not populated by terminally differentiated neuronal types. This region is the so-called Ciliary Marginal Zone (CMZ) and it acts as a stem cell niche, where multipotent progenitors are maintained during homeostasis and continually generate new neurons to promote post-embryonic eye growth in fish, amphibians and birds [60]. In contrast, mammals have few cells at the periphery of the retina that can be induced to express stem cell-like properties in culture, but that do not form a classically defined CMZ *in vivo* [60].

The organized architecture of the mature retina and its hemispheric shape are highly conserved features of the camera-type eye and can be found throughout vertebrates. Just as its final tissue architecture, also development of the neural retina is highly conserved across vertebrate species and, to a certain extent, across invertebrates [150]. Besides the fact that many orthologous genes and signaling pathways have been shown to be necessary for eye development both in *Drosophila* and vertebrates [39, 111], the pseudostratified arrangement of the developing Retinal Neuroepithelium (RNE) has been shown to be conserved across different systems of eye development. For instance, PSNE are found as organ precursors both in *in vitro* models of optic cup formation and in cephalopods, such as the squid and the octopus, which are the only species of molluscans to showcase a complex camera-type eye [185]. Retinal organoids that are developed from mouse and human pluripotent stem cells have been used as model systems of retinal development to reveal the self-organizing properties of stem-cell derived retinal neuroepithelial cells, as they organize into hemispherical shaped PSNE [53, 146]. Similarly, the retina of

cephalopods like the squid and the octopus originates from a PSNE, which is unusual for an invertebrate neurogenic tissue and represents a striking example of convergent evolution [147]. Therefore, the occurrence of PSNE as organ precursors for retinal development both in vertebrates and in cephalopods and even in *in vitro* organoids further strengthen the hypothesis that pseudostratification represents a functionally relevant tissue arrangement for building large and complex nervous systems. In conclusion, the retina represents a great model to study the emergence of ordered packing in neural tissues of the CNS.

1.4.2 Retinal morphogenesis from a PSE

The zebrafish retina emerges from the optic vesicle after eye-field specification and splitting of the optic primordium from the forebrain via expression of a conserved set of homeobox genes [118]. Already as part of the forebrain, the optic primordium shows a pseudostratified arrangement that is maintained throughout most of retinal morphogenesis, from the optic primordium to the onset of neuronal lamination in the RNE (Fig. 1.7 B & 1.8 B) [151]. After evagination, the optic vesicle features two pseudostratified neuroepithelial layers: the cells on the most proximal side will form the RPE, while those on the most distal side will give rise to the RNE. The specification of these two distinct tissues occurs during the reshaping of the optic vesicle into the optic cup, which ensures the formation of the typical hemispherical shape of the retina. While the RNE remains pseudostratified, the RPE cells flatten on the outside of the optic cup and constrict their basal processes using an actomyosin-dependent mechanism to enable optic cup formation [142]. In addition to this, so-called rim cells migrate from the RPE layer to the RNE to populate the future neuronal retina and integrate into the PSNE (Fig. 1.8) [112, 188, 191]. By 20-22 hours post fertilization (hpf), the typical hemispheric shape of the optic cup is established, consisting of a pseudostratified RNE and a squamous RPE, and the tissue grows continuously afterwards [130].

The pseudostratified RNE is formed already by 20 hpf and is composed of a single pool of multipotent progenitor cells that give rise to all neuronal and glial types of the mature retina. During the next 22 hours of development, the multipotent progenitors will proliferate and afterwards progressively undergo neurogenic cell fate commitment (Fig. 1.9 A). During this proliferative phase, multipotent progenitors are always arranged in a PSNE and elongate their shape to accommodate more and more cells. While nuclei initially do not occupy the basal side of the RNE, where an actomyosin basal enrichment is observed between 24 and 36 hpf, they do progressively fill the entire length of the tissue by 42 hpf [130]. As a result, nuclear packing increases over time and the nuclear component becomes predominant in the composition of the proliferating retinal PSNE [130, 14]. Moreover, the proliferation of multipotent progenitors is distributed throughout the RNE to ensure isotropic growth of the tissue, together with neuroepithelial cell shape elongation [130]. The rapid growth of the zebrafish RNE is sustained by a rapid cell cycle, with an average length of about 7 hours around 30 hpf reducing to about 5 hours

by 42 hpf [130]. In the RNE, spatiotemporal variations in cell cycle length are controlled by several cell-intrinsic and -extrinsic factors that interact with the cell cycle machinery. Specific regulators of proliferation are expressed by multipotent progenitors in the neural retina, such as the homeobox genes Rx/Rax, Pax6, Six3, Optx2/Six3 [118]. For example, overexpression of XOptx2 in *Xenopus* leads to increased retinal cell proliferation rate and enlarged retina [229]. Activation of the Wnt/β-catenin and Notch signaling pathways regulate the proliferative state of multipotent progenitors in the RNE and in the CMZ, for instance by acting upstream of cyclin D1 and p27 in chick and *Xenopus* embryos [110, 154]. Thus, several factors are involved in regulating proliferation versus cell cycle exit to ensure high rate of proliferation in the developing neural retina.

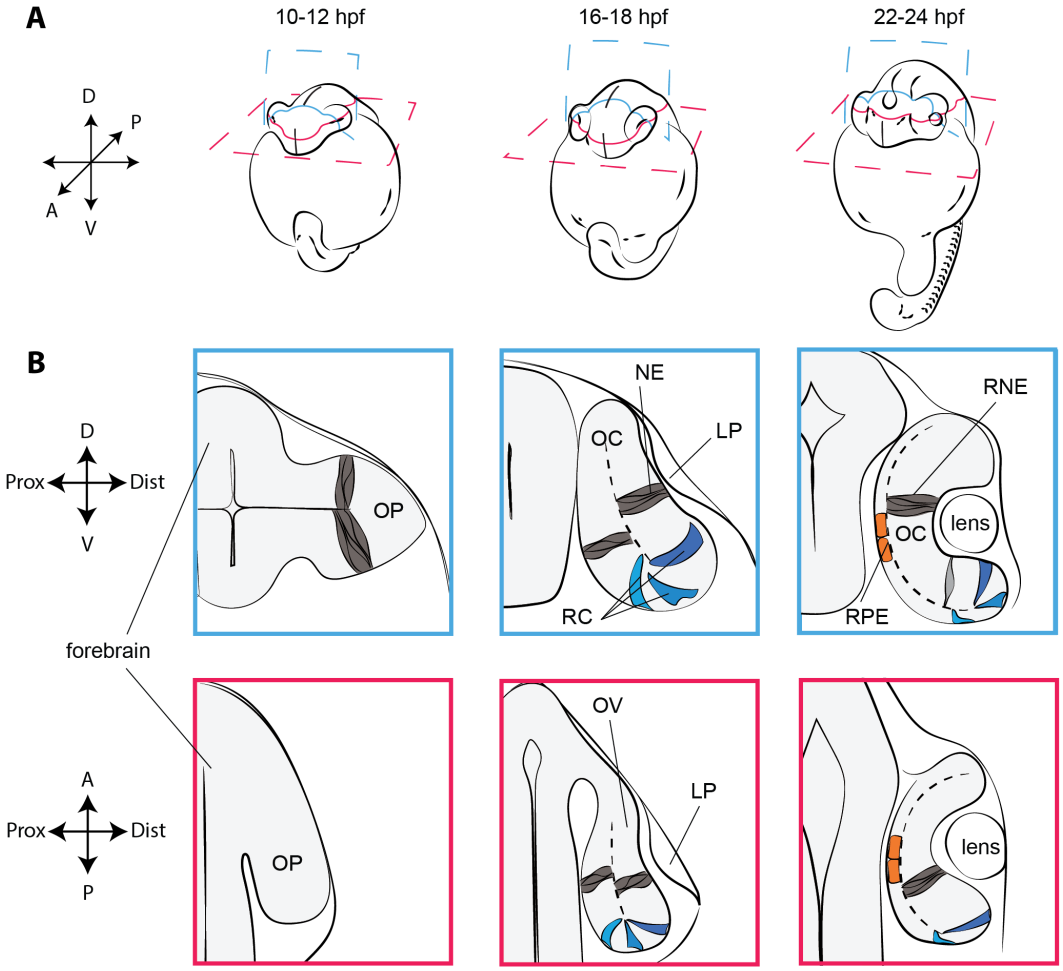

Figure 1.8: **Optic cup morphogenesis in *Danio rerio*.** A) Schematics of optic cup development in relation to the rest of the developing embryo. B) Dorsoventral (top, blue) and anteroposterior (bottom, red) view of cell rearrangements during zebrafish optic cup development. Abbreviations: A, anterior; P, posterior; D, dorsal; V, ventral; hpf, hours post fertilization; LP, lens placode; NE, neuroepithelium; OC, optic cup; OP, optic primordium; OV, optic vesicle; P, posterior; PSE, pseudostratified epithelium; RC, rim cells; RPE, retinal pigmented epithelium; V, ventral. Figure adapted from [151].

Already during the proliferative phase, multipotent progenitors progressively start

differentiating into neurogenic progenitors and ultimately exit the cell cycle to give rise to the retinal neurons (Fig. 1.9 B). The first neurogenic progenitors start expression of the pro-neural gene atonal bHLH transcription factor 7 (Atoh7, also known as Ath5), right before their cell division [86, 166]. This transcription factor is required for neuronal fate specification in RGCs [95], but all neuronal precursors that will give rise to PRs, HCs and ACs also express it as a component of their transcription factor network [95, 92, 217]. In the zebrafish retinal PSNE, expression of Atoh7 progresses in a fan-like fashion, starting with few cells at the ventro-nasal side around 28 hpf [83, 180, 128] and expanding to the temporal side by 48 hpf [4]. A second neurogenic wave driven by Atoh7-negative progenitors expressing the visual system homeobox gene 1, Vsx1, starts around 34 hpf and gives rise to BCs and some ACs by 72 hpf [155].The spatiotemporal regulation of neurogenesis is achieved via signal transduction of multiple cell-extrinsic factors that activate the transcription of proneuronal genes in multipotent progenitors. The initial expression of Atoh7 at the nasal side is induced by the secretion of fgf3 and fgf8 from the optic stalk [129, 128]. While FGF signaling is necessary to initiate Atoh7 transcription, the propagation of the neurogenic wave requires also the expression and secretion of SHH from the differentiating RGCs [216]. The balance between proliferating and differentiating progenitors is achieved through the asymmetric inheritance of several cellular components, such as Notch signaling endosomes [148]. In the retina, Notch signaling sustains the proliferative state of progenitor cells and suppresses neurogenesis via lateral inhibition by blocking the expression of pro-neural genes like Atoh7 [148, 16, 181, 131, 91]. Disruption of Notch signaling alters the number of progenitor cells that enter the neurogenic path. For instance, Notch inhibition causes tissue size reduction both in the vertebrate retina and telencephalon since it causes premature differentiation of progenitor cells into neurons [131, 91, 148]. Thus, disruption of the balance between proliferating and differentiating progenitors has tissue-wide consequences on the retinal PSNE. Overall, neurogenic progenitors undergo a finite number of cell divisions as they terminally differentiate into distinct retinal neuronal types following a stereotypical birth order [38].

Once committed to one cell fate, neuronal precursors deploy different strategies to migrate through the densely packed retinal tissue towards their final positions (Fig. 1.9 B) [7]. The first type of neurons to be generated, the RGCs, undergo directed translocation of their soma towards the basal side, while the cell stays attached to either both sides or the basal side of the tissue [166, 228, 86]. Positioning of RGCs is crucial to establish the spatiotemporal tissue patterning mediated by SHH: when distribution of the apical factor aPKC is altered in neuronal progenitors, cells divide non-apically and their positions are altered, causing ectopically differentiated RGCs to further induce neuronal lamination defects [86]. PR precursors undergo bidirectional somal translocation, moving first basally and then apically to their final position [170]. It has been shown that this counter-intuitive mode of translocation prevents cell crowding at the apical surface and allows multipotent progenitors to divide apically during the peak of the proliferative phase in the retinal PSNE

[130, 170]. In contrast to RGCs and PRs, ACs and HCs exhibit first a bipolar migration mode and then switch to an amoeboid-like multipolar migration mode that is less directed and shows more direction changes [6]. It is not clear what cues ACs and HCs follow to explore and navigate through the 3D volume of the INL, even though it is likely that these cues are of chemical nature rather than mechanical, since no evident gradient in stiffness was observed in the INL of the developing zebrafish retina [8]. Last but not least, BPs are the last neurons to be born in the retina and, once born, they reposition their nuclei and somas within the INL while establishing connections in the IPL and the OPL [221, 54]. Stereotyped birth order and many of the mechanisms involved in neuronal lamination have been shown to be conserved among vertebrate species, including frog, zebrafish, chicken, mouse and human [7]. Eventually, fine positioning of newly generated neurons establishes the intricate architecture of the laminated vertebrate retina. Though, how neuronal precursors migrate through the densely packed retinal tissue and how they manage to do this without disrupting the arrangement of proliferating multipotent progenitors or the positioning of other neurons is still not fully clear.

Overall, the zebrafish retina is formed through distinct developmental phases. First, the optic vesicle separates from the forebrain and invaginate to form the typical hemispherical shape of this tissue [112]. Second, multipotent progenitors undergo an intense proliferative phase to accumulate more progenitor cells in the tissue and their cell shape elongation enables the isotropic growth of the pseudostratified RNE [130]. This phase overlaps with the onset of neurogenesis and cell fate specification. Finally, neuronal progenitors migrate towards their final positions to form the laminated neural retina. All these processes occur within only three days of development in *Danio rerio*, making this species an exceptional model to study retinal morphogenesis. How the developing zebrafish retina transitions from a pseudostratified and monolayered neuroepithelium to a chaotic structure during neuronal lamination to, ultimately, an ordered and layered neuronal tissue is only now starting to be elucidated.

1.5 Aim of the thesis

The goal of this study is to characterize nuclear packing over development of the retinal PSNE and determine how potential changes in packing can affect retinal morphogenesis. To do this, my first aim was to produce a 3D characterization of nuclear packing in the zebrafish retinal tissue over time. Several studies have tried to quantified the extent of nuclear crowding in the retina before, but they either produced course-grained measurements of cellular shapes and sizes [130] or were limited to a 2D analysis of the tissue [100]. Thanks to recently improved deep-learning based algorithm, I could segment volumetric datasets of fixed retinal samples at different developmental stages and follow nuclear packing changes over time. In this way, I could compare the 3D packing of nuclei in the retinal PSNE to theoretical 3D packing of spherical objects in disordered and ordered arrangements (Fig. 1.10). This dataset allowed me to further quantify the ordering of nuclear

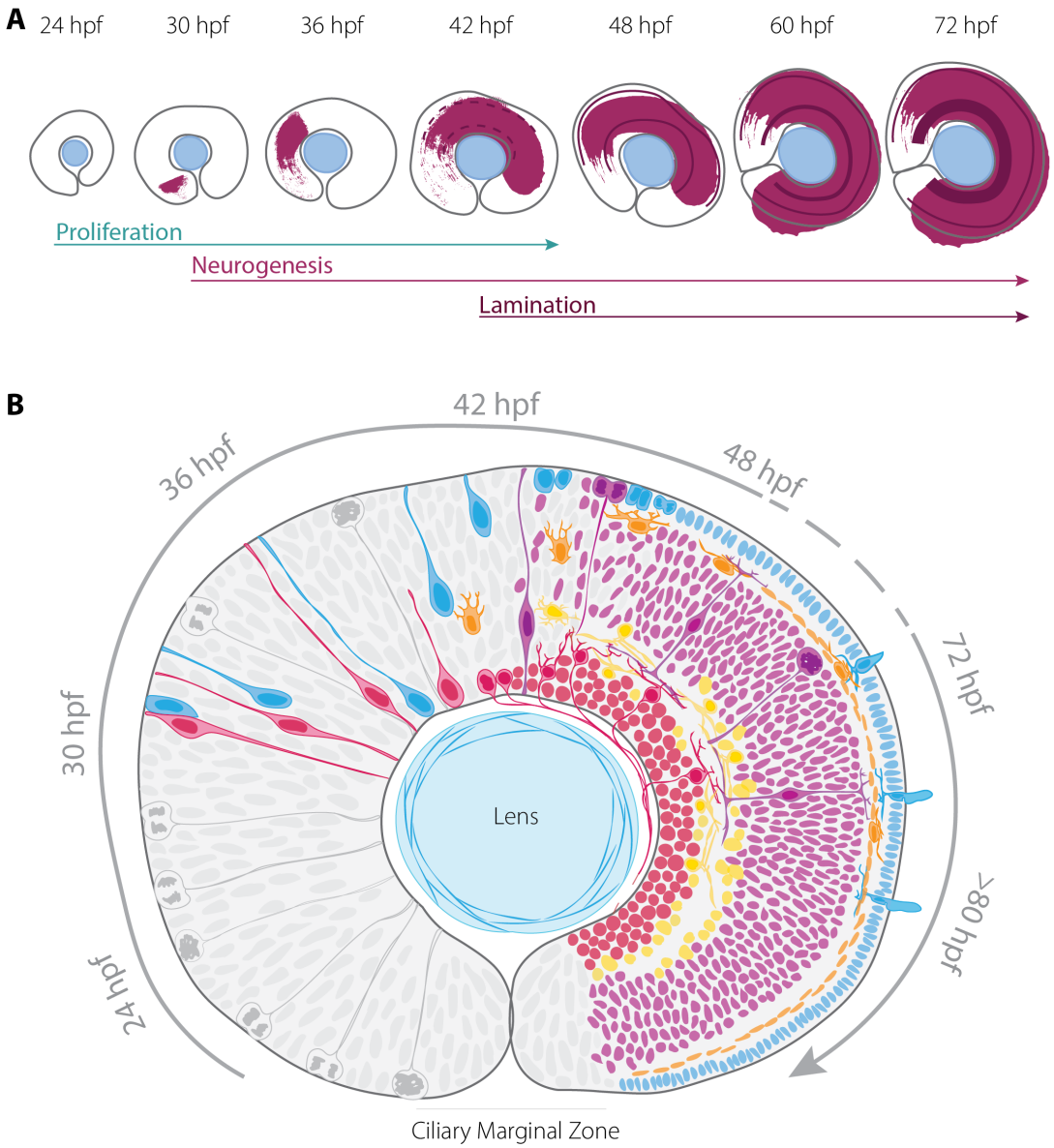

Figure 1.9: **Development of the vertebrate retina. A)** Schematic of vertebrate retinal development. After formation of the optic cup, the retinal PSE grows isotropically during a phase of intense cell proliferation. Multipotent progenitors progressively start differentiating in a fan-like fashion (marked in magenta) and ultimately delaminate to form a stratified neural retina. **B)** Schematics of migration and lamination of the different neuronal types within the densely packed zebrafish retina between 24 and 80 hpf. Nuclei and mitotic cells in the retinal PSNE are colored in grey. RGCs are marked in red, PRs in cyan, HCs in orange, ACs in yellow and BCs in purple. Adapted from [151]

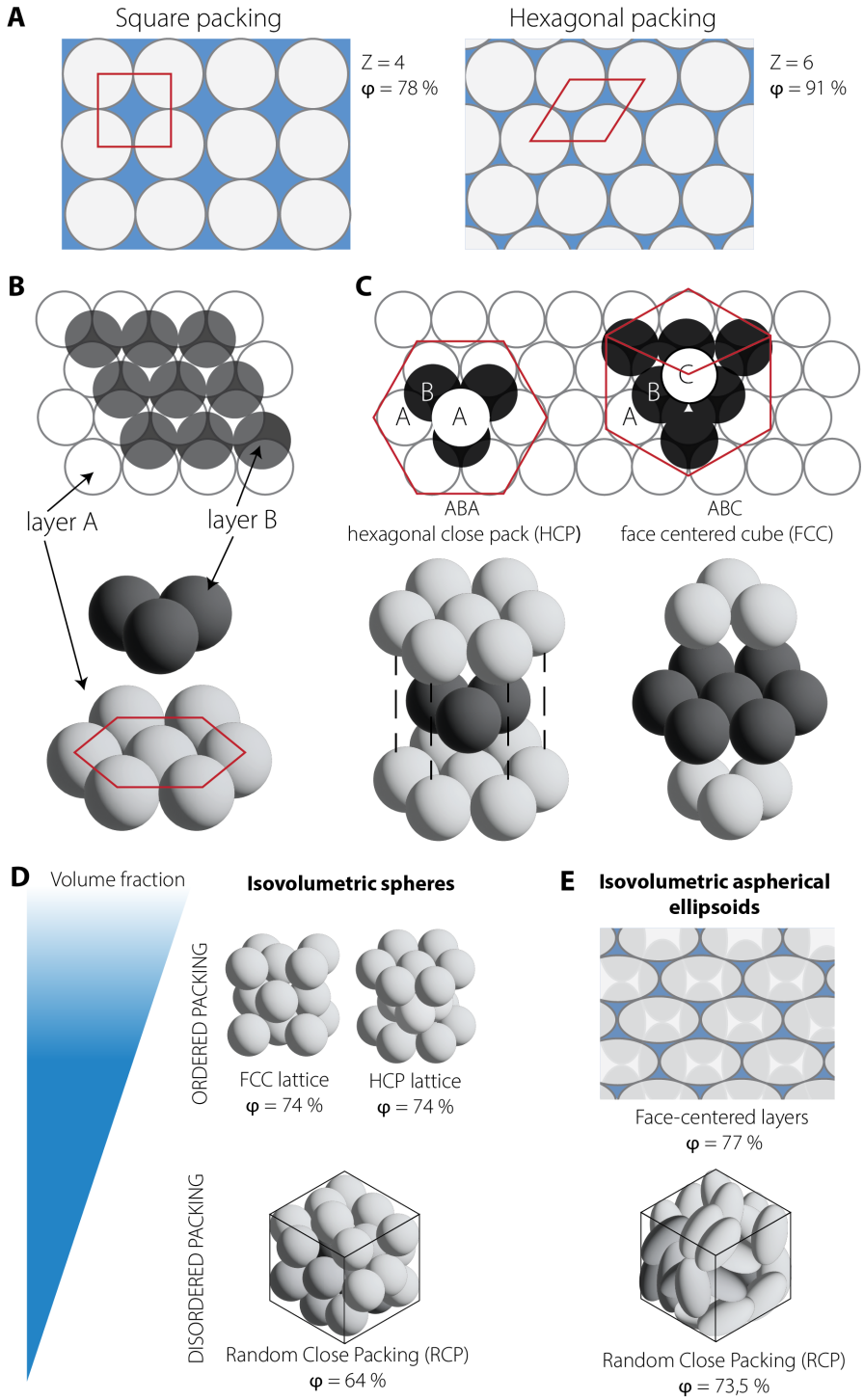

Figure 1.10: **Random and ordered 3D packing of spheroids and ellipsoids. A)** Examples of 2D lattices for isovolumetric spheres. Shown above are unit cells for the close-packed square and hexagonal lattices. The optimal packing in 2D is reached with hexagonal packing, with a volume fraction $\phi = 0.91$ and contact number z = 6. **B)** Building close-packed 3D lattices from a first layer of hexagonal packing. **C)** Structure of the hexagonal close packing (HCP) and face-centered cubic lattices. **D)** Comparison of the volume fraction occupied by monodispersed spheres between FCC or HCP lattices and in Random Close Packing (RCP). **E)** Aspherical ellipsoids can reach reach higher values of volume fraction both in an ordered and disordered arrangement. Adapted from [47].

arrangements during the transition from a pseudostratified monolayer to a crystal-like laminated neural tissue. Based on this knowledge, I aimed at understanding the effects that nuclear packing itself could have on the mechanical properties of the retinal PSNE during maturation of the tissue, as recently suggested by 2D theoretical modeling and analysis of the zebrafish retina [100]

Changes in material tissue properties have the potential to affect several cellular behaviors, such as neural crest migration in *Xenopus* and digit formation in *Mus Musculus* [18, 159]. For instance, it was proposed that a link between tissue packing and differentiation exists in developing neuroepithelia and in axon guidance [81, 205]. Whether dense nuclear packing could impact onset of neurogenesis in the retinal PSNE is not known. Furthermore, the extent by which proliferation and differentiation are coordinated with nuclear packing to allow correct growth of the retinal tissue is still elusive. To address these questions, I interfered with some of the gene regulatory networks that are involved in eye-field specification and with neurogenesis to alter the number of multipotent progenitors at different developmental times and test how the retinal tissue would respond.

Based on our 3D segmentation of nuclear packing, I observe orientational order of nuclei in the PSNE that is maintained throughout development also at later stages in the laminated retina. Upon perturbation of the number of multipotent progenitors in the optic cup, I find that the retinal PSNE buckles during the proliferative phase and this tissue deformation is not resolved during neuronal lamination. A similar phenotype is seen when blocking neurogenesis, that results in failure of nuclear shapes remodeling and neuronal lamination. Overall, these findings support the idea that pseudostratification can establish an orientational order that defines the radial structure of the retina also at later stages of development. Our results show that changes in nuclear packing allow for the PSNE to transition to a crystal-like arrangement and pack more progenitors without disrupting tissue shape. This is achieved via timely regulation of proliferation and differentiation and is likely coordinated with the maturation of surrounding tissues.

2

Results

All the experiments presented in the following chapters were designed and performed by myself, i.e. Lucrezia Camilla Ferme, under the supervision of Dr. Caren Norden, and based on input discussions with Dr. Carl Modes from MPI-CBG Dresden. A subset of the imaging dataset acquired at 72 hpf and images at 80 hpf stages were imaged by Elisa Nerli, another PhD student in the lab. The image annotation of the training and test datasets was performed by myself with the help of Elisa Nerli. The training and the evaluation of the Stardist-3D model was performed by myself. The image analysis pipeline was coded and established by myself with input advices from Dr. Robert Haase from PoL-TU Dresden and with the collaboration of Allyson Q. Ryan, a postdoctoral researcher in Dr. Carl Modes' and Dr. Robert Haase's groups at MPI-CBG and PoL-TU Dresden. The pipeline to quantify the Atoh7 intensity profile was designed by Dr. Robert Haase and Dr. Diana Garcia Moralez, a postdoctoral researcher in the lab, and implemented by myself on my dataset. The AFM measurements were performed in collaboration with Dr. Elias Barriga and Dr. Jaime A. Espina from IGC and PoL-TU Dresden. The cell depletion experiment was performed together with Dr. Jorge Carvalho from the Microfabrication and Microfluidics facility at IGC.

The work presented in this thesis contributed to the following publications:

- Ramos AP, Szalapak A, Ferme LC, Modes CD. **From cells to form: A roadmap to study shape emergence in vivo**. Biophysical Journal, 2023, Volume 122, Issue 18, 3587 - 3599
- Ferme LC, Ryan AQ, Haase R, Modes CD, Norden C. **Timely neurogenesis enables increased nuclear packing order during neuronal lamination**. biorxiv, 2024. DOI: 10.1101/2024.11.12.623216. under review

2.1 Quantifying 3D nuclear packing in the zebrafish retinal neuroepithelium

To understand how individual cells are positioned within proliferating neuroepithelia, we investigated the arrangements of nuclei in the developing retinal PSNE of *Danio rerio*. This neuroepithelium had already been described as an extremely densely populated tissue [130], thus allowing us to explore the hypothesis that pseudostratification could be advantageous to pack more cells within a proliferating monolayered epithelium.

2.1.1 Instance segmentation of nuclei in the zebrafish retinal PSNE

To analyze how nuclei of progenitor cells arrange themselves within the developing retina, we quantified their packing in the retinal pseudostratified neuroepithelium (PSNE) over time. To this end, the accurate segmentation of nuclei of volumetric (3D) fluorescence microscopy datasets was needed to enable the study of the 3D organization of nuclei in the tissue and, subsequently, capture the actual nuclear packing density and the changing arrangements of cells' bodies within the PSNE. So far, epithelial arrangements, including apical surfaces or nuclei, have been mainly described and quantified in 2D, often due to technical limitations and the lack of suitable segmentation methods to enable the detection of single cells and nuclei in volumetric datasets. Therefore, segmentation of volumetric imaging datasets represents the first step in characterizing cellular and nuclear arrangements within a 3D tissue. To expand on previous studies and facilitate 3D

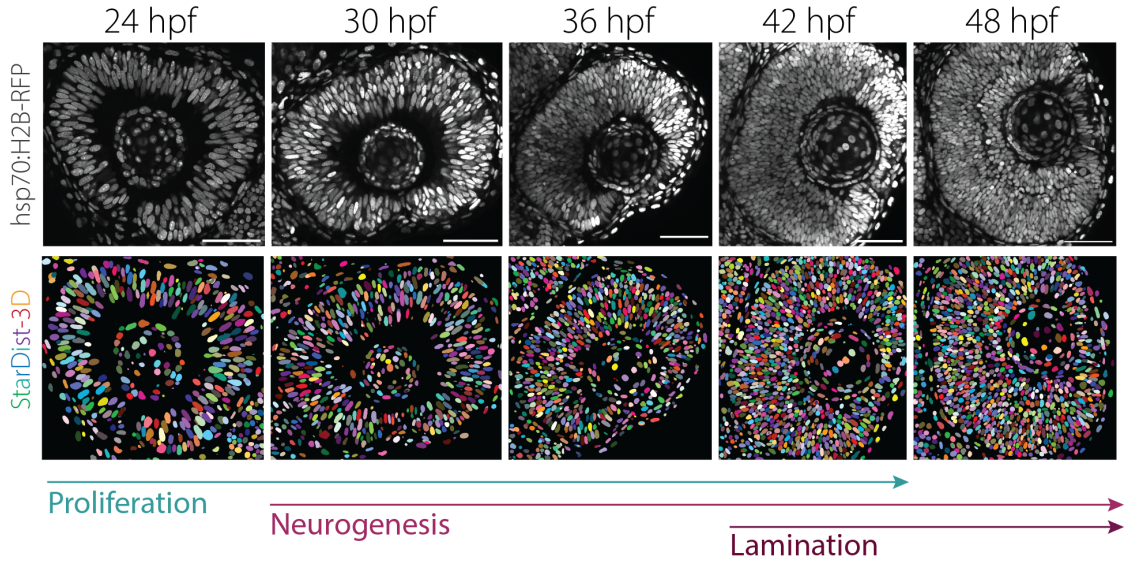

Figure 2.1: **A 3D instance segmentation zebrafish retinas using a custom trained StarDist-3D model.** Representative images of the retinal PSE (top row) and corresponding instance segmentation using StarDist-3D model A (lower row), during stages of proliferative growth (24 - 42 hpf) and at the onset of neuronal lamination(42 - 48 hpf). Nuclei are labeled with Tg(hsp70:H2B-RFP). Scale bar = 50 μm.

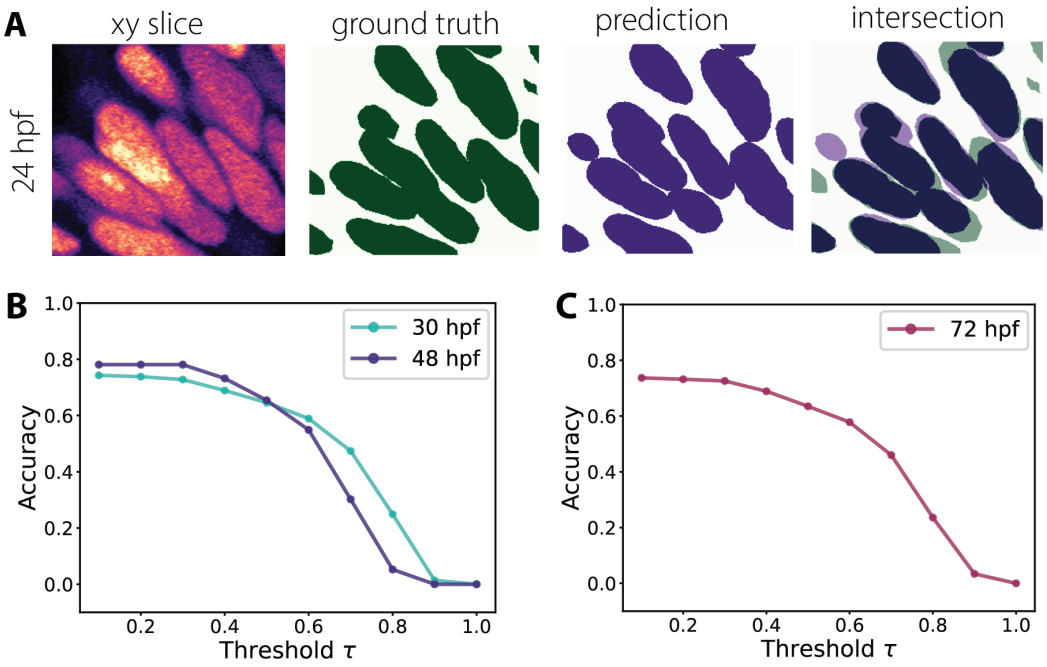

Figure 2.2: **Evaluation of StarDist-3D models trained on our dataset. A)** Representative cropped images of nuclei in the retinal PSNE at 24 hpf, the corresponding manually annotated labeled image, the StarDist-3D prediction and the overlap of the annotated and the predicted images. **B-C)** Accuracy of model A (shown in **B**) and model B (shown in **C**) on test datasets representing different stages for several thresholds τ of intersection over union.

segmentation of nuclei in the growing retina, we set to use deep learning (dl) methods and a transgenic line that could enable to visualize all nuclei within the developing embryo. To this end, we used the transgenic line tg(hsp70:H2B-RFP) that labels ?? with a red fluorescent protein (RFP), which allows to image the tissue using lasers at longer wavelengths to reduce light scattering and improve penetration depth. Furthermore, we considered that the more variable expression of H2B-RFP under a heat-shock promoter should facilitate the detection by DL methods of distinct nuclei compared to more evenly distributed staining with nuclear markers like DRAQ5 or to other constructs expressed under a constitutive promoter. Tg(hsp70:H2B-RFP) embryos were staged and fixed over neuroepithelial development at 6 ± 1 hours intervals, between 24 hours post fertilization (hpf), when optic cup morphogenesis is completed, and 48 hpf, when neuronal lamination starts to be visible (Fig. 2.1). This is the period during which retinal progenitor cells undergo intense proliferation until neurogenesis and neuronal lamination onset (Fig. 1.9 A). Fixed embryos were imaged using a laser-scanning confocal microscope (LSCM) in Airyscan 8Y mode to achieve higher resolution and facilitate the subsequent detection and segmentation of nuclei.

Detecting individual nuclei requires a specific type of computer vision task, called instance segmentation, which assigns a label mask to each single object. To locate and separate individual nuclei within a 3D volume, we tested several deep-learning methods,

namely CellPose, 3D-Unet and StarDist-3D using ZeroCostDL4Mic [218, 222, 198]. We compared the preliminary predictions we obtained and ultimately decided that StarDist-3D was the most promising method for our 3D segmentation task. To achieve a sufficiently accurate instance segmentation of nuclei, we trained our own StarDist-3D model on manually annotated datasets of embryos staged between 24 and 48 hpf and used this model for segmentation of nuclei in our volumetric dataset (Fig. 2.1). See Materials and Methods 4.4.2 for details on how training was performed.

The trained model showed high levels of accuracy when tested on new subset datasets, as shown in table 4.4. This analysis produced to our knowledge for the first time an accurate instance segmentation of nuclei in a densely populated PSNE in 3D. Based on this dataset, we established an image analysis pipeline that enabled us to explore the arrangement of nuclei, and thereby cells, within the retinal PSNE over time. To reach this ultimate goal, we extracted several single-nuclear parameters, such as nuclear volumes and other shape descriptors and further extracted individual nuclear position, neighbor statistics and nematic vectors for each labeled nucleus (Fig. 2.3). Together, these quantities allowed us to determine the degree of alignment between nuclei within the tissue and their positional ordering. With these measurements, we could also follow 3D nuclear shape changes in relation to the arrangement of nuclei throughout the proliferative phase of the retinal PSNE. For further details on this analysis, we refer the reader to the Methods section 4.4 and to the schematics in Fig. 4.1.

2.1.2 Nuclei keep an elongated ellipsoidal-like shape despite increasing packing density

To monitor possible changes in the structure of the retinal PSNE across the proliferative phase, we quantified the number of nuclei and the volume fractions of nuclear packing densities within a defined region of interests in the central part of the retina (ROIs – see Methods 4.4). This region was chosen to ensure that cells were in a similar differentiation state: in fact, neurogenesis proceeds in a wave-like fashion from the ventro-nasal side of the retinal PSNE to the temporal side [83, 4]. By measuring the volume fraction of nuclei within these ROIs at different developmental stages, we aimed to assess whether nuclear packing in the retinal neuroepithelium could approximate at any time 3D packing densities associated with phase transition boundaries that define the transition to different mechanical states, e.g. more fluid-like or solid-like. To do this, we compared our results to values from previous experimental work and theoretical simulations for the disordered and ordered packing of spherical particles in 3D (as reported in Donev et al 2004 [47]). In the case of disordered packing of particles, the Random Close Packing (RCP) density and the associated 3D jamming transition density are the maximum volume fractions that monodispersed spheres can occupy in a disordered arrangement and is associated with a volume fraction $\phi = 0.64$ (Fig. 1.10 D). In the case of ordered packings, face-centered cubic (FCC) or hexagonal-close packed (HCP) lattices allow the closest possible packing

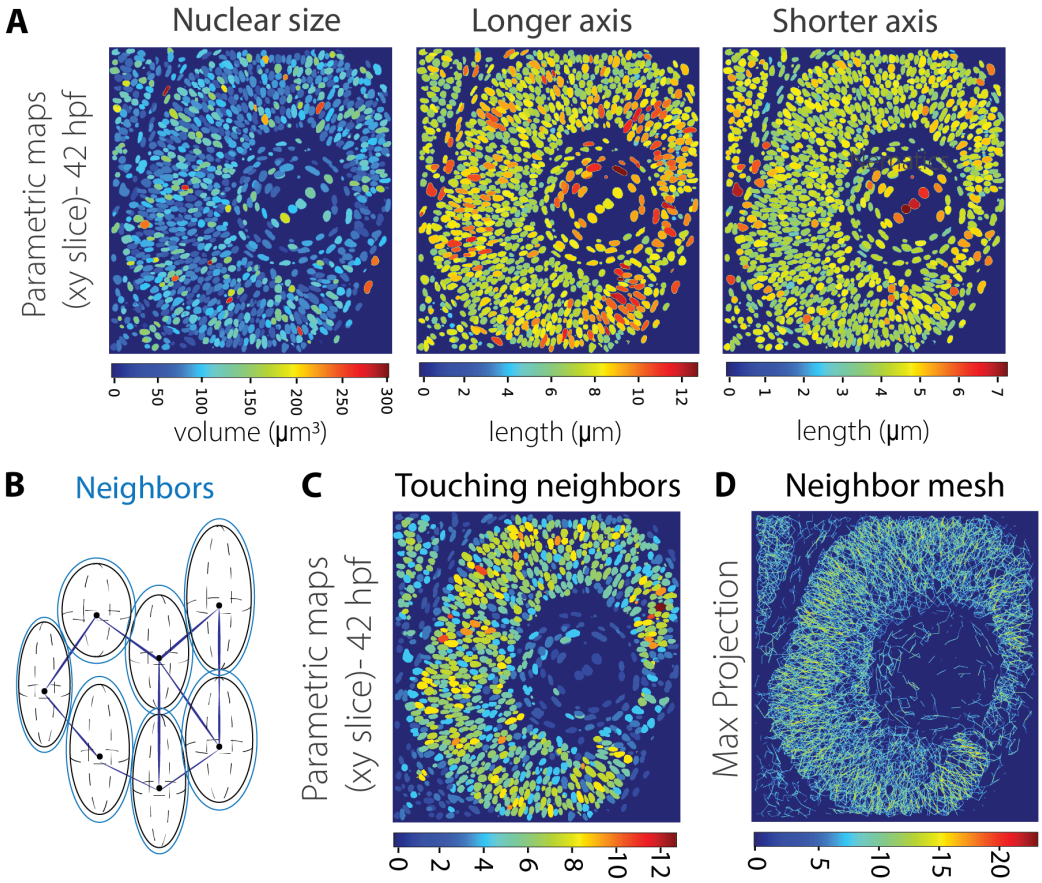

Figure 2.3: **Representative parametric images of nuclear features. A)** Parametric images of a 42 hpf retina reporting nuclear sizes, longer axis and shorter axis lengths. Each nucleus is labeled with the value that corresponds to the reported measurement. **B)** Scheme of touching neighbor definition. Nuclear boundaries were dilated by a given radius and neighbors were identified using a touch matrix. **C)** Parametric map of number of touching neighbors per nucleus as defined in B. **D)** Maximum intensity projection of a distance mesh of touching neigbors as shown in C.

of spheres, filling up to 74% of the volume, i.e. 0.74 (Fig. 1.10 D). Alternatively, it has been shown that randomly packed fully aspherical ellipsoidal particles can reach even denser packing fractions than spherical ones approaching the value 0.735 with no significant orientational ordering (Fig. 1.10 E) [47]. For the retinal PSNE, we found that the number of nuclei and the nuclear volume fraction appear to increase linearly between 30 and 42 hpf, reaching a median RCP density around 0.60 and 0.635 at 36-42 hpf and further increasing at the onset of neuronal lamination, i.e. between 42 and 48 hpf (Fig. 2.4). Thus, we observed nuclear packing densities that approach or reach theoretical limiting volume fractions, without resulting in a premature rigidity transition of the tissue, i.e. a transition from a fluid-like to a solid-like state. Premature rigidity transition would cause a progressive impairment of single-cell or nuclear movements within the tissue, which is not observed in the developing retina during the proliferative phase [130].

Since the RCP density for aspherical ellipsoids is higher than for spheres and volume

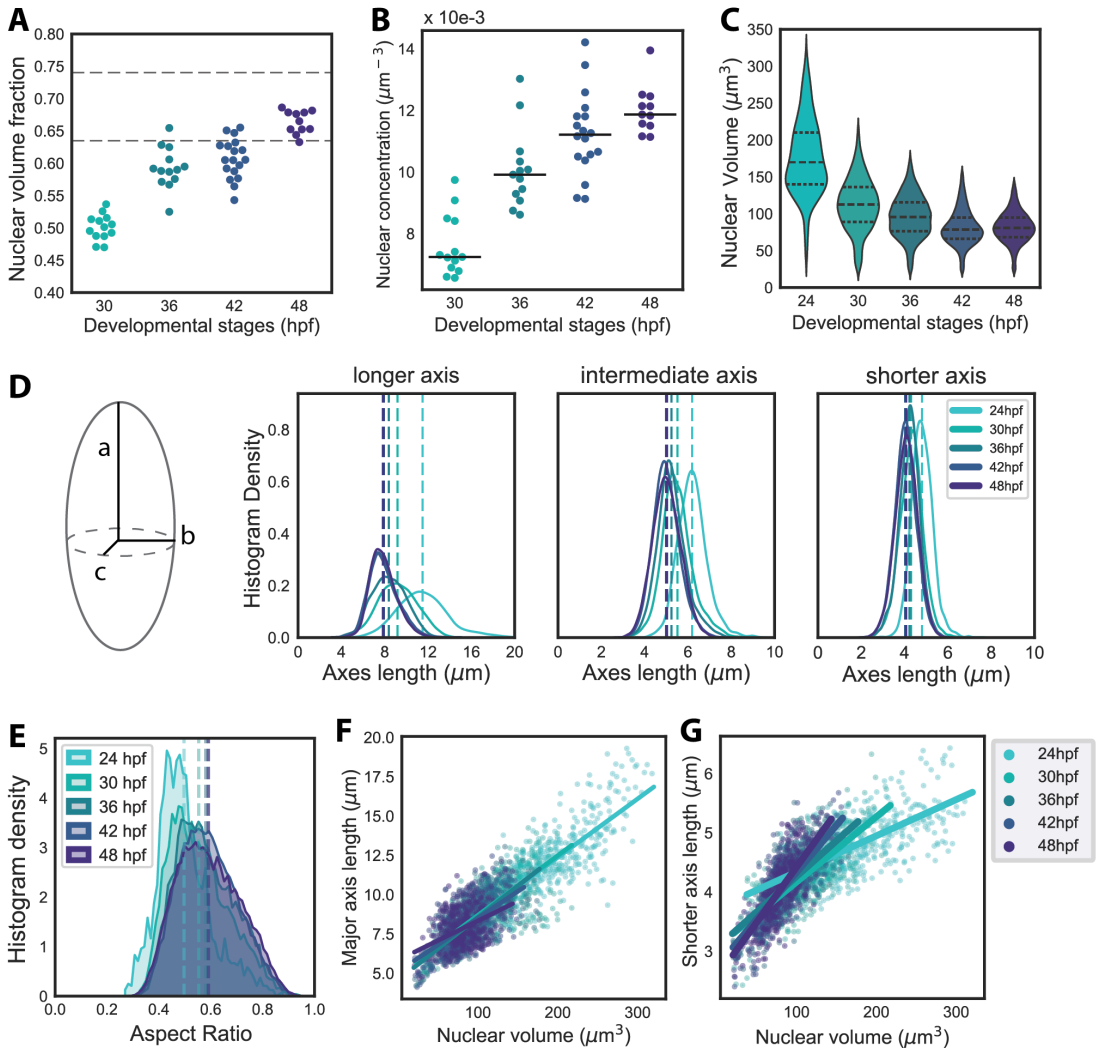

Figure 2.4: **Nuclear shapes and sizes change over the proliferative phase as packing increases between 24 and 48 hpf. A)** Nuclear volume fraction in the central region of the retinal PSNE., i.e. retinal ROIs. Segmented lines highlight the theoretical limiting volume fractions $\phi = 0.635$ for isovolumetric spheroids and $\phi = 0.735$ for ellipsoids. N = 13 embryos (30 hpf), N = 13 (36 hpf), N = 18 (42 hpf), N = 11 (48 hpf). **B)** Nuclear concentration in the ROIs. Solid black lines indicate medians. N embryos as in panel (A). **C)** Violin plots of nuclear volumes. **D)** Scheme of nuclear axes and histogram density distributions of nuclear axes at different developmental stages. In panels (C, D) the color-coded segmented lines indicate the mean values for each distribution. **E)** Histogram density distribution for nuclear aspect ratios. **F, G)** Scatter plot between major and minor nuclear axis length versus nuclear volume. Solid lines indicate linear regression of the two variables.

fraction varies as a function of ellipsoids' aspect ratios[47], we set out to quantify the volume and shape distributions of nuclei in the ROIs (24 hpf, n = 1935, N = 6; 30 hpf, n = 7701, N = 13; 36 hpf, n = 9390, N = 11; 42 hpf, n = 29529, N = 20; 48 hpf, n = 27185, N = 11 where n is number of nuclei and N is number of embryos). While nuclear volume decreased during the proliferative phase until the onset of lamination, nuclei retained their average elongated ellipsoidal shape throughout the proliferative phase, despite the

increasing tissue packing density (Fig. 2.4 A-D; tables 2.1 and 2.3). Because nuclei retained the same average aspect ratio, but volume was reduced, we monitored how the different nuclear axes lengths change over time to determine whether all three axes shorten at the same rate. Nuclear volume reduction seemed to result mainly from a shortening of the major axis, which decreased progressively at each developmental stage until 42 hpf (Fig. 2.4 D; table 2.2). After shrinking their volume between 24 and 42 hpf, nuclei maintained their shape and volume distribution between 42 and 48 hpf, when neuronal lamination starts. Correlation between nuclear volume and the length of the longer axis decreased over time (Fig. 2.4 F; Pearson's correlation coefficient: 24 hpf = 0.81; 30 hpf = 0.75; 36 hpf = 0.73; 42 hpf = 0.62; 48 hpf = 0.43), while the intermediate and shorter axes started to contribute more and more to explain the variability we observed in the distribution of nuclear volumes (Fig. 2.4 G; Pearson's correlation coefficient: 24 hpf = 0.64; 30 hpf = 0.72; 36 hpf = 0.71; 42 hpf = 0.75; 48 hpf = 0.75). These results indicate that nuclei were packed within the retinal PSNE at progressively higher densities until the onset of lamination and increased packing correlated with nuclear volume reduction and shortening of the longer nuclear axis. While nuclei occupied the whole apicobasal tissue axis by 42 hpf, the further increase in packing densities between 42 and 48 hpf did not correspond to any further shift in the distribution of nuclear volumes. Therefore, the decrease in nuclear size accompanied the increase in nuclear packing while the PSNE was proliferating, but not during the beginning of neuronal layering.

Nuclear volume(μm^3)		Mann Whitney test		
Stage	$\mu \pm \sigma$	H0: same distribution	p value	alpha = 0.01
24 hpf	177.87± 55.77	–	–	–
30 hpf	113.52 ± 39.92	(24 hpf) = (30 hpf)	4.572e-216	Reject
36 hpf	95.76 ± 30.54	(30 hpf) = (36 hpf)	2.170e-47	Reject
42 hpf	81.67 ± 23.40	(36 hpf) = (42 hpf)	3.505e-43	Reject
48 hpf	81.92 ± 23.06	(42 hpf) = (48 hpf)	0.1798	Cannot reject

Table 2.1: Statistical test on nuclear volume distributions between 24 and 48 hpf

While nuclear size was remodeled, the distribution of nuclear aspect ratios appeared to be strongly right-skewed at 24 hpf and progressively shifted to a more symmetric distribution over time (Table 2.2). Between 36 and 48 hpf, the average nuclear aspect ratio did not significantly change, staying around 0.58 ± 0.111 (Table 2.2). This means that the distribution of nuclear shapes did not vary over the course of 12 hours, despite increasing nuclear packing and high proliferation rate [130].

Overall, our data showed that nuclei in the retinal PSNE retained an aspherical ellipsoid-like shape throughout the proliferative phase. While we expected nuclei to become more rounded as differentiation progressed and neuronal precursors would lose their apical or basal protrusions, the distribution of the aspect ratios did not change between 36 and 48 hpf. During this time period, nuclei were positioned along the whole apicobasal axis

[130], therefore fully occupying the so-called 'nuclear exclusion zone' at the basal side of the tissue , and nuclear packing increased to approach theoretical limiting packing densities for isovolumetric spheres [47]. The fact that the skewness in the distribution of nuclear aspect ratios decreased over time could be a direct effect of morphological changes associated with cell specification, together with the reduction in variability of nuclear volumes. Nevertheless, nuclei retained an average aspect ratio below 0.6, which suggested that an elongated nuclear shape could represent a relevant feature of pseudo-stratification in the proliferating retinal neuroepithelium.

Nuclear axis lengths (μm)				A/(B+C)	
Stage	A ($\mu \pm \sigma$)	B($\mu \pm \sigma$)	C ($\mu \pm \sigma$)	($\mu \pm \sigma$)	Skeweness
24 hpf	11.5 ± 2.59	6.17 ± 0.87	4.81 ± 0.66	0.49 ± 0.101	0.82
30 hpf	9.08 ± 2.00	5.50 ± 0.9	4.31 ± 0.70	0.55 ± 0.111	0.59
36 hpf	8.34 ±1.68	5.25 ± 0.78	4.22 ± 0.57	0.58 ± 0.113	0.43
42 hpf	7.85± 1.43	5.00 ± 0.71	4.04 ± 0.57	0.59 ± 0.111	0.27
48 hpf	7.85 ± 1.33	5.02 ± 0.72	4.08 ± 0.58	0.59 ± 0.120	0.23

Table 2.2: Axes lengths and aspect ratios of nuclei in the central RNE between 24 and 48 hpf.

Mann Whitney Test		
H0: same distribution	P value (U test)	Alpha = 0.01
(24 hpf) = (30 hpf)	6.179e-34	Reject H0
(30 hpf) = (36 hpf)	3.091e-06	Reject H0
(36 hpf) = (42 hpf)	0.0163	Cannot reject
(42 hpf) = (48 hpf)	0.899	Cannot reject

Table 2.3: Two-tailed U test of nuclear aspect ratios distributions between 24 and 48 hpf

2.1.3 Correlation between number of neighbors and nuclear shape anisotropy

Ellipsoidal particles can pack more densely than spheres in a disordered arrangement [47]. Because nuclei in the retinal PSNE retain an elongated aspect ratio during the proliferative phase, we wanted to determine how local packing density changed for each nucleus depending on its sphericity. One important parameter for monitoring the packing density of a particulate material is the contact number z, which defines the average number of touching neighbors per particle. Depending on the anisotropy of the object, i.e. the nucleus in our case, a minimal contact number exists below which the system would no longer be expected to be in mechanical equilibrium. Above this limit, instead, the higher nuclear packing should result in a stable solid-like state. For example, in the case of densest (FCC) lattice packing of spheres the maximum contact number observed is z = 12 . Theoretical and experimental work on frictionless particles has shown that fully aspherical

ellipsoids can contact higher number of neighbors compared to more spherical objects [47]. Because ellipsoidal particles are characterized by additional rotational degrees of freedom than spheres and because this should enable them to contact more neighbors without necessarily affecting the physical state of the tissue, we decided to determine whether a relation exist between the average coordination number and the shape of nuclei in the retinal PSNE over time.

Neighbor nuclei should not actually touch because of the presence of cell membranes between them. Thus, we dilated nuclear boundaries by a given radius and defined as neighbors those nuclei that were touching after dilation (Fig. 2.3 B). After iteratively dilating nuclei with increasing radii and observing a large difference already between the average number of touching neighbors with no dilation and with a dilation's radius equal to approximately 0.25 μm, we decided to adopt this value as the effective touching-through-cell-membrane length scale and to use it to capture the number of touching neighbors (Fig. 2.5 A). Based on this definition, we counted the number of touching neighbors per nucleus (here also referred to as coordination number) and compared this measurement to the aspect ratio of each nucleus. In this way, we wanted to detect whether any relation existed between nuclear shape and coordination number, where we expected more elongated nuclei to show higher numbers of touching neighbors. Indeed, we observed that as the nuclear aspect ratio decreases, the average contact number increases and this is true at all developmental stages between 24 and 48 hpf (Fig. 2.5 B). Therefore, it appeared that a linear correlation between the average contact number and the nuclear aspect ratio existed. Interestingly, nuclei showing the most aspherical aspect ratios at 48 hpf reached an average contact number z = 10, which is close to the limiting contact numbers of z = 12 and z = 14 measured for crystal arrangements of spheres and ordered packing of fully aspherical ellipsoids in 3D, respectively. This suggested that nuclear packing in the retinal PSNE approached a limiting packing density over time. This confirmed our previous data showing that increasing nuclear packing approximated theoretical limiting packing densities at the onset of neuronal lamination.

Overall, our results confirmed that nuclear shape influenced the contact number of nuclei in the retinal PSNE. The fact that nuclei resemble aspherical ellipsoids throughout the proliferative phase suggested that this nuclear shape could facilitate the packing of cells' bodies within the tissue. We expected to see a progressive reduction in. nuclear volume and progressive change in nuclear shape as tissue packing increases and neurogenesis progresses. Instead, what we observed was that nuclei displayed an elongated nuclear shape until the onset of neuronal lamination with little difference across developmental stages between 30 and 48 hpf, i.e. as long as the tissue retained a PSE-like arrangement,.

2.1.4 Spatial patterns of increasing nuclear packing vary over time

Neighborhood statistics can inform us not only about the local packing density of cell bodies within a tissue, but it also provides a measurement to determine how cells are

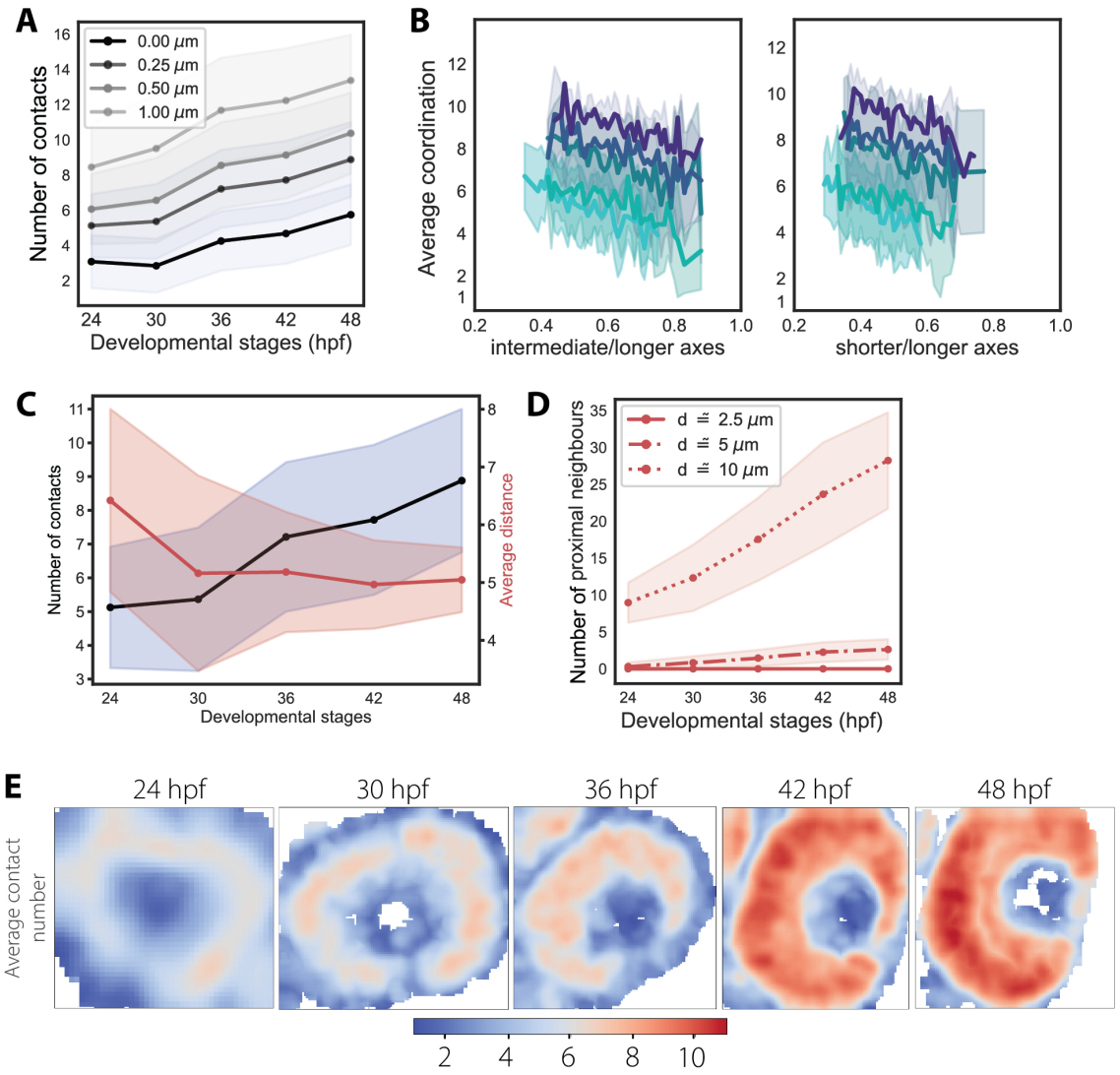

Figure 2.5: **Number of contacts increase with nuclear packing. A)** Number of contacts between touching neighbors after different dilations of nuclear boundaries. All sow the same increasing trend. **B)** Correlation between mean number of contacts (average coordination) and nuclear aspect ratios. Solid lines show mean values, shaded area indicate the standard deviation from the mean. Colors indicate the developmental stage as reported in figure 2.4. **C)** Mean number of contacts increase, while the average distance between touching neighbors stays constant. Solid lines show mean values, shaded area indicate the standard deviation from the mean. **D)** Number of proximal neighbors for different distance radii. **E)** Median intensity projection of color maps reporting the average number of contacts per nucleus after image smoothing.

positioned relative to each other. Based on this, we explored whether and how the number of cell neighbors and their relative positioning in the tissue changed at different developmental stages in relation to nuclear packing.

As tissue packing increased, we expected to observe nuclei getting closer and closer to one another and possibly to transition to an ordered arrangement. Thus, we measured the

average internuclear distance of touching neighbors at different developmental stages and compared to the average contact number as a proxy for nuclear packing density. While the average contact number does not change over the first 6 hours of our observations of retinal PSNE development, i.e. between 24 and 30 hpf, it increased continuously starting by 30 hpf (Fig. 2.5 C). Meanwhile, the average internuclear distance of touching neighbors stayed constant between 30 and 48 hpf, at around 5 μm from centroid to centroid, which corresponded to the average value of the intermediate and shorter nuclear axes (Fig. 2.5 C). This suggested that the distance between nuclei reduced to the minimum at 30 hpf, just before the reported peak in proliferation [130]. This meant that most of the touching neighbors contacted each other along the plane orthogonal to the longer axis. When considering the number of proximal neighbors at longer distances, e.g. within 5 and 10 μum radius, we found that packing of nuclei continuously raise already by 24 hpf (Fig. 2.5 D). This reduction in internuclear distance and the increasing number of neighbors, both touching and proximal neighbors, confirmed that nuclear packing approximated limiting packing densities over time and that nuclei within the developing PSNE tended to reach the closest possible packing for this arrangement already during the proliferative phase.

Though, this analysis did not take into consideration the fact that nuclear crowding differs across the apicobasal axis, for instance due to a basal bias in actomyosin distribution and because of apical mitosis. Over the course of proliferation, nuclear packing could vary spatially along the apicobasal axis and this could impact the overall arrangement of progenitor cells' bodies in the tissue. To qualitatively assess the spatial differences in nuclear packing densities in the developing retinal PSNE, we scanned the volume of our 3D images to calculate the contact number per nucleus and obtain a smoothed dataset where the local average coordination could be spatially mapped (see Methods 4.4.5). We observed that the average number of contacts increased within the retinal PSNE between 24 and 48 hpf, reaching higher values in the inner part of the tissue, away from its boundaries (Fig. 2.5 E). In particular, the average contact number reached its highest values in the inner part of the RNE between 42 and 48 hpf, over the onset of neuronal lamination. During this time window, the average contact number did not increase at the same rate everywhere in the tissue, but we observed lower values of the coordination number at the basal side, where the Retinal Ganglion Cell Layer was forming.

In conclusion, our data showed that nuclear packing varies along the apicobasal axis of the RNE. By the time the average contact number approximated values that have been described for jamming of ellipsoidal particles in 3D, i.e. z = 12-14, nuclei started to be rearranged into ordered layers. Moreover, variability in internuclear distances progressively decreased, suggesting that the arrangement of nuclei might become progressively more ordered as nuclear packing density raise.

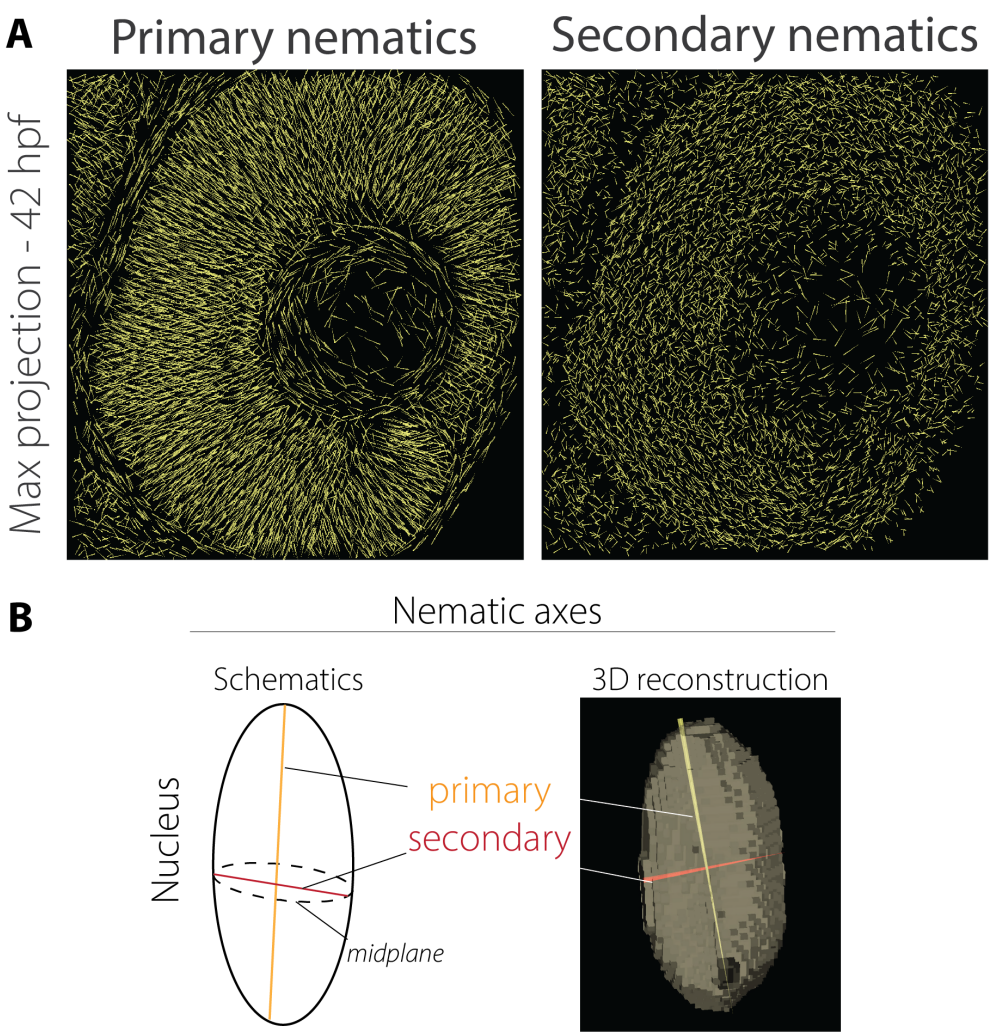

Figure 2.6: **Representative parametric images of the primary and secondary nematic axes. A)** Maximum intensity projections of the primary and secondary nematic axes extracted from each nucleus segmented using StarDist-3D. **B)** Scheme and 3D reconstruction of primary and secondary nematics extracted from a single segmented nucleus.

2.1.5 Nuclei are arranged with orientational nematic order and positional disorder

The average internuclear distance between touching neighbors did not change over time between 30 and 48 hpf, though its standard deviation did decrease. This suggested that variability in internuclear distances reduced over time. This observation prompted us to ask whether regular positional ordering of nuclei was emerging over time. To explore this notion, we computed the radial distribution function (RDF) for nuclei within ROIs at each developmental stage (see Methods 4.4.8). The RDF describes how particle density changes as a function of distance from a given position and it can be used to describe the physical state of materials, i.e. liquid, solid or gaseous state (Fig. 2.7 A). This function also provides insights into whether a material is ordered in a crystalline-like structure, which is defined by the appearance of regularly spaced peaks that indicate the high probability

of finding a molecule at that distance, as shown in fig. 4.3, where the RDF for artificial images of spheroids arranged either randomly or in a lattice was computed. Therefore, we computed the RDF iteratively over those nuclei that were present within the central region of the selected ROIs and plotted the average value for each δr. Our results showed highest probability to find a neighbor nucleus at 5 μm distance, therefore confirming our previous measurement of average internuclear distance for touching neighbors (Fig. 2.7 B). At longer distances, i.e. at higher values of r, the g(r) progressively decays as nuclear positioning is independent of each other, showing a g(r) profile similar to that of a liquid-like state (Fig. 2.7 B). In conclusion, the computed RDF confirmed that the arrangement of nuclei in the retinal PSNE was disordered, meaning that no positional order was emerging during the proliferative phase.

Our results so far showed that nuclei were positionally disorder and featured anisotropic shapes throughout the proliferative phase. In particular, nuclei were elongated along the apicobasal axis of the tissue. The presence of such alignment along one direction could indicate the presence of a collective long-range orientational order of nuclei, called nematic order. This arrangement represents the simplest ordering of particles in a mesophase, i.e. a phase of material that lies in between a solid and liquid state. Indeed, nematic ordering has substantial implications for the material properties of soft matter composed of anisotropic particles, like liquid crystals. To determine whether nuclei in the retinal PSNE are actually arranged as in a nematic order, we extracted the elongation axis of each nucleus within the ROIs, called here primary nematic (Fig. 2.6 A, B), and calculated the angle between the primary nematic and the average local direction, i.e. the director (Fig. 2.7 C). We found that nuclei were strongly aligned along their primary nematic axis, with an average angle between each nematic axis and the director around 10 degrees within the PSNE (Fig. 2.7 E). In addition, we calculated the local order parameter S, which is a scalar value that represents how one elongated object is aligned along the director. For the primary nematic, we computed a local average value S $\approx$ 0.9, where S=1 corresponds to perfect alignment (Fig. 2.7 D). This, together with the fact that nuclei are characterized by elongated shape and a positionally disordered arrangement, suggested that nuclei were indeed arranged in a nematic order. Furthermore, we performed the same analysis for a secondary nematic, which was defined as the elongation axis on the midplane of the nucleus, to investigate whether nuclei might be aligned along other directors, which could indicate the presence of a secondary axis of orientational order and other constraints in the tissue. Our data showed that local long-range alignment was detected not only along the apicobasal axis, but along a secondary axis of alignment, even though to a weaker extent compared to the primary one (Fig. 2.7 D, E).

In conclusion, the measurements we obtained supported the idea that nuclei in PSNE resembled particles in a biaxial nematic state. In this case, nuclei were orientationally ordered not only along a one-dimensional axis, but along two directions, and this could enable the nuclei to be more densely packed without causing a transition to a more solid-like state.

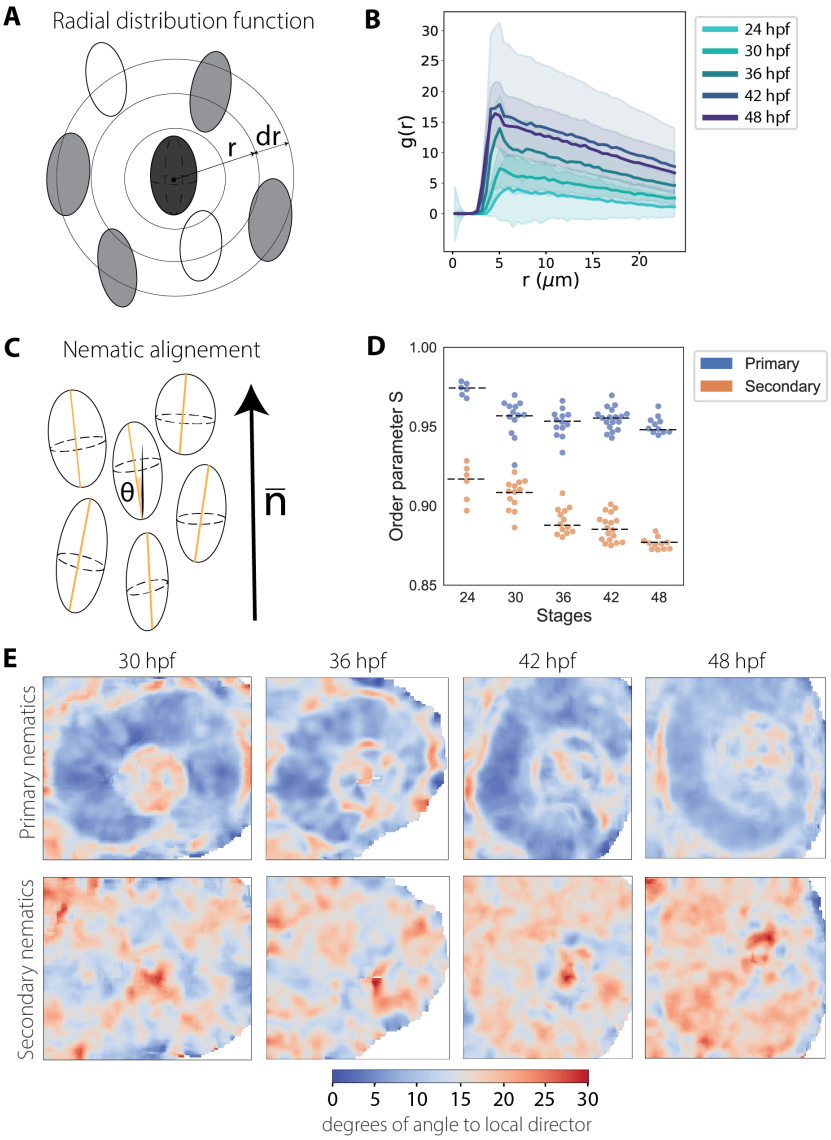

Figure 2.7: **Nuclei are arranged in a nematic-like order in the developing retinal PSNE. A)** Scheme of radial distribution function (RDF) computed for a spherical shell of radius r around one nucleus (darker). **B)** The RDF g(r) calculated for nuclei in ROIs at different developmental stages between 24 and 48 hpf indicate a liquid-like state. **C)** Scheme of nuclei aligned along a common direction axis n, showing the angle θ calculateed between the average direction axis and the nuclear nematic axis. **D)** Order parameter S for different developmental stages. **E)** Median intensity projection of color maps reporting the average degree between the nematics and the local average direction axis, between 30 and 48 hpf.

2.2 Comparing the RNE to the developing hindbrain

The retinal neuroepithelium is characterized by a hemispherical tissue shape, where the apical surface is greater than the basal one. It has been previously shown that nuclear positioning mechanisms vary between differently shaped PSNE even within the same organism, e.g. the retina and hindbrain in the developing zebrafish embryo [225].

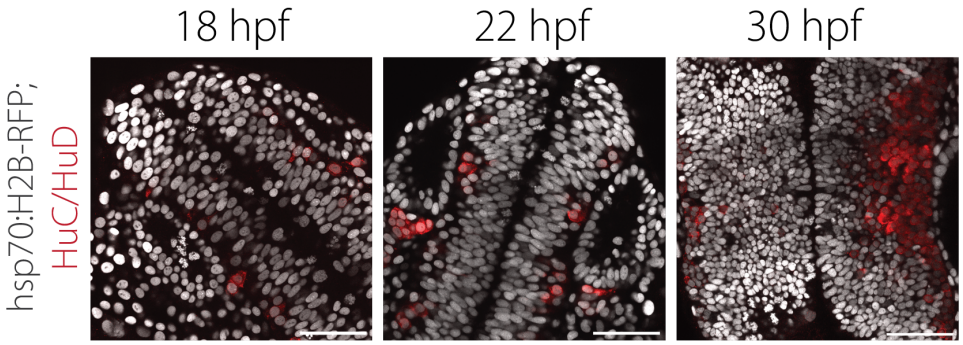

Figure 2.8: **Neurons are already detectable in the hindbrain upon formation of the neural keel.** Huc/HuD-positive neuronal precursors are marked in red. Nuclei are labeled with Tg(hsp70:H2B-RFP). Scale bar = 50 μm.

Neuroepithelial progenitor cells in the developing hindbrain show a more columnar shape due to the different architecture of this neuroepithelium compared to neuroepithelial cells in the retinal RNE. The hindbrain is one of the three main parts of the brain located in the posterior part of the head and, just like the rest of the central nervous system, it originates from a pseudostratified neuroepithelium. Differently from the retina, the hindbrain is patterned into different domains, called rhombomeres, early on in development and these rhombomeres define distinct regions of neurogenic gene expression and proliferation for non-boundary and boundary cells, respectively [108]. Progenitor cells in the rhombomeric regions divide asymmetrically to produce HuC+ neuronal precursors immediately after the closure of the neural keel, which occurs at 16 hpf, and markers of neuronal differentiation are detectable already by 24 hpf (Fig. 2.8) [80]. Lamination of newly formed neurons to the mantle is evident by 30 hpf and differentiated neurons are visible in the boundary regions around the same time (Fig. 2.8) [80]. Thus, the developing hindbrain differs from the developing retina not only in its shape and boundary conditions, but also shows a different regulation of proliferation and differentiation specific to distinct domains of the rhombomeres. How these processes, together with tissue shape, can affect the packing densities of cells within a growing neuroepithelium has not been explored so far. Therefore, we compared the hemispheric retina to the developing hindbrain to test the conservation of nuclear packing arrangements found in the retinal neuroepithelium.

2.2.1 Nematic-like ordering is a hallmark of pseudostratification also at looser packing regimes as in the case of the hindbrain neuroepithelium

To follow the changes in nuclear packing densities within the hindbrain PSNE, we performed the same image analysis pipeline as described for the retina upon manual selection of ROIs (see Methods 2.1). Due to the earlier neurogenesis onset, we staged and imaged the hindbrain neuroepithelium between 18 and 30 hpf at 4 hours intervals (Fig. 2.9). HuC/HuD+ neuronal precursors were already detectable by 18 hpf (Fig. 2.8).

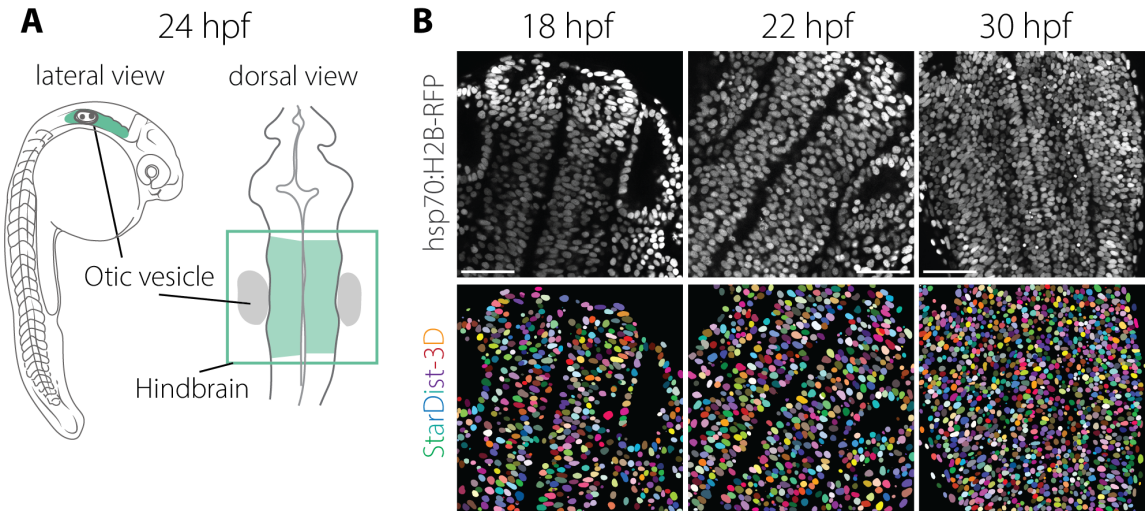

Figure 2.9: **Instance segmentation of nuclei in the developing hindbrain. A)** Scheme of the hindbrain in a zebrafish embryo at 24 hpf. **B)** Representative images of the hindbrain PSE during early development and corresponding instance segmentation using StarDist-3D model A. Nuclei are labeled with Tg(hsp70:H2B-RFP). Scale bar = 50 μm.

While in the retina nuclear packing increased steadily before and after lamination, the volume fraction occupied by nuclei in the hindbrain approached the value of 0.55 and remained below a packing fraction of 0.60 (Fig. 2.10 A, B). These values have been reported to correspond to the minimum threshold for equal spheres in random loose packing (RLP)[156]. RLP generally refers to the loosest possible packing of objects that can be mechanically stable. This observation suggested that nuclear packing in the hindbrain slowly approached a mechanically stable state, as defined by RLP configurations, and ultimately reached higher packing fractions later on, as recently reported in other studies [100]. This means that nuclei in the hindbrain were not as densely packed as in the retina during the proliferative phase.

Similarly to what was observed in the retinal PSNE, nuclear volumes decreased over time starting around 24 hpf, just before neuronal lamination (Fig. 2.10 C; table 2.4; 18-19 hpf, n = 14364, N = 24; 22 hpf, n= 6824, N = 10; 24 hpf, n = 5471, N = 7; 30 hpf, n = 9974, N = 5; where n is number of nuclei and N is number of embryos). Though, nuclei were more spherical when compared to nuclei in the retinal PSE and the average contact number did not appear to correlate with nuclear aspect ratios (Fig. 2.11 D, E). This could be related to the fact that nuclear packing was not reaching limiting densities at these developmental stages, thereby uncoupling shape from changes in the coordination number. In addition, the mean contact number per nucleus ranged between 4 and 6 over 12 hours of development and did not approach values associated with limiting packing as in the retina. (Fig. 2.11 A). However, nuclei were still arranged as in a biaxial nematic order as seen by the RDF and the measurements of the primary and secondary nematics' angles and order parameter S, meaning that nuclear packing in the hindbrain was characterized

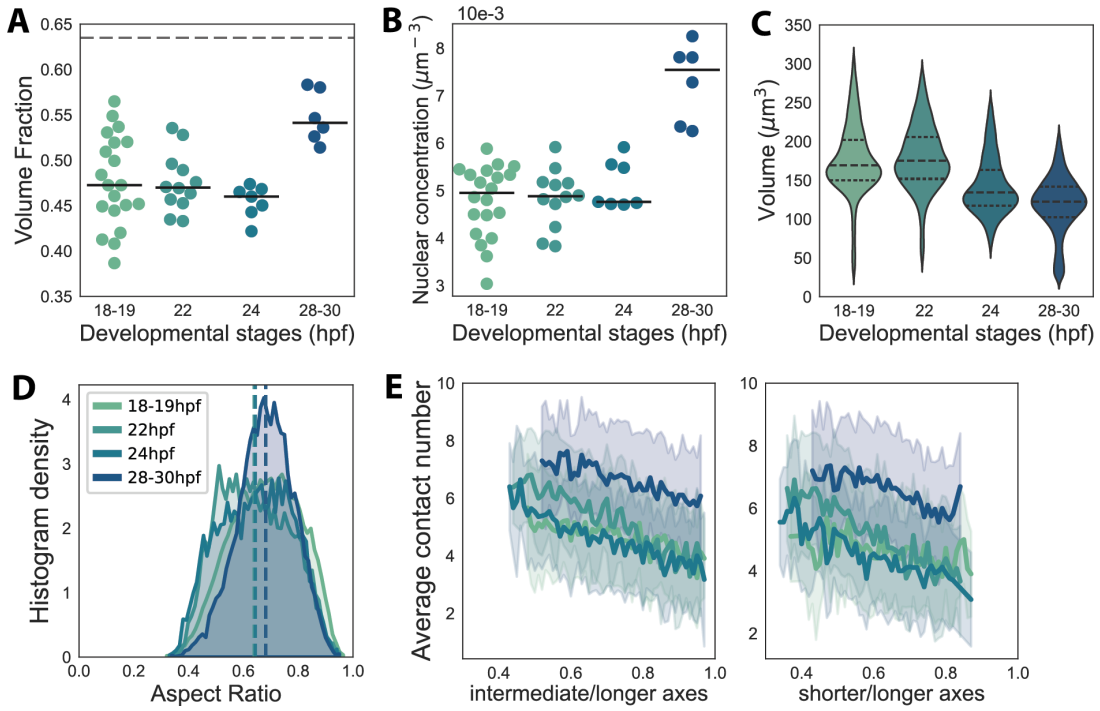

Figure 2.10: **Nuclei are arranged in a nematic-like order in the developing hindbrain and are arranged in random loose packing densities. A)** Nuclear volume fractions over time. The segmented gray line marks $\phi = 0.635$ for nuclear volume fraction. N = 20 embryos (18-19 hpf), N = 11 (22 hpf), N = 7 (24 hpf), N = 6 (30 hpf). **B)** Nuclear concentration over time. Solid lines show median values in A and B. N of embryos as in panel (A). **C)** Violin plot of nuclear volume distributions over time. Segmented lines indicate first and third quartiles and medians. **D)** Histogram density distributions of nuclear aspect ratios. Segmented lines indicate the mean. **E)** Correlation between mean number of contacts (average coordination) and nuclear aspect ratios. Solid lines show mean values, shaded area indicate the standard deviation from the mean. Colors indicate the developmental stage as reported in panels (A-D).

by positionally disorder and orientational order (Fig. 2.11 B, C, D).

Overall, our data suggested that alignment of nuclei as in a nematic order is conserved across different PSNE, regardless of their packing density. We showed that the arrangement of nuclei differs in the developing hindbrain prior to formation of the mantle, probably due to the physical segmentation of the hindbrain PSNE into rhombomeres that defines different regions of proliferation and neurogenesis along the anterior-posterior axis of the tissue. Nevertheless, the elongation of neuroepithelial cells within the hindbrain resulted still in long-range alignment of their nuclei, which was maintained in proliferating cells upon lamination, when the first neuronal precursors localized to the mantle and started changing their nuclear shape.

Nuclear volume(μm^3)		Mann Whitney test		
Stage	$\mu \pm \sigma$	H0: same distribution	p value	alpha = 0.01
18 hpf	315.68± 41.88	–	–	–
22 hpf	279.37 ± 46.43	(18hpf) = (22 hpf)	0.2323	Cannot reject
24 hpf	241.93 ± 75.72	(22 hpf) = (24 hpf)	3.294e-78	Reject
30 hpf	201.66± 20.11	(24 hpf) = (30 hpf)	9.545e-34	Reject

Table 2.4: Two-tailed U-test on nuclear volume distributions in the hindbrain between 18 and 30 hpf

Nuclear axis lengths (μm)				A/(B+C)	
Stage	Longer ($\mu \pm \sigma$)	Intermediate ($\mu \pm \sigma$)	Shorter ($\mu \pm \sigma$)	($\mu \pm \sigma$)	Skeweness
18 hpf	9.34 ± 1.82	6.57 ± 0.77	5.63 ± 0.70	0.67 ± 0.13	-0.09
22 hpf	9.68 ± 1.80	6.48 ± 0.77	5.45 ± 0.66	0.63 ± 013	0.17
24 hpf	8.99 ±1.61	6.09 ± 0.68	5.01 ± 0.64	0.64 ± 0.13	-0.01
30 hpf	7.97± 1.49	5.79 ± 0.81	4.87 ± 0.61	0.69 ± 0.10	-0.20

Table 2.5: Axes lengths of nuclei in the hindbrain between 18 and 30 hpf

Mann Whitney Test		
H0: same distribution	P value (U test)	Alpha = 0.01
(18 hpf) = (22 hpf)	5.748e-13	Reject H0
(22 hpf) = (24 hpf)	0.2917	Cannot reject H0
(24 hpf) = (30 hpf)	2.386e-12	Reject H0

Table 2.6: Two-tailed U test of nuclear aspect ratios in the hindbrain between 18 and 30 hpf

2.3 Nuclear packing dynamics in the laminated retina

We showed in previous chapters that pseudostratification resulted in neuroepithelial cells having a strong orientational order due to their elongated morphology spanning the apicobasal tissue axis. Thus, even though nuclei were changing their size, the aforementioned alignment was maintained throughout the proliferative phase. Most neuroepithelial cells populating the retinal PSNE during this time period are multipotent progenitors spanning both sides of the tissue. Once these cells start differentiating, they change their cell shape and lose their apical or basal attachment, depending on their neurogenic cell fate. Since long-range alignment seems to be a hallmark of pseudostratification and neurogenesis progresses in parallel to tissue growth and proliferation, we wondered whether this ordering could be maintained also at later stages of retinal development. Thus, we asked how ordering of cell bodies was progressively modified during the transition from a monolayered PSNE to a layered neuronal structure.

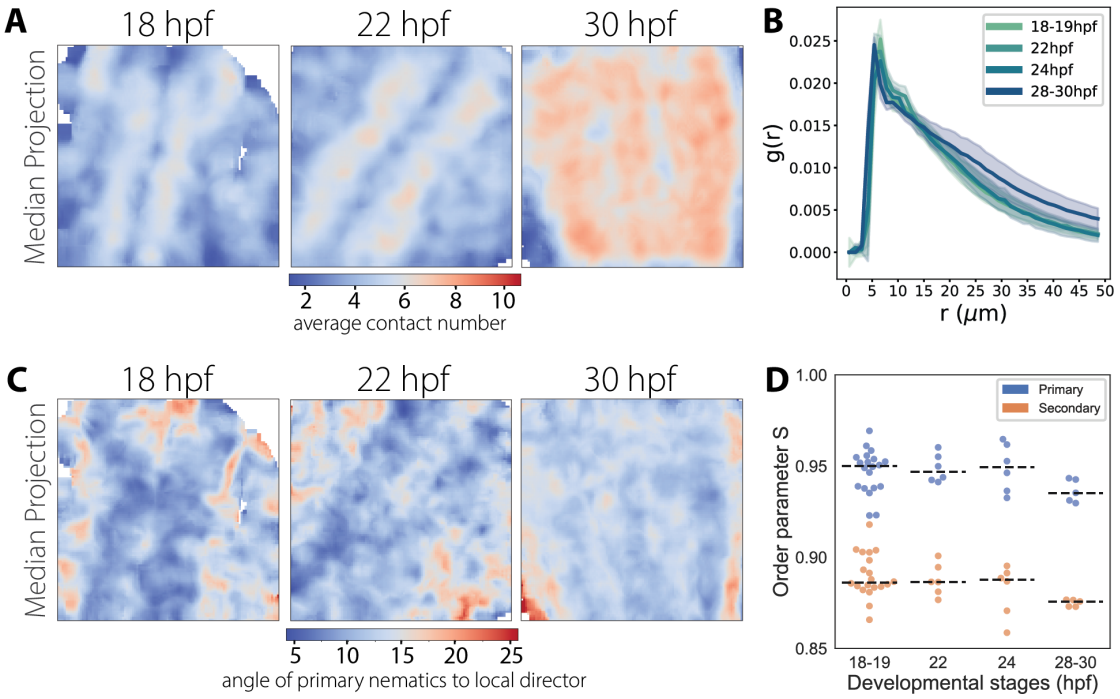

Figure 2.11: **Nuclei are arranged in a nematic-like order in the developing hindbrain. A)** Median intensity projection of color maps reporting the average contact number for each nucleus. **B)** The RDF g(r) between 18 and 30 hpf. **C)** Median intensity projection of the average degree θ between primary nematics and the local direction axis. **D)** Order parameter S for primary and secondary nematics.

2.3.1 Neurons are characterized by different nuclear shapes and arrangements within the laminated retina

Our analysis of the developing retinal PSNE indicated that nuclear packing density increased over time during the proliferative phase, which ranges between 24 hpf and 42 hpf. Based on our results, we expected nuclei in the retinal PSNE to reach their closest possible packing configuration by 42-48 hpf. Instead, nuclear packing densities kept increasing at the onset of neuronal lamination, when the transition from a monolayered to a stratified tissue has started. Since neuronal lamination implies a restructuring of cells bodies, and thereby nuclei, within the tissue, we hypothesized that the timing of lamination allows to pack more cells within the retina at a higher rate than its growth without resulting in a premature rigidity transition. To explore this notion, we first asked how nuclear rearrangements within the different nuclear layers occur and how nuclear packing changes during the maturation of the laminated retina. In this way, we characterized the transition from a seemingly disordered pseudostratified tissue to a laminated neuronal structure in the vertebrate retina to better understand how tissue packing is regulated during organogenesis of densely packed neuroepithelia.

The mature retina is composed of two plexiform layers, where axonal and dendritic processes of retinal neurons form connections, and three nuclear layers, where the neuronal

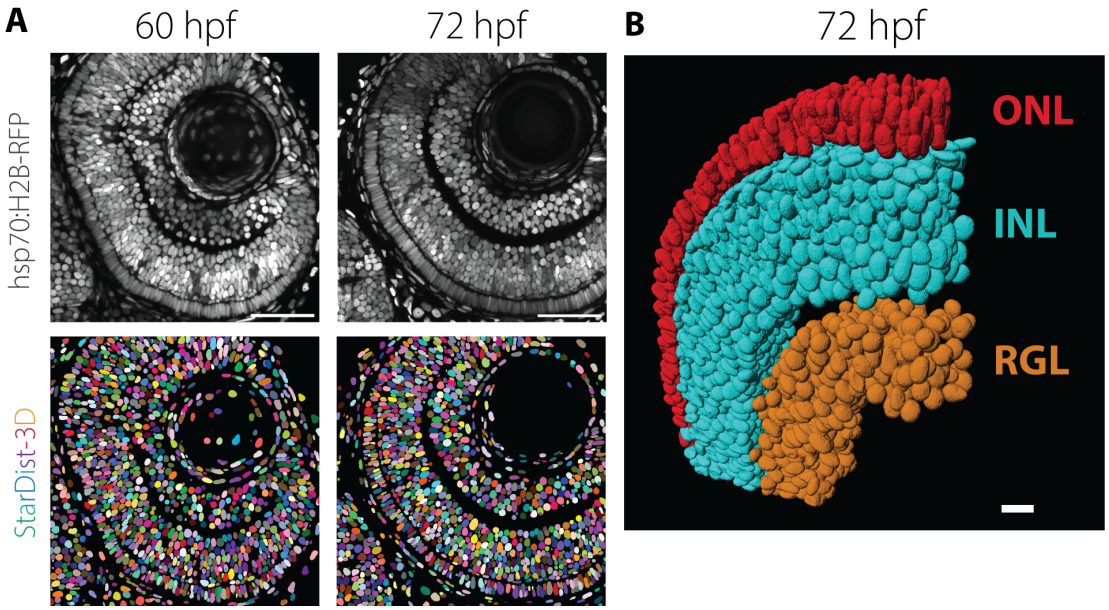

Figure 2.12: **Instance segmentation in the nuclear layers of the laminated retina. A)** Representative images of the layered retina during neuronal lamination and corresponding instance segmentation using StarDist-3D model B. Nuclei are labeled with Tg(hsp70:H2B-RFP). Scale bar = 50 μm. **B)** 3D rendering of the ROI selected from (A) showing segmented nuclei color-coded for the different nuclear layers. Inner Nuclear Layer (INL); Outer Nuclear Layer (ONL); Retinal Ganglion cell Layer (RGL). Scale bar = 10 μm.

cell bodies are segregated. Nuclear layers are distinguished as follows: the most basal one is the Retinal Ganglion cell Layer (RGL), the most apical one is the Outer Nuclear Layer (ONL) and the Inner Nuclear Layer (INL), which is located in between the other two nuclear layers and the plexiform layers. Neuronal differentiation results in changes in cells and nuclear morphologies that can be observed qualitatively. To quantitatively track these changes in neuronal precursors over time, we trained a further StarDist-3D model on another manually annotated dataset including annotations from the different layers of laminated retinas from embryos staged between 48 hpf, when neuronal lamination has started, and 80 hpf, when even late-born neurons in the INL have formed (Fig. 2.12 A). In this way, nuclei were segmented with a level of accuracy comparable to the model trained for the earlier developmental stages (Table 4.5). We then analyzed the segmented dataset using the previously established analysis pipeline and separated the nuclei belonging to the different nuclear layers using a customized semiautomatic script (Fig. 2.12 B).

In the case of the ONL, only one or two layers of nuclei compose this layer during the time window we analyzed i.e. between 60 and 72 hpf. Because the ONL has no bulk region compared to the INL and RGL, we set to investigate more in depth nuclear packing densities in these latter layers to better understand how nuclei are progressively arranged in these layers during neuronal lamination. Nuclear packing density varied over time between the RGL and the INL (Fig. 2.13 A, B). Nuclei in the INL reached the highest

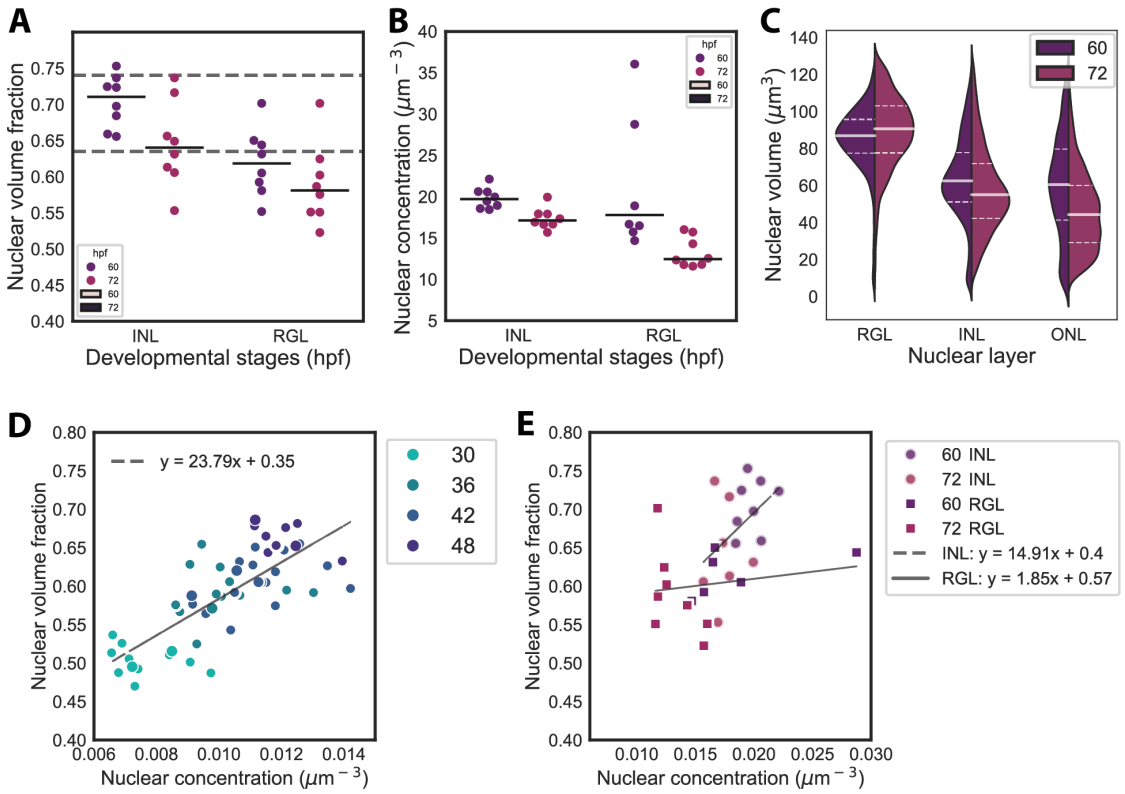

Figure 2.13: **Nuclear packing in the INL reaches limiting packing fractions during neuronal lamination. A)** Nuclear volume fractions over time. N = 7 embryos (60 hpf), N = 8 (72 hpf). **B)** Nuclear concentration over time. Solid lines show median values in A and B. N embryos as in panel (A). **C)** Violin plot of nuclear volume distributions over time. Segmented lines indicate first and third quartiles and medians. **D)** Linear correlation between nuclear volume fraction and concentration during early stages of retinal development over time. **E)** Strong positive linear correlation between nuclear volume fraction and concentration in the INL (circles) and moderate correlation in the RGL (squares) over time.

packing densities at around 60 hpf, approaching limiting volume fractions consistent with FCC crystals or random close packing of highly anisotropic ellipsoids (Fig. 2.13 A). These values represent the closest packing densities measured for disordered and ordered packing of hard spheroids, suggesting that nuclei in the INL might approach a jamming transition by 60 hpf. Interestingly, nuclear packing in the INL already decreased over the course of the next 12 hours, by 72 hpf. Similarly, the volume fraction occupied by nuclei in the RGL progressively decreased over time (Fig. 2.13 A). Meanwhile, nuclear volume progressively decreased between 60 and 72 hpf in the ONL and INL, but not in the RGL (Fig. 2.13 C; table 2.7). When we compared the relation between nuclear volume fraction and density of nuclei in the ROIs for earlier stages and for the INL and RGL, we observed steeper slopes between 30 and 48 hpf and between 60 and 72 hpf in the INL compared to the RGL (Fig. 2.13 D, E). This might possibly due to the fact that RGCs are the first type of neurons to differentiate and mature in the retina, therefore resulting in uncoupling of

nuclear concentration and volume fraction values in the laminated retina.

During neuronal lamination, nuclear aspect ratios showed very different distributions in the three nuclear layers, especially in the shorter axes lengths (Fig. 2.14 A, B). Intermediate and shorter nuclear axis lengths shortened steadily from the RGL to the INL to the ONL. In contrast, the distribution of the major axis lengths did not significantly vary across the three layers, even though it did change between different stages, from 60 to 72 hpf (Fig. 2.14 A, B). Specifically, nuclei in the RGL and INL became more spherical over time, while photoreceptor precursors in the ONL were characterized by strong anisotropic nuclear shape (Fig. 2.14 B). As nuclei assumed different shapes and sizes depending on their neuronal fate, for instance as rounder nuclei in the RGL or more rod-like shaped nuclei in the ONL, also their local neighbor statistics changed over time. Our analysis revealed that the linear correlation between number of contacts and nuclear aspect ratio was mostly lost for nuclei INL (Fig. 2.14 C). Because the average coordination number for nuclei in the INL reached limiting values, such as z = 12 at 72 hpf, we speculated that these nuclei were reaching their closest packing density. This would explain the loss of correlation between z and nuclear aspect ratios. In the other nuclear layers, this relationship between average coordination and nuclear shape became weaker as well. As a consequence, nuclei in the RGL show lower average coordination and their mean internuclear distance did not significantly change between stages (Fig. 2.14 C, D). RGC are the earliest born neurons and the fact that their relative nuclear positioning did not change at later stages of development suggested that they might have already reached their final arrangement by 60 hpf. In contrast, internuclear distance in the INL decreased over time when later born neurons are still finalizing their positioning between 60 and 72 hpf (Fig. 2.14 D). Because we observed stronger variation in nuclear packing densities and average internuclear distance in the INL compared to the RGL, we wondered whether this could be explained by differences in the arrangement of different neuronal types populating the INL, as these neuronal progenitors were still undergoing cell fate commitment between 60 and 72 hpf.

Nuclear volume(μm^3)			Mann Whitney test		
Layer	Stage	$\mu \pm \sigma$	H0: same distribution	p value	alpha = 0.01
ONL	60 hpf	56.77± 29.12	–	–	–
	72 hpf	45.89 ± 22.80	(60 hpf) = (72 hpf)	5.611e-18	Reject
INL	60 hpf	59.11± 23.33	–	–	–
	72 hpf	58.39 ± 24.37	(60 hpf) = (72 hpf)	0.0582	Cannot reject
RGL	60 hpf	79.41± 19.44	–	–	–
	72 hpf	90.11 ± 21.24	(60 hpf) = (72 hpf)	9.148e-43	Reject

Table 2.7: Statistical test on nuclear volume distributions between 60 and 72 hpf

To distinguish the different neuronal types in the INL, we looked at the expression of Ptf1a, which is a transcription factor specifying the neuronal fates of Amacrine Cells (ACs)

	Nuclear axis lengths (μm)			A/(B+C)	
Layer	Longer ($\mu \pm \sigma$)	Intermediate ($\mu \pm \sigma$)	Shorter ($\mu \pm \sigma$)	($\mu \pm \sigma$)	Skeweness
ONL	7.02 ± 1.53	3.94 ± 0.80	3.12 ± 0.66	0.50 ± 0.10	0.65
INL	6.47 ± 1.09	4.55 ± 0.76	3.73 ± 0.73	0.64 ± 011	0.14
RGL	6.80 ±1.00	5.44 ± 0.54	4.70 ± 0.59	0.75 ± 0.10	-0.46

Table 2.8: Axes lengths of nuclei in the central RNE at 72 hpf

and Horizontal Cells (HCs). Thus, ptf1a expression in the transgenic line tg(ptf1a:GFP) enabled us to discriminate ACs and HCs from BCs. To quantify nuclear packing in the INL, we crossed the tg(ptf1a:GFP) and tg(hsp70:H2B-RFP) zebrafish adults and imaged their offspring at 80 hpf. In this way, we could quantify the sizes and shapes and neighbor statistics of these three class of neurons within the INL (Fig 2.15 A). Our analysis revealed that ACs were characterized by bigger nuclear volumes and higher average internuclear distances than bipolar cells at 80 hpf, though their aspect ratios were comparable (Fig. 2.15 B, C). For both neurons, changes in aspect ratios did not affect their average coordination, suggesting again that nuclei in the INL had reached their maximum packing density. The fact that BCs cells showed lower variation in their average internuclear distance suggested that these neurons could be more regularly spaced than ACs. To quantify how regular was the spacing between neighboring nuclei of these neuronal types, we computed the solid angle of tetrahedra formed by touching neighbors. We observed similar variation between these neuronal types, suggesting that both ACs and BCs were arranged in a close packing density, where the only variable that seemed to affect internuclear distances was nuclear size (Fig. 2.15 E, F). This observation was confirmed by the count of touching neighbors in the INL, which appear to reach the densest packing in the lamianted retina (Fig. 2.16 A). Our results showed that BCs in the INL contacted more neighboring nuclei than ACs (Fig. 2.15 D). Thus, despite differences in nuclear size dictated by their neuronal fate, both ACs and BCs appeared to be arranged in closest packing configuration. This suggested that neurons in the INL reach particularly high packing densities, compared to the rest of the tissue, and further neuronal maturation resulted in reshaping of nuclear size and morphology, thereby enabling to pack more nuclei within this layer at later stages of development without increasing the volume fraction. We speculated that this could be achieved if nuclei were positioned in a regular fashion within the tissue.

2.3.2 Nuclei are arranged with orientational and positional order

We showed that nuclear packing density reached the maximum values we could measure during retinal development at 60 hpf, after which volume fraction values decreased. We hypothesized that this result could be explained by either a reduction in the generation of newly formed neurons or emergence of positional order in the nuclear layer or both.

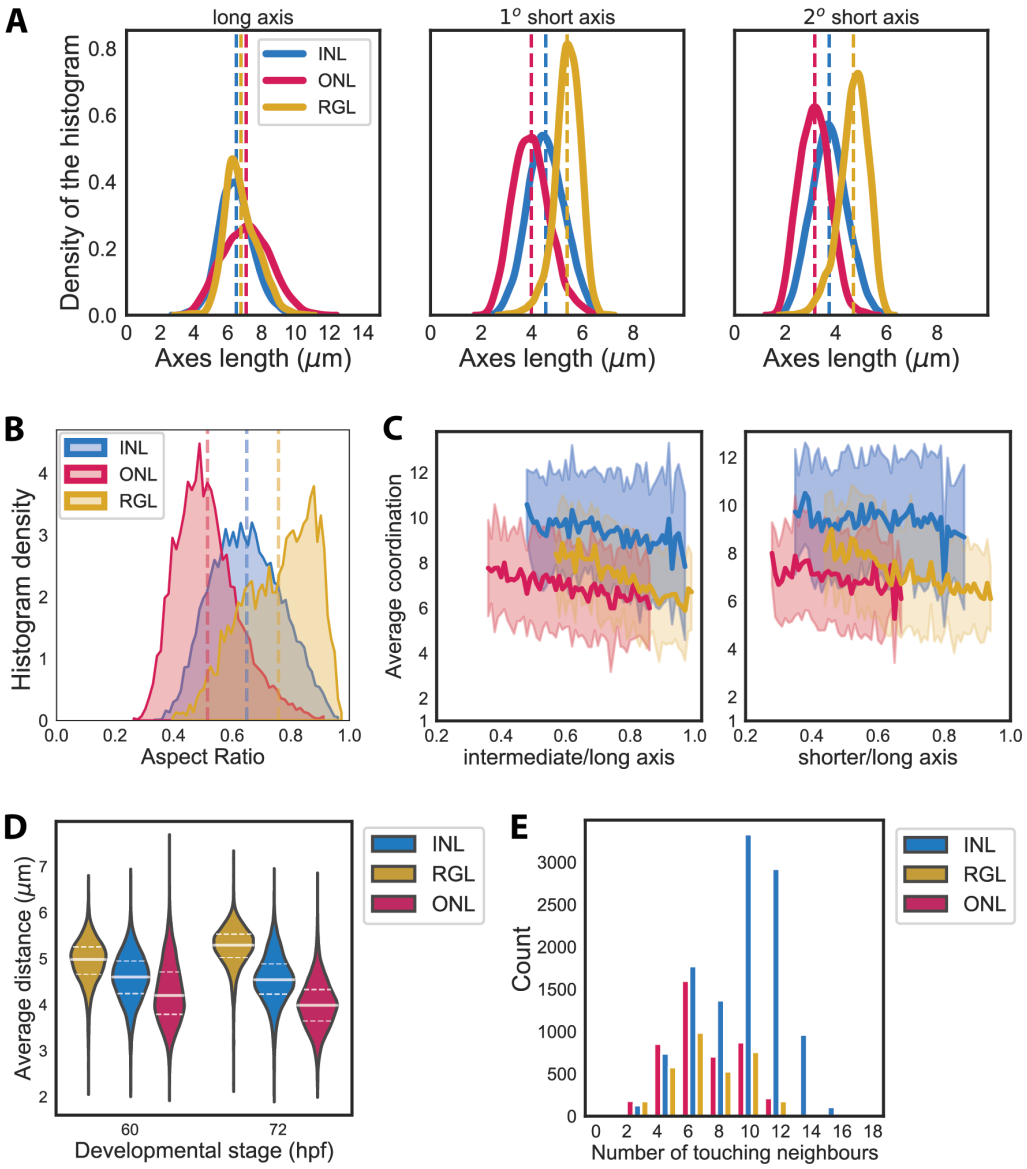

Figure 2.14: **Nuclear shape changes during neuronal differentiation. A)** Histogram density distributions of nuclear axes in the ONL, INL and RGL at 72 hpf. Segmented lines indicate the mean values for each distribution. **B)** Histogram density distribution for nuclear aspect ratios at 72 hpf. Segmented lines indicate the mean values for each distribution. **C)** Correlation between average coordination and nuclear shape across the INL, ONL and RGL at 72 hpf. Solid lines show mean values, shaded areas indicate the standard deviation from the mean. **E)** Violin plot of average distance between touching neighbors in the ONL, INL, RGL at 72 hpf. **F)** Histogram of numbr of touching neighbors at 72 hpf.

Indeed, it has been shown that mitotic events in the central retina become less frequent after 60 hpf [221]. Thus, we decided to test whether the positioning of nuclei became more ordered over time by performing our 3D image analysis pipeline.

To do this, we computed the RDF of nuclei in the INL and RGL between 60 and 80 hpf, once neurons in the INL have finalized their nuclear positioning. This analysis showed

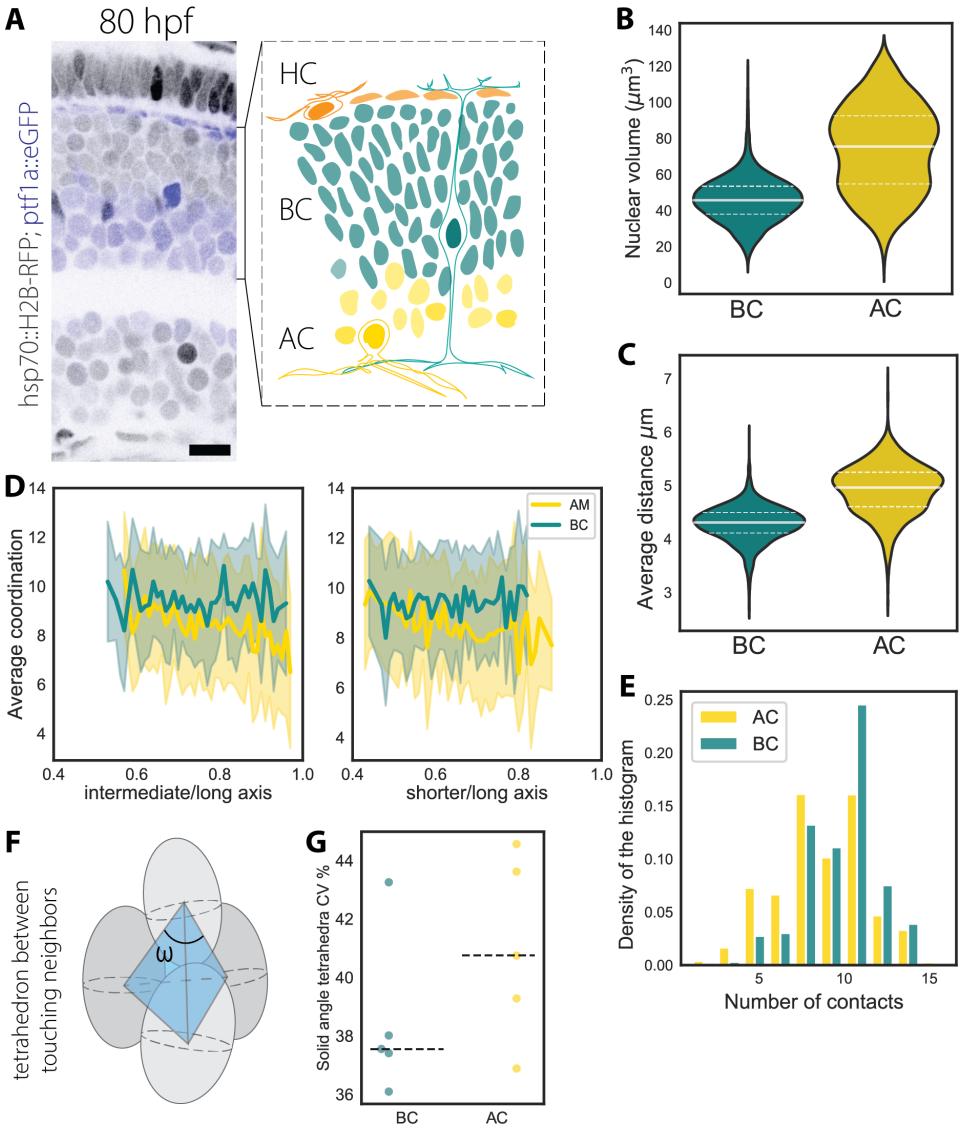

Figure 2.15: **Different neuronal types show different degree of ordered packing within INL. A)** Optical slice of the zebrafish retina at 80 hpf. In gray, nuclei are marked with Tg(hsp70:H2B-RFP). Scheme shows the different neuronal types populating the INL. Amacrine cells, AC; bipolar cells, BC; horizontal cells, HC. Scale bar = 10 μm. **B)** Violin plot of nuclear volume distributions for BC and AC. **C)** Violin plot of average distance distributions between touching neighbors for BC and AC. **D)** Histogram of number of touching neighbors for BC and AC. **E)** Scheme of tetrahedra formed by touching neighbors and the solid angle ω. **F)** Coefficient of variation of solid angle distributions in tetrahedra in ACs and BCs of distinct retinas. N = 5 embryos.

the highest probability of finding a nucleus at 5 um of internuclear distance, i.e. from centroid to centroid, for nuclei in the RGL between 60 and 80 hpf (Fig. 2.16 B, C). By 80 hpf, we observed the emergence of another peak around 10 um, which indicated the emergence of regular positioning as we would expect for a solid-like material (Fig. 2.16 C). Similarly, the RDF computed for nuclei in the INL showed a highest peak at 5 um internuclear distance and the emergence of a smoother peak around 10 um by 80 hpf (Fig.

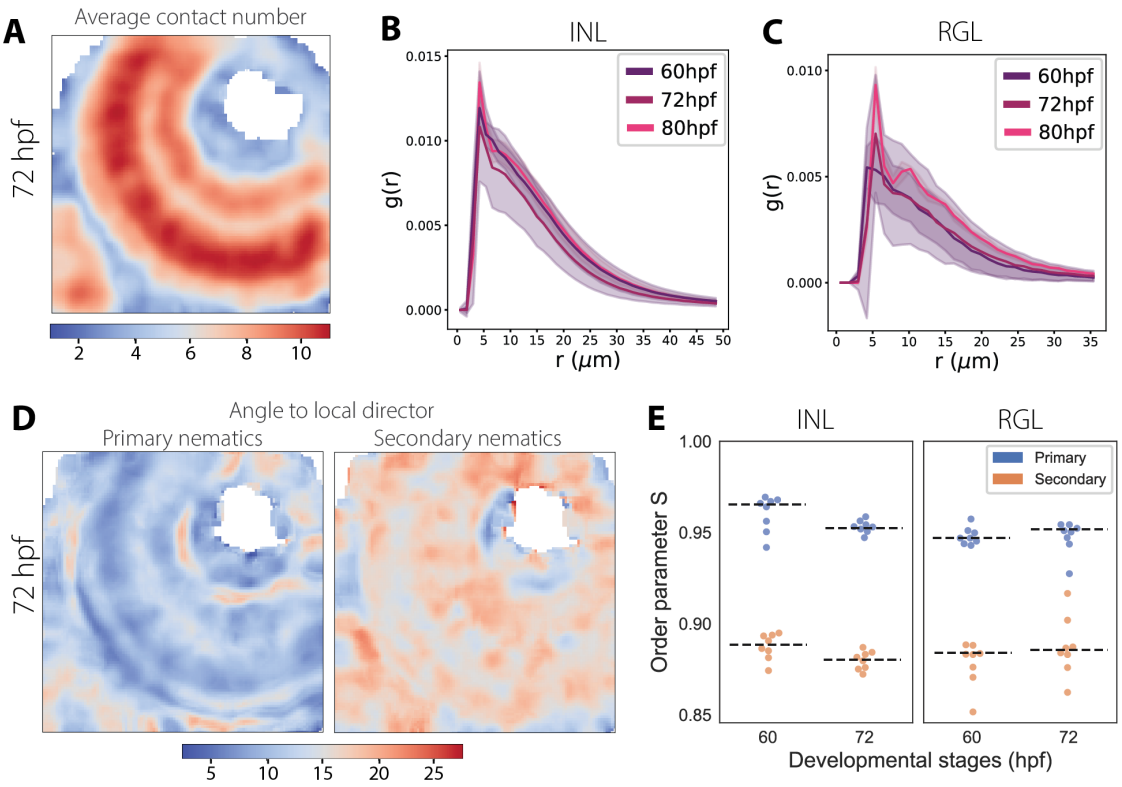

Figure 2.16: **Nuclei in the laminated neural retina are arranged in orientational and positional order. A)** Median intensity projection of color maps reporting the average number of contacts per nucleus after image smoothing. Representative image a retina at 72 hpf. **B)** RDF in the INL over time. **C)** RDF in the RGL over time. **D)** Median intensity projection of color maps reporting the average angle θ between the primary (left) and the secondary (right) nematics and the average local direction axis. Representative image a retina at 72 hpf. **E)** Order parameter S in the INL and RGL over time.

2.16 B). These results showed the emergence of a periodic structure, with discrete peaks at given values of the RDF both in the INL and the RGL between 72 and 80 hpf, meaning that nuclei are positioned in an ordered arrangement. Moreover, we analyzed the alignment of nuclei across the three nuclear layers and found that nuclei appeared to maintain a strong orientation along their primary nematics even at later stages of development (Fig. 2.16 D, E). Thus, ordering of nuclei in the INL and RGL presented characteristics typical of orientational order, where nuclei are elongated and aligned along a main director, but they also showed the emergence of positional ordering, which had been absent at the earlier stages, i.e. during the proliferative phase between 24 and 48 hpf.

In conclusion, our data suggested that neuronal precursors were progressively arranged in a more regular crystalline-like configuration within the INL and RGL, while keeping a long-range alignment along the apicobasal tissue axis, which was reminiscent of the orientational order that characterized neuroepithelial cells in the retinal PSNE during the proliferative phase. We hypothesize that the presence of both positional and long-range orientational order could represent an important feature for optically transparent

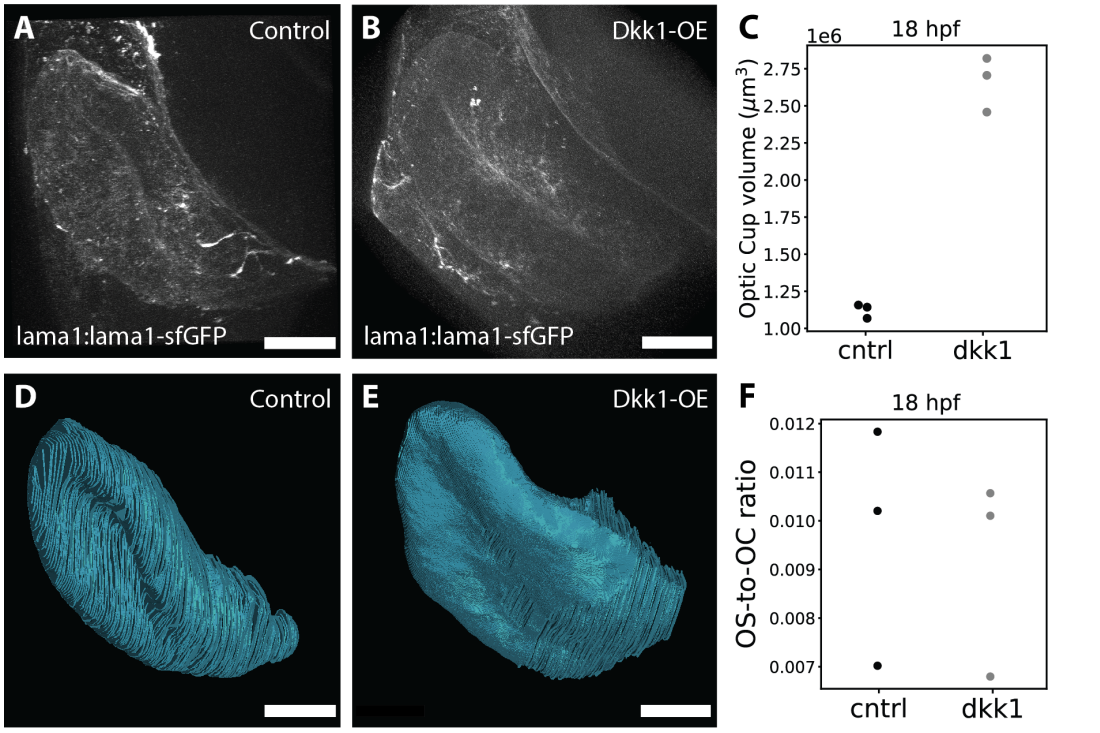

Figure 2.17: **Size changes in the optic cup and optic stalk in dkk1-overexpressing embryos. A, B)** Representative 3D rendering of control and Tg(hsp70:Dkk1-GFP) embryos at 18 hpf. Basal lamina is marked with Tg(lama1:lama1:sfGFP). Scale bar = 20 μm. **C)** Optic cup volume in of control and Tg(hsp70:Dkk1-GFP) embryos at 18 hpf. N = 3 embryos per condition, p value < 0.01 for two tailed independent t-test. **D, E)** 3D rendering of segmented optic cups shown in fig. A. **F)** Ratio of contact surface between optic stalk and optic cup and optic cup volume. N = 3 embryos per condition, p value n.s. for two tailed independent t-test.

tissues, like the retina.

2.4 Testing the interplay between proliferation, differentiation and nuclear packing

2.4.1 Increasing the number of progenitor cells causes the retinal neuroepithelium to buckle

Proliferation and differentiation need to be tightly balanced in most neuronal tissues to produce a big enough pool of specialized postmitotic neurons. This is particularly relevant in the context of fast-growing neuroepithelia, such as the retina, which is one of the first structures of the central nervous system being formed in vertebrates. Based on our characterization of nuclear packing dynamics in the proliferating retinal PSNE, we hypothesized that pseudostratification could enable to pack high numbers of multipotent progenitors within a monolayered tissue without reaching a rigidity transition. To explore this notion, we set out to increase the number of multipotent progenitors and examine

whether nuclear packing densities would change at any time in the PSNE and, if so, what this could entail for the development of the tissue.

To increase the number of neuroepithelial cells already in the optic vesicle, we used the tg(hsp70:dkk1-GFP) transgenic line, in which the Wnt antagonist Dkk-1 is overexpressed under a heat-shock inducible promoter [196]. Dkk1 has been shown to be involved into forebrain specification and its temporary overexpression right before gastrulation results in extensive anteriorization of the neuroectoderm in zebrafish embryos, leading to enlarged forebrain and eyes [187, 78]. Upon heat-shock at 6 hpf, embryos expressing the construct showed an optic vesicle 2.5 times larger than control embryos from the same clutch that did not show expression of Dkk1-GFP (Fig. 2.17 A -E). Though, when we observed the morphology of the retina in Dkk1-overexpressing embryos during the rest of the proliferative phase, i.e. at 36, 42 and 48 hpf, tissue folding and apical buckling events were detectable in nearly 50% of the imaged embryos between 30 and 36 hpf and in 60% by 48 hpf (24 hpf, n = 2/12 embryos; 30 hpf, n = 7/14 embryos; 36 hpf, n = 4/8 embryos; 48 hpf, 7/12 embryos; fig. 2.21). Such tissue buckling was never observed in controls. The fact that we could not detect folding in all the Dkk1-overexpressing retinas could be due to the variability in the activation of the hsp70 promoter itself that led to different strength of overexpression among embryos of the same clutch. Interestingly, the presence of this buckling phenotype coincided with the peak in proliferation between 30 and 36 hpf. Next, we asked whether nuclear packing densities in Dkk1-overexpressing embryos were comparable to the packing densities we measured in control embryos. At 24 hpf, nuclei in the optic cup were arranged similarly to nuclei in control embryos and analysis of segmented nuclei obtained using our StarDist-3D model and image analysis pipeline did not detect any difference in nuclear packing and nuclear concentration Dkk1-overexpressing and control retinas (Fig. 2.19 A, B). Also, the distribution of nuclear volumes between control and Dkk1-overexpressing embryos did not differ (Fig. 2.19 C; control: 22 hpf, n= 1714 N = 6; 30 hpf, n = 2944, N = 6; 36 hpf, n = 4230, N = 4; *hsp70:DKK1-eGFP*: 22 hpf, n= 1665, N = 4; 30 hpf, n = 4844, N = 6; 36 hpf, n = 4815, N = 4; where n is number of nuclei and N is number of embryos). Indeed, we found that nuclear packing densities did not massively differ between Dkk1-overexpressing embryos and controls during the proliferative phase, indicating that nuclei were not more densely packed in the embryos overexpressing DKK1-GFP compared to controls (Fig. 2.19 A, B, C). This indicated that only the size of the tissue was altered (Fig. 2.19 D). By 36 hpf, the thickness of the retinal PSNE in control embryos appeared to approximate the thickness of Dkk1-overexpressing (Fig. 2.19 D). This suggested that growth of enlarged retinal PSNE slowed down and approximated the same size as controls already by 48 hpf, as previously reported [226, 78].

Overall, our data indicated that an increased number of multipotent progenitor cells could be accommodated in the retinal tissue during the first stages of development. This increase in cell number did not result in increased nuclear packing due to compensatory increase in the optic vesicle size. Though, proliferation in the retinal PSNE ultimately led

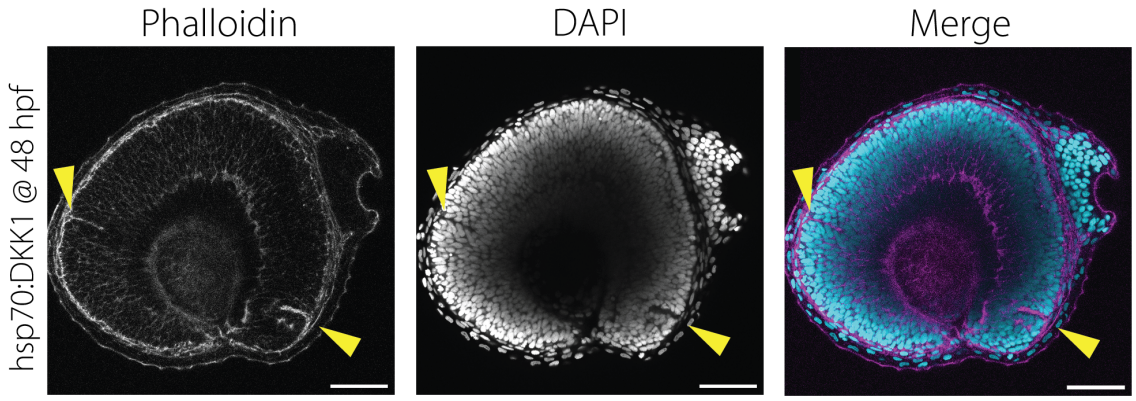

Figure 2.18: **The retinal PSNE of DKK1 overexpressing embryos shows apical folding of the tissue.** Representative images of a folded retina in Tg(hsp70:Dkk1-GFP) embryo at 48 hpf. Nuclei are marked with DAPI; cell membranes are outlined with phalloidin. Scale bar = 50 μm.

to folding of the tissue. Deformations of the retinal neuroepithelium were not associated with higher nuclear packing densities. This suggested that the packing densities observed in wild-type embryos have the potential to lead to a rigidity transition of the retinal neuroepithelium. What changed between control and Dkk1-overexpressing embryos was the size of the retinal neuroepithelium during the proliferative phase, suggesting that there might be an external constraint that limits the size of the eyes at later stages as development progresses.

2.4.2 Enlarged eyes contain folded neural retina

The observation that, in many instances, the retinal neuroepithelium buckles during the proliferative phase in tg(hsp70:Dkk1-GFP) embryos upon heat-shock led us to ask whether this perturbed tissue architecture impaired differentiation and neuronal lamination. It was proposed that neurogenesis is accelerated in Dkk1-overexpressing embryos and that this could be a mechanism to control eye size [226]. To explore this notion, we investigated the onset of neurogenesis in tg(hsp70:Dkk1-GFP) embryos to determine whether neuronal layering in the tissue was perturbed upon buckling of the neuroepithelium and whether the timing of the neurogenic wave differed from control embryos.

We crossed tg(hsp70:Dkk1-GFP) embryos with the tg(atoh7:gap-RFP) transgenic line to follow the emergence of early neurogenic progenitors. Upon overexpression of DKK1, we observe several Atoh7-positive progenitor cells in the neuroepithelium already around 25 hpf, when Atoh7 can be only detected in few cells located in the CMZ in control embryos. Our data confirmed that onset of neurogenesis was premature in the retinal PSNE of dkk1 overexpressing embryos (Fig. 2.20 A-D). Then, we compared the profile of Atoh7 expression in the retinas of control and Dkk1-overexpressing embryos over the course of 20 hours using light-sheet microscopy (LSFM) and found no difference in

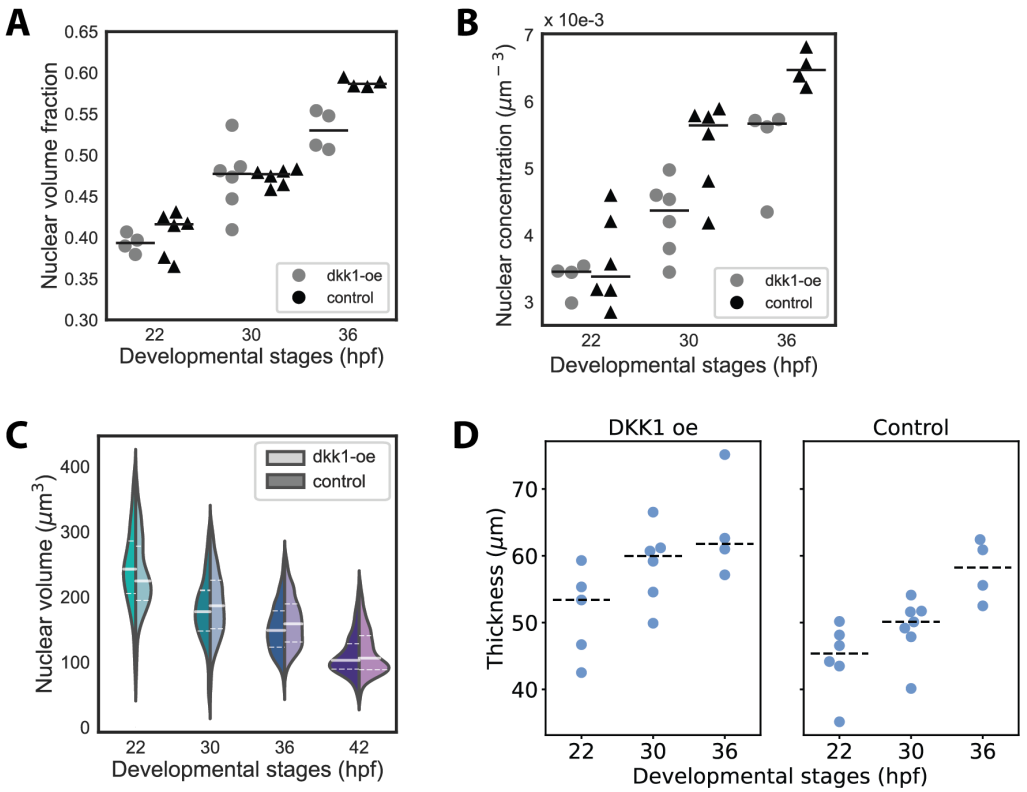

Figure 2.19: **Nuclear packing neither increases nor change between control and enlarged retinal PSNE. A)** Nuclear volume fractions of control and tg(hsp70:Dkk1-eGFP) retinas. N = 4 to 6 embryos per condition. Comparison at 22 hpf, n.s.; comparison at 30 hpf, n.s.; comparison at 36 hpf, p value < 0.01. Mann Whitney U test. **B)** Nuclear concentration of control and tg(hsp70:Dkk1-eGFP) retinas. N = 4 to 6 embryos per condition. Comparison at 22 hpf, 30 hpf and 36 hpf were all n.s. using the Mann Whitney U test. **C)** Violin plot of nuclear volume distributions of control and tg(hsp70:Dkk1-eGFP) retinas over time. **D)** Spread data of apicobasal tissue thickness of control and tg(hsp70:Dkk1-eGFP) retinas over time.

the progression of neurogenesis between the two conditions, except for the premature neurogenesis onset in the latter (Fig. 2.20 E). Since we do not observe any difference in nuclear packing, we excluded that the onset of neurogenesis in hsp70:Dkk1-expressing embryos was directly influenced by packing itself. Though, the formation of apical folds in some of the enlarged retinas suggested that compressive stresses were generated within the tissue during the proliferative phase even when nuclear packing densities were not higher compared to controls. To further determine whether the patterning of neuronal precursors was disorganized as a consequence of buckling, we visually inspected the dkk1-overexpressing and control embryos that had been imaged in parallel using light-sheet microscopy (shown in fig. 2.20 E). Imaging of whole retina revealed that Atoh7-positive cells correctly migrated toward their final position as they differentiate into RGCs or PR, even in those regions where the neuroepithelium has buckled (Fig. 2.21 A, B). Thus, our data showed that enlarged eyes contained folded neuronal retina, where the apicobasal polarity of the PSNE was maintained and where neuronal precursors managed to correctly

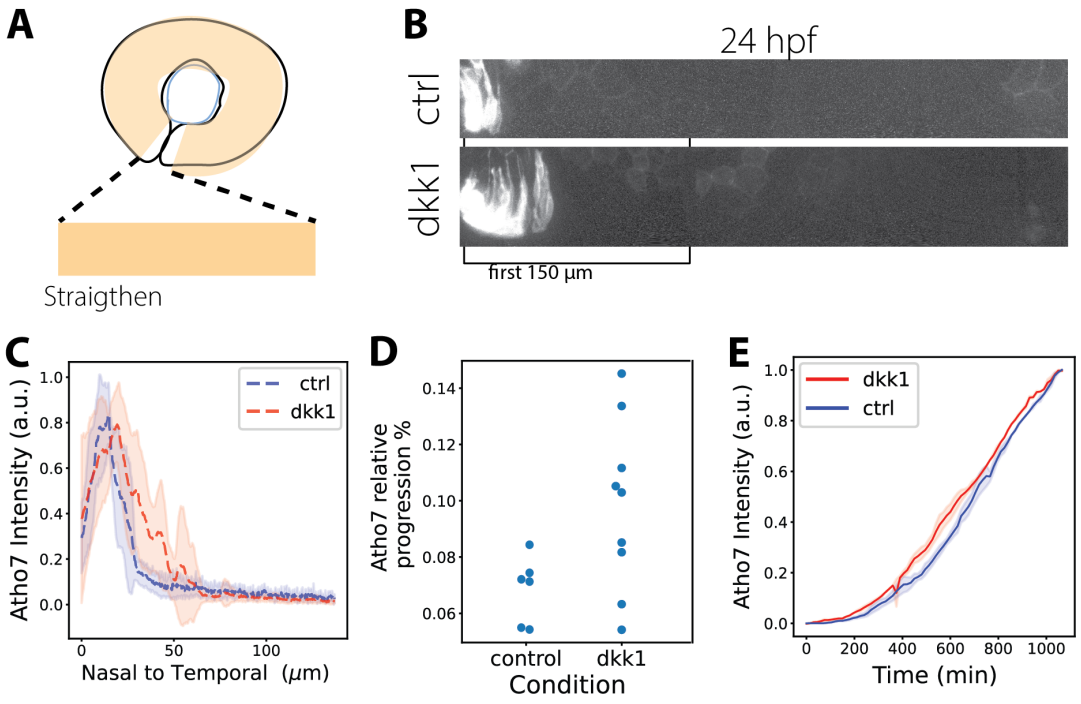

Figure 2.20: **Earlier onset of neurogenesis in Dkk1-overexpressing embryos, but the rprofile of the neurogenic wave does not change. A)** Scheme of the quantification of pixel intensity in Tg(atoh7:gap-RFP) embryos. A curved line is drawn to cover the retinal PSNE and is then straighten. **B)** Example of straighten retinal PSNE in control and Tg(hsp70:Dkk1-GFP) at 24 hpf. The first 150 μm are highlighted. **C)** Average normalized intensity profiles of Atoh7 expression in control and Tg(hsp70:Dkk1-GFP) at 24 hpf. Segmented lines show mean values, shaded areas indicate standard deviation from the mean. **D)** Ratio of Atoh7-positive segment length over the full length of the straightened retinal PSNE from figure C. **E)** Normalized intensity profile of Atoh7 expression in control and Tg(hsp70:Dkk1-GFP) over time, starting at 24 hpf. n = 2 retinas in N = 1 per condition.

laminate. Moreover, we observed that premature neurogenesis was not sufficient to prevent the neuroepithelium from buckling. This implied that neuronal differentiation per se could not act as a mechanism to resolve tissue-wide deformations like buckling.

We next looked at how neurogenesis starts earlier in the RNE in enlarged retinas. To test whether overexpression of Dkk1 could directly affect onset of neurogenesis, we heat-shocked tg(hsp70:Dkk1-GFP) embryos around 20 hpf. This did not result in earlier expression of Atoh7 in the RNE, suggesting that repression of Wnt signaling by Dkk1 does not directly impact this process, at least during the time window between 20 and 25 hpf. Since neurogenesis is triggered by the release of fgf3 and fgf8 from the optic stalk and because the direct contact between the optic stalk and the retinal PSNE is necessary to start differentiation in the neuroepithelium [129], we asked whether the early onset of differentiation could be due to an extended surface contact between these two tissues in Dkk1-overexpressing embryos. The optic stalk should be enlarged upon overexpression of Dkk1, like other anterior structures such as the forebrain and the eye [187, 78]. To explore this notion, we imaged tg(hsp70:Dkk1-GFP) crossed with tg(lama1:lama-mKate)

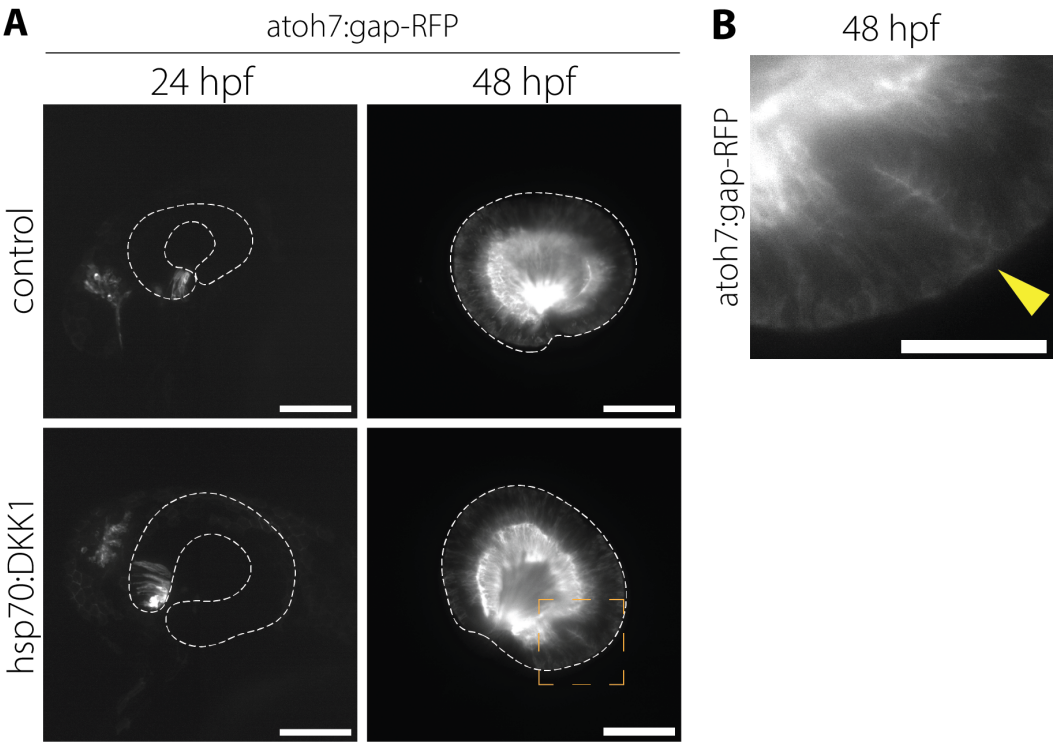

Figure 2.21: **The retinal PSNE of DKK1 overexpressing embryos undergo buckling during the proliferative phase. A)** Representative optical slices of retinas in control (top row) and Tg(hsp70:Dkk1-GFP) (bottom row) embryos at 24 and 48 hpf. The segmented white line outlines the shape of the retinal PSNE. Neuronal progenitors are marked with Tg(atoh7:gap-RFP). Orange square highlights the apical folding in the Tg(hsp70:Dkk1-GFP) embryo at 48 hpf. Scale bar = 50 μm. **B)** Crop of the region outlined in panel (A). Yellow triangle point to the apical folding. Scale bar = 20 μm.

embryos to visualize the basal lamina and segment the optic cup. Then, we measured the thickness to the optic stalk at 18 hpf, when the connection between these tissues was easily detectable. Our quantification showed that the surface between optic stalk and optic cup was expanded in dkk1-overexpressing embryos, but the ratio between this surface and the volume of the optic cup did not differ between overexpressing and control embryos (Fig. 2.17 F). Thus, it appeared that the connection between optic stalk and the retinal PSNE was not proportionally bigger in enlarged eyes. Though, this did not exclude that the absolute extension of this connection might be sufficient to contact more neuroepithelial cells and initiate premature neurogenesis outside the CMZ.

In conclusion, our analysis showed that onset of neurogenesis was premature in Dkk1-overexpressing embryos, but this was not sufficient to undo the deformations of the retinal PSNE that were produced during the proliferative phase. As a result, neuronal progenitors laminated within the buckled neuroepithelium and formed a stratified and folded neural retina. Because the profiles of the neurogenic waves in the retinal PSNE of dkk1-overexpressing embryos and controls appeared to have same shape, our results suggested that neurogenesis was not accelerated over time in response to mechanism

that would sense tissue size at later stages. Our analysis pointed uniquely to an earlier onset of neurogenesis. Direct effect of Dkk1 overexpression on Premature neurogenesis could be a result of changes in signaling dynamics between the RNE and other tissues, for instance due to a wider surface contact with the optic stalk. Also, we could not exclude that Dkk1 might influence onset of neurogenesis via indirect effect on the expression of other molecules and that this could lead to changes in neurogenesis timing in the retina by 25 hpf.

2.4.3 Depletion of progenitor cells from the optic cup locally delays neurogenesis

It is known that eyes in zebrafish larvae can recover their size upon genetic or physical reduction of the eye field during development [226]. It was proposed that this recovery could occur during the proliferative phase of retinal development and that this was achieved by delaying neurogenesis of retinal progenitor cells in smaller eyes [226]. Since we observed premature neurogensis in enlarged eyes upon heat-shock of the tg(hsp70:Dkk1-eGFP), which might be involved in readjusting the size of the RNE, according to this theory, we set out to test whether we could delay cell fate committment of multipotent progenitors by reducing the number of cells in the RNE.

To test this hypothesis, we physically removed cells from the optic cup of transgenic zebrafish larvae expressing the early neuronal marker Atoh7 and a nuclear marker. We manipulated embryos around 16-18 hpf, before the beginning of the expression of Atoh7 in the eye, which occurs around 24 hpf in few cells of the CMZ. For each embryo, we removed cells only from one optic cup, so we could examine the neurogenic wave in the other unperturbed eye within the same embryo (Fig. 2.22 A). Around 16 hours after cell removal, we examined the extent of the neurogenic wave in the two eyes and compared their profiles. In some cases, it was impossible to distinguish a difference, either due to insufficient removal of cells from the retinal neuroepithelium or due to incorrect removal of cells from other tissues. In those instances where we could detect a difference between the two eyes of a manipulated embryo, we observed fewer or no Atoh7+ neuronal precursor in regions of the manipulated retinal neuroepithelium (Fig. 2.22B-E; n = 5/18 embryos). Upon qualitative assessment, these regions appeared to be less populated compared to other regions of the retinal neuroepithelium within the same eye, suggesting a correlation between local tissue density and neurogenesis. This could be related to molecular mechanisms of cell fate specification based on cell-to-cell contacts. For instance, it is known that expression of the neuronal marker Atoh7 in the RNE is dependent on contact with the optic stalk [129] and that progenitor cells are kept in a proliferative state through lateral contact inhibition via Notch signaling [148]. Though, it was not possible to exclude that the temporary block in neurogenesis could be due to signals coming from dying cells after the procedure or from signals related to wound healing. Either way, our results suggested that retinal multipotent progenitors could delay their fate commitment

and these findings should be further explored to assess how this could be regulated.

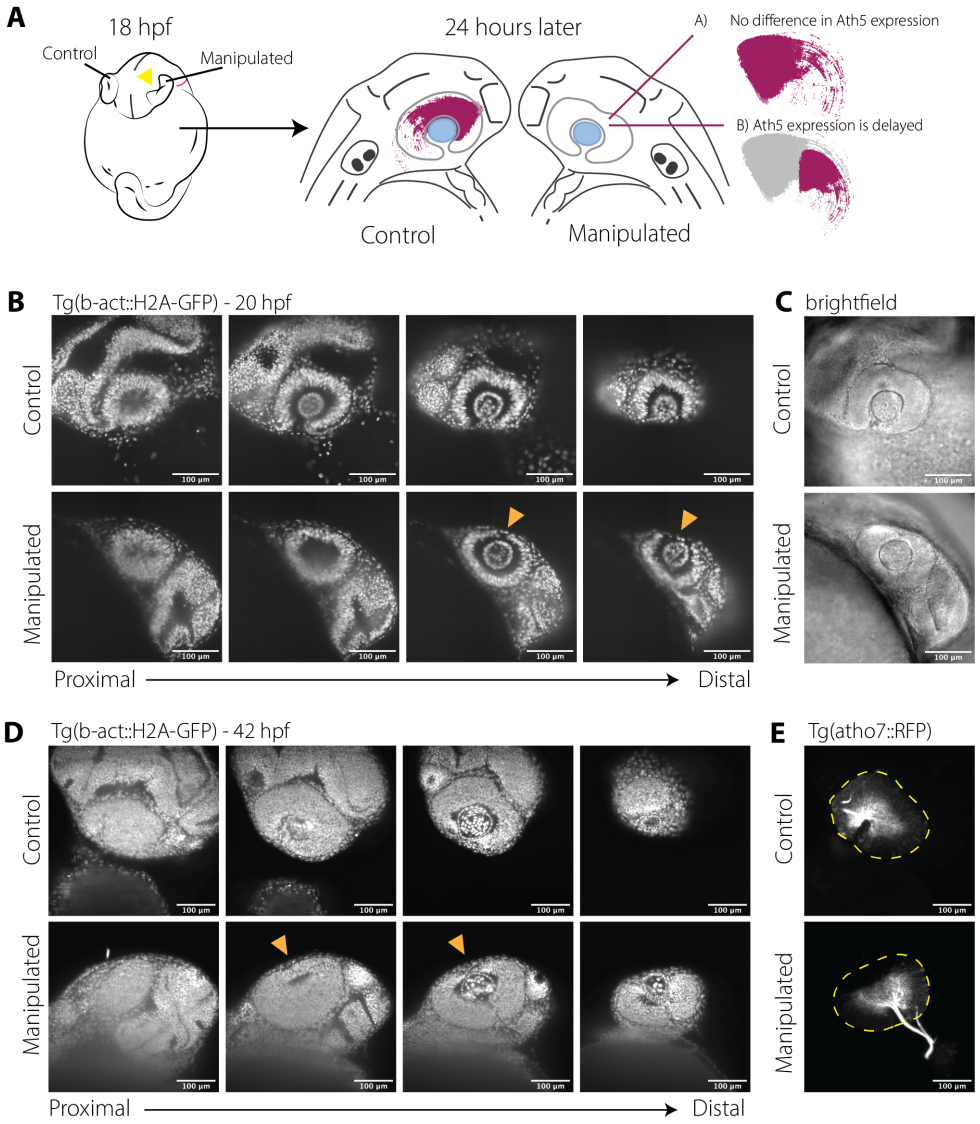

Figure 2.22: **Removal of progenitor cells from the optic cup delays neurogenesis. A)** Cells were aspirated from one eye vesicle around 18 hpf and the Atoh7 expression profiles of the two retinas within the same embryo were compared 24 hours later. **B)** Panel of different optical slices for both eyes of a manipulated embryo. Nuclei are marked with Tg(b-act:H2A-GFP). **C)** Brighfield optical slices of embryo shown in fig. B. **D)** Panel of different optical slices for both eyes of embryo shown in panel B-C 24 hours after manipulation. **E)** Maximum intensity projection of Atoh7 expression in retinas shown in panel D. Segmented line outlines the retina. Scale bar = 100 μm. Triangles in panels point to the region where cells were aspirated.

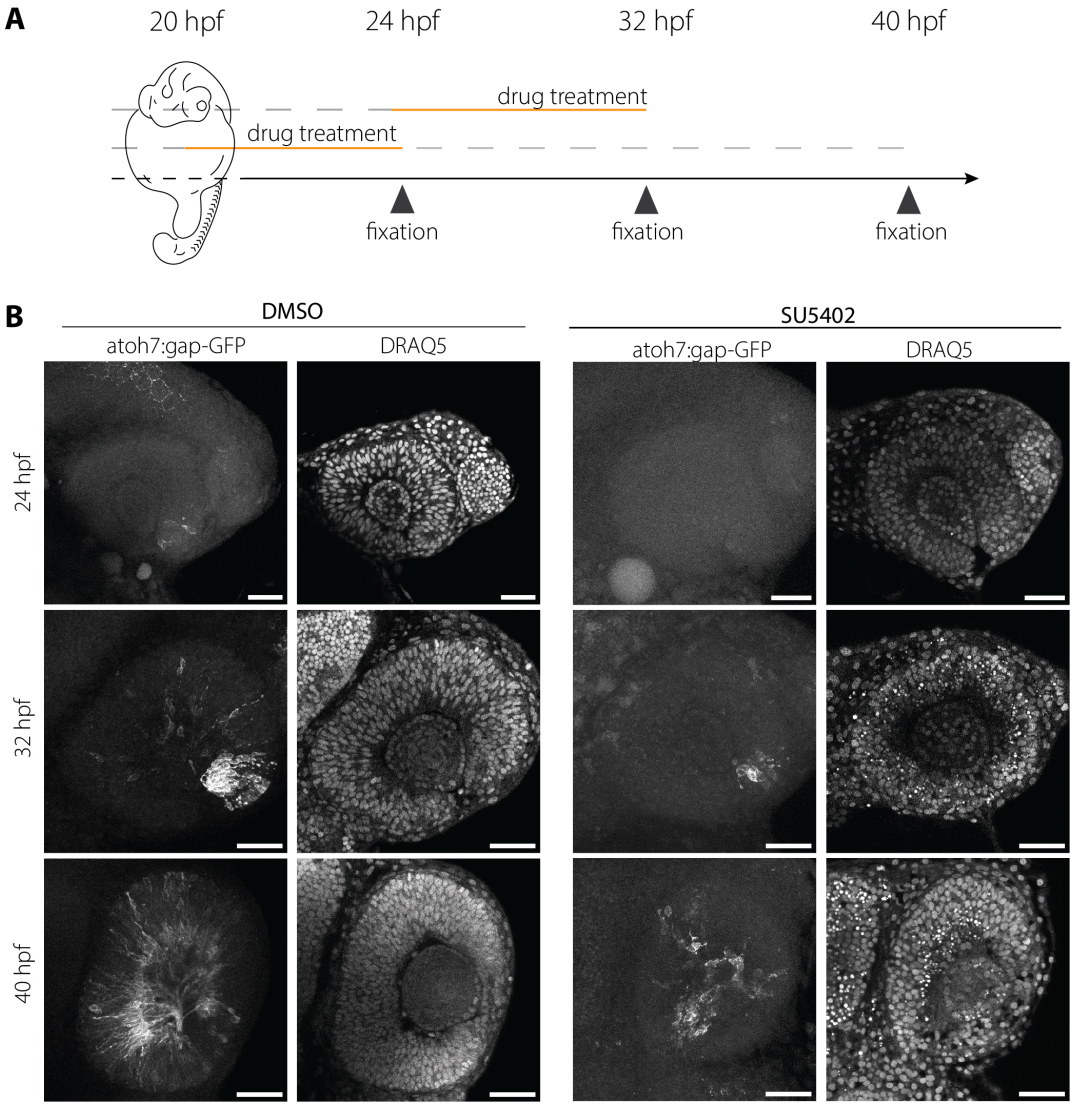

Figure 2.23: **Inhibition of FGF signaling leads to cell death in neuroepithelia. A)** Schematics of the drug treatment: embryos were incubated with the drug for a set amount of time and then fixed at different developmental stages. **B)** Representative images of retinas in control embryos. Optical slices of nuclei were marked with DRAQ5 (top row) and corresponding maximum intensity projections of Atoh7 expression marked with Tg(ato7:gap-GFP) (bottom row). **C)** Representative images of retinas in treated embryos. Optical slices of nuclei were marked with DRAQ5 (top row) and corresponding maximum intensity projections of Atoh7 expression marked with Tg(ato7:gap-GFP) (bottom row). Scale bar = 50 μm.

2.4.4 Block of neurogenesis leads to impaired nuclear shape remodeling and buckling of the retinal neuroepithelium

In the previous chapters, we showed that abnormally high number of multipotent progenitors at early stages of development resulted in deformation of the retinal neuroepithelium in dkk1-overexpressing embryos. Though, this phenotype was not evident in all dkk1-overexpressing embryos and size of the retinal PSNE was shown to adjust during the process of neuronal lamination [226]. Since apoptosis is not detectable in the RNE during the first three days of development [124], differentiation represents the sole mechanism to regulate cell number in the developing zebrafish retina. In addition to this: we had shown that the retinal neuroepithelium progressively transitioned from a nematic-like to a crystalline-like order as more neurons were formed and matured and that the highest nuclear packing values were measured in the INL around 60 hpf, only to decrease by 72 hpf. This data suggested that neuronal lamination was instrumental to pack more neuronal precursors within the developing retina without reaching a premature jamming transition. This prompted us to ask whether nuclear packing approached a maximum value in the pseudostratified retinal tissue at the onset of neuronal lamination. Therefore, we wondered whether the retinal tissues could reach a rigidity transition by delaying or blocking neurogenesis and by keeping the retinal neuroepithelium in a PSE-like arrangement for a longer period of time. To do this, we set out to probe the limits of nuclear packing in the PSNE by perturbing the transition to a more ordered arrangement.

To impair neuronal lamination, we set out to completely block or delay neurogenesis in the RNE. Since onset of cell fate specification is determined by the secretion of fgf3 and fgf8 from the optic stalk [128], we tested the established FGF receptor inhibitor SU5402 on tg(atoh7:gap-GFP) embryos (Fig. 2.23 A). In line with previous reports that inhibition of FGF signaling blocks neurogenesis, we found no Atoh7-positive progenitor in the retinal PSNE at 24 hpf, while control retinas showed few cells expressing this neuronal marker in the CMZ (Fig. 2.23 B). In contrast, embryos treated during the same time window and then incubated in E3 and fixed at 40 hpf showed extensive signs of cell death, i.e. pyknotic nuclei in the RNE (Fig. 2.23 B). Likewise, we observed reduced number of Atoh7-positive cells in the CMZ and cell death in embryos treated between 24 and 32 hpf (Fig. 2.23 B). Therefore, inhibition of FGF signaling at the onset of neurogenesis proved to be lethal for multipotent progenitors in the retinal PSNE. Since selective knock-down of the early neurogenic marker Atoh7 has been shown to selectively ablate RGC production but does not block or delay overall neurogenesis [4, 149], we set out to prevent cell fate specification by perturbing chromatin remodeling [46].

To do this, we used a previously established Histone Deacetylase 1 (Hdac-1) morpholino knock-down (KD) approach that blocks neurogenesis and, subsequently, impairs neuronal lamination [130]. In wild-type, Hdac1 suppresses Wnt and Notch signaling in the retinal neuroepithelium, therefore regulating the balance between proliferation

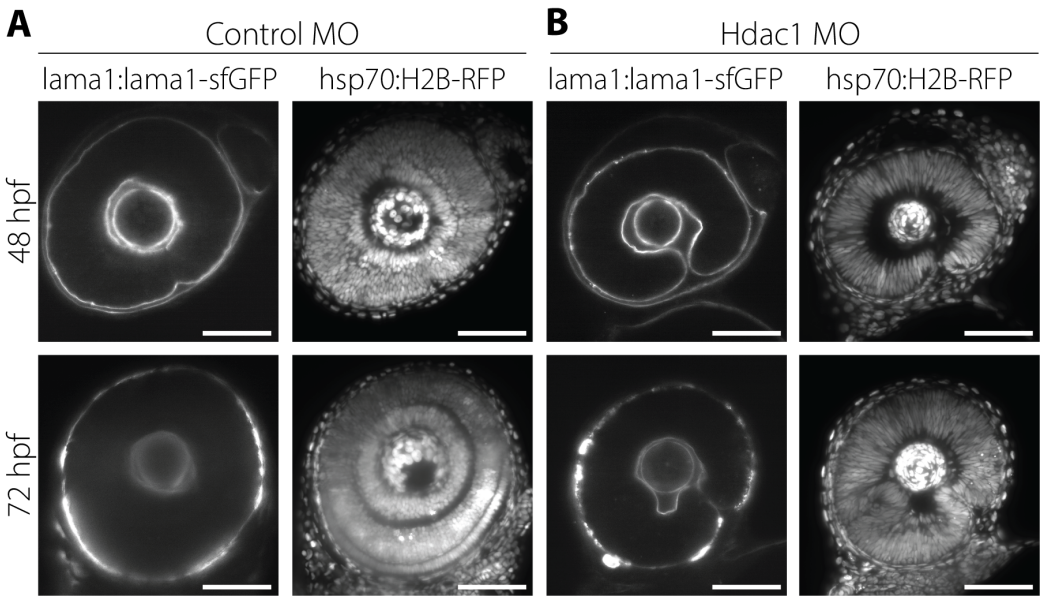

Figure 2.24: **Retinal PSE of hdac1 morphants buckle within the basal lamina.** Representative images of retinas in control (left panel) and Hdac1 (right panel) morphants. Nuclei were marked with Tg(hsp70:H2B-RFP)(right column), basal lamina was marked with Tg(lama1:lama1-sfGFP) (left column). Scale bar = 50 μm.

and neuronal differentiation of multipotent progenitors in the retina [45, 194, 79]. Moreover, knock-down of Hdac1 results in sustained proliferation, while the tissue retains a PSE-like structure at later stages [130]. Ultimately, upon Hdac1 knockdown, the retinal neuroepithelium starts buckling after 48-50 hpf and is folded by 72 hpf [130].

Given that cells in the Hdac1 morphants continue to proliferate also at stages when normally neuronal precursors are maturing into postmitotic neurons, we asked whether the overall volume of the retinal neuroepithelium was bigger in the morphants than in the control embryos. To address this question, we used the tg(lama1:lama-GFP) transgenic line to visualize the basal lamina and segment the eye (Fig. 2.24 A, B). The retinal volumes were smaller in the Hdca1 morphants compared to controls at 48 hpf and this difference increased at 72 hpf, when the control tissue is fully laminated (Fig. 2.26 A). This confirmed that neurogenesis is instrumental to remodel cell shape and tissue thickness and to allow the growth of the retina, as previously shown [130].

In order to assess whether nuclear packing was implicated in generating the stresses that led to tissue buckling in the morphants, we injected tg(hsp70::H2B-RFP) embryos with the hdac1 morpholino and imaged them at 48 and 72 hpf, i.e. before and after buckling (Fig. 2.25 A). This dataset was used to segment nuclei using StarDist-3D (see Materials and Methods 4.4.2). At 48 hpf, nuclei were bigger and extremely elongated along their major axis, whilst the distributions of their shorter axes did not differ significantly from those of nuclei in controls at the same developmental stage (Fig. 2.25 B; 2.26B, C,E,H). The extreme elongation of these nuclei suggested that they were deformed by increasing lateral compression stress generated in the tissue between 42 and 48 hpf, when the first

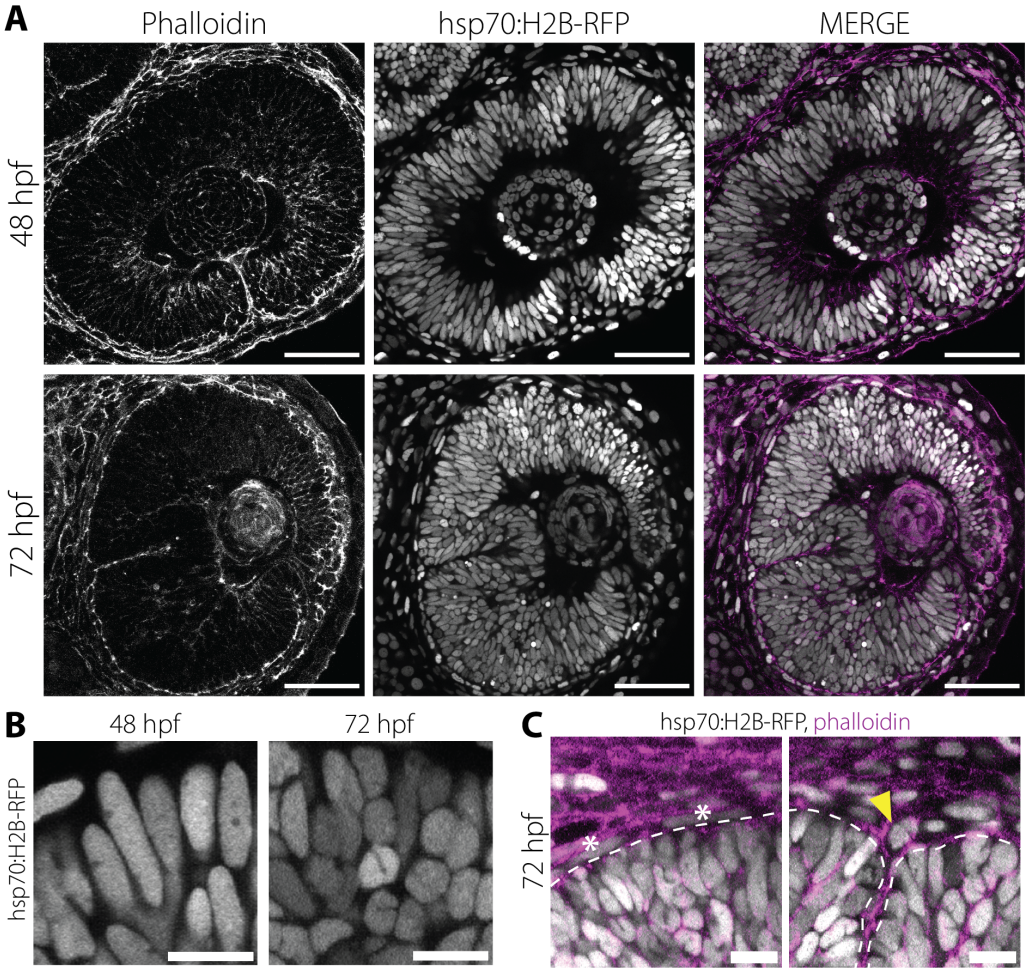

Figure 2.25: **The retinal neuroepithelium retian a PSE-like structure and buckles at later stages when the retina is normally laminated. A)** Representative images of retinas in Hdac1 morphants at 48 hpf (top row) and 72 hpf (bottom row). Nuclei were marked with Tg(hsp70:H2B-RFP), cell embranes are outlined with phalloidin. Scale bar = 50 μm. **B)** Zoomed crop from images in panel (A). Scale bar = 10 μm. **C)** Zoomed crop from images in panel (A) at 72 hpf showing the different shape of nuclei in RPE. Asterix marks elongated nuclei in RPE, triangle points to a round RPE nucleus on top of apical folding of the PSE. Scale bar = 10 μm.

buckling event were observed. Nuclear size was reduced in Hdac1 morphants only upon buckling of the tissue and the nuclear average aspect ratio shifted to higher values once the tissue was completely deformed (Fig. 2.26 B). While the average nuclear volume at 72 hpf was smaller than before buckling, nuclear size could not decrease to the same values reported for nuclei of neuronal precursors in control retinas where neuronal lamination was not impaired (Fig. 2.26 B). These results indicated that retinal progenitor cells in Hdac1 morphants could not fully remodel their nuclear size and shape as seen for cells in control embryos. This suggested that most of the reshaping of nuclei was linked to differentiation and could only in part be ascribed to the stress generated by tissue packing itself.

Lower values of aspect ratios for nuclei correlated with higher values of contact number than higher aspect ratios at the same developmental stage in Hdac1 morphants (Fig. 2.26 D). Despite this correlation, the average coordination did not increase to the same values measured in the laminated retina. In control retinas, the correlation between nuclear aspect ratio and contact number changed its trend for more elongated nuclei at 72 hpf due to the photoreceptors, which were characterized by low nuclear aspect ratio and low average coordination. Therefore, despite their extremely elongated shapes, nuclei in the Hdac1 morphants could not contact more neighbors than nuclei in controls, suggesting that nuclei in this condition were reaching their closest configuration for this arrangement. Moreover, measurement of the volume fraction of nuclei in Hdac1 morphants showed that nuclear packing did not increase between 48 and 72 hpf and did not overpass the values of volume fraction that we calculated at the onset of neurogenesis in control embryos (Fig. 2.26 F; comparison at 48 hpf, n.s. ; comparison at 72 hpf (INL), p value < 0.01; comparison at 72 hpf (RGL), n.s. for independent t-test). Even though nuclear volume fractions were lower in Hdac1 morphants comparerd to control, nuclear concentration was higher both at 48 and at 72 hpf (Fig. 2.26 G; comparison at 48 hpf, p value < 0.00001; comparison at 72 hpf (INL), p value < 0.00001; comparison at 72 hpf (RGL), p value < 0.01 for independent t-test.).

In conclusion, our comparison of eye volumes between Hdac1 morphants and controls showed that cell shape changes occurring during neuronal lamination were instrumental to allow overall volume growth of the tissue. The eye appeared to be smaller in hdac1 morphants, despite the sustained proliferation of neuroepithelial cells. Blocking the rearrangement of cells and, thereby of their nuclei, led to extensive buckling of the retinal neuroepithelium at stages when normally the tissue should have been fully stratified. Deformations of nuclear shapes due to the compressive forces preceded the buckling and were visible by 48 hpf. Nuclear packing reached a volume fraction of 0.635 by 48 hpf and did not increase at later stages (Fig. 2.26 F), suggesting again that the nuclei in retinal neuroepithelium of Hdac1 morphants were approaching their limiting packing density for a proliferating PSNE. Thus, this implied that higher nuclear packing densities could be reached only upon rearrangements of nuclei in separate layers, as it happened in embryos injected with control morpholinos.

2.4.5 Pseudostratification of the developing RNE is involved in maintenance of tissue shape

Our analysis suggested that pseudostratification enabled dense packing of nuclei, and thereby cells, during the proliferative phase and until the onset of neuronal lamination, when the arrangement of nuclei had to be modified to accommodate the newly generated neurons. As a hallmark of pseudostratification, nuclei were found to be arranged in a nematic-like order in the retinal PSNE and this long long-range orientation was maintained throughout later stages in the laminated neural retina. When neuronal differentiation

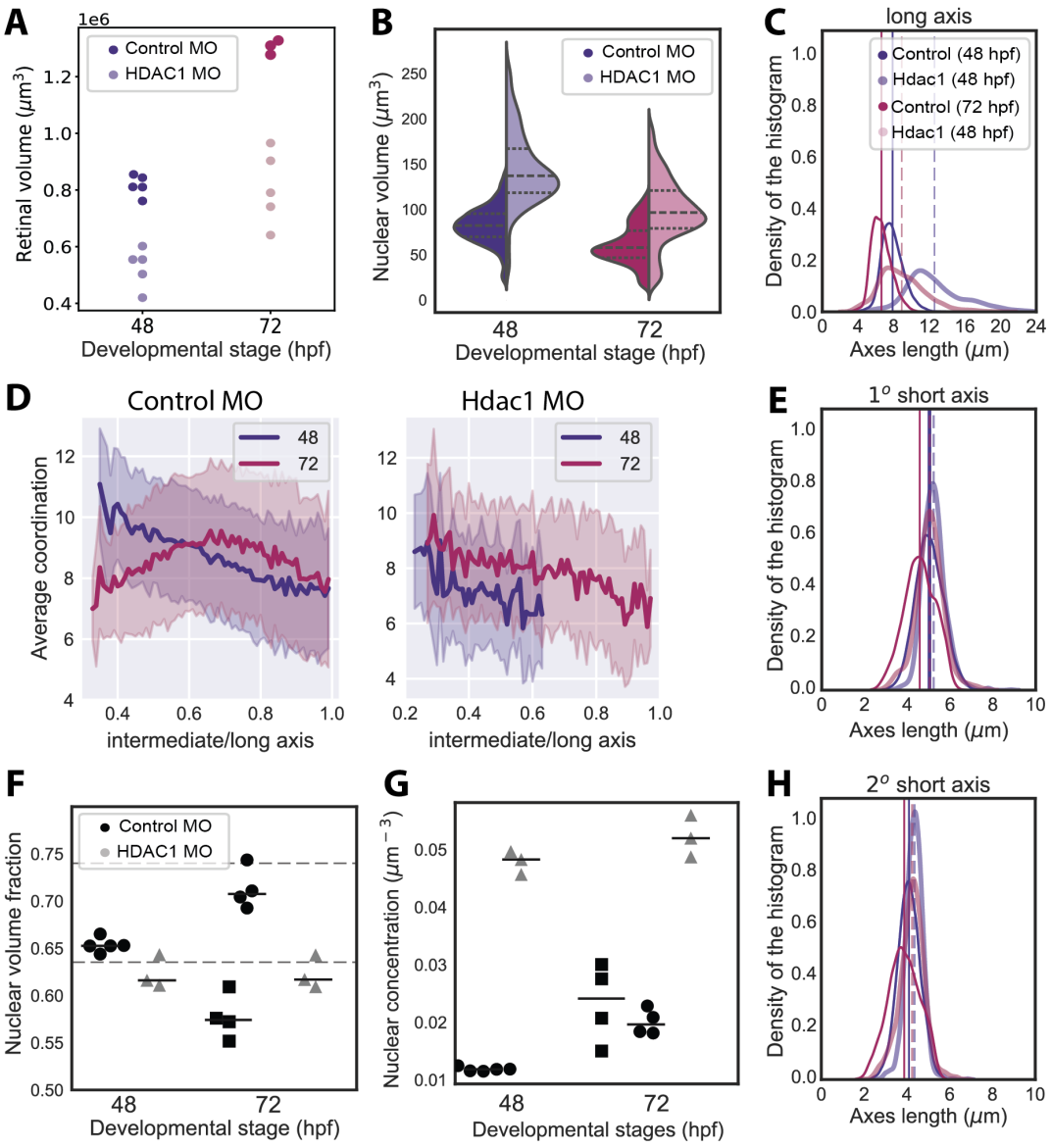

Figure 2.26: **Blocking neurogenesis impairs the remodeling of nuclear shape and perturb nuclear packing. A)** Eye volume from fig. 2.24. N = 3 to 4 embryos per condition. **B)** Nuclear volume distributions. **C, E, H)** Histogram density of nuclear axes lengths. **D)** Correlation between average coordination and nuclear aspect ratios. **F)** Nuclear volume fractions. Circles at 72 hpf indicate measurments from the INL, squares from the RGL. N = 3 to 5 embryos per condition. **G)** Nuclear concentration in control and Hdac1 morphants. Color and shape codes are the same as in panel (F). N = 3 to 5 embryos per condition.

and lamination were impaired, the RNE underwent extensive tissue shape alterations, i.e. buckling. To investigate if pseudostratification itself is necessary to prime nuclear ordering in the laminated retina later during development, we perturbed the tissue architecture of the retinal PSNE without affecting neurogenesis. It was previously shown that displacement of newly formed multipotent progenitors can be achieved upon overexpression of a membrane-targeted aPKC-ζ (aPKC-CAAX) that restructures the actin cytoskeleton and

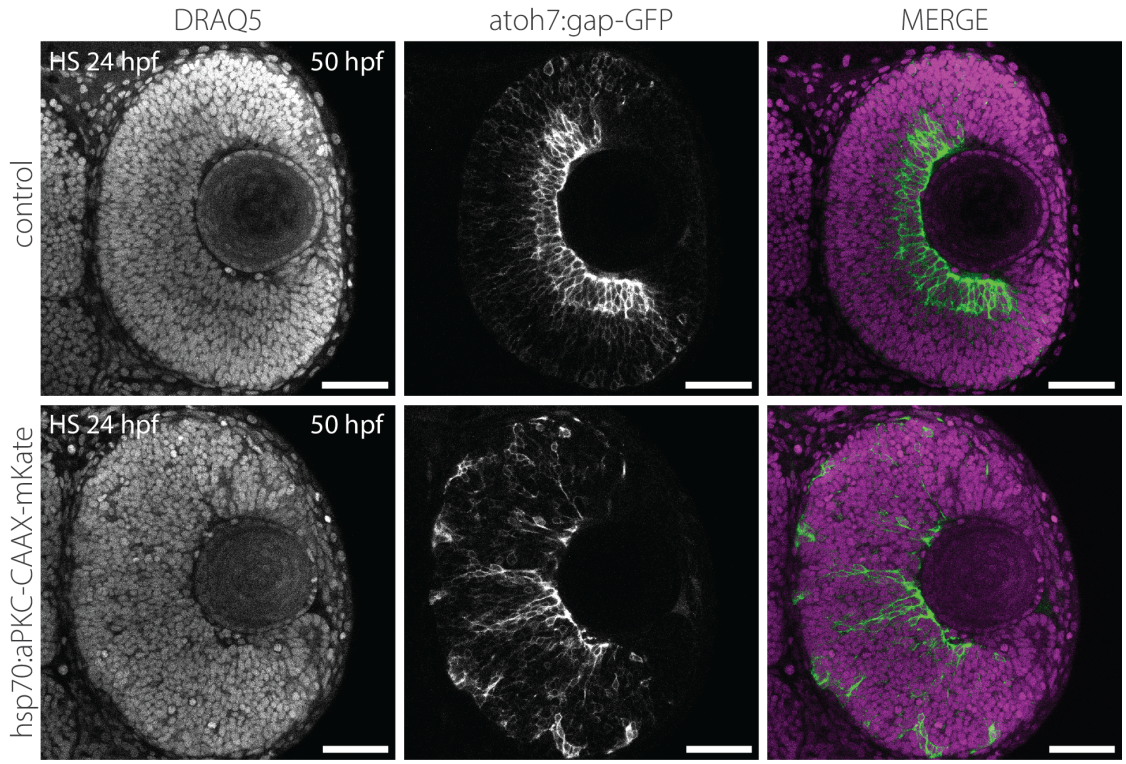

Figure 2.27: **Expression of aPKC-CAAX construct perturb the tissue architecture of the retinal PSNE.** Representative images of control and tg(hsp70:aPKC-CAAX-mKate) embryos at 50 hpf, i.e. 24 hours post heat shock (hphs). Neuronal precursors are marked with tg(atoh7:gap-GFP). Nuclei are marked with DRAQ5. Scale bar = 50 μm.

results in loss of apicobasal polarity in progenitors [199, 86]. To assess the effects of the aforementioned construct on neuronal lamination, we crossed the tg(hsp70:aPKC-CAAX-mKate) transgenic line with the tg(atoh7:gap-GFP) to visualize Atoh7-positive neuronal precursors. Heat shock was performed around 24 hpf so that aPKC-CAAX was present in multipotent progenitors before the emergence of RGC neuronal precursors. Embryos expressing the construct and control embryos from the same clutch were fixed at 48 hpf to assess how the tissue architecture was perturbed (Fig. 2.27). Atoh7-positive neuronal precursors were misplaced throughout the apicobasal axis of the tissue. Consequently, the RGL was not formed correctly. Therefore, overexpression of aPKC-CAAX in multipotent progenitors early on during the proliferative phase resulted in nonapical divisions, perturbed neuronal lamination and interfered with overall tissue architecture.

To further investigate the effects of impaired pseudostratification on retinal development, we examined the progeny of tg(hsp70:aPKC-CAAX-mKate) line crossed with the tg(b-act:H2A-GFP) line, so that we could visualize all nuclei in the retina. After heat shock around 24 hpf, embryos were fixed, stained and imaged at 48 hpf, when neuronal lamination is starting, and 120 hpf, when the retina is fully mature (Fig. 2.28 A, B). At 48 hpf, ectopic mitotic nuclei and increased deposition of cortical actin were visible throughout the RNE, highlighting the loss of orientational order in the tissue (Fig. 2.28 A).

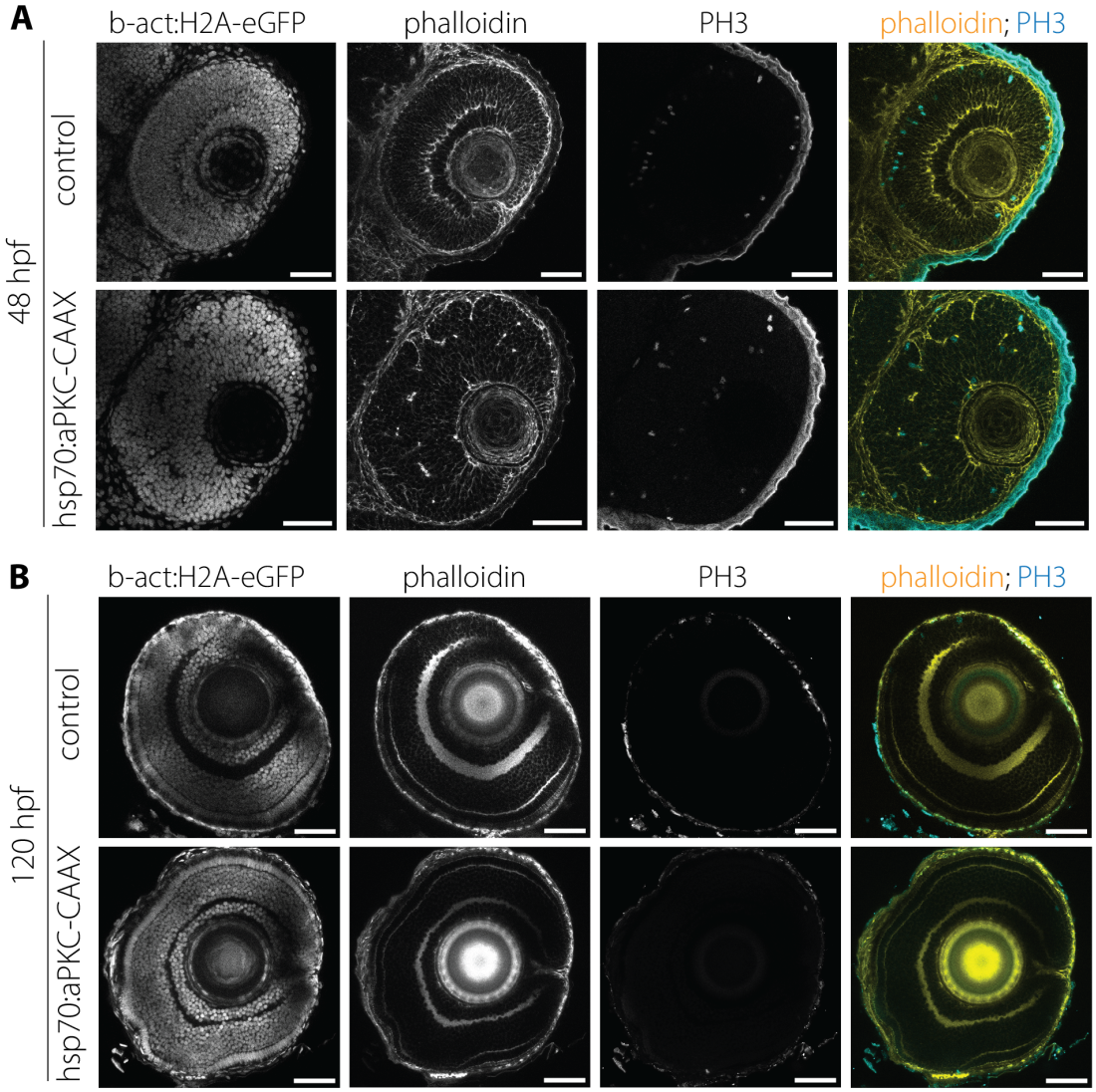

Figure 2.28: **Apical polarity of the retinal PSNE is necessary for tissue shape. A)** Representative images of control and tg(hsp70:aPKC-CAAX-mKate) embryos at 48 hpf, i.e. 24 hphs. Nuclei are marked with tg(atoh7:gap-GFP); cytoskeleton is marked with phalloidin, mitotic nuclei are stained with antibodies against PH3. **B)** Representative images of control and tg(hsp70:aPKC-CAAX-mKate) embryos at 120 hpf, i.e. 24 hphs. Nuclei are marked with tg(atoh7:gap-GFP); actin is marked with phalloidin, mitotic nuclei are stained with antibodies against PH3. Scale bar = 50 μm.

While embryos overexpressing the aPKC-CAAX construct were characterized by extensive disorganization of progenitor cells within the RNE, neurons appeared to have correctly delaminated by 120 hpf. All three nuclear layers were correctly formed in embryos overexpressing aPKC-CAAX, suggesting that neurons were eventually able to reach their final positions (Fig. 2.28 B). Despite this, the typical hemispherical shape of the neural retina appeared deformed and was characterized by folds of the tissue (aPKC-CAAX overexpressing, n = 6/6 embryos), indicating that disorganization of the RNE at earlier

stages might have affected the integrity of the tissue shape even if neurons managed to correctly delaminate. Overall, these findings suggest that, while pseudostratification is not necessary for neuronal lamination itself, but it appeared to be necessary to maintain the hemispherical shape of the retinal tissue over development.

2.5 Addendum: direct measurements of the mechanical properties of the developing zebrafish retina

The following chapters contain preliminary data that were collected over the course of this study but that, because of external limitations, could not be further developed to reach conclusive results. These findings concern various attempts to directly measure the mechanical properties of the retinal PSNE over retinal development, throughout the proliferative phase and neuronal lamination.

2.5.1 Direct measurement of endogenous forces in the retinal neuroepithelium

Our results revealed that, as development progressed, the packing density of nuclei in the retinal PSNE got closer to limiting packing values, which were calculated for disordered hard-sphere packings [47]. The proximity to these limiting packing values could result in a rigidity transition of the tissue and cause constraints in nuclear and cell movements. This change in tissue material properties can occur upon little variation of single cell features, such as cell shape or adhesion [11]. Therefore, we aimed to directly quantify the endogenous stresses that were formed within the tissue before, during and after neuronal lamination to monitor changes in the material state of the developing retinal PSNE.

To do this, we used biocompatible oil microdroplets that we could inject in the retinal neuroepithelium and whose deformations should provide a readout of the local stresses generated by surrounding cells or nuclei over time [35, 36]. To measure the forces generated by nuclear packing itself, the injected oil microdroplet needed to have a diameter no larger than twice the average nuclear diameter. Thus, we injected fluorescently labelled microdroplets of varying sizes within the desired range into the retinal neuroepithelium of zebrafish embryos around 28 hpf, 38 hpf and 48 hpf (Fig. 2.29 A). In this way, we expected to probe the endogenous forces that were generated in the retinal neuroepithelium at the proliferation peak, at the onset of lamination and once the lamination had already started, respectively. The microdroplets were composed of HFE-7300 oil mixed with rhodamine and treated embryos were imaged within 2 hours after injection, to allow recovery of the wound. Preliminary results showed that anisotropic stresses detected on the microdroplets' surfaces decreased over time and variations related to droplet size reduced at later stages, i.e. 50 hpf, compared to 30 hpf (Fig. 2.29 B). Surface deformations of droplets were minimal. This observation indicated that the surface tension of the oil microdroplets was higher than the stresses generated locally by the tissue. In this case,

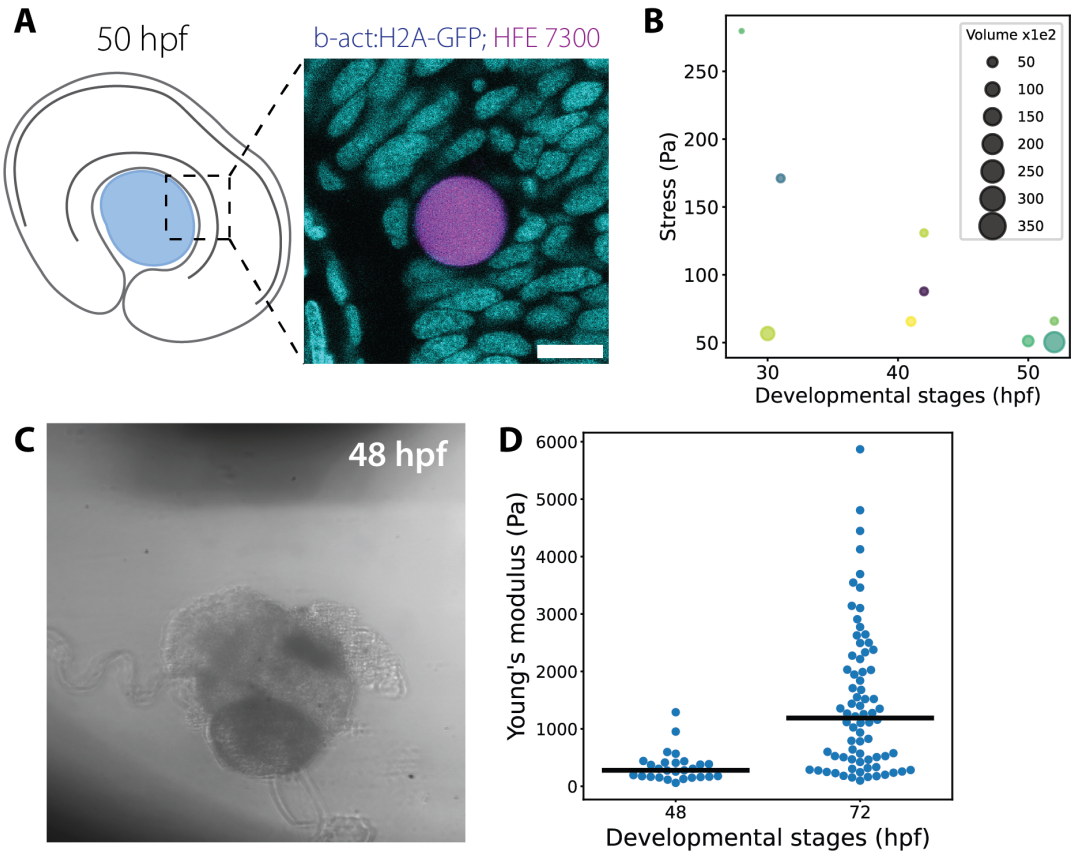

Figure 2.29: **Direct measurements of tissue material properties. A)** Scheme of oil microdroplets injection in the retina of living zebrafish embryos. Scale bar = 10 μm. **B)** Measurement of anisotropic stress applied to injected oil microdroplets at each stage. The size of the point relate to the actual size of the droplet in pixels. **C)** AFM measurement on sliced zebrafish retina. **D)** Spread of data for each stage, solid black lines show median (n = 26, N = 2, δ = 3.0 ± 1.09μm (48 hpf); n= 65, N = 4 , δ = 1.13 ± 0.63μm (72 hpf) where: n = number of AFM indentations; N = number of retinas; δ = indentation depth).

the measurements obtained in embryos injected at 28 hpf and 38 hpf likely could not capture the endogenous stresses generated within the retinal neuroepithelium. Instead, anisotropic stresses were detectable in embryos imaged at 50 hpf. Therefore, it will be possible to measure the anisotropic forces exerted by neuroepithelial cells at earlier stage only by decreasing the surface tension of the oil microdroplets.

2.5.2 Quantification of tissue stiffness using AFM

Both in the hdac1 morphants and dkk1-overexpressing embryos, we observed buckling of the retinal neuroepithelium (Fig. 2.25 D). In both these instances, the retinal pigmented epithelium remained as a squamous monolayer of epithelial cells surrounding the apical surface of the retinal PSNE. In particular, in the case of hdac1 morphants, RPE cells showed nuclei with an extremely elongated shape, suggesting stretching of this tissue above the regions where the retina was not buckling (Fig. 2.25 D). Conversely, RPE cell nuclei

showed a rounded and more relaxed morphology above the folded neuroepithelium (Fig. 2.25 D). Whether the RPE was passively stretched by the growing retina or was acting as an external shell was not clear. It has been shown that the RPE gets stiffer over time in eye organoids [53], suggesting that this tissue could actively change its cellular properties and indeed act as a rigid shell for the PSNE. To determine whether this was the case in zebrafish, we performed Atomic Force Microscopy measurements on eyes obtained from living embryos.

To do this, wild-type embryos were staged at 48 and 72 hpf and cut using a vibratome. Sliced retinas were then glued to a glass-bottom dish to measure their apparent elastic modulus (Fig. 2.29C). Because slicing through the retina and cutting through the RPE resulted in apparent disorganization of the retinal tissue, we limited our measurements to the surface of sliced retinas where the RPE layer was intact. In addition, each measurement had to be performed within one hour after the embryos were sacrificed, since the tissues showed signs of degradation over time, e.g. cells became stickier and the tissues softer. Our preliminary AFM measurements indicated that the surface of the zebrafish eye gradually became stiffer over time during neuronal lamination between 48 and 72 hpf (Fig. 2.29 D). These results suggested that the sliced retinas were characterized by increasing mechanical rigidity. This will need to be confirmed by further measurements of sliced retinas, including earlier stages, and compared with direct measurements of the retinal neuroepithelium without the RPE, where possible.

3

Discussion

In this thesis, we established a 3D image analysis pipeline to quantify changes in nuclear ordering in densely populated neuroepithelia of zebrafish embryos. So far, analysis of tissue arrangements in 3D has been hampered by technical limitation in segmentation. We made use of a recently developed deep learning method, i.e. StarDist-3D, to overcome this issue and provide a volumetric description of nuclear packing in developing neuroepithelia. This was the first time StarDist-3D was used for this purpose, to our knowledge. The resulting datasets allowed us to explore the arrangements of nuclei, and thereby cell bodies, within the zebrafish retinal neuroepithelium and hindbrain. In the retinal tissue, we were able to follow changes of these arrangements over the first days of development of the eye. In this way, we generated an understanding of progressive pseudostratification and how it influences the emergence of ordered tissue architecture in the retina and hindbrain. I found that pseudostratification allows to maintain a strong orientational order of nuclei over time. This long-range alignment is kept throughout the proliferative phase, with increasing nuclear packing densities, and appeared to be conserved also at later stages, when the retinal neuroepithelium has transitioned to a fully laminated structure. The particular ordering of cell bodies resulting from pseudostratification, i.e. orientational order and positional disorder, is a key hallmark detected also in another PSNE, the developing hindbrain, which present a loser packing regime. In the context of a fast-growing tissue like the zebrafish retinal neuroepithelium, we argue that pseudostratification allows for dense packing of cell bodies within a monolayered neuroepithelium. without altering retinal morphology. This hypothesis was supported by the observation that loss of the typical pseudostratified arrangement in the retinal PSNE resulted in altered shape of the laminated neural retina, even though neuronal lamination progressed correctly. In the retina, the transition to a layered tissue structure is driven by neuronal differentiation, which result in drastic nuclear shape changes depending on the neuronal fate of the cell. Our analysis showed that changes in nuclear shape morphologies resulted in different packing ordering in the three layers of the retina. Despite these morphological changes, orientational order of nuclei in the laminated retina was preserved over time. The transition to a layered tissue was accompanied with the emergence of positional order of cell bodies

and nuclear packing values were adjusted below theoretical limiting packing densities. When this transition was blocked or when the balance between the number of proliferating cells and timing of differentiation was disrupted, the retinal neuroepithelium eventually buckled.

3.1 Alignment of nuclei in PSNE is a hallmark of pseudostratification

Our analysis of nuclear packing in the retinal PSNE revealed that pseudostratification establishes a strong orientational order of nuclei, and thereby cell's bodies, within a proliferating neuroepithelium accompanied by increasing packing densities. We found that this long-range orientation was maintained not only during the proliferative phase, but also at later stages when the retina was re-organized into a layered structure. The fact that we could still observe nuclei being aligned along the apicobasal axis during neuronal layering, when retinal neurons are not attached to both sides of the tissue as in the PSNE, suggests that this orientational order is a relevant feature of the retinal neuroepithelium also in the mature retina. This long-range orientation might be involved in the formation of the ordered retinal tissue architecture. The alignment of the nematic axis of nuclei along the apicobasal axis of the tissue could be detected across the three nuclear layers in spite of the completely different shapes that nuclei featured upon neuronal differentiation and upon completion of neuronal lamination. In addition to showcasing orientational ordering, nuclei of retinal neuronal precursors were progressively arranged in a positionally ordered fashion during neuronal lamination. Thus, we observed that nuclear arrangements in the retinal PSNE move from a disordered to an ordered positional configuration that is reminiscent of a more crystalline-like structure.

Our systematic 3D analysis of nuclear ordering in the retinal PSNE confirmed some findings published recently in a study focusing on nuclear jamming transitions in development [100]. Building on a previously published active foam description of multicellular tissues, the authors established a theoretical model to investigate the contribution of nuclei to the material properties of a simulated 2D confluent tissue. Using this model, they found that cells are progressively more constrained and ordered as a consequence of nuclear interactions when the nuclear volume fraction approximates a $\phi = 0.64$ [100]. The authors further compared these simulations to nuclear packing in the developing zebrafish retina during neuronal lamination and showed that nuclei become jammed in the INL between 55 and 72 hpf [100]. The analysis of the zebrafish retina was performed only in 2D optical slices and does not capture the 3D nature of the zebrafish RNE and the actual nuclear shape and size changes in this tissue. Despite these limitations, these findings are consistent with our results, showing a peak in nuclear volume fraction in the INL around 60 hpf. In addition, both the mentioned study and this thesis report the formation of a more crystalline packing structure over maturation of the zebrafish retina

following increase in nuclear volume fractions [100]. Overall, these results indicate that high nuclear volume fraction can drive the ordering of tissue architectures, together with changes in nuclear shape anisotropy, thereby supporting our claims.

3.1.1 Pseudostratification affects retinal morphogenesis

The typical hemispherical shape of the retina is established early on during retinogenesis and is maintained over development thanks to the progressive elongation of retinal progenitors in the proliferating RNE [130]. The anisotropic shape of nuclei and their long-range alignment is related to the elongated shape of multipotent progenitors contacting both sides of the retinal PSNE. When retinal progenitor cells cannot perform mitosis at the apical side, daughter cells fail to reintegrate in the retinal PSNE and keep dividing at subapical positions, thus impeding correct neuronal lamination [199]. This is due to the fact that if progenitor cells cannot divide apically, one of the daughter cells fails to grow its processes to reach the apical side of the tissue and, as a consequence, this cell cannot correctly reintegrate into the epithelial tissue [199]. It was shown that delaminated cells continue to divide ectopically and assume a rounder morphology while creating cell clusters in the tissue, therefore perturbing the tissue architecture of the proliferating RNE [199]. Interestingly, we observed that the temporary expression of aPKC-CAAX in multipotent progenitors results in partial loss of the typical pseudostratified arrangement in the RNE and this in turn leads to altered morphology of the mature neural retina. In these samples, the hemispherical retina presents several curves at the apical surface of the tissue that could potentially impair its visual functions. Our findings suggest that pseudostratification plays a role in ensuring that the correct morphology of the retina is maintained throughout development. Deformations of the retinal tissue could be a result of altered mechanical properties of the tissue as a consequence of the loss of the nematic-like order that characterizes the pseudostratified arrangments. Further experiments should be performed to assess whether nuclear packing densities are changed in neuroepithelia of embryos expressing the aPKC-CAAX construct to confirm this hypothesis.

Perturbing the architecture of the retinal PSNE could also have implications for the cellular events that govern neurogenesis, besides affecting tissue morphology. In this case, if keeping an elongated cell shape spanning the apicobasal axis of the tissue was necessary for retinal progenitors to receive the correct signals to differentiate, then we would have expected to observe major lamination defects in embryos expressing the membrane-targeted aPKC-CAAK construct. While previous studies showed that expression of the aPKC-CAAX construct around the time RGC precursors emerge results in severe defects in neuronal lamination [86], we did not observe a comparable phenotype when the same construct was expressed in multipotent progenitors at an earlier stage. Our results demonstrated that neuronal precursors were able to correctly migrate to their final positions and form all three nuclear layers that compose a mature neural retina, despite initial disorganization of Atoh7-positive neuronal precursors. How neuronal precursors

managed to navigate through a disordered retinal PSNE is not clear. In future studies, it will be interesting to further perturb the morphology and positioning of multipotent progenitor cells in the RNE to observe how this impacts on signaling pathways involved in cell fate specification and migration through the tissue. For example, previous work from our lab showed that Notch signaling relies on the asymmetric inheritance of Sara-positive endosomes between daughter cells and on the direct contact inhibition between touching neighbors [148]. How this is impacted in disorganized embryos upon overexpression of the aPKC-CAAX construct could shed a light on the robustness of tissue patterning in the retinal PSNE. Furthermore, , it will be interesting to investigate how the elongated morphology of retinal progenitors can affect intercellular communication and intracellular polarity to clarify how tissue architecture could influence neurogenesis in the retina.

3.1.2 Positional and orientational order of nuclei in the retina and its implications for tissue transparency

It is possible that long range alignment of nuclei during the formation of neuronal layers in the vertebrate retina also serves the purpose to facilitate light penetration through the retina. We observe that the alignment of primary nematics of nuclei in the laminated retina coincides with the orientation along the physiological direction of light propagation. In vertebrates, the light that is focused by the lens on the retinal tissue has to pass through the retina itself before reaching the photoreceptors, which are located in the outermost layer. Because photons need to pass through the whole thickness of the retina to reach ONL, where photoreceptors are, correct and precise vision is ensured by minimal light scattering. Cells are known to be phase objects, meaning that they can change the phase of the light wave because they have different refractive indexes than their surrounding medium and even through the cell itself, due to their composition in lipid membranes and aqueous cytosol. Considering this, it was proposed that light scattering through the retina is reduced in two ways: 1) via the light -guiding capabilities of the Muller Glia ; and 2) via the ordered arrangement of photoreceptor nuclei in radial columns [169, 62]. In addition, it has been shown that position of heterochromatin within the nucleus of rod photoreceptors of nocturnal mammals is actively regulated to reduce light scattering [192, 107, 200]. While we cannot directly demonstrate that the crystalline-like arrangement of nuclei in the INL and RGL is reducing light scattering, the aforementioned studies show that the axon bundles and both plexiform layers are the main scattering elements within the inner retina. Altogether, these data argue that the ordered arrangement of nuclei along the direction of light propagation has the potential to improve the transparency of the retinal tissues, while ensuring high packing densities of neurons in the vertebrate retina.

3.1.3 Pseudostratification and nuclear order in different neuroepithelia

To better understand the conservation of nuclear packing dynamics in other neuroepithelia, we extended our 3D image analysis to the developing zebrafish hindbrain. In this context,

we observed that nuclei are arranged in a looser packing regime early during development and nuclear packing increases only upon onset of neuronal lamination. Moreover, we found that orientational order and positional disorder are hallmarks of both retinal and hindbrain PSNE and are conserved at looser packing regimes, as well. For both retinal and hindbrain neuroepithelia, the first phase in organogenesis involves the formation of their final organ shape, tubular in the case of the hindbrain and hemispherical for the retina. The following phases of growth and patterning are differently regulated in these two neuroepithelia and this is reflected by their different nuclear packing dynamics. Differently from the retina, the hindbrain first undergoes a process of segmentation that divides the tissue into rhombhomeres, which become lineage-restricted cellular compartments over time. In zebrafish embryos, neurogenic gene expression is widespread but lower at these rhombomeric boundaries until 26 hpf. Here, progenitor cells retain a neuronal stem cell identity for longer and the rate of cell proliferation is higher than in non-boundary cells. During this first phase of proliferation and cell specification, nuclear packing in the hindbrain does not change and it increases solely upon formation of the mantle by 30 hpf. In contrast, the retinal PSNE is not compartmentalized prior to differentiation. It is actually the process of cell specification itself that causes neuronal progenitors to commit to given neuronal fates and migrate through the tissue accordingly to form the neuronal layers. As soon as the typical curved shape of the retina is established around 20 hpf, the retinal RNE undergoes an intense proliferative phase which allows the isotropic growth of the tissue, while only a subset of multipotent progenitors progressively commits to a neurogenic identity around the peak of proliferation at 36 hpf. During this time window, nuclear packing continues increasing, reaching theoretical limiting volume fractions for frictionless spheres first and then for fully aspherical ellipsoids. Therefore, the proliferation and neurogenesis dynamics of these two neuroepithelia lead to two different nuclear packing regimes during the early phases of their morphogenesis. At early stages of the proliferative phase, nuclei are ordered following the same rules in both pseudostratified neuroepithelia regardless of the tissue packing. Later during neuronal lamination, more cells are generated and packed in the tissue and this progressively leads to more ordered and packed tissue architectures. Interestingly, our findings support recent 2D analysis and theoretical simulations showing that nuclear packing dynamics similar to the nuclear jamming transition reported in the developing retina occur in other brain tissues over development [100]. We propose that, while pseudostratification has the potential to pack high number of cells within a monolayered epithelium, the key hallmark of this tissue arrangement is the orientational order it imposes to elongated epithelial cells to establish a nematic-like order during early phases of tissue development that help to achieve correct morphogenesis.

3.2 Neurogenesis accompanies nuclear shape and size remodeling

Differentiation of multipotent retinal progenitors occurs progressively over time in a wave-like fashion from the nasal-ventral to the temporal-distal side of the retina. The first neuronal cell types being born are RGC and PR, which are the neuronal cell types that populate the most external nuclear layers of the laminated retina. Analysis of neighbors statistics showed that the emergence of the ONL and RGL at the onset of neuronal lamination, between 42 and 48 hpf, reduces the average contact number at the boundaries of the neuroepithelium, while the central part of the retinal tissue reaches higher packing values. When the switch from proliferation to differentiation is impaired, like in the case of Hdac1 morphants, multipotent progenitors cannot commit to a neurogenic fate and do not undergo delamination and neuronal migration [130]. As a consequence, multipotent progenitors fail to remodel their nuclear and cellular shape [130]. Theoretical studies proposed that in the case of proliferation under confinement, epithelial cells can relieve the stress by increasing their cell height until they reach a compression instability, after which the tissue deforms and buckles [76]. Neuroepithelial cells in Hdac1 morphants are characterized by extremely elongated nuclei, and thereby cells, prior to folding of the neuroepithelium and their nuclear morphology and size changes completely upon deformation of the retina. We postulate that the dramatic elongation of nuclei in this knock-down condition is due to the compressive stresses generated by the proliferating cells themselves that cannot be relieved by changes in nuclear volume or shape. As proliferation progresses and the retinal neuroepithelium retains a PSE-like architecture in Hdac1 morphants, the retinal neuroepithelium ultimately deforms and buckles as expected. This occurs only after 48 hpf, when the tissue should have already started transitioning to a multi-layered architecture to allow for tissue growth. In fact, despite the continued proliferation of retinal progenitor cells, the eye of Hdac1 morphants is smaller than embryos injected with control morpholino. Nuclear packing densities in Hdac1 morphants did not exceed the value 0.635, which is instead the case for normally developing retinas, both before and after buckling. An interpretation of these findings could be that the timing of neuronal lamination occurs when the retinal PSNE is approximating its maximum capacity. The timing of neuronal lamination could ensure the depletion of the progenitor pool and the formation of the right number of neurons while avoiding any deformation of the developing retina.

Neurogenesis does not only concur with nuclear shape remodeling, but it also coincides with nuclear size reduction. Nuclei of neuroepithelial cells in the Hdac1 morphants could not compact prior to buckling and, once the tissue folded, their volume was only partially reduced. In contrast, in the control scenario we observed a constant decrease of nuclear volume in parallel with the progression of neurogenesis. Because we could only block neuronal differentiation by downregulating Hdac1 activity, it is possible that the failed remodeling of nuclear size is a direct effect of a perturbed status of the chromatin. In

general, histone deacetylases have been shown to lead to compaction of nucleosomes and to a closed chromatin structure upon removal of acetyl groups from histones, thus leading to epigenetic regulation of target genes [136, 173, 126]. While we cannot exclude that knock-down of Hdac1 has an effect on the overall chromatin compaction in retinoblasts and that this could be a reason why we observed a deregulated nuclear size in Hdac1 morphants compared to controls, regulation of chromatin structure is tightly linked to cell fate specification and both processes feedback on each other. Therefore, we argue that by regulating the conversion of multipotent progenitors from a proliferative state to a neurogenic fate, Hdac1 could act as the main regulator of nuclear size and shape. This is particularly important to define the arrangement of nuclei, and thereby cell bodies, in densely packed neuroepithelia. Interestingly, it was reported that histone deacetylases could be involved in nuclear mechanosensing in human mesenchymal stem cells [99]. Future studies should try to further assess how Hdac1 is activated in retinoblasts and whether this histone deacetylase too can respond to mechanical stimuli. For instance, it would be interesting to determine whether compression of cells caused by the local packing density in the retinal PSNE could have an effect on the chromatin state of multipotent progenitors during retinal development.

3.2.1 Disrupting the balance that regulates the number of cells in the developing RNE leads to tissue buckling

The zebrafish retina is a fast-developing tissue, hence we expected tight regulation of proliferation and neurogenesis in the development of this neuroepithelium. To explore how this orchestration is regulated, we perturbed the balance between number of proliferating progenitor cells and cells entering neurogenesis. We achieved this in two ways: 1) via overexpression of DKK1 at the shield stage to increase the number of progenitor cells committed to produce the optic field; 2) via downregulation of Hdac1 to block neurogenesis and sustain proliferation of retinoblasts. In both cases, we observed deformations of the retinal neuroepithelium. Both perturbations pointed to the deregulation of proliferation of progenitor cells as the main cause of buckling of the retinal PSNE, though the temporal dynamics differed between them. We showed that increasing the number of proliferating progenitor cells at early stages of retinal development led to compression instability of the tissue and buckling. This was performed by overexpressing Dkk1 before gastrulation, which subsequently inhibited wnt signaling before the midblastula transition (MBT) and expanded the forebrain and optic field [187]. In Dkk1-overexpressing embryos, where neurogenesis is not impaired and neuroepithelial cells can remodel their cell and nuclear shapes, the folding of the retinal neuroepithelium occurs during the proliferative phase. Because the retinal PSNE is bigger as it is composed by a higher number of retinal progenitor cells, the buckling phenotype indicates that compressive stresses are generated within the retinal neuroepithelium of dkk1-overexpressing embryos, probably due to the

sustained proliferation of more retinoblasts and to the formation of an external confinement to tissue growth. In the other case scenario, the downregulation of Hdac1, which directly antagonizes canonical wnt signaling and represses the transcription of neurogenic inhibitors, resulted in sustained proliferation and block of neurogenesis [224] Buckling was observed in Hdac1 morphants only after 48 hpf, when neuronal precursors in the retinal neuroepithelium are normally undergoing neuronal lamination. Interestingly, similar folding of the retinal neuroepithelium has been reported also in other conditions where regulation of proliferation was disrupted. For instance, in the case of overexpression of the transcription factor Optx2 in the Xenopus eye, leading to enlarged folded retinas like in dkk1-overexpressing embryos [229].

Accumulation of more progenitor cells within the retinal PSNE of dkk1-overexpressing embryos resulted in increased tissue height, but did not affect nuclear packing densities. Indeed, volume fractions of nuclei in dkk1-overexpressing embryos matched the values measured in control retinas. This, together with the fact that nuclear size does not differ between treated and control embryos, indicates that nuclear arrangement is preserved during the proliferative phase, given that the retinal PSNE is not constricted and can expand along the apicobasal tissue axis. In few cases, the retinal neuroepithelium of dkk1-overexpressing embryos started bending after formation of the optic cup, suggesting that the eye reaches a size limit earlier than in control embryos and that the compressive stresses arising from proliferation are possibly influenced by the confinement of external tissues. In line with this assumption, several theoretical and experimental studies proposed that proliferation of epithelia under confinement induces bending instability in the tissue without the requirement of active bending mechanisms [76, 50, 208]. This has been shown to be the case in several epithelia in *in vivo* developmental contexts, both due to confinement mediated by other tissues or by the ECM [215]. Because overexpression of DKK1 resulted in expansion of the anterior head, we argue that buckling of the retinal PSNE could be due to alteration of the coordinated growth of the retinal PSNE and the tissues surrounding it, such as the RPE, the telencephalon and the periocular mesenchyme. The maturation of these tissues could provide a permissive environment to the formation of an enlarged retina at earlier stages of eye development and impose a confinement to the growth of the retinal neuroepithelium at later stages, e.g. during the proliferative phase. We hypothesize that the RPE layer and the periocular mesenchyme provide a stiffer environment at later stages of eye development in control embryos. In Hdac1 morphants, the first buckling events happen between 42 and 48 hpf, when the retinal tissue laminates in control embryos. During this time, the RPE normally flattens to cover the apical surface of the retinal neuroepithelium. RPE cells, which form a thin monolayer covering the whole apical side of the retina, do not buckle with the retinal neuroepithelium. We observed relaxed nuclear shapes of RPE cells above the sites of apical buckling, as if the RPE cells at this position were relaxed. Conversely, we observed extremely elongated nuclear shapes for RPE cells located in other parts of buckled retinas in Hdac1 morphants, suggesting that these cells are stretched over the apical surface of the retinal neuroepithelium. Hence, we

argued that the RPE layer and the RNE should have distinct material properties that result in different tissue-level deformation. According to this hypothesis, the RPE encapsulates the retinal neuroepithelium over development and might act as an external shell that confines retinal growth. Our preliminary AFM data supports this hypothesis as it confirms previous studies that proved that the RPE monolayer becomes stiffer than the retinal PSNE in retinal mouse organoids [53]. Similar buckling of growing epithelia under confinement were experimentally and theoretically described in the PSE of the developing *Drosophila* wing, during cortical gyration and in the gut, where surrounding tissues act as an external confinement of proliferating tissues, therefore producing folds without active bending mechanisms [206, 201, 177]. How growth and tissue maturation of the RNE and the developing RPE are coordinated during embryonic morphogenesis to maintain eye shape is still not clear. Previous work has focused on the coordination of post-embryonic growth between the neural retina and the RPE in medaka, since the eyes of teleost fish continue growing throughtout their lives and the near-perfect hemispherical shape of the medaka eye needs to be maintained to ensure precise vision [209]. In this study, experiments and simulations indicate that the proliferating stem cells in the CMZ of the neural retina drive the growth rate of the RPE, therefore implying the existence of a feedback between the two tissues [209]. Whether this feedback could be activated by a mechanical stimulus, like local cell density as implemented in the simulation, or a biochemical stimulus is not known. Future quantitative studies will need to investigate the relationship between retinal growth and the maturation of the surrounding environment, such as the development of the RPE and the periocular mesenchyme, to understand whether these tissues could play a role in regulating the size of the retina during embryonic morphogenesis.

3.2.2 Timing of neurogenesis, tissue growth and packing

A long-standing open question in development revolves around whether or not cells can sense local tissue density and act accordingly to proliferate or exit the cell cycle. One way to control this switch in stem cell population occurs via cell fate specification. Several studies have pointed out the robustness of zebrafish eye development, which manage to grow to a given volume proportional to the body size in spite of genetic and mechanical insults that perturbed the size of the optic field at early stages of development [226]. These compensatory mechanisms occur during the proliferative phase and the onset of neuronal lamination, i.e. the time window that is the object of our study. This suggests that the switch from proliferation to neurogenesis could be the key regulatory moment to adjust the overall size of the eye. Because we hypothesized that local differences in pressure caused by nuclear packing could be a mechanism for retinal progenitors to sense the tissue crowding, we set out to test this hypothesis by modifying the number of multipotent progenitors in the retinal PSNE. To do this, we made use of both of a transgenic zebrafish line, the hsp70:DKK1-GFP, and of a manipulation experiment, where we removed cells from the optic cup prior to Atoh7 expression in the retinal PSNE. In previous studies,

premature neurogenesis onset was observed in experimentally enlarged retinas of dkk1-overexpressing embryos and delayed neurogenesis was reported in embryos where retinal progenitor cells were removed from the optic vesicle [226]. Because no possible mechanism for this change in neurogenesis timing was described, we decided to check whether differences in local tissue density could correlate with premature and delayed onset of neurogenesis.

Volume fractions of nuclei in the central part of the RNE do not change between dkk1-overexpressing and control embryos, hinting that there is no correlation between nuclear packing densities and onset of neurogenesis. Thus, premature neuronal specification in dkk1-overexpressing embryos is likely caused by the deregulation of Wnt signaling, which is known to be involved in proliferation and gene expression of transcription factors in multipotent progenitors in the dorsal/central part of the RNE [63]. Overexpression of the hsp:DKK1 construct has been shown to cause deregulation of genes that are normally involved in maintenance of dorsal identity in the zebrafish RNE via canonical Wnt signaling, such as tbx5, bmp4, bmp2b and gf6a [212]. This, together with the fact that pax6 is normally expressed at 48 hpf despite loss of Wnt signaling [212], suggests that the retinal PSE is ventralized in dkk1-overexpressing embryos. Thus, we hypothesize that more multipotent progenitors at the ventro-nasal portion of the RNE might be capable to respond to the morphogens released by the optic stalk upon overexpression of Dkk1. The altered gene expression of transcription factors specifying retinal dorsal identity, together with an expanded contact surface between RNE and the optic stalk, might explain the earlier expression of Atoh7 in the RNE of dkk1-overexpressing embryos. Further studies will be necessary to explore this idea and define how neurogenesis is timely regulated in the retinal neuroepithelium.

While onset of neurogenesis does not seem to be directly affected by nuclear packing, the retinal PSNE in dkk1-overexpressing embryos undergo dramatic tissue deformations during the proliferative phase. In contrast, wild-type and control embryos never show buckling of the retinal neuroepithelium, despite having the same levels of nuclear packing densities measured in enlarged retinas of dkk1-overexpressing embryos. We reasoned that this buckling phenotype could be due to the compressive stresses generated by the higher number of proliferating progenitor cells. This could be due to a jamming transition dominated by the cellular component. In addition to this, altered timing of maturation of the surrounding tissues and premature growth of the enlarged retinae could explain the buckling phenotype. In this condition, retinal progenitor cells seem to proliferate at the same rate as in control retinas, but the differences in the initial number of progenitor cells results in differences in the overall tissue size. This could result in premature constrains imposed by the RPE and the periocular mesenchyme and explain the bending of the tissue. Since neurogenesis seem to be the main factor that controls the size of the retina, we followed the expression of the neurogenic marker Atoh7 in dkk1-overexpressing embryos. All enlarged retinae show premature neurogenesis in the RNE. Though, earlier onset of neuronal specification is not sufficient to prevent the retinal PSNE from bending and, as a

result, folded neural retinas are formed. While it has been shown that growth dynamics of experimentally enlarged retinas slow down between 36 and 48 hpf and eventually reach sizes comparable to wildtype retinas [226], our results indicate that the regulation of the rate of proliferation and differentiation of the retinal PSNE in hsp70:DKK1-expressing embryos is not rapidly adjusted to correct the buckling phenotype. In this case, eyes of the correct size might be produced, but with evident deformations that will impair vision.

Increasing the number of multipotent progenitor cells lead to dramatic deformations of the retinal neuroepithelium that are not corrected over the course of retinal development. Interestingly, several studies have shown that developing organs can recover their size upon cell loss during development, like in the case of the developing chick neural tube that can regenerate upon excision of parts of the neuroepithelium [74]. Thus, we set out to remove multipotent progenitors from the optic vesicle and monitor the expression of the neurogenic marker Atoh7 hours later to determine if this correlated with lower numbers of progenitor cells. We managed to deplete enough cells to observe an effect only in some cases. In these instances, Atoh7+ progenitor cells appear to be absent in regions from where cells were removed. This result suggests that retinal progenitors in these regions are not responsive to differentiation cues. We speculate that this could be due to the need to replenish the parts of the retinal neuroepithelium from where cells were removed. However, it is not clear what controls the proliferative state of these cells. Upon removal of multipotent progenitors from the optic vesicle, compensatory proliferation might be activated by apoptosis-induced pathways (AiP) as described in several wound healing processes in the fruit fly and mouse [61]. The fact that similar compensatory proliferation has been described in zebrafish embryos with reduced optic field due to genetic perturbations, where apoptosis was not induced, suggests that compensatory proliferation in the zebrafish developing eye is not necessarily dependent on AiP [226]. Other *in vitro* and *in vivo* studies have shown that epithelial cells can control their cell cycle progression and proliferative state depending on mechanical stimuli, such as stretching or compression of their substrate and cell density [197, 179]. Overall, these studies point to the existence of regulatory mechanisms to control proliferation and cell cycle exit depending on mechanical cues and independently from AiP. Whether any of these mechanisms is conserved in the developing zebrafish retina should be addressed in future studies.

3.3 Final remarks

This study showcased how nuclei, and thereby cell bodies, are arranged within the retinal neuroepithelium throughout development and provided valuable insights into the effects of increasing nuclear packing densities for morphogenesis. This was achieved after generating the first 3D instance segmentation of nuclei in a developing PSNE over time, using machine learning methods that have made possible the accurate detection of nuclei within crowded tissues, like the vertebrate retina. The systematic analysis of nuclear packing showed that packing densities increased to theoretical limiting values in the

retinal PSNE during the proliferative phase, unlike the hindbrain PSNE, where nuclear concentration increased only upon neuronal lamination. Nevertheless, both neuroepithelia were found to present a nematic-like order, where nuclei are orientationally ordered and positionally disordered, suggesting that this is a hallmark of pseudostratification. This order was then shown to progressively transition to a more crystalline-like structure during maturation of the laminated retina, while nuclei still retained a long-range orientation along the radial axis of the tissue and the retina preserved its almost-perfect hemispherical shape. Results reported in this thesis indicated that the physical properties of the retinal PSNE were affected by perturbations in the number of cells and in nuclear packing densities during retinal development, leading to buckling of the tissue. Furthermore, findings from this study highlighted the role of neurogenesis in remodeling nuclear shape over time as a key player in the regulation of growth and shape of the developing retina.

These insights were only possible by performing 3D nuclear segmentation over the entire proliferative and neurogenic phases of retinal development. This, together with genetic and mechanical perturbations and the use of transgenic reporter lines, allowed to shed light on the emergent physical state and architecture of the developing zebrafish retina. By combining these approaches, this study provided a quantitative characterization and analysis of nuclear packing in proliferative PSE that has the potential to guide the design of future experiments and to facilitate the establishment of similar experimental frameworks to study epithelial structures in other developmental contexts in zebrafish and other organisms.

Future experiments should aim at further dissecting the cross-talk between neurogenesis and tissue packing to determine whether cells can sense compression in densely packed tissues and react by regulating timing of cell fate determination. Further biophysical models of nuclear and cell packing could shed a light on the distribution of forces and stresses within proliferating and crowded PSE. This could possibly shed light on the molecular requirements for cells to move and position within densely populated tissues and could help understand how tissue structures and shapes are formed and maintained throughout development. Moreover, it will be interesting to compare the development of the RNE to surrounding tissues, such as the RPE, and test how these tissues interact to ensure coordination of growth and shape of the vertebrate eye.

4

Materials and Methods

4.1 Zebrafish methods

The experimental work reported in this thesis was performed on zebrafish embryos aged between 24 hours post fertilization (hpf) to 80 hpf. Wild-type zebrafish were bred and maintained at 26°C. Embryos used for experimental work were raised at 21°C, 28.5°C, or 32°C in E3 medium supplemented with 0.2 mM 1-phenyl-2-thiourea (Sigma-Aldrich) from 8 hpf to prevent pigmentation. Animals were staged according to C. B. Kimmel et al, 1995 [103]. All animal work was performed in accordance with European Union directive 2010/63/EU, as well as in accordance with the Portuguese legislation (Decreto-Lei nº 113/2013).

4.1.1 Transgenic lines

To visualize all nuclei in the retina, the Tg(β-act:H2A-GFP) and the Tg(hsp70:H2B-RFP) line were used [65, 52] and imaging was started around 3-4 hours after heat shock as described in Table 4.1. Tg(atoh7:gap-GFP) and Tg(atoh7:gap-RFP) [129, 228] zebrafish transgenic lines were used to identify Atoh7+ progenitors and Atoh7+ neurons. The Tg(ptf1a:eGFP) line was used to identify amacrine and horizontal neurons in the Inner Nuclear Layer [92, 4]. To overexpress DKK1 early in embryogenesis and enlarge the forebrain and optic field, the Tg(hsp70:dkk1-GFP) line was used [196] and heat-shock was performed as described in Table 4.1. The Tg(lama1:lama1-sfGFP) was used to visualize the outline of the optic cup [191].

4.1.2 Heat shock of embryos

Transgenic embryos were immersed in a warm water bath to induce transcription of the construct of interest, expressed under the heat-shock promoter hsp70. Table 4.1 provides the details on the heat shock protocol performed for each construct and/or transgenic line used. In the case of Tg(hsp70::H2B-RFP), embryos older than 36 hpf were heat shocked twice to enhance the signal: one time the day before and a second time as stated in table 4.1.

Transgenic line	Temperature	Time	Developmental stage
Tg(hsp70:H2B-RFP)	37°C	20 min	At least 4 hours before
Tg(hsp70:DKK1-eGFP)	37°C	20-30 min	At 6 hpf
Tg(hsp70:aPKC-CAAX-mKate)	37°C	30 min	At 24 hpf

Table 4.1: Heat-shock protocols

4.1.3 Morpholino experiments

All morpholinos were purchased by Gene Tools, LLC. The hdac1 morpholino was used to knock down the Hdac1 transcript in all cells, together with the p53 morpholino, which was added to the injection mix to alleviate the cell death resulting from the procedure itself and the knock-down.

Morpholino	Concentration	Sequence
p53	0.75 ng/embryo	5′ - GCGCCATTGCTTTGCAAGAATTG - 3′
hdac1	0.5 ng/embryo	5′ - TTGTTCCTTGAGAACTCAGCGCCAT - 3′

Table 4.2: Morpholinos used in this study

4.1.4 Drug treatments

The inhibitor SU5402 (Merck, Cat 572630), that targets FGF receptor 1, was dissolved in DMSO. and was used at the final concentration of 16 μM and 8 μM. Equal volumes of DMSO were used for controls. Up to 20 embryos were dechorionated and placed in a well of a 6-well plate in E3 medium supplemented with PTU and the appropriate treatment (drug or DMSO). Embryos were then incubated in the dark at 28 degrees for the duration of the experiment. Treatment time windows are specified in the figure and in the figure legend.

4.1.5 Whole-mount immunofluorescence

All immunostainings were performed on whole-mount embryos fixed overnight in 4% paraformaldehyde (Sigma-Aldrich) in PBS at 4ºC as previously described (Icha et al. 2016a; Nerli et al. 2023). Embryos were washed 3 to 5 times for 10 min in PBS-Tr (Triton X-100 in PBS) 0.8% and permeabilized in 0.25% Trypsin-EDTA on ice for different time depending on the developmental stage: 10 min for 28 hpf and 36 hpf, 12 min for 42 hpf, 15 min for 48 hpf and 17 min for 72 hpf. For embryos younger than 28 hpf, the permeabilization was performed using cold acetone: embryos were washed twice in water, incubated in acetone for 10 minutes at -20ºC, washed again twice in water. Embryos were then washed for 30 min on ice in PBS-Tr 0.8% on shaker and then incubated in blocking solution (10% goat serum or bovine serum in PBS-Tr 0.8%) for 3 hours at room temperature. Embryos

were then incubated with the primary antibodies (listed in table 4.3)for a period ranging between 24 and 72 hours at 4ºC on shaker. Embryos were washed 4 to 5 times for 30 min with PBS-Tr 0.8% and then incubated for 24-48 hours with fluorescently labelled secondary antibodies (Invitrogen and Molecular Probes).
To label all nuclei, DAPI (Thermo Fisher Scientific; 62251) or DRAQ5 (Thermo Fisher Scientific; 62251) were used and added to the II antibody solution at a concentration of 1:1000 and 1:2000, respectively. In the case of the Tg(hsp70::H2B-RFP) transgenic line, embryos were incubated in antibody solution with RFP booster to enhance the fluorescence signal of the expressed RFP. Phalloidin conjugated with Alexa Fluorophores (AF) was used to label F-Actin in all cells. Finally, embryos were washed several times with PBS-Tr 0.8% in ice on shaker and stored in PBS at 4ºC until imaging.

Antibody	**Concentration**	**Vendor**	**Catalog number**
GFP	1:100	Proteintech	50430-2-AP
Histone H3 (phospho S28)	1:500	Abcam	ab10543
RFP booster	1:200	ChromoTek,	rba594
Phalloidin AF 405	1:100	Biotium	00034-T
Phalloidin AF 488	1:50	Life Technologies	A12379
Phalloidin AF 647	1:50	Cell Signalling	8940

Table 4.3: Antibodies and dyes used in this study.

4.1.6 Cell removal experiment

Zebrafish embryos were manually dechorionated and staged around 16 and 18 hpf. Selected embryos were anesthetized by supplementing E3 medium with 0.04% tricaine methanesulfonate (MS-222, 1004671, Pharmaq) and placed in 2% agarose wells previously molded with a custom-made mold. Embryos were laid on their side and covered with 0.6% agarose in E3 containing MS-222. The surface of the agarose containing the embryos was then covered with E3 containing MS-222 and Penicillin/Streptomycin. Borosilicate Glass Capillaries (OD: 1.0 mm, ID: 0.75. 0.75mm 10cm length, (Sutter Instrument, B100-75-10) were pulled using a pipette puller Narishige PC-10 with the following settings: 1-step, 65% power. To produce a spike at the tip of the capillaries, a pipette beveler Sutter Instruments BV-10 was used with the following settings: Beveling disk: Very Fine 104E, angle: 15º. Glass capillaries were then mounted on an oil driven manual injection system (Eppendorf, model CellTram Oil) using mineral oil (Sigma -Aldrich, M5310). The injection system was controlled using a motorized three-axis manipulator (Sutter Instruments, model no. MP-285) controlled by a manipulator control unit (Sutter Instruments, model MPC-200 and ROE-200) and mounted on a motorized inverted light microscope Nikon Eclipse TI-E. Upon piercing of the external ectoderm, cells were removed from the retinal neuroepithelium in varying numbers. The flux was then inverted to clean the capillary and continue

the process of cell removal on another embryos. The whole process was visualized using a 10X objective.

4.1.7 Oil microdroplet experiment

4.1.7.1 Oil injection

Zebrafish embryos were manually dechorionated and staged around 28, 36 and 48 hpf. Selected embryos were anesthetized by supplementing E3 medium with 0.04% tricaine methanesulfonate (MS-222, 1004671, Pharmaq) and placed in 2% agarose wells previously molded with a custom-made mold. The surface of the agarose and the embryos were then covered with E3 containing MS-222. The oil Novec HFE 7300 and the surfactant 2% Krytox-PEG600 were mixed with rhodamine at a final concentration of 0.25 mM. The oil mix was then injected into the retinal neuroepithelium using a PicoPump (World Precision Instruments) and Borosilicate Glass Capillaries (OD: 1.0 mm, ID: 0.75. 0, 10cm length, (Sutter Instrument, B100-75-10) with filament. To produce a spike at the tip of the capillaries, a pipette beveler Sutter Instruments BV-10 was used with the following settings: Beveling disk: Very Fine 104E, angle: 45º.

4.1.7.2 Image acquisition and analysis of injected oil droplets

Injected embryos were imaged within 2 hours from injection to allow recovery of the tissue. The fluorescent microdroplets were imaged using an inverted Zeiss LSM 700, composed of a Zeiss Axio Observer.Z1 with inverted stand, and using a Zeiss Plan Apo 40x (1.2 NA) with Water immersion. Images were acquired with a size 512x512 pixels and optical resolution of 0.5 um/pixel and step size of 1 um at smallest pixel dwell time over few seconds to capture any shape fluctuation of the microdroplet. For postprocessing, 3D gaussian blur (radius = 2 on all axes) and binning to get isometric voxel was performed using FIJI. Data analysis of the microdroplets was performed using the STRESS package [68] in Matlab (R2022a) and Python3. The parameters used in the software were the following: interfacial tension 5 mN/m; high fidelity; maximum number of LBDV points. Results were plotted in Python3.

4.2 Atomic Force Microscopy (AFM)

4.2.1 Sample preparation

Zebrafish embryos were manually dechorionated, staged and subsequently anesthetized by supplementing E3 medium with 0.04% tricaine methanesulfonate (MS-222, 1004671, Pharmaq). Anesthetized embryos were then mounted in 1.5-2% agarose in E3 containing MS-222 and manually positioned in a line, facing the same direction. Once the agarose had solidified, it was cut into a small block and glued to the holder of a Leica Vibratome vt1000s. The chamber of the Vibratome was then filled with cold PBS 1X until the agarose

block containing the embryos was fully submerged. Embryos were sliced at a step size of 100 μm and retinal slices were collected and kept in cold PBS 1X on ice.

4.2.2 AFM measurements

AFM measurements were performed using a FLEX-ANA (Nanosurf) automated AFM device. The AFM head was mounted in a Leica DMI 6000 inverted microscope fitted with a x–y-motorized stage that allowed to image the tissue slices with a 10x/0,30 Leica dry objective while acquiring AFM data. We used cantilevers coated with a 10 μm diameter colloidal spheres (CP-qp-SCONT-Au-A, NanoAndMore GmbH). The size of the tip was chosen to ensure to capture the mechanical properties at the tissue level. Cantilevers were mounted on the AFM device and their spring constants were calculated using the thermal noise method. Cantilevers with spring constants between 12 and 15 nN/m were selected and used for the measurements. Retinal slices were glued on a glass-bottomed dish coated with CellTak (Cornig; 354240) and covered with cold PBS 1X on ice. Measurements were performed 1 hour after the embryos were cut and, for each retinal slice, 25 indentations were performed in a ROI of 30x30 μm. A maximum indentation force of 7 nN and the approach speed of 5 μm/s were used. AFM curves were selected for analysis as described below in AFM data analysis.

4.2.3 AFM data analysis

All AFM data was analysed with the software AtomicJ (v 2.3.1). Here, raw data of force–distance curves were fitted to a Hertz model for a spherical indenter:

$$F = \frac{4}{3} K \sqrt[2]{r} \delta^{\frac{3}{2}} = \frac{4}{3} \frac{E}{1 - v^2} \sqrt[2]{r} \delta^{\frac{3}{2}}$$

with applied force F, Young's modulus E, Poisson's ratio v, indenter radius r, indentation depth δ, and apparent elastic moduli $K = \frac{E}{1-2v}$, referred as 'stiffness' in the text and as 'apparent elasticity (Pa)' in the y-axis of each chart. The parameters used in the software were the following: contact estimator classical golden; estimator method based on contact model; model fit classical L2; model paraboloid (Hz); radius 5 μm; Poisson ratio 0.5; baseline degree 1. The quality of curves was addressed by their shape. Only the best curves were kept for plotting.

4.3 Fluorescence Microscopy techniques

4.3.1 Laser Scanning Confocal Microscopy

Dechorionated, fixed and immunostained samples were imaged with a Zeiss LSM980 Airyscan2 inverted microscope, equipped with two PMT and one GaAsP detector, using a 40X/1.1 C-Apochromat water immersion objective from Zeiss. Embryos were mounted in 0.75% low-melting agarose in glass-bottomed dishes (35 mm, MatTek Corporation) and

imaged at room temperature. The dataset used for nuclear segmentation was acquired with Airyscan CO-8Y mode. The microscope was operating using the proprietary ZEN Blue v3.3 software.

4.3.2 Light Sheet Fluorescence Microscopy

Dechorionated live or fixed embryos were mounted in 1 mm glass capillaries in 0.6% low-melting agarose. The sample chamber was filled with E3 medium containing 0.01% MS-222 (Sigma) and 0.2 mM PTU (Sigma). Imaging was performed on a Zeiss Lightsheet Z.1 microscope equipped with two PCO Edge 4.2 sCMOS cameras (max 30 fps with 2048x2048 pixels - pixel size 6.5 μm) and with a 20x/1.2 Zeiss Plan-Apochromat water-immersion objective. Live imaging was performed at 28.5°C. Z-stacks spanning the entire retinal epithelium were acquired with 1 μm optical sectioning every 10 or 15 min for 15-24 hours with double-sided illumination mode. The microscope was operating using the proprietary ZEN Black v3.0 software.

4.4 Image processing and analysis

All the image analysis pipelines were coded in Python 3.9 and the source code is available online. The analysis pipeline is shown in Fig. 4.1 and consisted of four major steps: segmentation of nuclei using StarDist-3D [222]; feature extraction; manual selection of the regions of interest (ROIs); data visualization and data analysis. The code for the image analysis pipeline is available at this GitHub repository: github.com/lcferme/ferme-phd-thesis-2024.

4.4.1 Segmentation of the optic cup

3D segmentation of the basement membrane was performed using the FIJI plugin for 3D segmentation LimeSeg (v 0.4.2) [123]. The algorithm is based on a particle-based active contour method and it is indicated for the segmentation of objects whose outline is labelled, like in the case of membranes. LimeSeg requires the user to define seeds that will be used by the algorithm to segment the image. Therefore, several rois where drawn inside the volume outlined by the lamin signal across the z-stack. Endpoints were defined by a single point. All rois where saved in the FIJI ROI manager and sorted according to their position along the z axis. The 'Skeleton Seg' approach was used with the following parameters: D0(minimal diameter of smallest object in pixel) equal to 16; F pressure (default pressure) of 0.0099; Range in d0 units equal to 1; number of integration steps of -1. The resulting 3D mesh of the object's surface was saved in .ply format and a script was coded to convert this mesh into a labelled mask in .tif format. Mistakes in the labelled object obtained from Limeseg were manually corrected using the label tools in Napari (v0.4.18).

4.4.2 Segmentation of nuclei

4.4.2.1 Image annotation

Deep learning (DL) methods generally requires vast amounts of pixel-wise annotated ground truth data for training. For this reason, we manually annotated 3D cropped stacks of various sizes, around 50x260x230 pixels, taken from datasets representing various developmental stages. The stacks sizes were defined by the volume of the nuclei, since they needed to contain fully visible nuclei, i.e. nuclei not touching the image border. This was necessary to facilitate the training of the StarDist-3D model. Manual annotation was performed using Labkit (FIJI plugin) and Napari. Input images could be multidimensional arrays containing different channels, in this case the model was trained using only the hsp70::H2B-RFP signal.

4.4.2.2 StarDist-3D training

Using the aforementioned annotated stacks, we trained two StarDist-3D models: one model (model A) was trained on 16 ground-truth stacks representing stages between 24 and 72 hpf, while the other model (model B) was trained on 14 stacks representing uniquely stages when the retina is laminated, i.e. from 48 to 80 hpf. As shown in table X, each stack contained between 10 and up to 400 entire labeled objects, i.e. nuclei that were not touching the image border. In both training datasets, the z step was twice the voxel size in xy and this anisotropic factor was kept in the imaging dataset. The voxel size used was usually the following (μm): zyx = [0.24, 0.102, 0.102]. To artificially increase the size of the training dataset and make the model more robust to pixel intensity fluctuations, the training dataset was augmented by rotating, flipping, transforming each labelled image and randomly changing pixel values. The following parameters were used to optimize the neural network for the training: number of rays, 256; grid size, [1, 4, 4]; anisotropy, [4.17, 1.27, 1.0]; backbone, u-net; u-net pool, [2, 4, 4]; train patch size, [32, 128, 128]; epoch; 400; steps per epoch, 100; train learning rate, 0.003. The script coded to perform the StarDist-3D training on our data can be found in this repository.
StarDist-3D is well suited for objects that can be represented by star-convex polyhedral, such as in the case of round and elliptical nuclei. While this proved to work for the segmentation of data acquired upon imaging of wild-type embryos, our trained StarDist-3D models failed to accurately segment nuclei whose shapes were extremely elongated due to genetic perturbation, namely in the case of hdac1-morpholino treated embryos. In this case, a small dataset was segmented using our StarDist-3D model and the predictions were manually curated using Napari (v0.4.18) and the annotation tool from Segment Anything for Microscopy (SAM, v0.3.0) .

4.4.2.3 StarDist-3D model evaluation

In order to evaluate the trained models, predictions were run on another manually annotated dataset that had never been shown to StarDist-3D during training. Tables 4.4 and 4.5 report the accuracy, precision and recall for several Intersection over Union (IoU) thresholds τ for test datasets representing different developmental stages, i.e. 30, 48 and 72 hours post fertilization (hpf). The number of test ground-truth crops per stage is, respectively : N = 2; N = 3; N = 4. The total number of nuclei per stage, respectively: n = 272; n = 225; n = 647. StarDist-3D model A was tested on datasets from 30 and 48 hpf embryos, while model B was tested on dataset from 72 hpf embryos.

Threshold τ	0.10	0.20	0.30	0.40	0.50	0.60	0.70	0.80	0.90
					30 hpf				
Accuracy	0.743	0.738	0.728	0.689	0.646	0.589	0.474	0.249	0.0137
Precision	0.789	0.787	0.781	0.755	0.727	0.687	0.596	0.369	0.025
Recall	0.926	0.922	0.915	0.886	0.853	0.805	0.699	0.434	0.029
					48 hpf				
Accuracy	0.781	0.781	0.781	0.732	0.654	0.549	0.302	0.0526	0.000
Precision	0.898	0.898	0.898	0.865	0.809	0.726	0.474	0.102	0.000
Recall	0.858	0.858	0.858	0.827	0.773	0.693	0.453	0.098	0.000

Table 4.4: Evaluation of StarDist-3D model A

Threshold τ	0.10	0.20	0.30	0.40	0.50	0.60	0.70	0.80	0.90
					72 hpf				
Accuracy	0.737	0.732	0.726	0.689	0.635	0.578	0.460	0.236	0.034
Precision	0.945	0.941	0.937	0.909	0.865	0.816	0.702	0.425	0.072
Recall	0.769	0.767	0.764	0.740	0.705	0.665	0.571	0.346	0.059

Table 4.5: Evaluation of StarDist-3D model B

4.4.3 Feature extraction

The final dataset obtained using StarDist-3D consisted of 32-bit float files as Tag Image File Format (tiff). To facilitate downstream image processing, the dataset was converted to integer data type. Each segmented nucleus was identified by one unique value and all segmented nuclei touching the borders of the image were excluded from the analysis. The images were rescaled to obtain almost isovolumetric voxels that would facilitate the extraction of some of the features of interests. Voxels were rescaled to the size of the z-step. The following parameters were iteratively calculated for each labelled nucleus in the image: the volume, the major, intermediate and shorter axis, the primary and secondary nematics and the centroid coordinates. The nuclear axes lengths were calculated from the central moments of each nucleus for the longest, the intermediate and the shortest axes from the

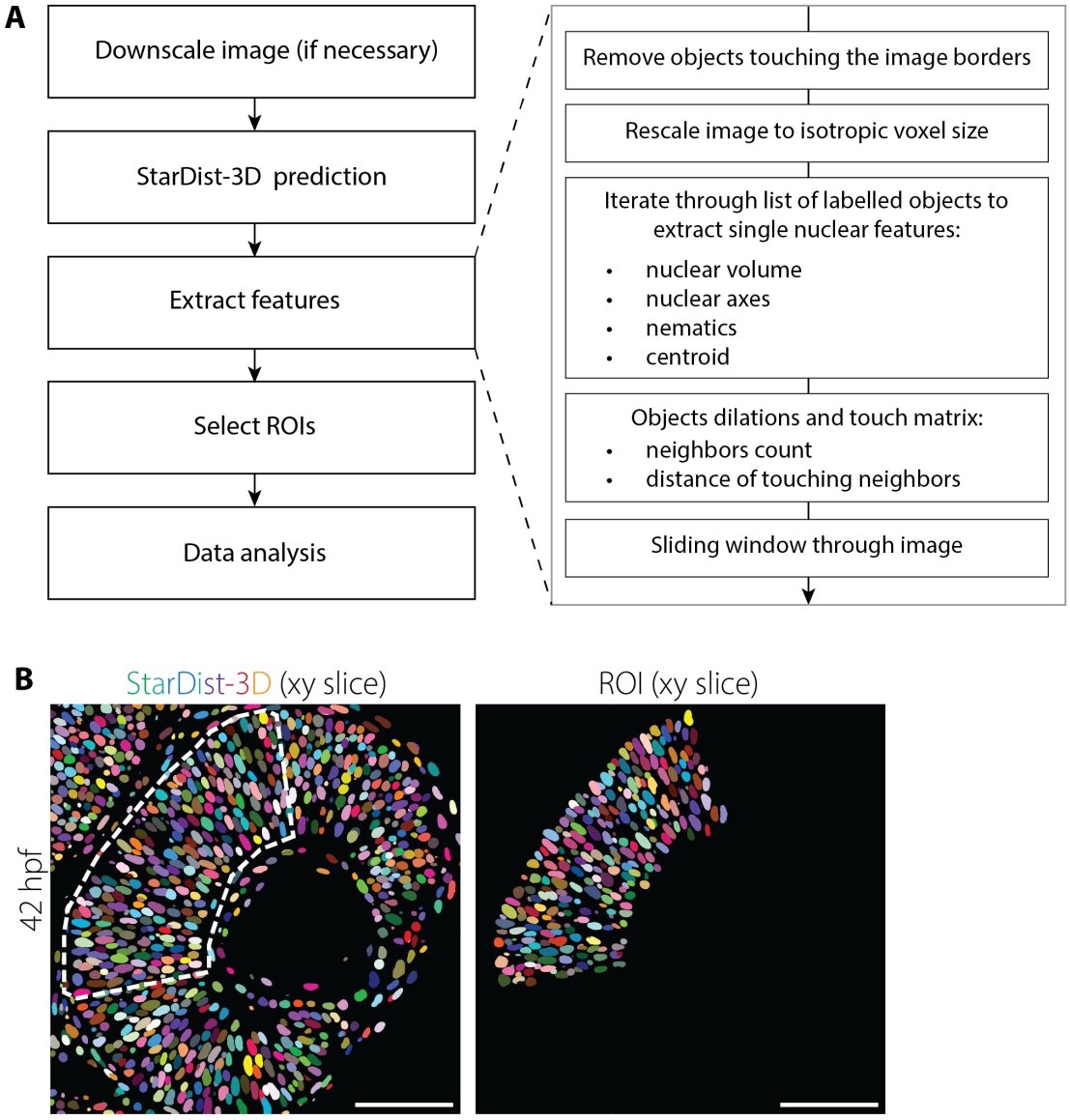

Figure 4.1: **Image analysis pipeline to quantify nuclear packing in proliferating PSNE. A)** Diagram of the sequential steps taken to analyze nuclear packing in volumetric imaging datasets. The code for each step can be found at the github repo for this thesis. **B)** Reprsentative images of the procedure to selecte the region of interest, i.e. the central region of the retinal PSNE. Scale bar = 50 μm.

centroid to the nuclear boundaries. The primary nematic was calculated as the longest pairwise distance between points composing the nuclear boundaries. The secondary nematic was defined as the maximum pairwise distance between points of the nuclear boundaries lying on the midplane to the primary nematic. Since nuclei supposedly do not touch each other, the nuclear boundaries of each nucleus were dilated by 1 pixel to count the number of touching neighbors at different radii. To compute the neighbour statistics of each nucleus, the pyclesperanto package was used to generate a touch matrix and extract the number of touching neighbours, proximal neighbours and internuclear distances in 3D. This analysis was performed using Python3.

4.4.4 Semi-automated selection of regions of interest (ROIs)

Nuclei within regions of interest were manually selected using a python script that enables the visualization and user interaction with the dataset using Napari (v0.4.18). In this way, the user can draw a polygon over the area of interest and specify the range of slices desired. The script, then, iterates through all the labelled nuclei present within this region and creates a new image stack containing only those nuclei. Then, another Napari GUI automatically opens to allow the user to manually mark the labeled objects that were erroneously included in the new image. In this way, it was possible to correct the image and obtain a csv file reporting the labels of nuclei contained in the selected ROI.

4.4.5 Window averaging of extracted features

In order to explore the local spatial variations of some of the extracted features, an automatic script was coded to scan each image StarDist-3D prediction with a 3-dimensional window of a given size. The mean value for the feature of choice was measured within the volumetric window, e.g. the average number of contacts. Since the volumetric windows were overlapping to a 20%, each pixel was averaged by the times the window looped on it. This created a smoothed image stack where each pixel reported the mean value for the measurement of interest. This analysis was performed using Python3.

4.4.6 Analysis of the orientational order of nuclei

The description of a nematic liquid crystals involves the quantification of the order of the system. First, the average direction axis (called local director) was calculated as the average of primary nematic vectors and the angle between each primary nematic vector and the primary director was calculated. This was performed iteratively within each window and averaged to obtain a spatial map of the average local primary nematic angle, as described in section 4.4.5. The same procedure was performed for the secondary nematics. The calculated angles were used to compute the scalar order parameter S:

$$S = \frac{3\langle \cos^2 \theta \rangle - 1}{2}$$

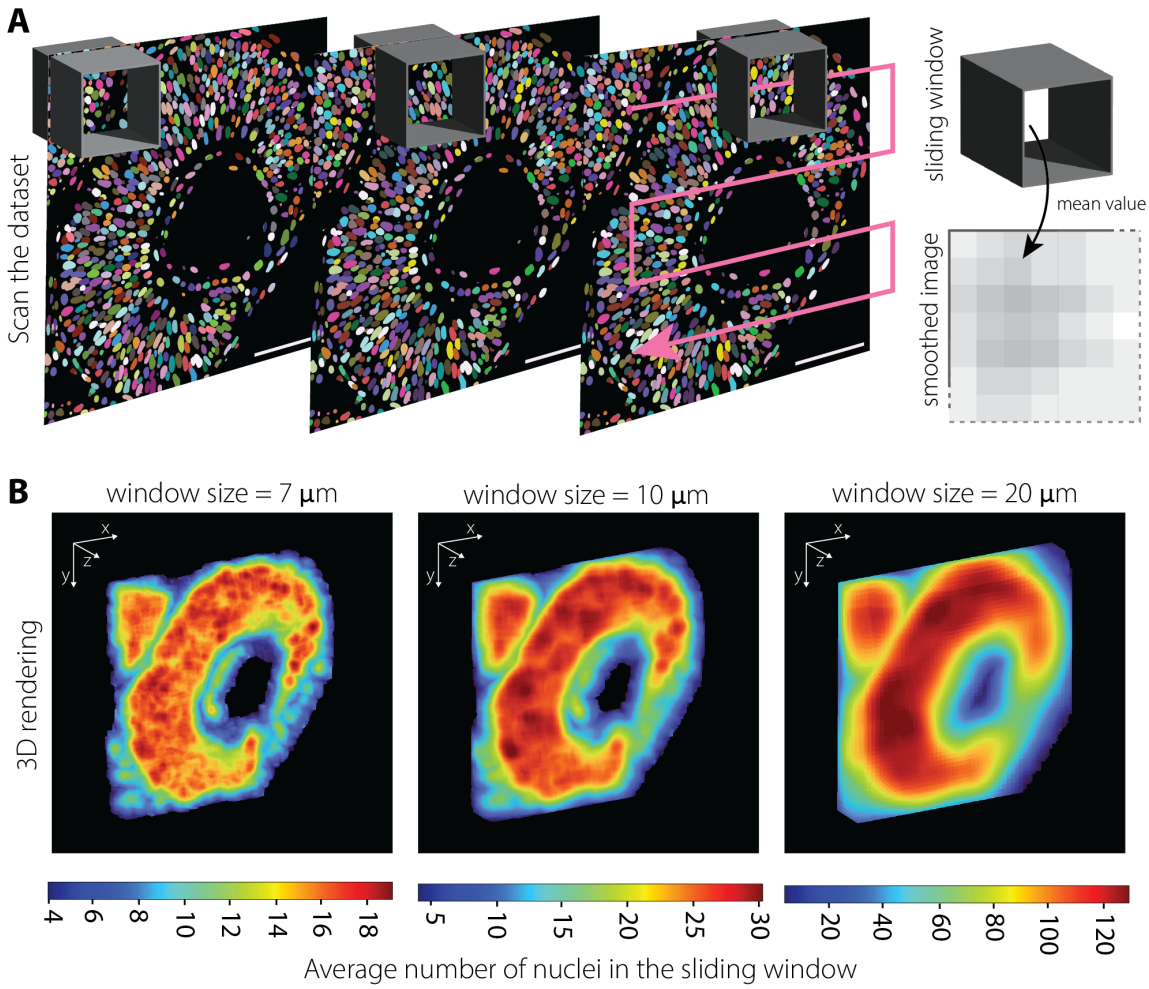

Figure 4.2: **Image smoothing of extracted features. A)** Diagram showing the procedure to iterate through the image stack and calculate the average value of the measured feature. within a cubic window. Ultimately, a smoothed dataset reporting average values computed for each pixel is generated .Scale bar = 50 μm. **B)** Representative 3D renderings of an image stack after smoothing with different window sizes. The pixel intensities correspond to the average number of nuclei within the window. All smoothed images shown in the results were analyzed with a window size of 10x10x10 μm.

where θ is the angle between the liquid-crystal molecular axis and the local director. For a completely random and isotropic sample, S = 0, whereas for a perfectly aligned sample S=1. For a typical nematic liquid crystal sample, S is on the order of 0.3 to 0.8.

4.4.7 Quantification of solid angles within a tetrahedron

To quantify the reciprocal positioning of nuclei within the INL, we measured the solid angles and facet angles of tetrahedra formed between touching neighbors. After filtering N nuclei that were contained in the selected ROIs, nuclear boundaries were dilated of

one pixel radius and a matrix NxN was generated, where each position ij reported the distance in pixels between touching labeled nuclei i and j. This matrix was then used to produce a graph and, for each node, permutations of neighboring nodes were inspected to determine if they composed a tetrahedron. If this was the case, the solid angles were measured such as the solid angle for the vertex a of a tetrahedron whose vertices are named abcd would be:

$$SA.a = DA.ab + DA.ac + DA.ad - \pi$$

where DA is the dihedral angle between two vertices. The DA between the vertices a and b was calculated as:

$$DA.ab = \arccos(n_{abc} \cdot n_{abd})$$

where n_{abc} is the unit vector of the cross product between the AB and AC edges. This analysis was performed using Python3.

4.4.8 Analysis of the radial distribution function

The radial distribution function $g(r)$ (RDF) g(r) provides a statistical description of the local packing and particle density of a system and is defined as:

$$g(r) = \frac{n(r)}{n_0 \, 4\pi r^2 \, dr}$$

where $n(r)$ is the number of particles in a spherical shell of radius r and thickness dr, n_0 is the average number density of particles and $4\pi r^2 \, dr$ is the volume of the spherical shell.

To compute the three-dimensional RDF of nuclei within the ROI, a sphere of a given maximum radius was drawn around each nucleus, namely no more than 50 μm. The $g(r)$ was calculated iteratively for the increment dr for increasing the radius of the spherical shell. To calculate the number density of nuclei within the ROI, the nuclear boundaries were dilated so that the space between the nuclei would be completely filled. Then, this labeled object was eroded to mask the nuclei in the ROI. The number density was calculated as the ratio between the number of nuclei in the mask and the volume of the mask itself. No compensation for edge effect was performed. In the case of artificial images shown in fig. 4.3, the maximum radius of the sphere was defined as half of the image side length.

4.4.9 Selection of Ptf1a-positive cells in the INL

The INL is populated by different neuronal cell types that can be distinguished based on their position and expression of the transcription factor Ptf1a. Volumetric datasets of retinas expressing this neuronal marker together with a nuclear marker, in this case hsp70::H2B-RFP, were processed to enable to the masking of segmented nuclei based on

the signal of ptf1a. The intensity of the neuronal marker was normalized using percentile normalization and converted to a binary mask based on otsu thresholding. Nuclei were segmented using our StartDist-3D model and selected based on the mask obtained from the ptf1a signal as described above.

4.4.10 Analysis of Atoh7 spatial distribution

To quantify the expression profile of Atoh7 throughout the whole retina, a maximum intensity projection was performed on the full stack using FIJI. In case of live imaging datasets, the timelapse was registered using StackReg plugin in FIJI, starting from the final frame and selecting the affine transformation. To extract the pixel intensity profile from the projected stack, a segmented line of 300 μm thickness was drawn throughout the retina, from the nasal to the temporal side or vice versa, keeping the first and last points aligned but separate. After drawing the line, a spline was fit to it to make it smooth and circular, using the Fit Spline option. The resulting line was then straighten and the pixel intensity was plotted in Python after percentile normalization. In case of timelapse data, the line was resliced to produce a kymograph and the intensity profile was then plotted after percentile normalization. The whole image processing was performed in FIJI and plotting of the intensity profiles was done in Python.

4.4.11 Data visualization and statistics

All statistical tests used are indicated in the figure or table legends, as well as the definitions of error bars. Likewise, p values and sample sizes are reported in the figure legends or in dedicated tables. Data was plotted after removing outliers, i.e. measurements below 0.01 percentile and above 0.99 percentiles per stage. Data visualization and statistical analysis were performed using the Matplotlib, Seaborn and Scipy Statistics packages in Python 3. Further information about the exact libraries, together with their versions, are detailed in the Git repository.

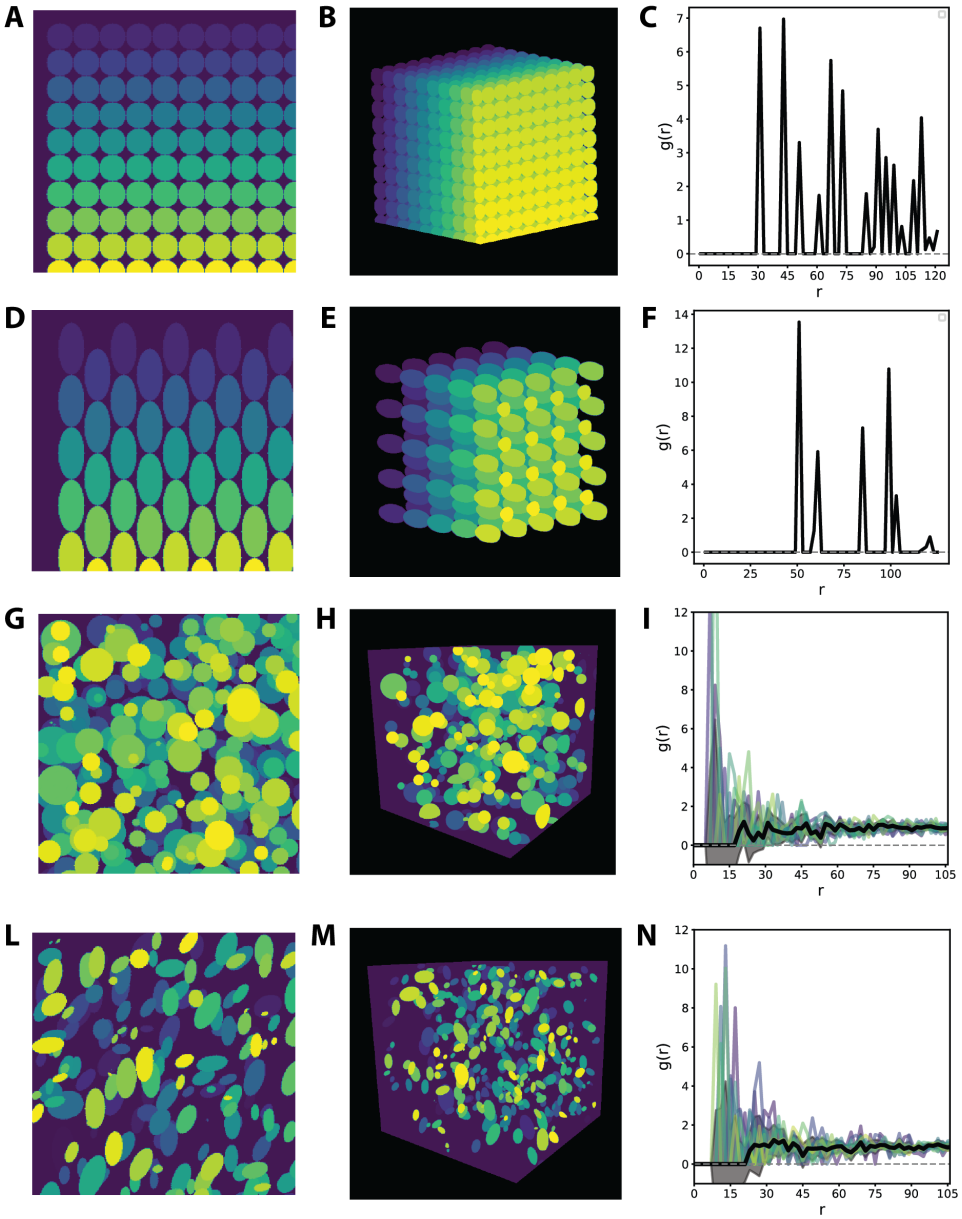

Figure 4.3: **Radial distribution function profiles for spheroids and ellipsoids arranged in a lattice or random packing. A-B)** Max projection and 3D rendering of close square packing of isovolumetric spheres in 3D. **C)** RDF of the square packing in A-B. **D-E)** Max projection and 3D rendering of layered packing of isovolumetric ellipsoids in 3D. **F)** RDF of the square packing in D-E. **G-H)** Max projection and 3D rendering of random packing of polydisperse spheres in 3D. **I)** RDF of the random packing in G-H, resembling a gas- like or liquid-like configuration. **L-M)** Max projection and 3D rendering of random packing of polydisperse ellipsoids in 3D. **N)** RDF of the random packing in L-M, resembling a gas-like or liquid-like configuration.

Bibliography

[1] D. Aboav. "The arrangement of grains in a polycrystal". In: *Metallography* 3.4 (1970), pp. 383–390. ISSN: 0026-0800. DOI: https://doi.org/10.1016/0026-0800(70)90038-8. URL: https://www.sciencedirect.com/science/article/pii/0026080070900388 (cit. on p. 24).

[2] J. A. Adelmann, R. Vetter, and D. Iber. "The impact of cell size on morphogen gradient precision". In: *Development* 150.10 (2023-05-15), dev201702. ISSN: 0950-1991, 1477-9129. DOI: 10.1242/dev.201702. URL: https://journals.biologists.com/dev/article/150/10/dev201702/310824/The-impact-of-cell-size-on-morphogen-gradient (visited on 2024-07-28) (cit. on pp. 12, 14).

[3] W. T. Allison et al. "Ontogeny of cone photoreceptor mosaics in zebrafish". In: *Journal of Comparative Neurology* 518.20 (2010-10-15), pp. 4182–4195. ISSN: 0021-9967, 1096-9861. DOI: 10.1002/cne.22447. URL: https://onlinelibrary.wiley.com/doi/10.1002/cne.22447 (visited on 2024-08-13) (cit. on p. 23).

[4] A. D. Almeida et al. "Spectrum of Fates: A new approach to the study of the developing zebrafish retina". In: *Development (Cambridge)* 141.14 (2014), pp. 2912–2912. DOI: 10.1242/dev.114108 (cit. on pp. 30, 38, 70, 92).

[5] S. Alt, P. Ganguly, and G. Salbreux. "Vertex models: from cell mechanics to tissue morphogenesis". In: *Philosophical Transactions of the Royal Society B: Biological Sciences* 372.1720 (2017-05-19), p. 20150520. ISSN: 0962-8436, 1471-2970. DOI: 10.1098/rstb.2015.0520. URL: https://royalsocietypublishing.org/doi/10.1098/rstb.2015.0520 (visited on 2024-08-13) (cit. on p. 17).

[6] R. Amini, A. A. Labudina, and C. Norden. "Stochastic single cell migration leads to robust horizontal cell layer formation in the vertebrate retina". In: *Development* 146.12 (2019), dev173450–dev173450. ISSN: 0000000239745. DOI: 10.1242/dev.173450 (cit. on p. 31).

[7] R. Amini, M. Rocha-Martins, and C. Norden. "Neuronal migration and lamination in the vertebrate retina". In: *Frontiers in Neuroscience* 11 (JAN 2018), pp. 1–16. DOI: 10.3389/fnins.2017.00742 (cit. on pp. 1, 26, 30, 31).

[8] R. Amini et al. "Amoeboid-like migration ensures correct horizontal cell layer formation in the developing vertebrate retina". In: *eLife* 11 (2022-05). Ed. by M. E. Bronner, e76408. ISSN: 2050-084X. DOI: 10.7554/eLife.76408. URL: https://doi.org/10.7554/eLife.76408 (cit. on p. 31).

[9] T. E. Angelini et al. "Glass-like dynamics of collective cell migration". In: *Proceedings of the National Academy of Sciences of the United States of America* 108.12 (2011), pp. 4714–4719. DOI: 10.1073/pnas.1010059108 (cit. on pp. 17, 20, 21).

[10] E. Assémat et al. "Polarity complex proteins". In: *Biochimica et Biophysica Acta (BBA) - Biomembranes* 1778.3 (2008). Apical Junctional Complexes Part I, pp. 614–630. ISSN: 0005-2736. DOI: https://doi.org/10.1016/j.bbamem.2007.08.029. URL: https://www.sciencedirect.com/science/article/pii/S000527360700332X (cit. on p. 4).

[11] L. Atia et al. "Are cell jamming and unjamming essential in tissue development?" In: *Cells and Development* (April 2021). Publisher: Elsevier B.V., pp. 203727–203727. DOI: 10.1016/j.cdev.2021.203727. URL: https://doi.org/10.1016/j.cdev.2021.203727 (cit. on pp. 17, 20, 22, 77).

[12] L. Atia et al. "Geometric constraints during epithelial jamming". In: *Nature Physics* (2018). Publisher: Springer US. DOI: 10.1038/s41567-018-0089-9. URL: http://dx.doi.org/10.1038/s41567-018-0089-9 (cit. on pp. 20, 21).

[13] C. Autorino and N. I. Petridou. "Critical phenomena in embryonic organization". In: *Current Opinion in Systems Biology* 31 (2022-09), p. 100433. ISSN: 24523100. DOI: 10.1016/j.coisb.2022.100433. URL: https://linkinghub.elsevier.com/retrieve/pii/S2452310022000191 (visited on 2024-08-13) (cit. on p. 22).

[14] A. Azizi et al. "Nuclear crowding and nonlinear diffusion during interkinetic nuclear migration in the zebrafish retina". In: *eLife* 9 (2020), pp. 1–31. DOI: 10.7554/eLife.58635 (cit. on pp. 9, 10, 28).

[15] T. Baden, T. Euler, and P. Berens. "Understanding the retinal basis of vision across species". In: *Nature Reviews Neuroscience* 21.1 (2020-01), pp. 5–20. ISSN: 1471-003X, 1471-0048. DOI: 10.1038/s41583-019-0242-1. URL: https://www.nature.com/articles/s41583-019-0242-1 (visited on 2024-08-13) (cit. on p. 25).

[16] Z.-Z. Bao and C. L. Cepko. "The Expression and Function of *Notch* Pathway Genes in the Developing Rat Eye". In: *The Journal of Neuroscience* 17.4 (1997-02-15), pp. 1425–1434. ISSN: 0270-6474, 1529-2401. DOI: 10.1523/JNEUROSCI.17-04-01425.1997. URL: https://www.jneurosci.org/lookup/doi/10.1523/JNEUROSCI.17-04-01425.1997 (visited on 2024-08-13) (cit. on p. 30).

[17] P.-L. Bardet et al. "PTEN Controls Junction Lengthening and Stability during Cell Rearrangement in Epithelial Tissue". In: *Developmental Cell* 25.5 (2013-06), pp. 534–546. ISSN: 15345807. DOI: 10.1016/j.devcel.2013.04.020. URL: https://linkinghub.elsevier.com/retrieve/pii/S1534580713002499 (visited on 2024-07-27) (cit. on p. 24).

[18] E. H. Barriga et al. "Tissue stiffening coordinates morphogenesis by triggering collective cell migration in vivo". In: *Nature* 554.7693 (2018-02), pp. 523–527. ISSN: 0028-0836, 1476-4687. DOI: 10.1038/nature25742. URL: https://www.nature.com/articles/nature25742 (visited on 2024-04-29) (cit. on pp. 16, 34).

[19] M. Basan et al. "Alignment of cellular motility forces with tissue flow as a mechanism for efficient wound healing". In: *Proceedings of the National Academy of Sciences* 110.7 (2013-02-12), pp. 2452–2459. ISSN: 0027-8424, 1091-6490. DOI: 10.1073/pnas.1219937110. URL: https://pnas.org/doi/full/10.1073/pnas.1219937110 (visited on 2024-08-13) (cit. on pp. 17, 21).

[20] B. Bénazéraf et al. "A random cell motility gradient downstream of FGF controls elongation of an amniote embryo". In: *Nature* 466.7303 (2010-07), pp. 248–252. ISSN: 0028-0836, 1476-4687. DOI: 10.1038/nature09151. URL: https://www.nature.com/articles/nature09151 (visited on 2024-08-29) (cit. on p. 21).

[21] C. Bertet, L. Sulak, and T. Lecuit. "Myosin-dependent junction remodelling controls planar cell intercalation and axis elongation". In: *Nature* 429.6992 (2004-06), pp. 667–671. ISSN: 0028-0836, 1476-4687. DOI: 10.1038/nature02590. URL: https://www.nature.com/articles/nature02590 (visited on 2024-08-20) (cit. on p. 16).

[22] L. Berthier, E. Flenner, and G. Szamel. "Glassy dynamics in dense systems of active particles". In: *The Journal of Chemical Physics* 150.20 (2019-05-28), p. 200901. ISSN: 0021-9606, 1089-7690. DOI: 10.1063/1.5093240. URL: https://pubs.aip.org/jcp/article/150/20/200901/199089/Glassy-dynamics-in-dense-systems-of-active (visited on 2024-08-13) (cit. on pp. 20, 21).

[23] C. Bertipaglia, J. C. Gonçalves, and R. B. Vallee. "Nuclear migration in mammalian brain development". In: *Seminars in Cell & Developmental Biology* 82 (2018-10), pp. 57–66. ISSN: 10849521. DOI: 10.1016/j.semcdb.2017.11.033. URL: https://linkinghub.elsevier.com/retrieve/pii/S1084952117305359 (visited on 2024-08-18) (cit. on p. 9).

[24] O. Beutel et al. "Phase Separation of Zonula Occludens Proteins Drives Formation of Tight Junctions". In: *Cell* 179.4 (2019), 923–936.e11. ISSN: 0092-8674. DOI: https://doi.org/10.1016/j.cell.2019.10.011. URL: https://www.sciencedirect.com/science/article/pii/S0092867419311274 (cit. on p. 5).

[25] D. Bi et al. "Energy barriers and cell migration in densely packed tissues". In: *Soft Matter* 10.12 (2014), p. 1885. ISSN: 1744-683X, 1744-6848. DOI: 10.1039/c3sm52893f. URL: https://xlink.rsc.org/?DOI=c3sm52893f (visited on 2024-08-13) (cit. on pp. 17, 21).

[26] D. Bi et al. "Motility-driven glass and jamming transitions in biological tissues". In: *Physical Review X* 6.2 (2016), pp. 1–13. DOI: 10.1103/PhysRevX.6.021011 (cit. on p. 17).

[27] J. T. Blankenship et al. "Multicellular Rosette Formation Links Planar Cell Polarity to Tissue Morphogenesis". In: *Developmental Cell* 11.4 (2006-10), pp. 459–470. ISSN: 15345807. DOI: 10.1016/j.devcel.2006.09.007. URL: https://linkinghub.elsevier.com/retrieve/pii/S153458070600400X (visited on 2024-08-20) (cit. on p. 16).

[28] L. Bocanegra-Moreno et al. "Cell cycle dynamics control fluidity of the developing mouse neuroepithelium". In: *Nature Physics* (2023-04-06). ISSN: 1745-2473, 1745-2481. DOI: 10.1038/s41567-023-01977-w. URL: https://www.nature.com/articles/s41567-023-01977-w (visited on 2023-05-11) (cit. on pp. 12, 14, 15).

[29] R. Bort et al. "Hex homeobox gene controls the transition of the endoderm to a pseudostratified, cell emergent epithelium for liver bud development". In: *Developmental Biology* 290.1 (2006-02), pp. 44–56. ISSN: 00121606. DOI: 10.1016/j.ydbio.2005.11.006. URL: https://linkinghub.elsevier.com/retrieve/pii/S0012160605007803 (visited on 2024-08-16) (cit. on pp. 3, 7, 8).

[30] A. Boutillon, S. P. Banavar, and O. Campàs. "Conserved physical mechanisms of cell and tissue elongation". In: *Development* 151.10 (2024-05-15), dev202687. ISSN: 0950-1991, 1477-9129. DOI: 10.1242/dev.202687. URL: https://journals.biologists.com/dev/article/151/10/dev202687/347561/Conserved-physical-mechanisms-of-cell-and-tissue (visited on 2024-08-13) (cit. on p. 16).

[31] D. K. Breslow and A. J. Holland. "Mechanism and Regulation of Centriole and Cilium Biogenesis". In: *Annual Review of Biochemistry* 88.1 (2019-06-20), pp. 691–724. ISSN: 0066-4154, 1545-4509. DOI: 10.1146/annurev-biochem-013118-111153. URL: https://www.annualreviews.org/doi/10.1146/annurev-biochem-013118-111153 (visited on 2024-07-29) (cit. on p. 4).

[32] W. E. Browne et al. "Stages of embryonic development in the amphipod crustacean,Parhyale hawaiensis". In: *genesis* 42.3 (2005-07), pp. 124–149. ISSN: 1526-954X, 1526-968X. DOI: 10.1002/gene.20145. URL: https://onlinelibrary.wiley.com/doi/10.1002/gene.20145 (visited on 2024-08-13) (cit. on p. 23).

[33] I. Y. Buchsbaum and S. Cappello. "Neuronal migration in the CNS during development and disease: insights from in vivo and in vitro models". In: (2019). DOI: 10.1242/dev.163766. URL: https://doi.org/10.1242/dev.163766 (cit. on p. 1).

[34] C. E. Buckley and D. St Johnston. "Apical–basal polarity and the control of epithelial form and function". In: *Nature Reviews Molecular Cell Biology* 23.8 (2022-08), pp. 559–577. ISSN: 1471-0072, 1471-0080. DOI: 10.1038/s41580-022-00465-y. URL: https://www.nature.com/articles/s41580-022-00465-y (visited on 2024-07-28) (cit. on p. 4).

[35] O. Campàs. "A toolbox to explore the mechanics of living embryonic tissues". In: *Seminars in Cell and Developmental Biology* 55 (2016). Publisher: Elsevier Ltd, pp. 119–130. DOI: 10.1016/j.semcdb.2016.03.011. URL: http://dx.doi.org/10.1016/j.semcdb.2016.03.011 (cit. on p. 77).

[36] O. Campàs et al. "Quantifying cell-generated mechanical forces within living embryonic tissues". In: *Nature Methods* 11.2 (2014), pp. 183–189. DOI: 10.1038/nmeth.2761 (cit. on p. 77).

[37] T. D. Carroll et al. "Interkinetic nuclear migration and basal tethering facilitates post-mitotic daughter separation in intestinal organoids". In: *Journal of Cell Science* 130.22 (2017-11-15), pp. 3862–3877. ISSN: 1477-9137, 0021-9533. DOI: 10.1242/jcs.211656. URL: https://journals.biologists.com/jcs/article/130/22/3862/56470/Interkinetic-nuclear-migration-and-basal-tethering (visited on 2024-07-31) (cit. on p. 6).

[38] C. Cepko. "Intrinsically different retinal progenitor cells produce specific types of progeny". In: *Nature Reviews Neuroscience* 15.9 (2014-09), pp. 615–627. ISSN: 1471-003X, 1471-0048. DOI: 10.1038/nrn3767. URL: https://www.nature.com/articles/nrn3767 (visited on 2024-08-13) (cit. on p. 30).

[39] R. L. Chow et al. "Pax6 induces ectopic eyes in a vertebrate". In: *Development* 126.19 (1999-10-01), pp. 4213–4222. ISSN: 0950-1991, 1477-9129. DOI: 10.1242/dev.126.19.4213. URL: https://journals.biologists.com/dev/article/126/19/4213/40426/Pax6-induces-ectopic-eyes-in-a-vertebrate (visited on 2024-08-13) (cit. on p. 27).

[40] D. J. Cislo et al. "Active cell divisions generate fourfold orientationally ordered phase in living tissue". In: *Nature Physics* 19.8 (2023-08), pp. 1201–1210. ISSN: 1745-2473, 1745-2481. DOI: 10.1038/s41567-023-02025-3. URL: https://www.nature.com/articles/s41567-023-02025-3 (visited on 2024-07-26) (cit. on p. 23).

[41] A.-K. Classen et al. "Hexagonal Packing of Drosophila Wing Epithelial Cells by the Planar Cell Polarity Pathway". In: *Developmental Cell* 9.6 (2005-12), pp. 805–817. ISSN: 15345807. DOI: 10.1016/j.devcel.2005.10.016. URL: https://linkinghub.elsevier.com/retrieve/pii/S153458070500420X (visited on 2024-08-01) (cit. on pp. 22–24).

[42] R. Cohen et al. "Mechanical forces drive ordered patterning of hair cells in the mammalian inner ear". In: *Nat Commun* 11.1 (2020-10-12), p. 5137. ISSN: 2041-1723. DOI: 10.1038/s41467-020-18894-8. URL: https://www.nature.com/articles/s41467-020-18894-8 (visited on 2023-05-17) (cit. on pp. 2, 23).

[43] J. Comelles et al. "Epithelial colonies in vitro elongate through collective effects". In: *eLife* 10 (2021-01). Ed. by I. Giardina, A. M. Walczak, and B. Ladoux, e57730. ISSN: 2050-084X. DOI: 10.7554/eLife.57730. URL: https://doi.org/10.7554/eLife.57730 (cit. on p. 18).

[44] P. T. Conduit, A. Wainman, and J. W. Raff. "Centrosome function and assembly in animal cells". In: *Nature Reviews Molecular Cell Biology* 16.10 (2015-10), pp. 611–624. ISSN: 1471-0072, 1471-0080. DOI: 10.1038/nrm4062. URL: https://www.nature.com/articles/nrm4062 (visited on 2024-08-27) (cit. on p. 4).

[45] V. T. Cunliffe. "Histone deacetylase 1 is required to repress Notch target gene expression during zebrafish neurogenesis and to maintain the production of motoneurones in response to hedgehog signalling". In: *Development* 131.12 (2004-06-15), pp. 2983–2995. ISSN: 1477-9129, 0950-1991. DOI: 10.1242/dev.01166. URL: https://journals.biologists.com/dev/article/131/12/2983/42249/Histone-deacetylase-1-is-required-to-repress-Notch (visited on 2023-03-24) (cit. on p. 71).

[46] M. Daghsni and I. Aldiri. "Building a Mammalian Retina: An Eye on Chromatin Structure". In: *Frontiers in Genetics* 12 (2021-10-25), p. 775205. ISSN: 1664-8021. DOI: 10.3389/fgene.2021.775205. URL: https://www.frontiersin.org/articles/10.3389/fgene.2021.775205/full (visited on 2024-08-26) (cit. on p. 70).

[47] A. Donev et al. "Improving the Density of Jammed Disordered Packings Using Ellipsoids". In: *Science* 303.5660 (2004), pp. 990–993. DOI: 10.1126/science.1093010 (cit. on pp. 33, 38–40, 42, 43, 77).

[48] A. Doostmohammadi and B. Ladoux. "Physics of liquid crystals in cell biology". In: *Trends in Cell Biology* 32.2 (2022-02), pp. 140–150. ISSN: 09628924. DOI: 10.1016/j.tcb.2021.09.012. URL: https://linkinghub.elsevier.com/retrieve/pii/S0962892421002014 (visited on 2024-08-06) (cit. on pp. 18, 19).

[49] B. L. Doss et al. "Cell response to substrate rigidity is regulated by active and passive cytoskeletal stress". In: *Proceedings of the National Academy of Sciences* 117.23 (2020-06-09), pp. 12817–12825. ISSN: 0027-8424, 1091-6490. DOI: 10.1073/pnas.1917555117. URL: https://pnas.org/doi/full/10.1073/pnas.1917555117 (visited on 2024-08-06) (cit. on p. 19).

[50] D. Drasdo. "Buckling Instabilities of One-Layered Growing Tissues". In: *Physical Review Letters* 84.18 (2000-05-01), pp. 4244–4247. ISSN: 0031-9007, 1079-7114. DOI: 10.1103/PhysRevLett.84.4244. URL: https://link.aps.org/doi/10.1103/PhysRevLett.84.4244 (visited on 2024-07-25) (cit. on p. 87).

[51] N. A. Dye et al. "Self-organized patterning of cell morphology via mechanosensitive feedback". In: *eLife* 10 (2021), pp. 1–41. DOI: 10.7554/eLife.57964 (cit. on p. 14).

[52] E. Dzafic et al. "Centriole Amplification in Zebrafish Affects Proliferation and Survival but Not Differentiation of Neural Progenitor Cells". In: *Cell Reports* 13.1 (2015), pp. 168–182. DOI: 10.1016/j.celrep.2015.08.067. URL: https://doi.org/10.1016/j.celrep.2015.08.067 (cit. on p. 92).

[53] M. Eiraku et al. "Self-organizing optic-cup morphogenesis in three-dimensional culture". In: *Nature* 472.7341 (2011). Publisher: Nature Publishing Group, pp. 51–58. DOI: 10.1038/nature09941 (cit. on pp. 1, 3, 27, 79, 88).

[54] P. Engerer et al. "Uncoupling of neurogenesis and differentiation during retinal development". In: *The EMBO Journal* 36.9 (2017-05), pp. 1134–1146. DOI: 10.15252/embj.201694230. URL: https://doi.org/10.15252/embj.201694230 (cit. on p. 31).

[55] R. Esposito et al. "The ascidian pigmented sensory organs: structures and developmental programs". In: *Genesis* 53.1 (2015-01). Epub 2014 Nov 26, pp. 15–33. DOI: 10.1002/dvg.22836. URL: https://doi.org/10.1002/dvg.22836 (cit. on p. 25).

[56] L. Even-Faitelson and S. Ravid. "PAK1 and aPKC Regulate Myosin II-B Phosphorylation: A Novel Signaling Pathway Regulating Filament Assembly". In: *Molecular Biology of the Cell* 17.7 (2006), pp. 2869–2881. DOI: 10.1091/mbc.e05-11-1001. URL: https://doi.org/10.1091/mbc.e05-11-1001 (cit. on p. 4).

[57] R. Farhadifar et al. "The Influence of Cell Mechanics, Cell-Cell Interactions, and Proliferation on Epithelial Packing". In: *Current Biology* 17.24 (2007-12), pp. 2095–2104. ISSN: 09609822. DOI: 10.1016/j.cub.2007.11.049. URL: https://linkinghub.elsevier.com/retrieve/pii/S0960982207023342 (visited on 2024-08-13) (cit. on p. 17).

[58] M. A. Ferreira et al. "Interkinetic nuclear movements promote apical expansion in pseudostratified epithelia at the expense of apicobasal elongation". In: *PLOS Computational Biology* 15.12 (2019-12-23). Ed. by P. K. Maini, e1007171. ISSN: 1553-7358. DOI: 10.1371/journal.pcbi.1007171. URL: https://dx.plos.org/10.1371/journal.pcbi.1007171 (visited on 2024-05-22) (cit. on p. 8).

[59] J. Firmino et al. "Cell Division Drives Epithelial Cell Rearrangements during Gastrulation in Chick". In: *Developmental Cell* 36.3 (2016-02), pp. 249–261. ISSN: 15345807. DOI: 10.1016/j.devcel.2016.01.007. URL: https://linkinghub.elsevier.com/retrieve/pii/S1534580716000411 (visited on 2024-04-29) (cit. on p. 12).

[60] A. J. Fischer, J. L. Bosse, and H. M. El-Hodiri. "The ciliary marginal zone (CMZ) in development and regeneration of the vertebrate eye". In: *Experimental Eye Research* 116 (2013-11), pp. 199–204. ISSN: 00144835. DOI: 10.1016/j.exer.2013.08.018. URL: https://linkinghub.elsevier.com/retrieve/pii/S0014483513002571 (visited on 2024-08-22) (cit. on p. 27).

[61] C. E. Fogarty and A. Bergmann. "Killers creating new life: caspases drive apoptosis-induced proliferation in tissue repair and disease". In: *Cell Death & Differentiation* 24.8 (2017-08), pp. 1390–1400. ISSN: 1350-9047, 1476-5403. DOI: 10.1038/cdd.2017.47. URL: https://www.nature.com/articles/cdd201747 (visited on 2024-07-25) (cit. on p. 90).

[62] K. Franze et al. "Müller cells are living optical fibers in the vertebrate retina". In: *Proceedings of the National Academy of Sciences* 104.20 (2007-05-15), pp. 8287–8292. ISSN: 0027-8424, 1091-6490. DOI: 10.1073/pnas.0611180104. URL: https://pnas.org/doi/full/10.1073/pnas.0611180104 (visited on 2024-05-14) (cit. on p. 83).

[63] N. Fujimura. "WNT/-Catenin Signaling in Vertebrate Eye Development". In: *Frontiers in Cell and Developmental Biology* 4 (2016-11-30). ISSN: 2296-634X. DOI: 10.3389/fcell.2016.00138. URL: http://journal.frontiersin.org/article/10.3389/fcell.2016.00138/full (visited on 2024-08-12) (cit. on p. 89).

[64] S. Garcia et al. "Physics of active jamming during collective cellular motion in a monolayer". In: *Proceedings of the National Academy of Sciences* 112.50 (2015-12-15), pp. 15314–15319. ISSN: 0027-8424, 1091-6490. DOI: 10.1073/pnas.1510973112. URL: https://pnas.org/doi/full/10.1073/pnas.1510973112 (visited on 2024-08-13) (cit. on p. 17).

[65] B. Geldmacher-Voss et al. "A 90° rotation of the mitotic spindle changes the orientation of mitoses of zebrafish neuroepithelial cells". In: *Development* 130.16 (2003-08-15), pp. 3767–3780. ISSN: 1477-9129, 0950-1991. DOI: 10.1242/dev.00603. URL: https://journals.biologists.com/dev/article/130/16/3767/52119/A-90-rotation-of-the-mitotic-spindle-changes-the (visited on 2024-08-28) (cit. on p. 92).

[66] H. F. Gómez et al. "3D cell neighbour dynamics in growing pseudostratified epithelia". In: *eLife* 10 (2021), pp. 1–25. DOI: 10.7554/eLife.68135 (cit. on pp. 12, 14, 24).

[67] P. Gómez-Gálvez et al. "Scutoids are a geometrical solution to three-dimensional packing of epithelia". In: *Nature Communications* 9.1 (2018-07-27), p. 2960. ISSN: 2041-1723. DOI: 10.1038/s41467-018-05376-1. URL: https://www.nature.com/articles/s41467-018-05376-1 (visited on 2024-08-13) (cit. on p. 24).

[68] B. Gross et al. "STRESS, an automated geometrical characterization of deformable particles for in vivo measurements of cell and tissue mechanical stresses". In: *bioRxiv* (2021). DOI: 10.1101/2021.03.26.437148. eprint: https://www.biorxiv.org/content/early/2021/03/26/2021.03.26.437148.full.pdf. URL: https://www.biorxiv.org/content/early/2021/03/26/2021.03.26.437148 (cit. on p. 95).

[69] A. S. Grosse et al. "Cell dynamics in fetal intestinal epithelium: implications for intestinal growth and morphogenesis". In: *Development* 138.20 (2011-10-15), pp. 4423–4432. ISSN: 1477-9129, 0950-1991. DOI: 10.1242/dev.065789. URL: https://journals.biologists.com/dev/article/138/20/4423/44674/Cell-dynamics-in-fetal-intestinal-epithelium (visited on 2024-08-28) (cit. on p. 7).

[70] P. Guerrero et al. "Neuronal differentiation influences progenitor arrangement in the vertebrate neuroepithelium". In: *Development (Cambridge)* 146.23 (2019). ISSN: 0000000345. DOI: 10.1242/dev.176297 (cit. on pp. 14, 15).

[71] F. Guilak, J. R. Tedrow, and R. Burgkart. "Viscoelastic properties of the cell nucleus". In: *Biochemical and Biophysical Research Communications* 269.3 (2000), pp. 781–786. DOI: 10.1006/bbrc.2000.2360 (cit. on p. 15).

[72] P. Guillamat et al. "Integer topological defects organize stresses driving tissue morphogenesis". In: *Nature Materials* 21.5 (2022-05), pp. 588–597. ISSN: 1476-1122, 1476-4660. DOI: 10.1038/s41563-022-01194-5. URL: https://www.nature.com/articles/s41563-022-01194-5 (visited on 2024-08-06) (cit. on pp. 18, 19).

[73] J. Hahn et al. "Evolution of neuronal cell classes and types in the vertebrate retina". In: *Nature* 624.7991 (2023-12-14), pp. 415–424. ISSN: 0028-0836, 1476-4687. DOI: 10.1038/s41586-023-06638-9. URL: https://www.nature.com/articles/s41586-023-06638-9 (visited on 2024-08-13) (cit. on p. 25).

[74] G. Halasi et al. "Proliferation and recapitulation of developmental patterning associated with regulative regeneration of the spinal cord neural tube". In: *Developmental Biology* 365.1 (2012), pp. 118–132. ISSN: 0012-1606. DOI: https://doi.org/10.1016/j.ydbio.2012.02.012. URL: https://www.sciencedirect.com/science/article/pii/S0012160612000814 (cit. on p. 90).

[75] E. Hannezo and C. P. Heisenberg. "Mechanochemical Feedback Loops in Development and Disease". In: *Cell* 178.1 (2019). Publisher: Elsevier Inc., pp. 12–25. DOI: 10.1016/j.cell.2019.05.052. URL: https://doi.org/10.1016/j.cell.2019.05.052 (cit. on p. 17).

[76] E. Hannezo, J. Prost, and J.-F. Joanny. "Theory of epithelial sheet morphology in three dimensions". In: *Proceedings of the National Academy of Sciences* 111.1 (2014-01-07), pp. 27–32. ISSN: 0027-8424, 1091-6490. DOI: 10.1073/pnas.1312076111. URL:

https://pnas.org/doi/full/10.1073/pnas.1312076111 (visited on 2024-07-25) (cit. on pp. 85, 87).

[77] R. L. Hannibal, A. L. Price, and N. H. Patel. "The functional relationship between ectodermal and mesodermal segmentation in the crustacean Parhyale hawaiensis". In: *Developmental Biology* 361.2 (2012), pp. 427–438. ISSN: 0012-1606. DOI: https://doi.org/10.1016/j.ydbio.2011.09.033. URL: https://www.sciencedirect.com/science/article/pii/S0012160611012772 (cit. on p. 22).

[78] H. Hashimoto et al. "Zebrafish Dkk1 functions in forebrain specification and axial mesendoderm formation". In: *Developmental Biology* 217.1 (2000), pp. 138–152. DOI: 10.1006/dbio.1999.9537 (cit. on pp. 62, 65).

[79] Y. He et al. "Histone deacetylase 1 is required for the development of the zebrafish inner ear". In: *Scientific Reports* 6.1 (2016-02-01), p. 16535. ISSN: 2045-2322. DOI: 10.1038/srep16535. URL: https://www.nature.com/articles/srep16535 (visited on 2023-03-24) (cit. on p. 71).

[80] C. F. Hevia et al. "The neurogenic fate of the hindbrain boundaries relies on Notch3-dependent asymmetric cell divisions". In: *Cell Reports* 39.10 (2022-06), p. 110915. ISSN: 22111247. DOI: 10.1016/j.celrep.2022.110915. URL: https://linkinghub.elsevier.com/retrieve/pii/S2211124722006921 (visited on 2023-02-14) (cit. on p. 49).

[81] T. W. Hiscock et al. "Feedback between tissue packing and neurogenesis in the zebrafish neural tube". In: *Development (Cambridge)* 145.9 (2018). DOI: 10.1242/dev.157040 (cit. on p. 34).

[82] M. Hoon et al. "Functional architecture of the retina: Development and disease". In: *Progress in Retinal and Eye Research* 42 (2014-09), pp. 44–84. ISSN: 13509462. DOI: 10.1016/j.preteyeres.2014.06.003. URL: https://linkinghub.elsevier.com/retrieve/pii/S135094621400038X (visited on 2024-08-13) (cit. on pp. 24, 25).

[83] M. Hu and S. S. Easter. "Retinal Neurogenesis: The Formation of the Initial Central Patch of Postmitotic Cells". In: *Developmental Biology* 207.2 (1999-03), pp. 309–321. ISSN: 00121606. DOI: 10.1006/dbio.1998.9031. URL: https://linkinghub.elsevier.com/retrieve/pii/S0012160698990315 (visited on 2024-07-23) (cit. on pp. 30, 38).

[84] D. Iber and R. Vetter. "3D Organisation of Cells in Pseudostratified Epithelia". In: *Frontiers in Physics* 10 (2022-05-12), p. 898160. ISSN: 2296-424X. DOI: 10.3389/fphy.2022.898160. URL: https://www.frontiersin.org/articles/10.3389/fphy.2022.898160/full (visited on 2024-08-13) (cit. on p. 13).

[85] D. Iber and R. Vetter. "Relationship between epithelial organization and morphogen interpretation". In: *Current Opinion in Genetics & Development* 75 (2022-08), p. 101916. ISSN: 0959437X. DOI: 10.1016/j.gde.2022.101916. URL: https://linkinghub.elsevier.com/retrieve/pii/S0959437X22000259 (visited on 2024-04-08) (cit. on pp. 12, 13).

[86] J. Icha et al. "Independent modes of ganglion cell translocation ensure correct lamination of the zebrafish retina". In: *Journal of Cell Biology* 215.2 (2016), pp. 259–275. DOI: 10.1083/jcb.201604095 (cit. on pp. 4, 5, 30, 75, 82).

[87] O. Ilina et al. "Cell–cell adhesion and 3D matrix confinement determine jamming transitions in breast cancer invasion". In: *Nature Cell Biology* 22.9 (2020). Publisher: Springer US, pp. 1103–1115. DOI: 10.1038/s41556-020-0552-6. URL: http://dx.doi.org/10.1038/s41556-020-0552-6 (cit. on p. 21).

[88] M. Ishii et al. "Stalling interkinetic nuclear migration in curved pseudostratified epithelium of developing cochlea". In: *Royal Society Open Science* 8.12 (2021). DOI: 10.1098/rsos.211024 (cit. on p. 16).

[89] A. Iulianella et al. "*Cux2* (*Cutl2*) integrates neural progenitor development with cell-cycle progression during spinal cord neurogenesis". In: *Development* 135.4 (2008-02-15), pp. 729–741. ISSN: 1477-9129, 0950-1991. DOI: 10.1242/dev.013276. URL: https://journals.biologists.com/dev/article/135/4/729/64918/Cux2-Cutl2-integrates-neural-progenitor (visited on 2024-08-28) (cit. on p. 7).

[90] M. Iwahashi and Y. Kasahara. "Dynamic molecular movements and aggregation structures of lipids in a liquid state". In: *Current Opinion in Colloid & Interface Science* 16.5 (2011-10), pp. 359–366. ISSN: 13590294. DOI: 10.1016/j.cocis.2011.06.005. URL: https://linkinghub.elsevier.com/retrieve/pii/S1359029411000811 (visited on 2024-08-06) (cit. on p. 19).

[91] A. P. Jadhav, H. A. Mason, and C. L. Cepko. "Notch 1 inhibits photoreceptor production in the developing mammalian retina". In: *Development* 133.5 (2006-03-01), pp. 913–923. ISSN: 1477-9129, 0950-1991. DOI: 10.1242/dev.02245. URL: https://journals.biologists.com/dev/article/133/5/913/43470/Notch-1-inhibits-photoreceptor-production-in-the (visited on 2024-08-13) (cit. on p. 30).

[92] P. R. Jusuf et al. "Origin and Determination of Inhibitory Cell Lineages in the Vertebrate Retina". In: *The Journal of Neuroscience* 31.7 (2011-02-16), pp. 2549–2562. ISSN: 0270-6474, 1529-2401. DOI: 10.1523/JNEUROSCI.4713-10.2011. URL: https://www.jneurosci.org/lookup/doi/10.1523/JNEUROSCI.4713-10.2011 (visited on 2024-08-13) (cit. on pp. 30, 92).

[93] Y. Kalukula et al. "Mechanics and functional consequences of nuclear deformations". In: *Nature Reviews Molecular Cell Biology* 23.9 (2022-09), pp. 583–602. ISSN: 1471-0072, 1471-0080. DOI: 10.1038/s41580-022-00480-z. URL: https://www.nature.com/articles/s41580-022-00480-z (visited on 2024-08-16) (cit. on pp. 10, 16).

[94] K. Kawaguchi, R. Kageyama, and M. Sano. "Topological defects control collective dynamics in neural progenitor cell cultures". In: *Nature* 545.7654 (2017-05-18), pp. 327–331. ISSN: 0028-0836, 1476-4687. DOI: 10.1038/nature22321. URL: https://www.nature.com/articles/nature22321 (visited on 2024-08-13) (cit. on p. 19).

[95] J. N. Kay et al. "Retinal ganglion cell genesis requires lakritz, a zebrafish atonal homolog". In: *Neuron* 30.3 (2001), pp. 725–736. DOI: 10.1016/S0896-6273(01)00312-9 (cit. on p. 30).

[96] R. Keller. "Mechanisms of elongation in embryogenesis". In: *Development* 133.12 (2006-06-15), pp. 2291–2302. ISSN: 1477-9129, 0950-1991. DOI: 10.1242/dev.02406. URL: https://journals.biologists.com/dev/article/133/12/2291/43092/Mechanisms-of-elongation-in-embryogenesis (visited on 2024-08-29) (cit. on p. 24).

[97] A. Kicheva and J. Briscoe. "Developmental Pattern Formation in Phases". In: *Trends in Cell Biology* 25.10 (2015). Publisher: Elsevier Ltd, pp. 579–591. ISSN: 1879-3088 (Electronic)\r0962-8924 (Linking). DOI: 10.1016/j.tcb.2015.07.006. URL: http://dx.doi.org/10.1016/j.tcb.2015.07.006 (cit. on p. 15).

[98] A. Kicheva et al. "Coordination of progenitor specification and growth in mouse and chick spinal cord". In: *Science* 345.6204 (2014). ISSN: 1223326500. DOI: 10.1126/science (cit. on pp. 8, 15).

[99] A. R. Killaars, C. J. Walker, and K. S. Anseth. "Nuclear mechanosensing controls MSC osteogenic potential through HDAC epigenetic remodeling". In: *Proceedings of the National Academy of Sciences* 117.35 (2020-09), pp. 21258–21266. ISSN: 0027-8424, 1091-6490. DOI: 10.1073/pnas.2006765117. URL: https://pnas.org/doi/full/10.1073/pnas.2006765117 (visited on 2023-10-09) (cit. on p. 86).

[100] S. Kim et al. "A nuclear jamming transition in vertebrate organogenesis". In: *Nature Materials* (2024-08-12). ISSN: 1476-1122, 1476-4660. DOI: 10.1038/s41563-024-01972-3. URL: https://www.nature.com/articles/s41563-024-01972-3 (visited on 2024-08-13) (cit. on pp. 2, 16, 31, 34, 50, 81, 82, 84).

[101] S. Kim et al. "Embryonic tissues as active foams". In: *Nature Physics* 17.7 (2021), pp. 859–866. DOI: 10.1038/s41567-021-01215-1 (cit. on pp. 17, 21).

[102] S. Kim et al. "Hexagonal Patterning of the Insect Compound Eye: Facet Area Variation, Defects, and Disorder". In: *Biophysical Journal* 111.12 (2016-12), pp. 2735–2746. ISSN: 00063495. DOI: 10.1016/j.bpj.2016.11.004. URL: https://linkinghub.elsevier.com/retrieve/pii/S0006349516310311 (visited on 2024-04-10) (cit. on p. 23).

[103] C. B. Kimmel et al. "Stages of embryonic development of the zebrafish". In: *Developmental Dynamics* 203.3 (1995), pp. 253–310. DOI: 10.1002/aja.1002030302 (cit. on p. 92).

[104] N. J. Kirkland et al. "Tissue Mechanics Regulate Mitotic Nuclear Dynamics during Epithelial Development". In: *Current Biology* 30.13 (2020-07), 2419–2432.e4. ISSN: 09609822. DOI: 10.1016/j.cub.2020.04.041. URL: https://linkinghub.elsevier.com/retrieve/pii/S0960982220305558 (visited on 2024-07-28) (cit. on pp. 8, 12).

[105] M. Kokic et al. "Minimisation of surface energy drives apical epithelial organisation and gives rise to Lewis ' law". In: (2019) (cit. on pp. 14, 24).

[106] Y. Kosodo et al. "Regulation of interkinetic nuclear migration by cell cycle-coupled active and passive mechanisms in the developing brain: Mechanisms of interkinetic nuclear migration". In: *The EMBO Journal* 30.9 (2011-05-04), pp. 1690–1704. ISSN: 02614189. DOI: 10.1038/emboj.2011.81. URL: http://emboj.embopress.org/cgi/doi/10.1038/emboj.2011.81 (visited on 2024-08-18) (cit. on pp. 9, 10).

[107] M. Kreysing et al. "Physical insight into light scattering by photoreceptor cell nuclei". In: *Optics Letters* 35.15 (2010-08-01), p. 2639. ISSN: 0146-9592, 1539-4794. DOI: 10.1364/OL.35.002639. URL: https://opg.optica.org/abstract.cfm?URI=ol-35-15-2639 (visited on 2023-06-05) (cit. on p. 83).

[108] R. Krumlauf and D. G. Wilkinson. "Segmentation and patterning of the vertebrate hindbrain". In: *Development* 148.15 (2021-08-01), dev186460. ISSN: 0950-1991, 1477-9129. DOI: 10.1242/dev.186460. URL: https://journals.biologists.com/dev/article/148/15/dev186460/271090/Segmentation-and-patterning-of-the-vertebrate (visited on 2023-05-31) (cit. on p. 49).

[109] X. Kuang et al. "MorphoSim: an efficient and scalable phase-field framework for accurately simulating multicellular morphologies". In: *npj Systems Biology and Applications* 9.1 (2023-02-17), p. 6. ISSN: 2056-7189. DOI: 10.1038/s41540-023-00265-w. URL: https://www.nature.com/articles/s41540-023-00265-w (visited on 2024-08-13) (cit. on p. 17).

[110] F. Kubo, M. Takeichi, and S. Nakagawa. "Wnt2b controls retinal cell differentiation at the ciliary marginal zone". In: *Development* 130.3 (2003-02-01), pp. 587–598. ISSN: 1477-9129, 0950-1991. DOI: 10.1242/dev.00244. URL: https://journals.biologists.com/dev/article/130/3/587/42063/Wnt2b-controls-retinal-cell-differentiation-at-the (visited on 2024-08-13) (cit. on p. 29).

[111] J. P. Kumar and K. Moses. "Eye specification in Drosophila: perspectives and implications". In: *Seminars in Cell & Developmental Biology* 12.6 (2001-12), pp. 469–474. ISSN: 10849521. DOI: 10.1006/scdb.2001.0270. URL: https://linkinghub.elsevier.com/retrieve/pii/S1084952101902708 (visited on 2024-08-13) (cit. on p. 27).

[112] K. M. Kwan et al. "A complex choreography of cell movements shapes the vertebrate eye". In: *Development* 139.2 (2012), pp. 359–372. DOI: 10.1242/dev.071407 (cit. on pp. 28, 31).

[113] M. A. Lancaster et al. "Cerebral organoids model human brain development and microcephaly". In: *Nature* 501.7467 (2013-09-19), pp. 373–379. ISSN: 0028-0836, 1476-4687. DOI: 10.1038/nature12517. URL: https://www.nature.com/articles/nature12517 (visited on 2023-05-17) (cit. on pp. 1, 3).

[114] M. F. Land. "The optical structures of animal eyes". In: *Current Biology* 15.9 (2005-05), R319–R323. DOI: 10.1016/j.cub.2005.04.005. URL: https://www.cell.com/current-biology/fulltext/S0960-9822(05)00340-9 (cit. on p. 24).

[115] E. Lawson-Keister et al. "Differences in boundary behavior in the 3D vertex and Voronoi models". In: *PLOS Computational Biology* 20.1 (2024-01-05). Ed. by T. Bollenbach, e1011724. ISSN: 1553-7358. DOI: 10.1371/journal.pcbi.1011724. URL: https://dx.plos.org/10.1371/journal.pcbi.1011724 (visited on 2024-08-13) (cit. on p. 17).

[116] P.-F. Lenne and V. Trivedi. "Sculpting tissues by phase transitions". In: *Nature Communications* 13.1 (2022-02-03), p. 664. ISSN: 2041-1723. DOI: 10.1038/s41467-022-28151-9. URL: https://www.nature.com/articles/s41467-022-28151-9 (visited on 2024-08-13) (cit. on pp. 17, 20, 22).

[117] L. Leung et al. "Apical migration of nuclei during G2 is a prerequisite for all nuclear motion in zebrafish neuroepithelia". In: *Development* 139.14 (2012-07-15), pp. 2635–2635. ISSN: 1477-9129, 0950-1991. DOI: 10.1242/dev.085456. URL: https://journals.biologists.com/dev/article/139/14/2635/45193/Apical-migration-of-nuclei-during-G2-is-a (visited on 2024-08-18) (cit. on p. 9).

[118] E. M. Levine and E. S. Green. "Cell-intrinsic regulators of proliferation in vertebrate retinal progenitors". In: *Seminars in Cell & Developmental Biology* 15.1 (2004-02), pp. 63–74. ISSN: 10849521. DOI: 10.1016/j.semcdb.2003.09.001. URL: https://linkinghub.elsevier.com/retrieve/pii/S1084952103000648 (visited on 2024-08-13) (cit. on pp. 28, 29).

[119] F. T. Lewis. "The correlation between cell division and the shapes and sizes of prismatic cells in the epidermis of Cucumis". In: *The Anatomical Record* 38.3 (1928), pp. 341–376. DOI: 10.1002/ar.1090380305. URL: https://onlinelibrary.wiley.com/doi/10.1002/ar.1090380305 (cit. on p. 24).

[120] A. Lomakin et al. "The nucleus acts as a ruler tailoring cell responses to spatial constraints". In: *Science* 2894 (October 2019). DOI: 10.1101/863514 (cit. on pp. 10, 16).

[121] J. M. Lourenço. *The NOVAthesis LaTeX Template User's Manual*. NOVA University Lisbon. 2021. URL: https://github.com/joaomlourenco/novathesis/raw/main/template.pdf (cit. on p. i).

[122] R. B. MacDonald et al. "Müller glia provide essential tensile strength to the developing retina". In: *Journal of Cell Biology* 210.7 (2015-09-28), pp. 1075–1083. ISSN: 0021-9525, 1540-8140. DOI: 10.1083/jcb.201503115. URL: https://rupress.org/jcb/article/210/7/1075/38476/Muller-glia-provide-essential-tensile-strength-to (visited on 2024-08-13) (cit. on p. 27).

[123] S. Machado, V. Mercier, and N. Chiaruttini. "LimeSeg: a coarse-grained lipid membrane simulation for 3D image segmentation". In: *BMC Bioinformatics* 20.1 (2019), p. 2. DOI: 10.1186/s12859-018-2559-3. URL: https://bmcbioinformatics.biomedcentral.com/articles/10.1186/s12859-018-2559-3 (cit. on p. 97).

[124] M. Maia-Gil et al. *Nuclear deformability facilitates apical nuclear migration in the developing zebrafish retina*. 2024-04-04. DOI: 10.1101/2024.04.04.588091. URL: http://biorxiv.org/lookup/doi/10.1101/2024.04.04.588091 (visited on 2024-07-23) (cit. on p. 70).

[125] M. L. Manning et al. "Coaction of intercellular adhesion and cortical tension specifies tissue surface tension". In: *Proceedings of the National Academy of Sciences* 107.28 (2010-07-13), pp. 12517–12522. ISSN: 0027-8424, 1091-6490. DOI: 10.1073/pnas.1003743107. URL: https://pnas.org/doi/full/10.1073/pnas.1003743107 (visited on 2024-08-13) (cit. on pp. 17, 21).

[126] P. Marks. "Histone deacetylases". In: *Current Opinion in Pharmacology* 3.4 (2003-08), pp. 344–351. ISSN: 14714892. DOI: 10.1016/S1471-4892(03)00084-5. URL: https://linkinghub.elsevier.com/retrieve/pii/S1471489203000845 (visited on 2024-07-25) (cit. on p. 86).

[127] Y. Maroudas-Sacks et al. "Topological defects in the nematic order of actin fibres as organization centres of Hydra morphogenesis". In: *Nature Physics* 17.2 (2021-02), pp. 251–259. ISSN: 1745-2473, 1745-2481. DOI: 10.1038/s41567-020-01083-1. URL: https://www.nature.com/articles/s41567-020-01083-1 (visited on 2024-08-06) (cit. on pp. 18, 19).

[128] J. R. Martinez-Morales et al. "Differentiation of the vertebrate retina is coordinated by an FGF signaling center". In: *Developmental Cell* 8.4 (2005), pp. 565–574. DOI: 10.1016/j.devcel.2005.01.022 (cit. on pp. 30, 70).

[129] I. Masai et al. "Midline Signals Regulate Retinal Neurogenesis in Zebrafish". In: *Neuron* 27.2 (2000-08), pp. 251–263. ISSN: 08966273. DOI: 10.1016/S0896-6273(00)00034-9. URL: https://linkinghub.elsevier.com/retrieve/pii/S0896627300000349 (visited on 2023-10-06) (cit. on pp. 30, 65, 67, 92).

[130] M. Matejčić, G. Salbreux, and C. Norden. "A non-cell-autonomous actin redistribution enables isotropic retinal growth". In: *PLoS Biology* 16.8 (2018), pp. 1–29. ISSN: 1111111111. DOI: 10.1371/journal.pbio.2006018 (cit. on pp. 8, 10, 11, 14, 15, 28, 29, 31, 36, 39, 41, 42, 45, 70, 71, 82, 85).

[131] K. A. Maurer, A. N. Riesenberg, and N. L. Brown. "Notch signaling differentially regulates *Atoh7* and *Neurog2* in the distal mouse retina". In: *Development* 141.16 (2014-08-15), pp. 3243–3254. ISSN: 1477-9129, 0950-1991. DOI: 10.1242/dev.106245. URL: https://journals.biologists.com/dev/article/141/16/3243/46398/Notch-signaling-differentially-regulates-Atoh7-and (visited on 2024-08-13) (cit. on p. 30).

[132] E. McKenzie, A. Krupin, and M. W. Kelley. "Cellular growth and rearrangement during the development of the mammalian organ of Corti". In: *Developmental Dynamics* 229.4 (2004-04), pp. 802–812. ISSN: 1058-8388, 1097-0177. DOI: 10.1002/dvdy.10500. URL: https://anatomypubs.onlinelibrary.wiley.com/doi/10.1002/dvdy.10500 (visited on 2024-08-13) (cit. on pp. 23, 24).

[133] M. Merkel and M. L. Manning. "A geometrically controlled rigidity transition in a model for confluent 3D tissues". In: *New Journal of Physics* 20.2 (2018-02-15), p. 022002. ISSN: 1367-2630. DOI: 10.1088/1367-2630/aaaa13. URL: https://iopscience.iop.org/article/10.1088/1367-2630/aaaa13 (visited on 2024-08-13) (cit. on pp. 17, 21).

[134] A. L. Mescher. "Epithelial Tissue". In: *Junqueira's Basic Histology: Text and Atlas, 17th Edition*. New York, NY: McGraw Hill, 2024. URL: accessmedicine.mhmedical.com/content.aspx?aid=1208287904 (cit. on p. 2).

[135] E. J. Meyer, A. Ikmi, and M. C. Gibson. "Interkinetic nuclear migration is a broadly conserved feature of cell division in pseudostratified epithelia". In: *Current Biology* 21.6 (2011). Publisher: Elsevier Ltd, pp. 485–491. DOI: 10.1016/j.cub.2011.02.002. URL: http://dx.doi.org/10.1016/j.cub.2011.02.002 (cit. on pp. 1, 3, 6, 7, 9).

[136] G. Milazzo et al. "Histone Deacetylases (HDACs): Evolution, Specificity, Role in Transcriptional Complexes, and Pharmacological Actionability". In: *Genes* 11.5 (2020-05-15), p. 556. ISSN: 2073-4425. DOI: 10.3390/genes11050556. URL: https://www.mdpi.com/2073-4425/11/5/556 (visited on 2024-03-09) (cit. on p. 86).

[137] F. H. Millarte V. "The Golgi in cell migration: regulation by signal transduction and its implications for cancer cell metastasis." In: *ScientificWorldJournal.* (2012). DOI: 10.1100/2012/498278. URL: https://doi.org/10.1100/2012/498278 (cit. on p. 4).

[138] M. Mitov. "Cholesteric liquid crystals in living matter". In: *Soft Matter* 13.23 (2017), pp. 4176–4209. ISSN: 1744-683X, 1744-6848. DOI: 10.1039/C7SM00384F. URL: https://xlink.rsc.org/?DOI=C7SM00384F (visited on 2024-08-06) (cit. on p. 19).

[139] T. Miyata. "Development of three-dimensional architecture of the neuroepithelium: Role of pseudostratification and cellular 'community'". In: *Development, Growth & Differentiation* 50 (s1 2008-06). ISSN: 0012-1592, 1440-169X. DOI: 10.1111/j.1440-169X.2007.00980.x. URL: https://onlinelibrary.wiley.com/doi/10.1111/j.1440-169X.2007.00980.x (visited on 2024-07-29) (cit. on pp. 7, 12).

[140] A. Mongera et al. "A fluid-to-solid jamming transition underlies vertebrate body axis elongation". In: *Nature* 561.7723 (2018). Publisher: Springer US, pp. 401–405. DOI: 10.1038/s41586-018-0479-2. URL: http://dx.doi.org/10.1038/s41586-018-0479-2 (cit. on pp. 16, 21).

[141] E. Morais-de-Sá, V. Mirouse, and D. St Johnston. "aPKC Phosphorylation of Bazooka Defines the Apical/Lateral Border in Drosophila Epithelial Cells". In: *Cell* 141.3 (2010), pp. 509–523. ISSN: 0092-8674. DOI: https://doi.org/10.1016/j.cell.2010.02.040. URL: https://www.sciencedirect.com/science/article/pii/S0092867410001935 (cit. on p. 4).

[142] T. Moreno-Mármol et al. "Stretching of the retinal pigment epithelium contributes to zebrafish optic cup morphogenesis". In: *eLife* 10 (2021), pp. 1–28. DOI: 10.7554/eLife.63396 (cit. on p. 28).

[143] X. Morin, F. Jaouen, and P. Durbec. "Control of planar divisions by the G-protein regulator LGN maintains progenitors in the chick neuroepithelium". In: *Nature Neuroscience* 10.11 (2007-11), pp. 1440–1448. ISSN: 1097-6256, 1546-1726. DOI: 10.1038/nn1984. URL: https://www.nature.com/articles/nn1984 (visited on 2024-08-28) (cit. on p. 11).

[144] M. A. Morrissey and D. R. Sherwood. "An active role for basement membrane assembly and modification in tissue sculpting". In: *Journal of Cell Science* (2015-01-01), jcs.168021. ISSN: 1477-9137, 0021-9533. DOI: 10.1242/jcs.168021. URL: https://journals.biologists.com/jcs/article/doi/10.1242/jcs.168021/260513/An-active-role-for-basement-membrane-assembly-and (visited on 2024-07-30) (cit. on pp. 5, 6).

[145] Y.-i. Nakajima et al. "Epithelial junctions maintain tissue architecture by directing planar spindle orientation". In: *Nature* 500.7462 (2013-08), pp. 359–362. ISSN: 0028-0836, 1476-4687. DOI: 10.1038/nature12335. URL: https://www.nature.com/articles/nature12335 (visited on 2024-08-28) (cit. on p. 11).

[146] T. Nakano et al. "Self-formation of optic cups and storable stratified neural retina from human ESCs". In: *Cell Stem Cell* 10.6 (2012). Publisher: Elsevier Inc., pp. 771–785. DOI: 10.1016/j.stem.2012.05.009. URL: http://dx.doi.org/10.1016/j.stem.2012.05.009 (cit. on pp. 1, 3, 27).

[147] F. R. Napoli et al. "Cephalopod retinal development shows vertebrate-like mechanisms of neurogenesis". In: *Current Biology* 32.23 (2022-12), 5045–5056.e3. ISSN: 09609822. DOI: 10.1016/j.cub.2022.10.027. URL: https://linkinghub.elsevier.com/retrieve/pii/S0960982222016724 (visited on 2024-08-05) (cit. on pp. 6, 28).

[148] E. Nerli, M. Rocha-Martins, and C. Norden. "Asymmetric neurogenic commitment of retinal progenitors involves notch through the endocytic pathway". In: *eLife* 9 (2020), pp. 1–25. DOI: 10.7554/eLife.60462 (cit. on pp. 10, 30, 67, 83).

[149] E. Nerli et al. "Deterministic and probabilistic fate decisions co-exist in a single retinal lineage". In: *The EMBO Journal* 42.14 (2023-07-17), e112657. ISSN: 0261-4189, 1460-2075. DOI: 10.15252/embj.2022112657. URL: https://www.embopress.org/doi/10.15252/embj.2022112657 (visited on 2024-02-09) (cit. on p. 70).

[150] D.-E. Nilsson. "The evolution of eyes and visually guided behaviour". In: *Philosophical Transactions of the Royal Society B: Biological Sciences* 364.1531 (2009-10-12), pp. 2833–2847. ISSN: 0962-8436, 1471-2970. DOI: 10.1098/rstb.2009.0083. URL: https://royalsocietypublishing.org/doi/10.1098/rstb.2009.0083 (visited on 2024-08-09) (cit. on pp. 24, 25, 27).

[151] C. Norden. "A Fish Eye View: Retinal Morphogenesis from Optic Cup to Neuronal Lamination". In: *Annual Review of Cell and Developmental Biology* 39.1 (2023-10-16), pp. 175–196. ISSN: 1081-0706, 1530-8995. DOI: 10.1146/annurev-cellbio-012023-013036. URL: https://www.annualreviews.org/doi/10.1146/annurev-cellbio-012023-013036 (visited on 2023-12-15) (cit. on pp. 26, 28, 29, 32).

[152] C. Norden. "Pseudostratified epithelia – cell biology, diversity and roles in organ formation at a glance". In: *Journal of Cell Science* 130.11 (2017), pp. 1859–1863. DOI: 10.1242/jcs.192997 (cit. on pp. 3, 5, 6, 8).

[153] C. Norden et al. "Actomyosin Is the Main Driver of Interkinetic Nuclear Migration in the Retina". In: *Cell* 138.6 (2009). Publisher: Elsevier Ltd, pp. 1195–1208. DOI: 10.1016/j.cell.2009.06.032. URL: http://dx.doi.org/10.1016/j.cell.2009.06.032 (cit. on pp. 6, 7, 9, 10).

[154] S.-i. Ohnuma et al. "Co-ordinating retinal histogenesis: early cell cycle exit enhances early cell fate determination in the *Xenopus* retina". In: *Development* 129.10 (2002-05-15), pp. 2435–2446. ISSN: 1477-9129, 0950-1991. DOI: 10.1242/dev.129.10.2435. URL: https://journals.biologists.com/dev/article/129/10/2435/41716/Co-ordinating-retinal-histogenesis-early-cell (visited on 2024-08-13) (cit. on p. 29).

[155] A. Ohtoshi et al. "Regulation of Retinal Cone Bipolar Cell Differentiation and Photopic Vision by the CVC Homeobox Gene Vsx1". In: *Current Biology* 14.6 (2004-03), pp. 530–536. ISSN: 09609822. DOI: 10.1016/j.cub.2004.02.027. URL: https://linkinghub.elsevier.com/retrieve/pii/S0960982204000922 (visited on 2024-08-13) (cit. on p. 30).

[156] G. Y. Onoda and E. G. Liniger. "Random loose packings of uniform spheres and the dilatancy onset". In: *Physical Review Letters* 64.22 (1990-05-28), pp. 2727–2730. ISSN: 0031-9007. DOI: 10.1103/PhysRevLett.64.2727. URL: https://link.aps.org/doi/10.1103/PhysRevLett.64.2727 (visited on 2023-03-07) (cit. on p. 50).

[157] L. Oswald et al. "Jamming transitions in cancer". In: *Journal of Physics D: Applied Physics* 50.48 (2017-12-06), p. 483001. ISSN: 0022-3727, 1361-6463. DOI: 10.1088/1361-6463/aa8e83. URL: https://iopscience.iop.org/article/10.1088/1361-6463/aa8e83 (visited on 2024-08-13) (cit. on p. 21).

[158] D. W. Oxtoby, H. P. Gillis, and A. Campion. "Phase Transition". In: *Principles of Modern Chemistry. 6th Edition*. Singapore: Thomson/Brooks/Cole, 2008, pp. 428–430 (cit. on p. 17).

[159] C. Parada et al. "Mechanical feedback defines organizing centers to drive digit emergence". In: *Developmental Cell* 57.7 (2022-04), 854–866.e6. ISSN: 15345807. DOI: 10.1016/j.devcel.2022.03.004. URL: https://linkinghub.elsevier.com/retrieve/pii/S1534580722001642 (visited on 2024-05-02) (cit. on p. 34).

[160] J. A. Park et al. "Unjamming and cell shape in the asthmatic airway epithelium". In: *Nature Materials* 14.10 (2015), pp. 1040–1048. DOI: 10.1038/nmat4357 (cit. on pp. 20, 21).

[161] J.-A. Park et al. "Collective migration and cell jamming in asthma, cancer and development". In: *Journal of Cell Science* 129.18 (2016-09-15), pp. 3375–3383. ISSN: 1477-9137, 0021-9533. DOI: 10.1242/jcs.187922. URL: https://journals.biologists.com/jcs/article/129/18/3375/55731/Collective-migration-and-cell-jamming-in-asthma (visited on 2024-08-13) (cit. on p. 17).

[162] J. C. Pastor-Pareja and T. Xu. "Shaping Cells and Organs in Drosophila by Opposing Roles of Fat Body-Secreted Collagen IV and Perlecan". In: *Developmental Cell* 21.2 (2011), pp. 245–256. ISSN: 1534-5807. DOI: https://doi.org/10.1016/j.devcel.2011.06.026. URL: https://www.sciencedirect.com/science/article/pii/S1534580711002607 (cit. on pp. 6, 11).

[163] N. I. Petridou et al. "Fluidization-mediated tissue spreading by mitotic cell rounding and non-canonical Wnt signalling". In: *Nature Cell Biology* 21.2 (2019). Publisher: Springer US, pp. 169–178. DOI: 10.1038/s41556-018-0247-4. URL: http://dx.doi.org/10.1038/s41556-018-0247-4 (cit. on pp. 16, 19, 21).

[164] N. I. Petridou et al. "Rigidity percolation uncovers a structural basis for embryonic tissue phase transitions". In: *Cell* 184.7 (2021-04), 1914–1928.e19. ISSN: 00928674. DOI: 10.1016/j.cell.2021.02.017. URL: https://linkinghub.elsevier.com/retrieve/pii/S0092867421001677 (visited on 2024-08-04) (cit. on pp. 16, 19, 21).

[165] N. Picciani et al. "Prolific Origination of Eyes in Cnidaria with Co-option of Non-visual Opsins". In: *Current Biology* 28.15 (2018), 2413–2419.e4. ISSN: 0960-9822. DOI: https://doi.org/10.1016/j.cub.2018.05.055. URL: https://www.sciencedirect.com/science/article/pii/S0960982218306912 (cit. on p. 25).

[166] L. Poggi et al. "Influences on neural lineage and mode of division in the zebrafish retina in vivo". In: *The Journal of Cell Biology* 171.6 (2005-12-19), pp. 991–999. ISSN: 1540-8140, 0021-9525. DOI: 10.1083/jcb.200509098. URL: https://rupress.org/jcb/article/171/6/991/52086/Influences-on-neural-lineage-and-mode-of-division (visited on 2024-08-13) (cit. on p. 30).

[167] P. Rakic. "Mode of cell migration to the superficial layers of fetal monkey neocortex". In: *The Journal of Comparative Neurology* 145-1 (1972), pp. 61–83. URL: https://doi.org/10.1002/cne.901450105 (cit. on p. 7).

[168] Y. Ravichandran, B. Goud, and J.-B. Manneville. "The Golgi apparatus and cell polarity: Roles of the cytoskeleton, the Golgi matrix, and Golgi membranes". In: *Current Opinion in Cell Biology* 62 (2020). Cell Architecture, pp. 104–113. ISSN: 0955-0674. DOI: https://doi.org/10.1016/j.ceb.2019.10.003. URL: https://www.sciencedirect.com/science/article/pii/S0955067419300900 (cit. on p. 4).

[169] A. Reichenbach et al. "How light traverses the inverted vertebrate retina: No flaw of nature". In: *e-Neuroforum* 5.4 (2014-11), pp. 93–100. ISSN: 1868-856X. DOI: 10.1007/s13295-014-0054-8. URL: http://link.springer.com/10.1007/s13295-014-0054-8 (visited on 2024-05-14) (cit. on p. 83).

[170] M. Rocha-Martins et al. "Neuronal migration prevents spatial competition in retinal morphogenesis". In: *Nature* 620.7974 (2023-08-17), pp. 615–624. ISSN: 0028-0836, 1476-4687. DOI: 10.1038/s41586-023-06392-y. URL: https://www.nature.com/articles/s41586-023-06392-y (visited on 2024-02-21) (cit. on pp. 10, 12, 30, 31).

[171] K. Röper. "Anisotropy of Crumbs and aPKC Drives Myosin Cable Assembly during Tube Formation". In: *Developmental Cell* 23.5 (2012), pp. 939–953. ISSN: 1534-5807. DOI: https://doi.org/10.1016/j.devcel.2012.09.013. URL: https://www.sciencedirect.com/science/article/pii/S1534580712004248 (cit. on p. 4).

[172] C. Royer et al. "ASPP2 maintains the integrity of mechanically stressed pseudostratified epithelia during morphogenesis". In: *Nature Communications* 13.1 (2022-02-17), p. 941. ISSN: 2041-1723. DOI: 10.1038/s41467-022-28590-4. URL: https://www.nature.com/articles/s41467-022-28590-4 (visited on 2024-07-29) (cit. on pp. 5, 6, 11).

[173] A. J. D. Ruijter et al. "Histone deacetylases (HDACs): characterization of the classical HDAC family". In: *Biochemical Journal* 370.3 (2003-03-15), pp. 737–749. ISSN: 0264-6021, 1470-8728. DOI: 10.1042/bj20021321. URL: https://portlandpress.com/biochemj/article/370/3/737/40550/Histone-deacetylases-HDACs-characterization-of-the (visited on 2024-07-25) (cit. on p. 86).

[174] M. A. Rujano et al. "The microcephaly protein Asp regulates neuroepithelium morphogenesis by controlling the spatial distribution of myosin II". In: *Nature Cell Biology* 15.11 (2013-11), pp. 1294–1306. ISSN: 1465-7392, 1476-4679. DOI: 10.1038/ncb2858. URL: https://www.nature.com/articles/ncb2858 (visited on 2024-08-18) (cit. on pp. 3, 6, 9).

[175] S. Runser, R. Vetter, and D. Iber. "SimuCell3D: three-dimensional simulation of tissue mechanics with cell polarization". In: *Nature Computational Science* 4.4 (2024-04-09), pp. 299–309. ISSN: 2662-8457. DOI: 10.1038/s43588-024-00620-9. URL: https://www.nature.com/articles/s43588-024-00620-9 (visited on 2024-08-13) (cit. on p. 17).

[176] F. C. Sauer. "Mitosis in the neural tube". In: *Journal of Comparative Neurology* 62 (2 1935), pp. 377–405. DOI: 10.1002/cne.900620207. URL: https://doi.org/10.1002/cne.900620207 (cit. on pp. 4, 6, 11).

[177] T. Savin et al. "On the growth and form of the gut". In: *Nature* 476.7358 (2011-08), pp. 57–62. ISSN: 0028-0836, 1476-4687. DOI: 10.1038/nature10277. URL: https://www.nature.com/articles/nature10277 (visited on 2024-07-25) (cit. on p. 88).

[178] T. B. Saw et al. "Topological defects in epithelia govern cell death and extrusion". In: *Nature* 544.7649 (2017-04-13), pp. 212–216. ISSN: 0028-0836, 1476-4687. DOI: 10.1038/nature21718. URL: https://www.nature.com/articles/nature21718 (visited on 2024-08-13) (cit. on p. 19).

[179] T. Schluck et al. "Mechanical Control of Organ Size in the Development of the Drosophila Wing Disc". In: *PLoS ONE* 8.10 (2013-10-25). Ed. by R. M. H. Merks, e76171. ISSN: 1932-6203. DOI: 10.1371/journal.pone.0076171. URL: https://dx.plos.org/10.1371/journal.pone.0076171 (visited on 2024-07-29) (cit. on p. 90).

[180] E. A. Schmitt and J. E. Dowling. "Early retinal development in the zebrafish,Danio rerio: Light and electron microscopic analyses". In: *The Journal of Comparative Neurology* 404.4 (1999-02-22), pp. 515–536. ISSN: 0021-9967, 1096-9861. DOI: 10.1002/(SICI)1096-9861(19990222)404:4<515::AID-CNE8>3.0.CO;2-A. URL: https://onlinelibrary.wiley.com/doi/10.1002/(SICI)1096-9861(19990222)404:4%3C515::AID-CNE8%3E3.0.CO;2-A (visited on 2024-08-13) (cit. on p. 30).

[181] M. L. Schneider, D. L. Turner, and M. L. Vetter. "Notch Signaling Can Inhibit Xath5 Function in the Neural Plate and Developing Retina". In: *Molecular and Cellular Neuroscience* 18.5 (2001-11), pp. 458–472. ISSN: 10447431. DOI: 10.1006/mcne.2001.1040. URL: https://linkinghub.elsevier.com/retrieve/pii/S1044743101910401 (visited on 2024-08-13) (cit. on p. 30).

[182] P. M. Schoenwolf GC. "Shaping of the chick neuroepithelium during primary and secondary neurulation: role of cell elongation." In: *The Anatomical Record* 218(2) (1987), pp. 182–95. DOI: 10.1002/ar.1092180214. URL: https://doi.org/10.1002/ar.1092180214 (cit. on p. 8).

[183] E. M. Schötz et al. "Glassy dynamics in three-dimensional embryonic tissues". In: *Journal of the Royal Society Interface* 10.89 (2013). DOI: 10.1098/rsif.2013.0726 (cit. on pp. 17, 21).

[184] C. Schwayer et al. "Mechanosensation of Tight Junctions Depends on ZO-1 Phase Separation and Flow". In: *Cell* 179.4 (2019-10), 937–952.e18. ISSN: 00928674. DOI: 10.1016/j.cell.2019.10.006. URL: https://linkinghub.elsevier.com/retrieve/pii/S0092867419311225 (visited on 2024-07-29) (cit. on p. 5).

[185] J. M. Serb and D. J. Eernisse. "Charting Evolution's Trajectory: Using Molluscan Eye Diversity to Understand Parallel and Convergent Evolution". In: *Evolution: Education and Outreach* 1.4 (2008), pp. 439–447. DOI: 10.1007/s12052-008-0084-1. URL: https://doi.org/10.1007/s12052-008-0084-1 (cit. on p. 27).

[186] T. Shinoda et al. "Elasticity-based boosting of neuroepithelial nucleokinesis via indirect energy transfer from mother to daughter". In: *PLOS Biology* 16.4 (2018-04-20). Ed. by H. Kennedy, e2004426. ISSN: 1545-7885. DOI: 10.1371/journal.pbio.2004426. URL: https://dx.plos.org/10.1371/journal.pbio.2004426 (visited on 2024-08-28) (cit. on pp. 9, 10).

[187] M. Shinya et al. "Zebrafish Dkk1, induced by the pre-MBT Wnt signaling, is secreted from the prechordal plate and patterns the anterior neural plate". In: *Mechanisms of Development* (2000) (cit. on pp. 62, 65, 86).

[188] J. Sidhaye and C. Norden. "Concerted action of neuroepithelial basal shrinkage and active epithelial migration ensures efficient optic cup morphogenesis". In: *eLife* 6 (2017), pp. 1–29. DOI: 10.7554/elife.22689 (cit. on p. 28).

[189] I. Smart. "Proliferative characteristics of the ependymal layer during the early development of the spinal cord in the mouse." In: *Journal of Anatomy* 111 (3 1972), pp. 365–380 (cit. on pp. 4, 7, 12, 15).

[190] K. G. Soans and C. Norden. "Shining a light on extracellular matrix dynamics in vivo". In: *Seminars in Cell & Developmental Biology* 120 (2021-12), pp. 85–93. ISSN: 10849521. DOI: 10.1016/j.semcdb.2021.05.008. URL: https://linkinghub.elsevier.com/retrieve/pii/S1084952121001178 (visited on 2024-07-30) (cit. on p. 6).

[191] K. G. Soans et al. "Collective cell migration during optic cup formation features changing cell-matrix interactions linked to matrix topology". In: *Current Biology* 32.22 (2022-11), 4817–4831.e9. ISSN: 09609822. DOI: 10.1016/j.cub.2022.09.034. URL: https://linkinghub.elsevier.com/retrieve/pii/S0960982222015032 (visited on 2024-06-10) (cit. on pp. 28, 92).

[192] I. Solovei et al. "Nuclear Architecture of Rod Photoreceptor Cells Adapts to Vision in Mammalian Evolution". In: *Cell* 137.2 (2009-04), pp. 356–368. ISSN: 00928674. DOI: 10.1016/j.cell.2009.01.052. URL: https://linkinghub.elsevier.com/retrieve/pii/S0092867409001378 (visited on 2023-05-31) (cit. on p. 83).

[193] J. O. Songco-Casey et al. "Cell types and molecular architecture of the Octopus bimaculoides visual system". In: *Current Biology* 32.23 (2022-12), 5031–5044.e4. ISSN: 09609822. DOI: 10.1016/j.cub.2022.10.015. URL: https://linkinghub.elsevier.com/retrieve/pii/S0960982222016232 (visited on 2024-08-13) (cit. on p. 25).

[194] J. A. Stadler et al. "Histone deacetylase 1 is required for cell cycle exit and differentiation in the zebrafish retina". In: *Developmental Dynamics* 233.3 (2005), pp. 883–889. DOI: 10.1002/dvdy.20427 (cit. on p. 71).

[195] M. J. Stephen and J. P. Straley. "Physics of liquid crystals". In: *Rev. Mod. Phys.* 46 (4 1974-10), pp. 617–704. DOI: 10.1103/RevModPhys.46.617. URL: https://link.aps.org/doi/10.1103/RevModPhys.46.617 (cit. on p. 17).

[196] C. L. Stoick-Cooper et al. "Distinct Wnt signaling pathways have opposing roles in appendage regeneration". In: *Development* 134 (2007), pp. 479–489. DOI: 10.1242/dev.001123 (cit. on pp. 62, 92).

[197] S. J. Streichan et al. "Spatial constraints control cell proliferation in tissues". In: *Proceedings of the National Academy of Sciences of the United States of America* 111.15 (2014), pp. 5586–5591. DOI: 10.1073/pnas.1323016111 (cit. on p. 90).

[198] C. Stringer et al. "Cellpose: a generalist algorithm for cellular segmentation". In: *Nature Methods* 18.1 (2021-01), pp. 100–106. ISSN: 1548-7091, 1548-7105. DOI: 10.1038/s41592-020-01018-x. URL: https://www.nature.com/articles/s41592-020-01018-x (visited on 2024-08-29) (cit. on p. 38).

[199] P. J. Strzyz et al. "Interkinetic Nuclear Migration Is Centrosome Independent and Ensures Apical Cell Division to Maintain Tissue Integrity". In: *Developmental Cell* 32.2 (2015). Publisher: Elsevier Inc., pp. 203–219. DOI: 10.1016/j.devcel.2014.12.001. URL: http://dx.doi.org/10.1016/j.devcel.2014.12.001 (cit. on pp. 4, 6, 9, 11, 12, 75, 82).

[200] K. Subramanian et al. "Rod nuclear architecture determines contrast transmission of the retina and behavioral sensitivity in mice". In: *eLife* 8 (2019-12-11), e49542. ISSN: 2050-084X. DOI: 10.7554/eLife.49542. URL: https://elifesciences.org/articles/49542 (visited on 2023-06-05) (cit. on p. 83).

[201] T. Tallinen et al. "Gyrification from constrained cortical expansion". In: *Proceedings of the National Academy of Sciences* 111.35 (2014-09-02), pp. 12667–12672. ISSN: 0027-8424, 1091-6490. DOI: 10.1073/pnas.1406015111. URL: https://pnas.org/doi/full/10.1073/pnas.1406015111 (visited on 2024-07-25) (cit. on p. 88).

[202] M. Tamada and J. A. Zallen. "Square Cell Packing in the Drosophila Embryo through Spatiotemporally Regulated EGF Receptor Signaling". In: *Developmental Cell* 35.2 (2015-10), pp. 151–161. ISSN: 15345807. DOI: 10.1016/j.devcel.2015.09.015. URL: https://linkinghub.elsevier.com/retrieve/pii/S1534580715006164 (visited on 2024-08-27) (cit. on p. 23).

[203] E. Taverna et al. "Non-canonical features of the Golgi apparatus in bipolar epithelial neural stem cells". In: *Scientific Reports* 6.1 (2016-02-16), p. 21206. ISSN: 2045-2322. DOI: 10.1038/srep21206. URL: https://doi.org/10.1038/srep21206 (cit. on p. 4).

[204] R. J. Tetley and Y. Mao. "The same but different: cell intercalation as a driver of tissue deformation and fluidity". In: *Philosophical Transactions of the Royal Society B: Biological Sciences* 373.1759 (2018-11-05), p. 20170328. ISSN: 0962-8436, 1471-2970. DOI: 10.1098/rstb.2017.0328. URL: https://royalsocietypublishing.org/doi/10.1098/rstb.2017.0328 (visited on 2024-08-20) (cit. on p. 16).

[205] A. J. Thompson et al. "Rapid changes in tissue mechanics regulate cell behaviour in the developing embryonic brain". In: *eLife* 8 (2019-01-15), e39356. ISSN: 2050-084X. DOI: 10.7554/eLife.39356. URL: https://elifesciences.org/articles/39356 (visited on 2024-08-13) (cit. on pp. 16, 34).

[206] M. Tozluoğlu et al. "Planar Differential Growth Rates Initiate Precise Fold Positions in Complex Epithelia". In: *Developmental Cell* 51.3 (2019-11), 299–312.e4. ISSN: 15345807. DOI: 10.1016/j.devcel.2019.09.009. URL: https://linkinghub.

elsevier.com/retrieve/pii/S1534580719307385 (visited on 2024-07-25) (cit. on p. 88).

[207] X. Trepat et al. "Physical forces during collective cell migration". In: *Nature Physics* 5.6 (2009-06), pp. 426–430. ISSN: 1745-2473, 1745-2481. DOI: 10.1038/nphys1269. URL: https://www.nature.com/articles/nphys1269 (visited on 2024-08-07) (cit. on p. 21).

[208] A. Trushko et al. "Buckling of an Epithelium Growing under Spherical Confinement". In: *Developmental Cell* 54.5 (2020-09), 655–668.e6. ISSN: 15345807. DOI: 10.1016/j.devcel.2020.07.019. URL: https://linkinghub.elsevier.com/retrieve/pii/S1534580720305943 (visited on 2024-05-15) (cit. on p. 87).

[209] E. Tsingos et al. "Retinal stem cells modulate proliferative parameters to coordinate post-embryonic morphogenesis in the eye of fish". In: *eLife* 8 (2019), pp. 1–38. DOI: 10.7554/eLife.42646 (cit. on p. 88).

[210] J. M. Tworig and M. B. Feller. "Müller Glia in Retinal Development: From Specification to Circuit Integration". In: *Frontiers in Neural Circuits* 15 (2022-02-04), p. 815923. ISSN: 1662-5110. DOI: 10.3389/fncir.2021.815923. URL: https://www.frontiersin.org/articles/10.3389/fncir.2021.815923/full (visited on 2024-08-13) (cit. on p. 27).

[211] T. J. Van Raay et al. "Frizzled 5 Signaling Governs the Neural Potential of Progenitors in the Developing Xenopus Retina". In: *Neuron* 46.1 (2005-04), pp. 23–36. ISSN: 08966273. DOI: 10.1016/j.neuron.2005.02.023. URL: https://linkinghub.elsevier.com/retrieve/pii/S0896627305001662 (visited on 2023-10-06) (cit. on p. 8).

[212] E. S. Veien et al. "Canonical Wnt signaling is required for maintenance of dorsal retinal identity". In: *Development* 135.24 (2008-12). Author manuscript; available in PMC 2009 Dec 1. Published online 2008 Nov 12., pp. 4101–4111. DOI: 10.1242/dev.027367 (cit. on p. 89).

[213] V. Venturini et al. "The nucleus measures shape changes for cellular proprioception to control dynamic cell behavior". In: *Science* 370.6514 (2020-10-16), eaba2644. ISSN: 0036-8075, 1095-9203. DOI: 10.1126/science.aba2644. URL: https://www.science.org/doi/10.1126/science.aba2644 (visited on 2024-08-18) (cit. on pp. 10, 16).

[214] R. Vetter and D. Iber. "Precision of morphogen gradients in neural tube development". In: *Nature Communications* 13.1 (2022-03-03), p. 1145. ISSN: 2041-1723. DOI: 10.1038/s41467-022-28834-3. URL: https://www.nature.com/articles/s41467-022-28834-3 (visited on 2024-08-18) (cit. on p. 14).

[215] C. Villeneuve et al. "Mechanical forces across compartments coordinate cell shape and fate transitions to generate tissue architecture". In: *Nature Cell Biology* 26.2 (2024-02), pp. 207–218. ISSN: 1465-7392, 1476-4679. DOI: 10.1038/s41556-023-01332-4. URL: https://www.nature.com/articles/s41556-023-01332-4 (visited on 2024-08-04) (cit. on p. 87).

[216] S. Vinothkumar et al. "Sequential and cooperative action of Fgfs and Shh in the zebrafish retina". In: *Developmental Biology* 314.1 (2008-02), pp. 200–214. ISSN: 00121606. DOI: 10.1016/j.ydbio.2007.11.034. URL: https://linkinghub.elsevier.com/retrieve/pii/S0012160607015680 (visited on 2024-08-13) (cit. on p. 30).

[217] M. Vitorino et al. "Vsx2 in the zebrafish retina: restricted lineages through derepression". In: *Neural Development* 4.1 (2009-12), p. 14. ISSN: 1749-8104. DOI: 10.1186/1749-8104-4-14. URL: https://neuraldevelopment.biomedcentral.com/articles/10.1186/1749-8104-4-14 (visited on 2024-08-13) (cit. on p. 30).

[218] L. Von Chamier et al. "Democratising deep learning for microscopy with ZeroCostDL4Mic". In: *Nature Communications* 12.1 (2021-04-15), p. 2276. ISSN: 2041-1723. DOI: 10.1038/s41467-021-22518-0. URL: https://www.nature.com/articles/s41467-021-22518-0 (visited on 2024-08-29) (cit. on p. 38).

[219] X. Wang et al. "Anisotropy links cell shapes to tissue flow during convergent extension". In: *Proceedings of the National Academy of Sciences* 117.24 (2020-06-16), pp. 13541–13551. ISSN: 0027-8424, 1091-6490. DOI: 10.1073/pnas.1916418117. URL: https://pnas.org/doi/full/10.1073/pnas.1916418117 (visited on 2024-08-13) (cit. on pp. 17, 21).

[220] Y. Wang and J. Nathans. "Tissue/planar cell polarity in vertebrates: new insights and new questions". In: *Development* 134.4 (2007-02-15), pp. 647–658. ISSN: 1477-9129, 0950-1991. DOI: 10.1242/dev.02772. URL: https://journals.biologists.com/dev/article/134/4/647/52973/Tissue-planar-cell-polarity-in-vertebrates-new (visited on 2024-08-13) (cit. on p. 24).

[221] I. P. Weber et al. "Mitotic Position and Morphology of Committed Precursor Cells in the Zebrafish Retina Adapt to Architectural Changes upon Tissue Maturation". In: *Cell Reports* 7.2 (2014-04), pp. 386–397. ISSN: 22111247. DOI: 10.1016/j.celrep.2014.03.014. URL: https://linkinghub.elsevier.com/retrieve/pii/S2211124714001922 (visited on 2024-07-24) (cit. on pp. 12, 31, 58).

[222] M. Weigert et al. "Star-convex Polyhedra for 3D Object Detection and Segmentation in Microscopy". In: 1 (2019). URL: http://arxiv.org/abs/1908.03636 (cit. on pp. 38, 97).

[223] T. J. Widmann and C. Dahmann. "Dpp signaling promotes the cuboidal-to-columnar shape transition of Drosophila wing disc epithelia by regulating Rho1". In: *Journal of Cell Science* 122.9 (2009-05-01), pp. 1362–1373. ISSN: 1477-9137, 0021-9533. DOI: 10.1242/jcs.044271. URL: https://journals.biologists.com/jcs/article/122/9/1362/35618/Dpp-signaling-promotes-the-cuboidal-to-columnar (visited on 2024-08-17) (cit. on pp. 8, 14).

[224] M. Yamaguchi et al. "Histone deacetylase 1 regulates retinal neurogenesis in zebrafish by suppressing Wnt ad Notch signaling pathways". In: *Development* 132.13 (2005), pp. 3027–3043. DOI: 10.1242/dev.01881 (cit. on p. 87).

[225] I. Yanakieva et al. "Cell and tissue morphology determine actin-dependent nuclear migration mechanisms in neuroepithelia". In: *The Journal of cell biology* 218.10 (2019), pp. 3272–3289. DOI: 10.1083/jcb.201901077 (cit. on pp. 8, 9, 48).

[226] R. M. Young et al. "Compensatory growth renders Tcf7l1a dispensable for eye formation despite its requirement in eye field specification". In: *eLife* 8 (2019), pp. 1–32. DOI: 10.7554/eLife.40093 (cit. on pp. 62, 63, 67, 70, 88–90).

[227] M. Zagorski et al. "Decoding of position in the developing neural tube from antiparallel morphogen gradients". In: *Science* (June 2017), pp. 1–5 (cit. on p. 14).

[228] F. R. Zolessi et al. "Polarization and orientation of retinal ganglion cells in vivo". In: *Neural Development* 1 (2006), p. 2. DOI: 10.1186/1749-8104-1-2. URL: https://neuraldevelopment.biomedcentral.com/articles/10.1186/1749-8104-1-2 (cit. on pp. 30, 92).

[229] M. E. Zuber et al. "Giant Eyes in Xenopus laevis by Overexpression of XOptx2". In: *Cell* 98.3 (1999-08), pp. 341–352. ISSN: 00928674. DOI: 10.1016/S0092-8674(00)81963-7. URL: https://linkinghub.elsevier.com/retrieve/pii/S0092867400819637 (visited on 2024-01-07) (cit. on pp. 29, 87).

ITQB NOVA, Avenida da República, 2780-157 Oeiras, Portugal | Tel +351 214 469 100 | itqb.unl.pt